Development and Validation of turbulence models for Lattice Boltzmann schemes

Von der
Fakultät Architektur, Bauingenieurwesen und Umweltwissenschaften
der Technischen Universität Carolo-Wilhelmina
zu Braunschweig

zur Erlangung des Grades eines
Doktoringenieurs (Dr.-Ing.)
genehmigte

Dissertation

von
Sonja Uphoff
geboren am 29. August 1983
in Bielefeld

Eingereicht am	25.11.2012
Mündliche Prüfung am	17.01.2013
Berichterstatter	Prof. Dr.-Ing. habil. Manfred Krafczyk
	Prof. Dr.-Ing. Sabine Langer

2013

Danksagung

Diese Arbeit entstand im Rahmen einer Forschungsarbeit am iRMB im Rahmen des GRK802 und des SFB 880. Ohne die Unterstützung verschiedener Menschen hätte diese Arbeit so nicht entstehen können. Bei ihnen möchte ich mich hier bedanken.

Zuerst möchte ich mich bedanken bei Prof. Manfred Krafczyk, der diese Arbeit betreut hat, dafür dass er mir Zeit gelassen hat wenn Dinge mal nicht gleich funktiontierten und mich mit vielen Vorschlägen und kritischen, detaillierten Nachfragen unterstützt hat. Ausserdem hat er mir besonders zu Beginn meiner Arbeit aber auch später geholfen die Richtung meiner Forschung zu finden.

Bei Frau Prof. Langer bedanke ich mich für die Übernahme des Ko-Referats.

Meinen Kollegen und Kolleginnen danke ich für Mittagspausen, Hilfe bei Programmierfragen und die Entwickung von Virtual Fluids (insbesondere bei Sebastian Geller), für kritisches Zuhören und Glätten von verworrenen Gedanken (bei Ying Wang und Maik Stiebler) und für einige gute Ideen (unter anderem bei Martin Geier). Ausserdem möchte ich mich bei den verschiedenen Kollegen bedanken, mit denen ich in den vergangenen 4 1/2 Jahren ein Büro teilen durfte und die mich auf unterschiedliche Weise unterstützt, abgelenkt und aufgemuntert haben. Das sind Jan, Sara, Sebastian, kurz Christian in RI, Ying & Fremont und Maik. Bei den Mitgliedern der Graduiertenkollegs 802 und Prof. Bartoli möchte ich mich für eine schöne Zeit and der Università degli Studi di Firenze bedanken, in der ich viel gelernt habe.

Den Kollegen und Freunden, die in den letzten Wochen teils sehr gründlich mit dem Korrekturlesen geholfen haben gebührt Dank: Johannes Gütschow, Tobias Wagner, Hodei Aizpurua, Stephan Uphoff, Anette Uphoff, Christian Janßen, Sebastian Geller, Ying Wang, Martin Geier, Maik Stiebler, Georg Eitel-Amor, Konstantin Kucher, Myriam El Bettah.

Außerdem möchte ich bei denjenigen bedanken, die mich in der ganzen Zeit unterstützt haben: Meinen Eltern, die mir das Studium ermöglicht haben. Meiner WG, für Ablenkung und Alltag. Schließlich möchte ich mich noch bei Johannes bedanken, für Geduld und Unterstützung, für die Wochenenden (vor allem die vor der Abgabe) hinter dem Computer und für die ohne Computer.

Zusammenfassung

Strömungsmechaniksimulationen sind in vielen Bereichen des Ingenieurwesens bereits Standard. Für die anspruchsvollen Simulationen von Strömungen auf Gebäudeskala im Bauingenieurwesen ist dies jedoch aufgrund des hohen Aufwands und der komplexen Geometrien noch nicht der Fall. Insbesondere zeitaufgelöste dreidimensionale Simulationen wie Large Eddy Simulationen finden in der Praxis kaum Anwendung. Andererseits kann damit gerechnet werden, dass mit der zunehmender Leistungsfähigkeit von Rechnersystemen und Fortschritten bei numerischen Methoden relevante Anwendungen immer praktikabler werden.

In dieser Arbeit wurde als Ausgangspunkt das Lattice Boltzmann Verfahren gewählt. Aufgrund der guten Parallelisierbarkeit eignet es sich für derart aufwändige Anwendungen besonders. Verschiedene Varianten des Lattice-Boltzmann-Verfahrens, nämlich das Lattice-Bhatnagar-Gross-Krook-Verfahren (LBGK), das Multiple-Relaxation-Time-Verfahren (MRT) und Varianten des Kaskadierten Lattice-Boltzmann-Verfahrens (CLB), wurden implementiert und anhand von Benchmarks verglichen. Desweiteren wurden verschiedene Turbulenzmodelle, wie das Smagorinsky-Modell, das wall adapting local eddy-viscosity-Modell und das Vreman-Modell untersucht. Dabei wurde ein besonderes Augenmerk auf die Anwendbarkeit der Lattice-Boltzmann-Modelle bei turbulenten Strömungen gerichtet und auch berücksichtigt, dass eine Wechselwirkung zwischen dem verwendeten Lattice-Boltzmann-Modell und dem Large-Eddy-Modell vorliegt. Ein Schwerpunkt lag hierbei auf der Untersuchung turbulenter Grenzschichtströmungen. Beispielhaft wurden dann die Strömung in und um einige Strukturen auf Gebäudeskala, bzw. entsprechender Windkanalmodelle, untersucht. Dazu wurden verteilte Rechnungen auf einem CPU-Cluster und auf Grafikkarten (GPGPUs) durchgeführt.

Im Allgemeinen hat das Lattice Boltzmann Verfahren gute Ergebnisse für turbulente Strömungen geliefert, wie an verschiedenen Beispielen gezeigt wird. Insbesondere die Ergebnisse zum faktorisierten CLB-Modell zeigen zum ersten Mal an einem komplexen Testfall, dass dieses Modell für turbulente Strömungen gut geeignet ist, wofür auch Erklärungsansätze geliefert werden.

Abstract

Computational fluid mechanics has become a standard approach in many branches of engineering. Simulation of flow on the building- and infrastructure scale, however, remains very challenging and is mostly restricted to basic research at the present stage. In particular, accurate, three-dimensional, time-resolved simulation such as Large Eddy Simulation is still rarely used despite its potential. On the other hand, it is reasonable to expect a growing influence of these methods as computers become more powerful and numerical methods evolve.

In the present work the Lattice Boltzmann method is chosen as a starting point to analyze simulations of flow around buildings. This approach appears to be particularly apt for such applications due to its very good scalability with respect to parallel computing. Different variants of the Lattice Boltzmann method, namely the Lattice Bhatnagar-Gross-Krook (LBGK) method, the Multiple Relaxation Time (MRT) method, and variants of the Cascaded Lattice Boltzmann (CLB) method have been implemented and compared on the basis of standard benchmarks. Furthermore, several turbulence models, such as the Smagorinsky model, the wall adapting local eddy-viscosity model, and Vreman's model have been investigated.

One focus was on the applicability of the Lattice Boltzmann method to turbulent flows, considering also the interdependence between the numerical method and the LES model. Particular attention was paid to the ability of these models to correctly reproduce turbulent shear flows. Some typical infrastructure elements have been studied and compared to wind-tunnel data. The simulations were carried out on a PC cluster and on graphics processing chips (GPGPUs).

Overall, the Lattice Boltzmann method has yielded good results for turbulent flow simulations, which is documented in several benchmarks. In particular, the results for the FCLB model show for the first time for a reasonably complex benchmark, that the model performs well for turbulent flows, for which an explanation is attempted.

Contents

List of Figures

List of Tables

1 Motivation and Outline

1.1 Motivation

Fluid dynamics is ubiquitous in every day life and one of the oldest domains of research, as becomes apparent from antique findings such as Archimedes principle. Today, the behavior of laminar flow is well-understood. Analytical solutions of the Navier Stokes equations, that govern fluid flow, are known for simple conditions such as laminar flow in a pipe. However, more complex conditions like turbulent flow remain challenging and a fascinating area of research. It is not even clear whether a theoretical model to describe the statistics of turbulent flow can be constructed. Further, seemingly unrelated disciplines can benefit from the long tradition of fluid-dynamics research. One such example is the study of the evolution of galaxies in astrophysics, which can approximately be described by the Navier Stokes equations. Apart from being an appealing field of research in itself, fluid dynamics is the base of various technical developments. In the field of medical engineering, for instance, fluid-dynamics experiments and numerical simulations are applied to better understand blood flow and pulmonary air flow, reporting on effects like particle deposition in the lung. Without an understanding of aerodynamics that developed in the 18th century, airplanes would have never been built. Last but not least, fluid dynamics has traditionally been a foundation of civil engineering, because of the impact that wind and water have on the built environment.

Most of this work was carried out in the framework of the GRK802, the International Graduate College for Risk Management of Natural and Civilization Hazards on Buildings and Infrastructure. PhD studies in the graduate school focused on different aspects of risk management, particularly vulnerability identification in civil engineering. This means that a specific type of structures, such as bridges, has been studied for a given hazard, such as wind.

In fact, storm damages make up for the highest percentage of damages of all natural disasters in Germany. According to the reinsurance company MunichRe 64% of all ensured damages caused by natural desasters were caused by winter gales [106]. The natural disaster database EM-DAT [173] identifies winter storms as a major source of monetary damage in Europe, but of intangible losses as well: Between 1990 and 2010 87 lives were lost in Europe due to wind storm. A better prediction of the local effects of storms could raise preparedness and thereby increase safety. Numerical simulation of wind effects in complex terrains, such as urban areas [117], is a promising approach to achieve this difficult task, but is not yet feasible to perform in real-time yet.

Computational fluid dynamics can contribute to a better understanding of strong wind situations by isolating particular physical effects in a controlled environment. Representative

building blocks and topologies, such as high-rise buildings and long-span bridges [95] can be studied as well as individual infrastructure components that are particularly exposed, such as a cables subject to ice accretion that were also studied within the GRK802 [168].
The Lattice Boltzmann approach can be considered as an alternative approach to numerically solving the Navier-Stokes equations. It is based directly on the distribution functions for the particle dynamics of the fluid. The method has successfully been employed to model and simulate a variety of complex fluid flow problems ranging from multi-component [88] and multi-phase flows [97] to thermal flows [91], fluid-structure interaction [54], non-Newtonian flows [10] as well as turbulent flows [72].
Despite extensive research and successful application of the lattice Boltzmann approach, optimal strategies to deal with turbulent flow in complex geometries remain unclear. The objective of this dissertation is improve and validate Lattice Boltzmann models to compute turbulent flow around sample components of the building infrastructure. Different Lattice Boltzmann variants and turbulence models will be assessed for their capability to deal with turbulent flow, ranging from the traditional Smagorinsky model and to non-linear Lattice Boltzmann collision operators such as the factorized cascaded Lattice Boltzmann collision operator. After studying basic flow configurations for which analytical solutions and reliable numerical data exist, the code will be validated on wind tunnel data for several representative benchmarks.

1.2 Outline

The thesis is divided into three parts. First, the fluid mechanical and numerical background of the work is introduced. The focus is on the Lattice Boltzmann equation and its derivation as well as the turbulence models that have been implemented. Secondly, basic validations of the various models studied are presented. In the third part, applications to more complex, turbulent flows are considered. The thesis concludes with an evaluation of the models studied and an overview of possible further developments is given.

2 Introduction

2.1 An outline of computational wind engineering

Computational wind engineering (CWE) deals with the prediction of wind action on infrastructure components by computational means. In the following discussion, we will limit ourselves to CFD-approaches, and exclude computationally demanding, but measurement data-based approaches. CWE complements traditional wind engineering based on wind tunnel testing and and algebraic calculations.
To date, computational techniques are by far not as widely accepted as wind tunnel testing. Building standards, such as the German building standard [26] still require wind tunnel testing. On the other hand, if wind tunnel studies and CWE are combined in a hybrid approach this can lead to a more timely design and save costs, as Cocharana et al. [20] point out in their review paper on the state of CWE. They highlight that CWE nowadays is often employed in preliminary studies, e.g. in the construction of long-span bridges. Material parameters, such as the viscosity and density can be adjusted more freely than in experiments, that would involve cryo-wind tunnels or water tunnels for high-Reynolds number tests. Because physical experiments are necessarily limited in size, computer models are advantageous in their ability to satisfy the various fundamental scaling laws, using very powerful computers or relatively simple models. At this point, CWE provides valuable contributions to the construction of individual objects, but is not yet part of standard engineering practice.
The most prominent task in CWE is the simulation of wind loading on infrastructure components such as roofs [126], long-span bridges e.g. [95] or smaller building components such as steel cables. A special case is the study of interference effects between different infrastructure elements, see e.g. [102]. CWE models have successfully been employed to predict mean pressures or forces that act on objects in strong wind situations. The prediction of the distribution of pressures over time and peak pressures is highly relevant, but far more difficult and error-prone [20]. The wind-induced motion of structures, such as wind-structure interaction of roofs has been studied using fluid-structure interaction [65].
Further fields of study are the dispersion of contaminants [117] and temperature-driven (indoor) ventilation. Meso-scale simulations are required for the simulation of wind fields in urban areas, such as wind through street canyons for pedestrian comfort. These examples show that wind field prediction is gaining more and more relevance.
Most of these applications deal with highly turbulent flows at large scales in complex geometries. The boundary conditions, such as the turbulent surrounding wind field in an urban area, are usually complicated and not always well defined. On the other hand, the physics that CWE deals with is usually simple: The flow is single-phase and often single component

and isothermal. Acoustic effects can usually be neglected. Because of this, Murakami [121] names the development of realistic inflow conditions and the development and assessment of turbulence models as the two mayor challenges in CWE. Much effort has gone into and continues to go into the design of inflow conditions that account for the inherent randomness of wind flow. With the increase of computational power LES models become applicable to fluid flow simulations in wind engineering. They promise a better description of flow around bluff bodies, as the level of modeling is lower than for Reynolds averaged Navier Stokes (RANS) models, see sec. 2.9. On the other hand, the computational cost is still very high and the use of LES is thus less widely accepted. This work will focus on modeling flow though and around single blocks of infrastructure with LES models.

2.2 Notation and dimensionless forms

Before going into details about the Lattice Boltzmann equation we need to fix some notation and introduce the specific form of the two major equations used in this work. Throughout the work, the Einstein summation convention is used

$$\sum_i x_i y_i \hat{=} x_i y_i \tag{2.1}$$

for two quantities x, y except for some cases were it seems necessary to highlight that a summation takes place. Partial derivatives are denoted by $\frac{\partial x}{\partial y}$ or $\partial_y x$. Coordinates have the variable names $\left(x, y, z\right)$ or (x_1, x_2, x_3). For partial derivatives of a variable x with respect to a coordinate x_i the notation $\partial_i x$ is used.
We now introduce the non-dimensional form of the two equations that describe the behavior of all systems studied in this work, the Navier Stokes equations and the Lattice Boltzmann equation. This form is preferred over the dimensional form in the current context for two reasons. First, several definitions throughout this work are made more straightforwardly. The transformation matrix from distribution functions to moments does not contain different powers of units but small integer numbers only. Second, in the asymptotic analysis the dimensionless expansions in time and space can be compared directly, i.e. definitions like $\Delta x = \Delta t$ are possible without introducing further scaling factors.
The fluid motion is usually governed by the incompressible Navier Stokes equations

$$\partial_t u_i + \partial_j u_i u_j + \partial_i p/\rho_{ref} - \nu \partial_{jj} u_i = 0 \tag{2.2}$$

This equation can be brought into non-dimensional form by replacing

$$\begin{aligned} x &\rightarrow x\,L \\ u &\rightarrow u\,\mathrm{v} \\ t &\rightarrow t\,L/\mathrm{v} \\ p &\rightarrow p\,\rho_{ref}\mathrm{v}^2 \\ \rho &\rightarrow \rho/\rho_{ref} \end{aligned} \tag{2.3}$$

(2.4)

with the non-dimensional form on the right hand side for some reference length L, reference velocity v and reference density ρ_{ref}. In non-dimensional form the incompressible Navier Stokes equations become

$$\partial_t u_i + \partial_j u_i u_j + \partial_i p - \frac{1}{Re}\partial_{jj} u_i = 0 \tag{2.5}$$

where $Re = L\mathrm{v}/\nu$ is the Reynolds number based on the characteristic quantities. The mass conservation equation transforms alike.
The LB equation is to be redefined in dimensionless form as well.

$$f_q\left(\mathbf{x} + \mathbf{e}_q c\Delta t, t + \Delta t\right) = f_q\left(\mathbf{x}, t\right) + \Delta t\lambda\left(f_q^{eq}\left(\mathbf{x}, t\right) - f_q\left(\mathbf{x}, t\right)\right) \tag{2.6}$$

The probability distribution per cell that depends on the discretized velocities has the inverse unit of a velocity $\left[f\right] = \Delta t/\Delta x$. To construct a dimensionless version of 2.6 f has to be replaced using $f \rightarrow f/\mathrm{v}$. We further redefine temporal, spatial variables, velocities and the density as in 2.3. The relaxation frequency $\lambda = \frac{1}{\nu/c_s^2 + 1/2\Delta t}$ has the dimension $[\lambda] = 1/\Delta t$. We redefine a dimensionless λ by $\lambda \rightarrow \Delta t\lambda$ such that we have

$$f_q\left(\mathbf{x} + \mathbf{e}_q c\Delta t, t + \Delta t\right) = f_q\left(\mathbf{x}, t\right) + \lambda\left(f_q^{eq}\left(\mathbf{x}, t\right) - f_q\left(\mathbf{x}, t\right)\right) \tag{2.7}$$

where $\mathbf{x}$, t, Δt have been replaced by their dimensionless counterparts and for dimensionless λ, f_q. Often, the reference length L is chosen as the grid spacing Δx and (Δ_x/Δ_t) as the reference velocity. In this form and for uniform grids, the implementation of the basic LB scheme becomes straightforward.
For the rest of the discussion of the LB method, all quantities should be interpreted as non-dimensional quantities. In the validation chapters, where specific experiments exist for comparison, the specific dimensions will be given for the flow variables.

2.3 Lattice Boltzmann

The Lattice Boltzmann scheme emerged in the 1990's from Lattice Gas Cellular Automata [110]. Unlike direct discretizations of the Navier Stokes equations, Lattice Boltzmann equations rely on a discretization of the Boltzmann equation that is a time-dependent description of the behavior of thermodynamical ensembles:

$$f_q(\mathbf{x} + \mathbf{e}_q c\Delta t, t + \Delta t) - f_q(\mathbf{x}, t) = \Omega_q. \tag{2.8}$$

Here, the $\mathbf{e}_q$ are a set of discretized particle velocities and Ω is the collision operator. The reference velocity $c = \Delta x/\Delta t$ relates the lattice spacing and the time step, such that $\mathbf{e}$ becomes a dimensionless quantity. The probability distribution functions f relax in time to equilibrium functions f^{eq}, which are often taken to be truncated versions of the Maxwell distribution, the probability distribution for the microscopic velocities of a gas of non-interacting particles. Chapman-Enskok analysis, e.g. [75], shows that the Lattice Boltzmann equation correctly models Navier-Stokes fluid dynamics for small Mach- and Knudsen-numbers, i.e when the typical velocities are much lower than the speed of sound and the mean free path is small against the dimensions of the system.
Algorithmically, eq. 2.8 splits into a relaxation step and a propagation step. The relaxation step accounts for the changes that the probability distribution undergoes due to the collision of the particles. Different collision models are described in sec. 2.4. The propagation step implements the effect of the motion of the particles on the distribution function f and is described in sec. 2.5. The macroscopic quantities ρ and u are related to the distribution function via

$$\rho = \sum_q f_q \tag{2.9}$$

$$u_i = \frac{1}{\rho}\sum_q f_q \mathbf{e}_{qi} \tag{2.10}$$

for compressible schemes and

$$\Delta\rho = \sum_q f_q \tag{2.11}$$

$$u_i = \sum_q f_q \mathbf{e}_{qi} \tag{2.12}$$

for incompressible schemes where the density splits into a constant part ρ_{ref} and a fluctuating part $\Delta\rho$. An advantage over conventional methods is that the Lattice Boltzmann method is intrinsically local and can thus be parallelized more easily. This is important for simulating turbulent flow because the computational cost of these problems is high. Usually, Lattice Boltzmann methods are constructed for Cartesian grids with second order accurate grid-refinement techniques using nested grids. As a result, the griding process is very fast. Accordingly, Lattice Boltzmann achieves very competitive results for flows with complex boundaries and moving grids, see e.g. [1]. In contrast to most other CFD methods, the Lattice Boltzmann scheme does not solve a Poisson equation for the pressure field. A constitutive equation that links the pressure to the density fluctuations is given instead. For small density differences the equation

$$c_s^2 = \frac{\partial p}{\partial \rho} \tag{2.13}$$

can be approximated by

$$\Delta p = c_s^2 \Delta\rho \tag{2.14}$$

where c_s is the speed of sound for the fluid under consideration. Eq. 2.14 is used to eliminate the pressure, as no absolute pressure occurs in the Navier Stokes and continuity equation but only its gradient.
The Lattice Boltzmann method has been applied to a variety of problems in CFD, e.g. non-Newtonian flows [10], multi-component flows [88], thermal flows [91], free surface flows [79], multi-phase flows ([41], [97]), or fluid-structure interaction [54]. The method can be applied to other partial differential equations as well, such as the advection-diffusion equation [60], magnetohydrodynamics [24], etc. The Lattice Boltzmann method is less appropriate for medium or high-Knudsen number flows, even though effort is being made to capture the Knudsen layer, a boundary layer that occurs in highly diluted fluids [22]. Another challenge for the Lattice Boltzmann method are high-Mach number flows, which occur in aerodynamics. Higher order and multi-speed models are subject to ongoing development, see [151] for an early solution. The Lattice Boltzmann equations can be evaluated in different bases to improve the stability or accuracy of the scheme. The most popular basis is momentum space where different relaxation rates $\lambda(i)$ can be used for different moments [90]. The scheme is thus called multi relaxation time (MRT) method. Another possibility are the two-relaxation time (TRT) schemes. Here the probability distributions are split into their even and odd parts. A different relaxation rate is used for each of these two sets. Optimal relaxation rates for different purposes are summarized in [61]. The TRT scheme is attractive because of the accurate boundary conditions that exist for this scheme [64].

2.4 Collision models

In the following, different collision models will be presented, that will be evaluated for turbulent flows later. These are the Lattice Bhatnagar-Gross-Krook (LBGK) model [6], the multi relaxation time model [90] and the Cascaded Lattice Boltzmann (CLB) model [47]. The difference resides in the equilibrium function and the relaxation factors used, resulting in different relaxation properties. With the LBGK model, the equilibrium may depend only on the velocities and the density while the relaxation coefficient remains the same for all moments. With the MRT model, the relaxation coefficients may be different for different moments. For the CLB model they may depend on any lower order moment. The three classes of Lattice Boltzmann models show a different behavior in terms of stability and accuracy at the boundaries.
Another class of Lattice Boltzmann models are Entropic Lattice Boltzmann (ELB) models. For these models the equilibrium distribution is constructed such that some function, termed “entropy function” is minimized, see e.g. [66]. Different choices for the entropy function lead to different equilibria. ELB models have been evaluated for turbulent flows, [82], [156]. The ELB models are used in a similar way as the CLB model, no additional turbulence model is added, but the dissipation comes from the numerical scheme itself. In this work entropic Lattice Boltzmann models have not been tested and thus will not be presented in more detail.

2.4.1 LBGK model

The LBGK approach model [6] evolved from Lattice gas automata ([110], [69], and [44]) and is the simplest model in terms of programming and computational effort. The relaxation step is carried out on the discretized probability distribution functions directly [132]

$$\Omega_q = \lambda(f_q^{eq}(\mathbf{x},t) - f_q(\mathbf{x},t)) \tag{2.15}$$

with a the relaxation factor $\lambda \in [0,2]$ that fixes the viscosity in the corresponding Navier Stokes equation (for the dimensional case) via

$$\nu = \left(\frac{1}{\lambda} - \frac{\Delta t}{2}\right) c_s^2 \tag{2.16}$$

with $\nu > 0$. The equilibrium is given by

$$f_q^{eq} = w_q \rho \left(1 + 3\frac{\mathbf{e}_q \cdot \mathbf{u}}{c_s^2} + \frac{9}{2}\frac{(\mathbf{e}_q \cdot \mathbf{u})^2}{c_s^4} - \frac{3}{2}\frac{\mathbf{u}^2}{c_s^2}\right) \tag{2.17}$$

It has been shown [71] that compressibility errors can be reduced by using a so-called incompressible model based on density fluctuations $\Delta\rho$ instead of absolute values for the density and redefining the velocities according to 2.9. The equilibrium for this model reads

$$f_q^{eq} = w_q \left(\Delta\rho + 3\frac{\mathbf{e}_q \cdot \mathbf{u}}{c_s^2} + \frac{9}{2}\frac{(\mathbf{e}_q \cdot \mathbf{u})^2}{c_s^4} - \frac{3}{2}\frac{\mathbf{u}^2}{c_s^2}\right) \tag{2.18}$$

The weight factors w_q are $w_0 = 4/9$, $w_1 = 1/9$, $w_2 = 1/36$ for the $D2Q9$ model. w_0 is used for the discrete velocity vector $(0,0)$, w_1 for the velocities $(\pm 1,0)$, $(0,\pm 1)$ and w_2 for the diagonal vectors. For the $D3Q19$ model the weight factors are $w_0 = 1/3$, $w_1 = 1/18$, $w_2 = 1/36$ and for the D3Q27 model $w_0 = 8/27$, $w_1 = 2/27$, $w_2 = 1/54$, $w_3 = 1/216$, where w_3 is used for the velocity vectors that point to the edges of the cube, cf. fig 2.1. The LBGK model is inferior to advanced models in terms of stability [29]. It has been criticized for a first-order interdependence between the resulting position of no-slip boundaries and the viscosity [64] and a linear dependence between the kinematic and bulk viscosity [92].

2.4.2 Multi-relaxation time Lattice Boltzmann model

[27] proposed to perform the relaxation step in momentum space, where different moments are relaxed with different relaxation times.

$$f_q(\mathbf{x} + \mathbf{e}_q \Delta t, t + \Delta_t) = f_q + M^{-1} S(M f(x,t) - m^{eq}(x,t)) \tag{2.19}$$

The transformation from probability functions to moment space is given by

$$m_{x^j y^k z^l} = \sum_q f_q \mathbf{e}_{qx}^j \mathbf{e}_{qy}^k \mathbf{e}_{qz}^l \tag{2.20}$$

The equilibrium moments are the moments of the equilibrium distribution function, in particular $m_0 = \rho$, $m_x = j_x$, $m_y = j_y$, and $m_z = j_z$. In many cases, we will not use the bare moments as defined in eq. 2.20 but linear combinations of such moments. A moment-generating polynomial $p(x,y,z) = \sum_{jkl} \alpha_{jkl}\, x^j y^k z^l$ is defined as the polynomial that generates the following linear combination of moments

$$m_p = \sum_q f_q \sum_{jkl} \alpha_{jkl}\, \mathbf{e}_{qx}^j \mathbf{e}_{qy}^k \mathbf{e}_{qz}^l \tag{2.21}$$

There are several choices for the relaxation factors. The most popular choice is the MRT model by d'Humieres et al. [29], which has good stability properties. The two-relaxation time model by [63] uses only two different relaxation rates: one for the even order moments (those of order $i+j+k = 2,4,6,\ldots$) and one for the odd order moments. The relaxation coefficient for the even moments needs to be equal to the BGK-relaxation coefficient, as can be seen from the asymptotic analysis, see sec. 2.6. The relaxation coefficient for the odd moments can be chosen arbitrarily to minimize certain errors such as the dependence of the boundary position on the viscosity. As opposed to the model described in [29] this model does not damp acoustic modes with an artificial bulk viscosity.

2.4.3 The D3Q27 stencil

We will now introduce the different stencils that are typically used with the LB method and their relation to the LB quantities. Lattice Boltzmann stencils coincide with the space vectors $\mathbf{e}_q \Delta t$. The stencil is denoted by $DdQq$ where d signifies the spatial dimension and q the number of discrete velocity vectors. In two dimensions we have the $D2Q9$ stencil which uses nine discrete velocity vectors, namely the four orthogonal directions, the four diagonal ones and the one representing the resting particles. Possible stencils in three dimensions with $e_{x,y,z} \in \{\pm 1, 0\}$ are made up of four sets of velocity vectors, numbered by the square of the vectors magnitude [29]

- set 0 $(0,0,0)$
- set 1 $(\pm 1,0,0)$, $(0,\pm 1,0)$, $(0,0,\pm 1)$
- set 2 $(\pm 1,\pm 1,0)$, $(\pm 1,0,\pm 1)$, $(0,\pm 1,\pm 1)$
- set 3 $(\pm 1,\pm 1,\pm 1)$

A minimum Lattice Boltzmann model in three dimensions should be able to independently represent the first ten moments ρ, μ_x, μ_y, μ_z, μ_{xx}, μ_{xy}, μ_{xz}, μ_{yy}, μ_{yz}, μ_{zz} for the model to correspond to the Navier Stokes equations. Accordingly, we need at least ten velocity vectors to reproduce these moments. For isotropy reasons we require the elements of the velocity sets introduced above to occur in the stencil only if all elements of the set occur. The minimal choice are thus the twelve velocity vectors from sets 1 and 2. This set, however, does not reproduce all of the necessary moments independently. If we construct ρ, μ_{xx}, μ_{yy} and

μ_{zz} according to 2.21 using only the $\mathbf{e}_q$ from sets 1 and 2 we obtain $\rho = \mu_{xx} + \mu_{yy} + \mu_{zz}$. The rest velocity $(0,0,0)$ is required to make these moments differ. As a sufficient condition, we thus see that the $D3Q13$ stencil using sets 0,1 and 2 is the minimum stencil. The $D3Q13$ MRT model was introduced in [28]. Further valid combinations of the velocity sets are: Sets 0,2,3 for the $D3Q15$ model, sets 0,1,2 for the $D3Q19$ model and sets 0,1,2,3 for the $D3Q27$ model. These stencils have been analyzed using the the standard asymptotic analysis as explained in 2.6 in more detail. For medium and high Mach numbers one has to allow for additional velocities and admit $\left|e_{x,y,z}\right| > 1$. An early development [86] is the $D2Q25$ model with velocities consisting of all vectors (e_x, e_y) for $e_x, e_y \in \{0, \pm 1, \pm 2\}$. A characterization of possible higher-order stencils for three dimensions is given in [18].

Studies of the effects of different stencils include [112] and [109] for the LBGK model. While the former study did not find a significant difference between the models for various laminar flow cases, the latter study found that the LBGK $D3Q27$ model with Smagorinsky LES gives better results for turbulent flow in a hexagonal arrangement of circular rods than the $D3Q19$ LBGK model with Smagorinsky LES. No significant differences were found for the laminar flow case. In sections 3.7 and 3.6 we show that substantial differences in accuracy do exist for collision models other than the LBGK model. The $D3Q27$ neighborhood scheme is the basis of the so-called Cascaded Lattice Boltzmann method [47].
The Cascaded model and its variants are almost always executed using $D3Q27$ neighborhood schemes to consistently exploit the higher-order contributions to the moments. In contrast, the $D3Q19$ neighborhood is in wide use for the MRT model and is also the standard scheme in the code VIRTUALFLUIDS of iRMB. Extensions to other stencil also exist for VIRTUALFLUIDS. Both neighborhood schemes are illustrated in Figure 2.1.

2.4.4 Symmetry in LB collision models

After introducing the most common stencils, we will now see which symmetry properties exist for different LB collision models. The Navier Stokes equations are invariant under rotations and reflections of the coordinate system. In discrete models no complete rotation invariance is possible, but one can still demand that the model converges towards a model invariant under rotation when the grid spacing goes to zero. A necessary condition is that the collision step itself does not violate the isotropy. This entails some restrictions for the MRT-collision factors.
Rotation and reflection of the coordinate system leads to rotation and reflection of the discrete velocities. We consider the polyhedron spanned by the discrete velocities, which is a cube for the $D3Q27$ model. The rotations and reflections acting on this object form a group. Subsets of this group leave certain linear combinations of discrete velocities invariant. For example, a reflection along the x-axis followed by a reflection across the y-axis leaves all even-order moments invariant while the odd-order moments change sign.
In the following a subdivision of the LB moment into different, orthogonal linear subspaces to possibly different relaxation factors is explicated. We consider the rotations of the cube

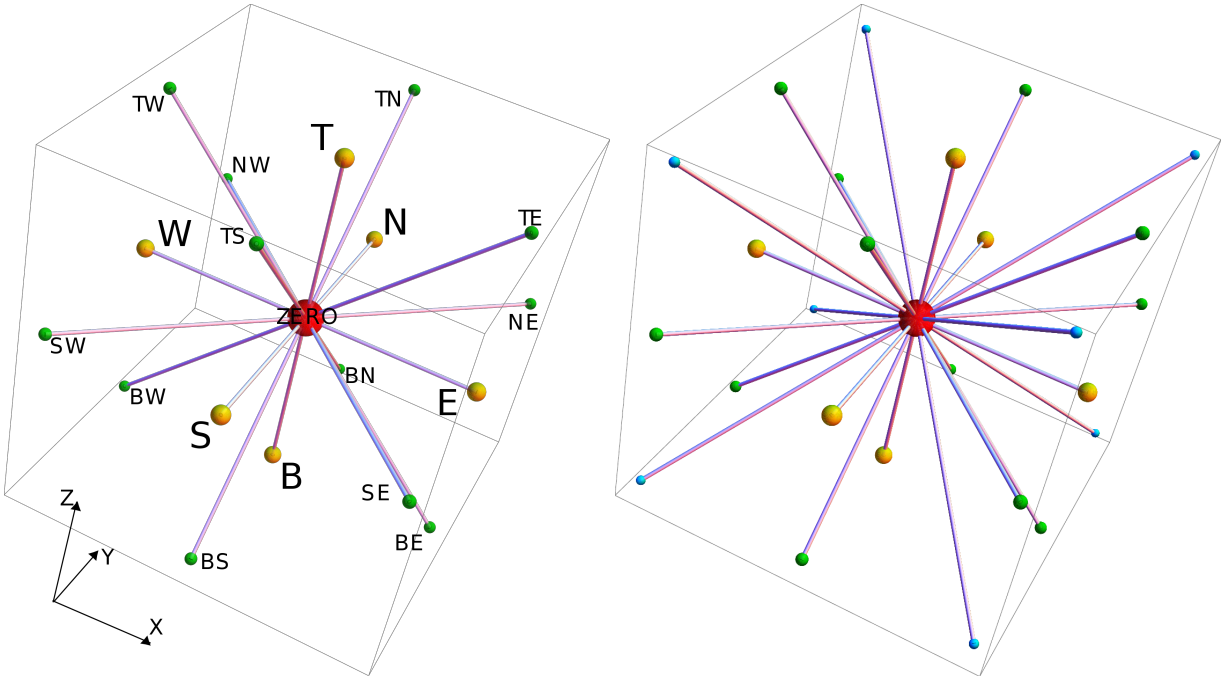

Figure 2.1: *Discrete velocities for the D3Q19 and D3Q27 stencils*

that map the cube as a whole onto itself. The corresponding rotation group in three dimensions is the group O. We first want to define a set of possible representations of this group, from which irreducible representations can be constructed. To do so, some terminology for finite groups is introduced [171].

A representation of a group G is a possible choice of a basis for a vector space upon which the elements of G act.

An irreducible representation $\Gamma_i(G)$ is a representation for which all basis vectors a mapped to other basis vectors by the action of the group G in such a way that no invariant subspaces exist.

The action of the entire group on all possible choices of the basis can be described by a direct sum over the irreducible representations.

$$\Gamma = \bigoplus_i \Gamma_i$$

In this particular representation Γ all elements of the group become block-diagonal matrices, where each block maps one irreducible representation onto itself. Vectors belonging to different irreducible representations are orthogonal.

As a suitable vector space we take subspaces of the space of polynomials in $\mathbb{R}^3$. These are taken to be the moment-generating polynomials for a given stencil as defined in eq. 2.21. For the $D3Q27$ stencil, for instance, we have all linear combinations of monomials $x^j y^k z^l$ with $j,k,l < 3$.

The rotation group O is a very common group and has been explored for many applications such as crystallography. Five irreducible representations exist [137]. Table 2.1 lists the

representation	polynomial basis
Γ^1	1
Γ^2	$\{x, y, z\}$
Γ^3	$\{x^2 - y^2, x^2 - z^2\}$
Γ^4	$\{xy, xz, yz\}$
Γ^5	$\{xyz\}$

Table 2.1: *List of the irreducible representations for the rotation of the cube without its multiplicities*

representation	polynomial basis
Γ^1	$\{1\},\{x^2+y^2+z^2\},\{x^2y^2+x^2z^2y^2z^2\},\{x^2y^2z^2\}$
Γ^2	$\{*x\},\{*x\left(yy+zz\right)\},\{*xyyzz\}$
Γ^3	$\{*(x^2-y^2)\},\{*(xxyy-xxzz)\}$
Γ^4	$\{*xy\},\{*x\left(y^2-z^2\right)\},\{*xyzz\}$
Γ^5	$\{xyz\}$

Table 2.2: *List of the irreducible representations that occur in the D3Q27 model*

irreducible representations for one basis set each. For the $D3Q27$ stencils additional polynomial bases can be constructed to represent all discrete velocities. Note that Γ^3 is a two-element representation that spans a two-dimensional space only. We propose the representations listed in Table 2.2. As a shorthand $*$ is used to symbolize all permutations of x, y, z, e.g. $\{*x\} = \{x, y, z\}$. Overall, 27 basis vectors are constructed in this way. Some representations occur multiple times such that we have four basis vectors from Γ^1, three times three basis vectors from Γ^2, two times two from Γ^3, three times three from Γ^4, and one from Γ^5 altogether. To show that Table 2.2 indeed shows an irreducible representation for the moment generating polynomials of the $D3Q27$ stencil, one has to check that all additional basis sets transform as those given in 2.1. Indeed, all candidates for equivalent representations yield the same rotation matrices as the representations from Table 2.2 as can be seen from Table 2.3 for three representative group elements. By Dx the smallest possible rotation (by $\pi/2$) around the x-axis is denoted, by Dxy the rotation by π around the xy-axis, that connects two opposing edges, and by $Dxyz$ the rotation around the cubes diagonal by $2/3\pi$. In our implementation of the $D3Q27$ models, a different, equivalent basis is used instead of Γ^3_b, namely $\{xxyy-2yyzz+xxzz, xxyy-2xxzz+yyzz\}$. These new basis vectors are linearly dependent on the first two basis vectors. Unlike prior constructions of bases for Lattice Boltzmann models, not all basis elements are orthogonalized among themselves or with respect to bases which transform in the same way. They are nevertheless orthogonal to all elements from different irreducible representations. Possible MRT collision models are those that respect the irreducible representations of Table 2.3. For each representation a different set of relaxation factors may be used.

The above discussion closely follows [137] who derived irreducible representations for dif-

representation	polynomial	alias	Dx	Dxy	$Dxyz$
Γ_a^1	$\{1\}$	A	A	A	A
Γ_b^1	$\{x^2+y^2+z^2\}$	A	A	A	A
Γ_c^1	$\{x^2y^2+x^2z^2+y^2z^2\}$	A	A	A	A
Γ_d^1	$\{x^2y^2z^2\}$	A	A	A	A
Γ_a^2	x	A	A	B	B
	y	B	C	A	C
	z	C	-B	-C	A
Γ_b^2	$x(yy+zz)$	A	A	B	B
	$y(xx+zz)$	B	C	A	C
	$z(xx+yy)$	C	-B	-C	A
Γ_c^2	$xyyzz$	A	A	B	B
	$xxyzz$	B	C	A	C
	$xxyyz$	C	-B	-C	A
Γ_a^3	(y^2-z^2)	A	-A	-B	B
	$-(x^2-z^2)$	B	-(A+B)	-A	A+B
Γ_b^3	$xxyy-xxzz$	A	-A	-B	B
	$-(xxzz-yyzz)$	B	-(A+B)	-A	A+B
Γ_a^4	yz	A	-A	-B	B
	xz	B	-C	-A	C
	xy	C	B	C	A
Γ_b^4	$x(y^2-z^2)$	A	-A	-B	B
	$-y(x^2-z^2)$	B	-C	-A	C
	$z(x^2-y^2)$	C	B	C	A
Γ_c^4	$xxyz$	A	-A	-B	B
	$xyyz$	B	-C	-A	C
	$xyzz$	C	B	C	A
Γ^5	xyz	A	-A	-A	A

Table 2.3: *Transformation table for irreducible representation corresponding to the moment-generating polynomials of the D3Q27 stencil*

ferent LB stencils and included inversions of the coordinate system to derive the TRT model. We arrive at a different, but equivalent basis. A further group theoretical approach on lattice symmetries for lattice gases including some LB stencils can be found in [136].
In practice orthogonal basis sets are often found manually using Gram-Schmidt orthogonalization. In this case care has to be taken to respect symmetry and allow for different relaxation factors responsible for shear and bulk viscosity.
Apparently, the present discussion and the group-theoretic approach include linear effects only. On the other hand, the interdependence between lower- and higher order moments, that the CLB and cumulant model aim to remove (2.4.5) may also influence isotropy properties. In the current work this issue is addressed by studying a few representative examples. In sections 3.7, 3.6, and 4.1 different sets of collision factors and (non-linear) collision models and stencils are compared with respect to their isotropy.

2.4.5 D3Q27 Cascaded and Cumulant models

Introduction

In this section we give an overview over Cascaded Lattice Boltzmann methods which were originally developed by Geier [47]. We start with an explanation of the idea behind CLB schemes and illustrate its effect on basic examples. Two more recent CLB schemes, the cumulant and the FCLB scheme are also presented. These variants extend the original CLB scheme by introducing different equilibria ([49] and [51]). Subsequently, the current implementation used in the work presented here and the original implementation of the CLB schemes are compared.
All CLB-methods rely on the basic idea to use central moments M_p^c instead of uncentered moments μ_p for the relaxation step which in this case is written as

$$M_p^{c,*} = \left(1 - s_p\right) M_p^c + s_p M_p^{c,eq} \tag{2.22}$$

for a moment generating polynomials p as in eq. 2.21 for the MRT model. The main task in the CLB method is to compute the central moments M_p^c from the pre-collision uncentered moments and the post-collision uncentered moments from the post-collision central moments, which we will do in the remainder of this section. In particular, lower order moments are used for the computation of the relaxation process for the higher order moments, which inspired the term “cascaded”.
To introduce central moments let us first define a normalized expectation value of a linear operator B acting on distribution functions f in discretized velocity space

$$\langle B \rangle = \sum_q \left(B(f)\right)_q / \sum_q \left(\mathbb{1}(f)\right)_q . \tag{2.23}$$

Moments are then defined as expectation values of powers of the discrete velocities

$$\mu_{x^i y^j z^k} = \left\langle e_x^i e_y^j e_z^k \right\rangle \tag{2.24}$$

in accordance with the definitions for distribution functions in continuous spaces that can be found e.g. in [149]. An alternative notation that avoids multiple subscripts is

$$\mu_{\underbrace{1\ldots1}_{i}\underbrace{2\ldots2}_{j}\underbrace{3\ldots3}_{k}} := \mu_{x^i y^j z^k}. \tag{2.25}$$

Central moments of a variable e_x in one-dimensional space are then defined as

$$M^c_{e_x^i} = \left\langle (e_x - \langle e_x \rangle)^i \right\rangle. \tag{2.26}$$

For three directions we have a product of one-dimensional terms.

$$M^c_{e_x^i e_y^j e_z^k} = \left\langle (e_x - \langle e_x \rangle)^i \left(e_y - \left\langle e_y \right\rangle\right)^j (e_z - \langle e_z \rangle)^k \right\rangle \tag{2.27}$$

A convenient way to compute central moments is via the binomial theorem.

$$M^c_{e_x^i} = \sum_{k=0}^{i} \binom{i}{k} (-1)^k \langle e_x \rangle^k \left\langle e_x^{n-k} \right\rangle \tag{2.28}$$

The CLB model chooses the co-moving frame of reference for each computational cell. The arbitrariness in choosing an exterior, resting, frame of reference is removed. Consider for example the variance which is defined as $var(v_x) = \left\langle v_x^2 \right\rangle - \langle v_x \rangle^2$ for a probability distribution $f(v_x)$. This definition corresponds directly to the definition of the second order central moment. The term v_x^2 is removed by the transformation from moments to central moments. The transformation to central moments thus allows us to operate on the variances directly. The transformation to central moments in velocity space is a transformation to the co-moving coordinate system for each computational cell. The arbitrariness in choosing an exterior, resting, frame of reference is removed. One may expect that Gallileian invariance is automatically fulfilled if all numerical operations are carried out in the co-moving reference frame of each computational node (given that acceleration is correctly accounted for). This was what was originally intended by the central moment scheme and is elaborated in [47]. Also in [47] it was shown that the stability of the model is significantly increased in comparison to the MRT model. This could be attributed to a "hyper-viscosity", or damping terms that are fourth order in ε (dubbed "hyper-viscosity" because ordinary viscosity terms are second order in ε.) The equilibrium central moments are chosen as the corresponding central moments of the Gauss function with a variance equal to the square of the speed of sound c_s^2. These are the same equilibria as those obtained from taking the central moments of the MRT-equilibria, given that third-order terms are taken into account for the MRT equilibria as well. In Appendix D a list of all central moments for the $D3Q27$ model is given. For models with less discrete velocities the non-existent moments can simply be omitted (such as M^c_{xyz} for the $D3Q19$ model).

Cumulants and the cumulant method

To push the idea of removing the effect of the lower order moments on the higher order moments further cumulants can be used instead of central moments [49]. One now intends

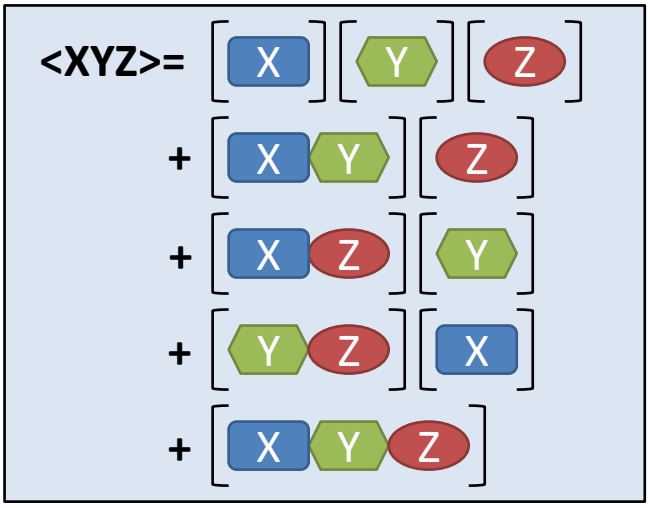

Figure 2.2: *Computation of the moment μ_{xyz} from cumulants. Each line corresponds to one element of the partition*

to remove not only the dependency of the velocity on the the higher order central moments, but to remove the inter-dependency between all moments. A central moment of order n may depend non-linearly on all central moments of order $m < n$. The central fourth moment of a normal distribution for example, is $M^c_{x^4} = 3M^c_{x^2}$. That means, if one changes the variance of the distribution, the fourth-order central moment changes even though the characteristic of the functions shape that is measured by the fourth-central moment, the kurtosis, does not change. We therefore define a transformation to a set of functions with the same ordering relation where the elements of higher order are independent of those of lower order. These functions are called cumulants. Cumulants have been employed as a basis space to solve the Boltzmann equations, e.g. in [145]. As such they may be appropriate for LBM. Cummulants are defined as

$$\langle X_1 ... X_n \rangle = \sum_{\pi} \prod_{B_i \in \pi} C_{X_n | n \in B_i}. \tag{2.29}$$

This means: to compute the expectation value from cumulants, take the sum over all partitions of the set $G = \{X_1, ..X_n\}$. A partition is defined as a grouping of the set B into subsets B_i such that $B = \bigcup_i B_i$. Take the product of the expectation values of the elements of these B_i. In our case, $\langle X_1 ... X_n \rangle = \mu_{X_1 ... X_n}$ and the X_i are the variables x, y, z of the moment-generating polynomials. Figure 2.2 illustrates the computation for the moment μ_{xyz}.

Note that, as the indices of the moments commute ($M^c_{xxy} = M^c_{xyx}$), prefactors other than one or zero may occur in front of the moments. It can be shown [134] that cumulants in one dimension can be computed recursively with a formula similar to 2.28 using the following formula

$$\mu_{x^n} = \sum_{i=1}^{n-1} \binom{n-1}{i-1} \mu_{x^{n-1}} C_{x^i}. \tag{2.30}$$

We consider normalized distribution functions such that $C_0 = 1$. Further we have $C_x = \mu_x$ and $C_{x^2} = \mu_{x^2} - \mu_x^2$ and

$$\mu_{x^n} = \sum_{m_1=1}^{n-1} \sum_{m_2=1}^{n-2} \dots \sum_{m_{n-2}=1}^{1} \binom{n-1}{m_1-1}\binom{n-2}{m_2-1}\dots\binom{1}{m_{n-1}-1} C_{x^{n-m_1}} C_{x^{n-m_2}} \dots C_{x^{n-m_{n-2}}}. \quad (2.31)$$

Comparison to eq. 2.29 implies that the sums cover all possible permutations of indices and the binomial coefficients give their multiplicity. Cumulants are closely related to central moments. Less computational operations are needed to compute the cumulant from central moments than from moments. Central moments and cumulants are equal up to third order. The first deviation occurs at the fourth-order. Consider e.g. C_{xxyy}, which contains four possible commutations of xy: ($\{x_1y_1, x_2y_2\}$,$\{x_1y_2, x_2y_1\}$, $\{x_2y_1, x_1y_2\}$, $\{x_2y_2, x_1y_1\}$), hence

$$C_{xxyy} = M^c_{xxyy} - M^c_{xx}M^c_{yy} - 4M^c_{xy}M^c_{xy}. \quad (2.32)$$

A normalized and centered Gaussian distribution function is completely characterized by its variance. Hence we completely define such a function by setting all cumulants to zero except for the second, which is equal to the variance. This gives a very compact way of representing the Lattice Boltzmann equilibrium. Here the second order cumulants are non-zero, $C_{x^2} = C_{y^2} = C_{z^2} = c_s^2$. All other cumulants of third order and above are zero. The cumulant model can be expected to be more robust than the $D3Q19$-MRT model, especially when dealing with higher Reynolds numbers as it is very similar to the CLB model. Additionally, some isotropy errors have been removed as has been shown in [49]. It is, however, by far not as widely used as the $D3Q19$ models and not tested as extensively. The additional transformations to and from central moments and cumulants demand considerable computational effort and careful programming.

The Factorized Cascaded Lattice Boltzmann method

Because of the high computational cost of the cumulant model a compromise between CLB and the Cumulant model was presented in [51], termed the Factorized Cascaded Lattice Boltzmann model (FCLB). With this model the collision is still carried out in central moment space, saving the transformation to cumulants. The equilibrium is modified, though. It may now depend on the post-collision values of all lower-order central moments.
In what follows, the FCLB model is being constructed as a simplification of the cumulant model. This approach differs from the one followed in the original paper in that the FCLB model was developed later than the cumulant models. The approach chosen here contributes to justify the equilibria for the FCLB model and to clarify the differences to the other models.

The construction of the method is based on two simplifications of the cumulant model. As a first step, the cumulants are being truncated at second order in ε

$$\begin{aligned} C^T_{xxyy} &= M^c_{xxyy} - M^c_{xx}M^c_{yy} \\ C^T_{xxyz} &= M^c_{xxyz} - M^c_{xx}M^c_{yz} \\ C^T_{xxyyz} &= 0 \\ C^T_{xxyyzz} &= M^c_{xxyyzz} - M^c_{xx}M^c_{yy}M^c_{zz} \end{aligned} \tag{2.33}$$

and analogously for the other cumulants. We use $C_\bullet$ to denote the cumulant of a not further specified polynomial and introduce the following abreviation for the transformation from central moments to truncated cumulants.

$$C^T_\bullet = M^c_\bullet - W_\bullet \tag{2.34}$$

These terms are relaxed by

$$C^{T,*}_\bullet = (1-\lambda)\left(M^c_\bullet - W_\bullet\right) + \left(\lambda C^{eq}_\bullet\right) \tag{2.35}$$

where $C^{eq}_\bullet = 0$ for all cumulants that are not of order two. In our discussion only cumulants of order ≥ 4 play a role, because those of lower order coincide with the central moments. The post-collision central moments now become

$$\begin{aligned} M^{c,*}_\bullet &= (1-\lambda)\left(M^c_\bullet - W_\bullet\right) + W^*_\bullet \\ &= (1-\lambda)\, M^c_\bullet + \lambda W^*_\bullet + (1-\lambda)\left(W^*_\bullet - W_\bullet\right) \end{aligned} \tag{2.36}$$

where $W^*_\bullet$ is the term $W_\bullet$ constructed from the post-collision central moments. The second simplification of the FCLB method consists in neglecting the last term on the right hand side. This is strictly true for the collision sets 1 and all-to-one where $\lambda = 1$. We now define the new FCLB-equilibrium as $M^{F,eq} = W^*_\bullet$, which leads to the CLB-relaxation process with a modified equilibrium

$$M^{c,*}_\bullet = (1-\lambda)\, M^c_\bullet + \lambda M^{F,eq}_\bullet \tag{2.37}$$

Table 5.5 in Appendix B lists all the FCLB equilibria for the D3Q27 stencil. For the special case that the even and odd combinations of second order moments are relaxed with the same relaxation factor $s_1 = s_2$, and $s_6 = s_7 = s_8 = 1$ (see Appendix C for a definition) for the fourth moments we have

$$\begin{aligned} M^{c,*}_{xxyy} &= M^{c,*}_{xx} M^{c,*}_{yy} \\ &= 1/9 + s_1 M^{c,neq}_{xx} M^{c,eq}_{yy} + s_1 M^{c,eq}_{xx} M^{c,neq}_{yy} + O(\varepsilon^4) \\ &= 1/9 + s_1\left(\mu^{neq}_{xx} + \mu^{neq}_{xx}\right)/3 + O(\varepsilon^4). \end{aligned} \tag{2.38}$$

Apparently, the fourth order moments are relaxed in the same way as the second order moments. A similar calculation shows that the same is true for the sixth moment. Thus, if all

relaxation factors are set to one except for $s_2 = s_1$ which is used for all second order moments, then one has a type of two-relaxation time model where all even order moments are relaxed in one way and the odd order moments in an other.
The strong similarity between FCLB and cumulant has been observed in various occasions throughout the work presented here. Examples are the simulation of a "frozen-in velocity peak" as defined in [47] considered here in sec. 3.6 and the square duct flow in sec. 3.7. The FCLB model was applied sucessfully to the simulation of turbulent jet flow in sec. 4.1 because of its good stability and isotropy at a lower computational expense than the cumulant model.

2.4.6 Comparison of the current approach to CLB to the original version

The original lattice Boltzmann implementation of [47] can be summarized as follows: the post-collision distributions f^* are computed as

$$f^* \leftarrow f + Kk \tag{2.39}$$

where $k = \mu^* - \mu$ is the change of the moments due to collision. K is a linear transformation from momentum space to phase space that does not depend on any distribution component. k is obtained using the non-linear transformation C from moments to central moments

$$k = -C^{*,-1}\left(S\,C\,K^{-1}\,f - S\,M^{c,eq}\right). \tag{2.40}$$

The transformation $C^{*,-1}$ is the transformation from the changes in central moments to the changes in moments after collision. S is the diagonal matrix of the collision factors and $M^{z,eq}$ is the vector of central moments. We consider the moments μ_{xy} and μ_{xxy} to see how this works in practice. The central moments are computed from the pre-collision distribution components only. For clarity we use indices that consist of the initial letter of the direction of the discrete distribution component instead of a set of consecutive integers as in sec. 2.4.1 and restrict ourselves to the two-dimensional case

$$k_{xy} = -s_{xy}\left(\left(f_{ne} + f_{sw} - f_{nw} - f_{se}\right) - v_x v_y\right)/4. \tag{2.41}$$

Figure 2.3 illustrates the position of the distribution components. For higher order moments the change in lower-order moments needs to be updated

$$\begin{aligned} k_{xxy} &= -s_{xxy}(-((f_{se} + f_{sw} - f_{ne} - f_{nw} - 2v_x^2 v_y \rho + v_y(\rho - f_n - f_s - f_{zero}))/4 \\ &+ v_x/2(f_{ne} - f_{nw} - f_{se} + f_{sw}))) + v_y/2(-3k_{xx+yy} - k_{xx-yy}) + 2v_x k_{xy}. \end{aligned} \tag{2.42}$$

The $k_{..}$ are constructed using both pre-collision values such as f_i and post-collision values such as k_i. The transformation C from moments to central moments is therefore not equal to the inverse of the transformation C^* from changes in central moments to changes in moments. If the lower-order moment μ_{xx-yy} changes its value during collision, then $k_{xx-yy} \neq 0$ which results in a change in k_{xxy}.

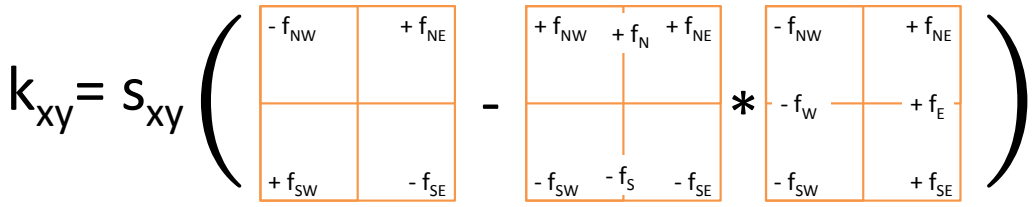

Figure 2.3: *Illustration of the notation used for eq. 2.41 and 2.42, a summation over the distribution components in each square is implied*

Our implementation differs from the original implementation as we do not compute the change in the moments, but recompute the entire moments

$$f^* = K\,C^{-1}\left((\mathbb{1}-S)\,C\,K^{-1}\,f + S\,M^{z,eq}\right) \tag{2.43}$$

with the transformation to moments K, the transformation from moments to central moments C and its inverse C^{-1}. With this implementation there is only one transformation C for both pre- and post-collision transformations. Again, we demonstrate the procedure for the moment μ_{xy}.

$$\mu_{xy} = (K^{-1}f)_{xy} = \left(f_{ne} + f_{sw} - f_{nw} - f_{se}\right) \tag{2.44}$$

The central moment is then

$$M^c_{xy} = (CKf)_{xy} = \mu_{xy} - v_x v_y. \tag{2.45}$$

Now relaxation toward the equilibrium $M^{z,eq}_{xy} = 0$ takes place.

$$M^{c,*}_{xy} = M^c_{xy} - s_{xy}\left(M^c_{xy} - M^{c,eq}_{xy}\right) \tag{2.46}$$

The central moment is then transformed back to its raw (uncentered) moment. After these steps have been completed for all moments, the new distribution can be computed. We devised this implementation because of its more modular properties. The transformation K is the same as for the MRT model and an additional transformation from central moments to cumulants (eq. 2.31) can be carried out for the cumulant model. The less compressed implementation is less prone to errors and makes it easier to change algorithmic details later. On the other hand, it is not as optimized as the original version with respect to the number of floating point operations (FLOPS). A large number of FLOPS can be eliminated if the free relaxation parameters are set to a fixed value, e.g. $s_i = 1$ for $i \neq 1$ with the definition of the s_i from Appendix C.

2.5 Propagation

After discussing variants of the relaxation step in sec. 2.4 we will now consider the other essential part of any Lattice Boltzmann model: the propagation step. It accounts for the effect

of the microscopic particle motions by a propagation of the distribution function. Algorithmically, the component of the distribution function for the discretized velocity $\mathbf{e}_q$ is propagated from its original location $\mathbf{x}$ to the lattice point $(\mathbf{x}+\mathbf{e}_q\Delta t)$. One may also consider the propagation step as an Euler-forward discretization of the first term in the discrete Boltzmann equation $(-\mathbf{e}_q\frac{\partial f_q}{\partial \mathbf{x}})$, as explained in 2.6. The basic algorithm

$$f_q\left(\mathbf{x}+\mathbf{e}_q\Delta t, t+\Delta t\right) = f_q^*\left(\mathbf{x}, t\right) \tag{2.47}$$

has the drawback of using two sets of distribution functions, thus requiring a large amount of memory. Propagation schemes have been designed to reduce the amount of temporary values needed, such as the AAP-scheme of [3]. A recent development among the single-distribution set approaches is the EsoTwist scheme [142], [102]. It relies on a non-local reading and writing process with combined push-and pull mechanisms. A major advantage of the EsoTwist scheme is that it is thread-safe. This means that it can be used in parallel computation without synchronization between the concurrent threads during the propagation process. This makes it apt for the use on parallel architectures such as GPGPUs. Superior performance as compared to the basic propagation scheme has been demonstrated in [102]. On the other hand, the algorithm is much less intuitive and more complicated to implement than the basic propagation step. In the work presented here, the EsoTwist scheme is used in some of the GPGPU-based computations, especially in the study of a naturally ventilated atrium in sec. 4.5.

2.6 Asymptotic analysis

In this section we will show how the Navier-Stokes equation can be derived from the Lattice Boltzmann Equation. For the sake of simplicity we will consider only the BGK-approximation.The Navier-Stokes equation are derived from the Boltzmann equation via Chapman-Enskog analysis. For this analysis, all quantities are expanded for two different time scales (the acoustic and the diffusive time scale) such as in [17] or [60]. In the Lattice Boltzmann context a different, momentum-based derivation is also in use, see e.g. [81] and [30]. In this kind of derivation, only one time scale is necessary but the equation itself has to be expanded, not only the quantities. The acoustic and diffusive equations are obtained as different orders of the expansion. Only one scaling (diffusive or acoustic) is considered at a time. Asymptotic analysis is based on a kind of Taylor expansion which is sometimes referred to as “Hilbert expansion”. An advantage of the asymptotic expansion is that the concept of the Taylor expansion is more familiar than an expansion using different types of spacial and temporal derivatives. We will be using this last approach and follow a five-step procedure

- Taylor expansion of the LBE
- transformation of the LBE to moment space

- expansion of the moments
- sorting the equations by order
- comparison with the Navier Stokes equation to determine equilibria and relaxation parameters

We derive these equations for the case of zero background velocity. This will later play a role when considering the order of accuracy of the scheme.

2.6.1 The Lattice Boltzmann equation, transformation to moments an expansion

We start the procedure from the Lattice Boltzmann equation with the relaxation step

$$f^*(\mathbf{x},t) = f(\mathbf{x},t) + \lambda\left(f^{eq}(\mathbf{x},t) - f(\mathbf{x},t)\right) \tag{2.48}$$

and the propagation step

$$f(\mathbf{x}+\mathbf{e}_i c\Delta_t, t+\Delta_t) = f^*(\mathbf{x},t). \tag{2.49}$$

The propagation step may be rewritten as

$$f(\mathbf{x},t+\Delta_t) = f^*(\mathbf{x}-\mathbf{e}_i c\Delta_t, t). \tag{2.50}$$

We now expand the left-hand side and the right-hand side of this equation separately in a Taylor expansion (see e.g. [12]), starting with the left-hand side

$$f(x,t+\Delta_t) = \sum_{n=0}^{\infty} \frac{\partial_{t^n}^n f(x,t)}{n!}\Delta_t^n \tag{2.51}$$

where $\partial_{t^n}^n f$ is the nth derivative of f. We replace $\mathbf{e}_i c\Delta_t = \mathbf{e}_i \Delta x$ using the definition of the reference speed $c = \Delta x/\Delta t$. For the right-hand side we have

$$f^*(\mathbf{x}-\Delta_x\mathbf{e}_i, t) = \sum_{n,m,k=0}^{\infty} \Delta_x^{n+m+k}(-1)^{n+m+k}\frac{e_x^n e_y^m e_z^k}{(n+m+k)!}\partial_{x^n y^m z^k}^{n+m+k} f^* \tag{2.52}$$

The propagation step is now rearranged

$$0 = \sum_{i=0}^{\infty}\frac{\partial_{t^i}^i f_q}{i!}\Delta_t^i - \sum_{i,j,l=0}^{\infty}\Delta_x^{i+j+l}(-1)^{i+j+l}\frac{e_x^i e_y^j e_z^l}{(i+j+l)!}\partial_{x^i y^j z^l}^{i+j+l} f_q^*. \tag{2.53}$$

We substitute the Taylor-expansions for the individual terms

$$f_q^*(\mathbf{x},t) - f_q(\mathbf{x},t) = \sum_{i=1}^{\infty}\frac{\partial_{t^i}^i f_q}{i!}\Delta_t^i - \sum_{\substack{i,j,l=0 \\ i+j+l>0}}^{\infty}\Delta_x^{i+j+l}(-1)^{i+j+l}\frac{e_x^i e_y^j e_z^l}{(i+j+l)!}\partial_{x^i y^j z^l}^{i+j+l} f_q^* \tag{2.54}$$

We now proceed to the next point on our agenda, the transformation of the LBE to moment space. First we recall definition 2.24 and define moments $m_{x^n y^m z^k}$ as

$$m_{x^n y^m z^k} = \sum_{q=1}^{Q} f_q(\mathbf{x}, t) e_{qx}^n e_{qy}^m e_{qz}^k \tag{2.55}$$

We now carry out the transformation of the propagation equation to momentum space

$$\sum_{q=1}^{Q} \left(\sum_{i=1}^{\infty} \frac{\partial_{t^i}^i f_q}{i!} \Delta_t^i - \sum_{\substack{i,j,l=0 \\ i+j+l>1}}^{\infty} \Delta_x^{i+j+l} (-1)^{i+j+l} \frac{e_x^i e_y^j e_z^l}{(i+j+l)!} \partial_{x^i y^j z^l}^{i+j+l} f_q^* \right) e_x^n e_y^m e_z^k$$
$$= \sum_q \left(f_q^* - f_q \right) e_x^n e_y^m e_z^k \tag{2.56}$$

which gives

$$\sum_{i=1}^{\infty} \frac{\partial_{t^i}^i m_{x^n y^m z^k}}{i!} \Delta_t^i - \sum_{\substack{i,j,l=0 \\ i+j+l>0}}^{\infty} \frac{\Delta_x^{i+j+l} (-1)^{i+j+l} \partial_{x^i y^j z^l}^{i+j+l}}{(i+j+l)!} m^*_{x^{n+i} y^{m+j} z^{k+l}} = m^*_{x^n y^m z^k} - m_{x^n y^m z^k}. \tag{2.57}$$

The second term on the left hand side has been summed taking into account that in phase space v and x are independent variables. So the derivatives in x and t can be thought of as derivatives of the whole term. (The summation goes over the entire, fixed, domain so the derivatives commute with the summation). The relaxation step simply becomes

$$m^*_{x^2 11} = m_{x^2 11}(1-\lambda) + \lambda m^{eq}_{x^2 11}. \tag{2.58}$$

To see where the expansion is taking us we take a look at the equation for the zero order moment. We postulate that the zero order moment is conserved, $m_{x^0 y^0 z^0} = m^*_{x^0 y^0 z^0} = \rho$, which entails an equation for the temporal derivative of ρ. We expect this to be a mass conservation equation of the form

$$\partial_t \rho + \rho \partial_{\mathbf{x}} \mathrm{v} = 0 \tag{2.59}$$

for a transport velocity v. In the following we will show that eq. 2.59 indeed holds for an appropriately defined v. But first we will look at eqn 2.57 a bit more in detail, to gain insight into the relation between the different derivatives and the order of the error.
We use diffusive scaling, which means setting $\Delta t = \Delta x^2 = \varepsilon^2$. Eq. 2.57 then becomes

$$\sum_{i=1}^{\infty} \frac{\partial_{t^i} m_{x^n y^m z^k}}{i!} \varepsilon^{2i} - \sum_{\substack{i,j,l=0 \\ i+j+l>0}}^{\infty} \varepsilon^{i+j+l} (-1)^{i+j+l} \frac{\partial_{x^i y^j z^l}^{i+j+l}}{(i+j+l)!} m^*_{x^{n+i} y^{m+j} z^{l+k}} = m^*_{x^n y^m z^k} - m_{x^n y^m z^k} \tag{2.60}$$

The idea behind the asymptotic or multi-scale analysis is to have components of the variables that vary with different time scales. In this equation we insert the definition of ε and introduce the coefficient $m_{..|i}$ as the total contribution of order i in ε

$$m_{...} = m_{...|0} + \varepsilon^1 m_{...|1} + \varepsilon^2 m_{...|2} + ... \tag{2.61}$$

Note that the term $m_{...|0}$ is constant and all derivatives of $m_{...|0}$ vanish.

2.6.2 Continuity equation

In particular, eq. 2.57 with $n = m = k = 0$ becomes

$$\varepsilon^4 \partial_t m_{0|2} = \varepsilon^2 \partial_{x_i} m_{x_i|1} + \varepsilon^3 \partial^2_{x_i x_j} m_{x_i x_j|1}/2 + \varepsilon^4 \partial^2_{x_i x_j} m_{x_i x_j|2}/2 + \varepsilon^3 \partial_{x_i} m_{x_i|2} + \varepsilon^4 \partial_{x_i} m_{x_i|3} + O(\varepsilon^6). \tag{2.62}$$

To the order ε^2 we have

$$\varepsilon^2 \partial_{x_i} m_{x_i} = 0 \tag{2.63}$$

We now define a reference density ρ_{ref}. The density splits into the constant part ρ_{ref} and the fluctuating part $\Delta\rho$. The macroscopic velocity v can then be defined via

$$m_{x_i} = \rho_{ref} \mathrm{v}_{x_i} \tag{2.64}$$

All derivatives of ρ_{ref} vanish which finally leads to the continuity equation for incompressible flows

$$\partial_{x_i} \mathrm{v}_{x_i} = 0. \tag{2.65}$$

The third-order terms are collected will be considered separately at the end of the section. With acoustic scaling ($\Delta t = \Delta x$ and $\rho = \rho_0 \varepsilon + \rho_1 \varepsilon^2 + ...$) the full mass conservation equation is obtained. In that case the transport velocity v is defined differently, $m_{x_i} = \rho \mathrm{v}_{x_i}$, which gives the temporal derivative and the divergence at the same order of ε.

2.6.3 Momentum equation

The equations for the first-order moment in x-direction in diffusive scaling are

$$\begin{aligned} \left(m^*_{x11|1} - m_{x11|1}\right)\varepsilon &= 0 \\ \partial_t m_{x11|1}\varepsilon^3 &+ \left(\partial_x m^*_{x^2 11|2} + \partial_y m^*_{xy1|2} + \partial_z m^*_{x1z|2}\right)\varepsilon^3 \\ -\frac{1}{2}\sum_{ij} \partial_{x_i}\partial_{x_j} m^*_{x x_i x_j|1}\varepsilon^3 &= \left(m^*_{x11|3} - m_{x11|3}\right)\varepsilon^3 \end{aligned} \tag{2.66}$$

The right hand side of the equations equals zero because the first order momentum is conserved. We now split the variables and derivatives into higher-and lower order contributions and omit the higher-order contributions. For the ε^3-terms we have

$$\left(\partial_t m_{x11|1} + \partial_x m^*_{x^2 11|2} + \partial_y m^*_{xy1|2} + \partial_z m^*_{x1z|2} - \frac{1}{2}\sum_{ij} \partial_{x_i}\partial_{x_j} m^*_{x x_i x_j|1}\right) = 0 \tag{2.67}$$

We need to rephrase and simplify this equation such that only first-order moments and moments in their equilibrium occur. The post-collision terms need to be eliminated. Here the BGK-approximation comes into play. The relaxation coefficient is the same for all orthogonal moments and thus the second moments are relaxed according to 2.58

$$m^*_{x^2 11} = m_{x^2 11}(1-\lambda) + \lambda m^{eq}_{x^2 11} \tag{2.68}$$

At the same time we have an equation for the second order moments $m_{x^2 11|2}$, $m_{xy1|2}$ and $m_{x1z|2}$ from 2.60

$$\begin{aligned}
\partial_t m_{x^2 11|0} + \partial_x m^*_{x^3 11|1} + \partial_y m^*_{x^2 y1|1} + \partial_2 m^*_{x^2 1z|1} &= m^*_{x^2 11|0} - m_{x^2 11|0} \\
\partial_t m_{x^2 11|0} + \partial_x m^*_{x^2 y1|1} + \partial_y m^*_{xy^2 1|1} + \partial_2 m^*_{xyz|1} &= m^*_{xy1|0} - m_{xy1|0} \\
\partial_t m_{x^2 11|0} + \partial_x m^*_{x^2 1z|1} + \partial_y m^*_{xyz|1} + \partial_2 m^*_{x1z^2|1} &= m^*_{x1z|0} - m_{x1z|0}
\end{aligned} \tag{2.69}$$

For the velocity spaces considered ($D2Q9$,$D3Q19$ and $D3Q27$, c.f. sec 2.4.3) an aliasing effect occurs, $e_i^3 = e_i$ or $m_{x^3 11} = m_{x11}$.
For the other third-order moments we again go back to eq. 2.60

$$\begin{aligned}
\varepsilon^3 \left(\partial_t m_{x^2 y1|1} + \partial_x m_{x^3 y1|2} + \partial_y m_{x^2 y^2 1|2} + \partial_z m_{x^2 yz|2} \right) + O\left(\varepsilon^4\right) \\
= \varepsilon \left(m^*_{x^2 y1|1} - m_{x^2 y1|1} \right) + \varepsilon^3 \left(m^*_{x^2 y1|3} - m_{x^2 y1|3} \right).
\end{aligned} \tag{2.70}$$

The first term on the right-hand side is the only term that is linear in ε. We see that the first-order contribution of $m_{x^2 y1}$ is conserved. All terms on the left-hand side are at least of third order in ε. We deduce $m_{x^2 y1} = m^{eq}_{x^2 y1} + O(\varepsilon^2)$. Summarizing, this gives

$$m^*_{x^2 11|2} = m^{eq}_{x^2 11|2} - \left(\frac{1}{\lambda} - 1 \right) \left(\partial_x m_{x11|1} + \partial_y m^{eq}_{x^2 y1|1} + \partial_z m^{eq}_{x^2 1z|1} \right) \tag{2.71}$$

We proceed in the same way with $\partial_y m^*_{xy1}$

$$m^*_{xy1|2} = m^{eq}_{xy1|2} - \left(\frac{1}{\lambda} - 1 \right) \left(\partial_x m^{eq}_{x^2 y1|1} + \partial_y m^{eq}_{xy^2 1|1} + \partial_z m^{eq}_{xyz|1} \right) \tag{2.72}$$

A first order contribution $m_{xyz|1}$ can only be its equilibrium $m^{eq}_{xyz|1}$. We now make an assumption. We assume that $m^{eq}_{xyz|1} = 0$. This assumption will be justified a posteriori if we arrive at the Navier Stokes equations with second order accuracy. We still have to consider the second-order derivatives in the Taylor expansion 2.67. Using eq. 2.70 these terms now simplify to give

$$-\frac{1}{2} \sum_{ij} \partial_{x_i} \partial_{x_j} m^*_{x x_i x_j|1} = -\frac{1}{2} \sum_{ij} \partial_{x_i} \partial_{x_j} m^{eq}_{x x_i x_j|1} + 0 \tag{2.73}$$

Finally we substitute back into eq. 2.67.

$$\begin{aligned}
\partial_t m_{x11|1} + \partial_x \Bigg(m^{eq}_{x^2 11|2} - \left(\frac{1}{\lambda} - 1 \right) \left(\partial_x m_{x11|1} + \partial_y m^{eq}_{x^2 y1|1} + \partial_z m^{eq}_{x^2 1z|1} \right) \Bigg) \\
+ \partial_y \left(m^{eq}_{xy1|2} - \left(\frac{1}{\lambda} - 1 \right) \left(\partial_x m^{eq}_{x^2 y1|1} + \partial_y m^{eq}_{xy^2 1|1} \right) \right) \\
+ \partial_z \left(m^{eq}_{x1z|2} - \left(\frac{1}{\lambda} - 1 \right) \left(\partial_x m^{eq}_{x^2 1z|1} + \partial_z m^{eq}_{x1z^2|1} \right) \right) \\
- \frac{1}{2} \sum_{ij} \partial_{x_i} \partial_{x_j} m^{eq}_{x x_i x_j|1} \\
= \quad 0
\end{aligned} \tag{2.74}$$

The equations for m_{1y1} and m_{11z} are obtained analogously. Using v from 2.64 we make the ansatz

$$\begin{aligned} m^{eq}_{x^2 11} &= \rho c_s^2 + \rho_{ref} \mathrm{v}_x^2 && (2.75)\\ m^{eq}_{xy1} &= \rho_{ref} \mathrm{v}_x \mathrm{v}_y && (2.76)\\ m^{eq}_{xz1} &= \rho_{ref} \mathrm{v}_x \mathrm{v}_z && (2.77)\\ m^{eq}_{x^2 y1} &= \rho_{ref} \mathrm{v}_y c_s^2 && (2.78) \end{aligned}$$

assuming $\left(\frac{1}{\lambda} - 1\right) = const$ for the sake of simplicity we have the equations

$$\begin{aligned} \rho_{ref}\partial_t \mathrm{v}_x + \partial_x(\rho c_s^2 + \rho_{ref}\mathrm{v}_x^2) - \rho_{ref}\left(\frac{1}{\lambda} - 1\right)\left(\partial_{x^2}\mathrm{v}_x + \partial_{xy}\mathrm{v}_y c_s^2 + \partial_{xz}\mathrm{v}_z c_s^2\right) \\ + \rho_{ref}\left(\partial_y \mathrm{v}_x \mathrm{v}_y - \left(\frac{1}{\lambda} - 1\right)\left(\partial_{xy}\mathrm{v}_y c_s^2 + \partial_{yy}\mathrm{v}_x c_s^2\right)\right) \\ + \rho_{ref}\left(\partial_z \mathrm{v}_x \mathrm{v}_z - \left(\frac{1}{\lambda} - 1\right)\left(\partial_{xz}\mathrm{v}_z c_s^2 + \partial_{zz}\mathrm{v}_x c_s^2\right)\right)\Big) \\ - \rho_{ref}\frac{1}{2}\left(\partial_{xx}\mathrm{v}_x + \partial_{yy}\mathrm{v}_x c_s^2 + \partial_{zz}\mathrm{v}_x c_s^2 + 2\partial_{xy}\mathrm{v}_y c_s^2 + 2\partial_{xz}\mathrm{v}_z c_s^2\right) \\ = 0 \end{aligned} \tag{2.79}$$

This is the leading-order equation for the momentum. The error terms will be considered toward the end of this section. The correct equations are also obtained for LES, where λ is allowed to depend on x and t and therefore does not commute with ∂_x. We may rearrange the equations above to give

$$\rho_{ref}\partial_t \mathrm{v}_x + \rho_{ref}\partial_{x_i}\mathrm{v}_{x_i}\mathrm{v}_x + \partial_x \rho c_s^2 = \rho_{ref}\left(\lambda - \frac{1}{2}\right) c_s^2 \left(\Delta \mathrm{v}_x + 2\partial_x\left(\partial_x \mathrm{v}_x + \partial_y \mathrm{v}_y + \partial_z \mathrm{v}_z\right)\right).$$

The last term accounts for the compressibility of the fluid. For the BGK model, the compressibility is modeled with a bulk viscosity of $\xi = 2c_s^2\nu$. In its lowest order approximation it can be neglected using the incompressibility condition. The bulk viscosity is responsible for the behavior (e.g. attenuation) of sound waves. These equations then lead to the incompressible dimensionless Navier Stokes equations

$$\rho_{ref}\left(\frac{\partial \mathrm{v}}{\partial t} + \mathrm{v}\nabla \mathrm{v}\right) = -\nabla p + \rho_{ref}\frac{1}{Re}\Delta \mathrm{v} \tag{2.80}$$

if λ is set to

$$\lambda = \frac{c_s^2}{Re} + \frac{1}{2} \tag{2.81}$$

and $c_s^2 = \frac{\Delta p}{\Delta \rho}$ with $c_s^2 = 1/3$ holds. The more well-known relationship between ν and λ

$$\nu = \left(\frac{1}{\lambda} - \frac{\Delta t}{2}\right) c_s^2 \tag{2.82}$$

can be obtained by multiplying eq. 2.80 with the reference length and the reference velocity to regain the standard form of the Navier Stokes equations.

2.6.4 Discussion

Note that no specific Lattice Boltzmann stencil entered in the derivation. We did assume that the density, velocity, the six second order moments (or three in two dimensions), and the third-order moments $\mu_{x_i^2 x_j}$, $i \neq j$ were linear independent from each other and from μ_x, μ_y, and μ_z. Furthermore, we requested that $e_i^3 = e_i$.
For MRT models the derivation becomes a bit more tedious, because eq. 2.70 is no longer valid and has to be replaced by a relaxation of the linear combination of second-order moments. E.g. in two dimensions

$$\mu^*_{xx+yy} = \mu^{eq}_{xx+yy} + \left(\frac{1}{\lambda_B} - 1\right)\left(\partial_x \mu^*_{x^3+xyy} + \partial_y \mu^*_{xxy+y^3}\right) \tag{2.83}$$

$$\mu^*_{xx-yy} = \mu^{eq}_{xx-yy} + \left(\frac{1}{\lambda_2} - 1\right)\left(\partial_x \mu^*_{x^3-xyy} + \partial_y \mu^*_{xxy-y^3}\right) \tag{2.84}$$

The relaxation coefficient λ_B fixes the bulk viscosity, the shear viscosity is recovered from λ_2. One proceeds for the third-order moments in the same way as one does in the case of $LBGK$. The MRT derivation then holds for the CLB-models as well because differences between the models occur for non-equilibrium contributions of the third- and higher-order moments only. Hold in mind that only some of the error terms are of numerical nature. Higher order terms in the expansion of the linearized continuous Boltzmann equation lead to the Burnett and super-Burnett equations [16]. Numerical errors are those that stem from the finite velocity sets as aliasing errors and from the numerical grid which occurs in the expansion as the Taylor expansion for the finite difference stencil. The expansion of the Boltzmann distribution function leads to non-numerical error terms. Boundary conditions were not considered in the discussion above. Several researchers have analyzed boundary conditions for Lattice Boltzmann by a similar asymptotic expansion, e.g. [64].

2.6.5 Error terms

In the remainder of the section we will show that the density and momentum equation are second order accurate if some conditions are fulfilled. We will proceed as follows: First we will derive a condition under which the density equation is second order accurate. After that we will consider the criteria for second order accuracy of the momentum equation. The scheme is second order accurate is the conditions for these equations match. We will need two corollaries. One concerns the first order contributions of the fourth order moments and will be dealt with before considering the momentum equation. The other will be our next step. As a preliminary, we show that the first order contributions of moments and equilibira are equal and equal their equilbria. We take eq. 2.60 and extract all terms of order ε^1. The first term

$$\sum_{i=1}^{\infty} \frac{\partial_{t^i} m_{x^n y^m z^k|\gamma}}{i!} \varepsilon^{2i} \tag{2.85}$$

would have a first-order contribution only for $\gamma = 1-2i$ which does not occur in the current expansion. The second term

$$\sum_{\substack{i,j,l=0 \\ i+j+l>0}}^{\infty} \varepsilon^{i+j+l}(-1)^{i+j+l}\frac{\partial^{i+j+l}}{x^i y^j z^l}\frac{}{(i+j+l)!}m^*_{x^{n+i}y^{m+j}z^{l+k}} \tag{2.86}$$

would yield a contribution only for the zero-moment contributions of the moments $m^*_{x^{n+i}y^{m+j}z^{l+k}}$. The derivatives of these are zero by construction. So only the right-hand side is non-zero. Because of $m^* = m + \lambda\left(m^{eq} - m\right)$ we have

$$m^*_{...|1} = m_{...|1} = m^{eq}_{...|1} \tag{2.87}$$

for any moment m of order ε^1.
We now consider the evolution equation for ρ.

$$\partial_t m_{0|1} + \partial_x m^*_{x11|2} + \partial_y m^*_{1y1|2} + \partial_z m^*_{11z|2} - \frac{1}{2}\sum_{ij}\partial_{x_i}\partial_{x_j} m^*_{x_i x_j|1} = m^*_{0|3} - m_{0|3}. \tag{2.88}$$

Note that, if a quantity is conserved, all orders of this quantity are conserved because ε can be chosen arbitrarily. Thus, the right hand side of this equation is zero because of mass conservation. For the third term on the left hand side we first consider the equation of the first order moments

$$\left(\partial_t m_{x11|0} + \partial_x m^*_{x^2 11|1} + \partial_y m^*_{xy1|1} + \partial_z m^*_{x1z|1}\right) = m^*_{x11|3} - m_{x11|3}. \tag{2.89}$$

which becomes

$$\partial_x m^*_{x^2 11|1} + \partial_y m^*_{xy1|1} + \partial_z m^*_{x1z|1} = 0. \tag{2.90}$$

because all derivatives of zero order moments are zero as they vary neither with spacial nor with temporal coordinates. For $m_{1y1|0}$ and $m_{11z|0}$ we have analouge evolution equations. If we take the partial derivative ∂_{x_i} for the equation for x_i and then sum over these three equations we have

$$\sum_{ij}\partial_{x_i}\partial_{x_j} m^*_{x_i x_j|1} = 0. \tag{2.91}$$

or that the last term of the left hand side of eq. 2.88 is zero. In all, eq. 2.88 becomes

$$\left(\partial_t m_{0|1} + \partial_x m_{x11|2} + \partial_y m_{1y1|2} + \partial_z m_{11z|2}\right) = 0. \tag{2.92}$$

If $m_{0|1} = m_{x11|2} = m_{1y1|2} = m_{11z|2} = 0$ is chosen as an initial condition and the boundary conditions are in accordance with this condition, then the equation for the density is at least second order accurate. For the ε^4-equation some error terms occur that do not vanish, namely the term $\partial^2_{x_i x_j} m_{x_i x_j|2}$. The incompressible continuity equation thus holds with second order accuracy.
We have thus arrived at a condition for the second order accuracy of this equation. We still

need to consider the equation for the momentum and see whether we arrive at a compatible condition for the momentum equations.
As a preparation for the momentum equations we consider the fourth order moments. We have the fourth order moments $m_{x^2y^2}$, m_{xxyz}, $m_{xxxy} = m_{xy}$, $m_{xxxx} = m_{xx}$ and the moments that are generated from these by permuting x, y, z. We define the equilibria

$$\begin{aligned} m^{eq}_{x^2y^2} &= \rho c_s^4 + \rho_{ref}\rho c_s^2 \mathrm{v}_x^2 + \rho_{ref} c_s^2 \mathrm{v}_y^2 && (2.93)\\ m^{eq}_{x^2yz} &= \rho_{ref} c_s^2 \mathrm{v}_x \mathrm{v}_z. && (2.94) \end{aligned}$$

We have requested that no background velocity be present, thus $\mathrm{v}_{x|0} = \mathrm{v}_{y|0} = \mathrm{v}_{z|0} = 0$. In 2.92 we have further chosen $\rho_1 = 0$. The first order contribution to the equilibrium thus becomes

$$\begin{aligned} m^{eq}_{x^2y^2|1} &= \rho_1 c_s^4 + 2c_s^2\rho_{ref}\mathrm{v}_{x|1}\mathrm{v}_{x|0} + 2c_s^2\rho_{ref}\mathrm{v}_{y|1}\mathrm{v}_{y|0} = 0 && (2.95)\\ m^{eq}_{x^2yz|1} &= \rho_{ref} c_s^2 \mathrm{v}_{x|1}\mathrm{v}_{z|0} + \rho_{ref} c_s^2 \mathrm{v}_{x|0}\mathrm{v}_{z|1} = 0 && (2.96)\\ m^{eq}_{x^3y|1} &= \rho_{ref} c_s^2 \mathrm{v}_{x|1}\mathrm{v}_{y|0} + \rho_{ref} c_s^2 \mathrm{v}_{x|0}\mathrm{v}_{y|1} = 0 && (2.97)\\ m^{eq}_{x^4|1} &= \rho_{ref} c_s^2 \mathrm{v}_{x|1}\mathrm{v}_{x|0} = 0 && (2.98)\\ & && (2.99) \end{aligned}$$

We can now finally turn to the momentum equation. The forth order momentum equation is

$$\begin{aligned} \partial_t m_{x11|2} &+ \partial_x m^*_{x^211|3} + \partial_y m^*_{xy1|3} + \partial_z m^*_{x1z|3} \\ &- \frac{1}{2}\sum_{ij}\partial_{x_i}\partial_{x_j} m^*_{xx_ix_j|2} \\ &+ \frac{1}{6}\sum_{ijk}\partial_{x_i}\partial_{x_j}\partial_{x_k} m^*_{xx_ix_jx_k|1} \qquad (2.100)\\ &= m^*_{x11|4} - m_{x11|4}. \end{aligned}$$

The right hand side is zero because the momentum is conserved. The terms $m^*_{xx_ix_jx_k|1}$ equal zero as shown in eq. 2.95. Consider the terms $m^*_{xx_ix_j|2}$

$$\partial_t m_{x_ix_j1|1} + \partial_{x_k} m^*_{x_ix_jx_k|2} - \frac{1}{2}\sum_{kl}\partial_{x_k}\partial_{x_l} m^*_{x_ix_jx_kx_l|1} = m^*_{x_ix_j1|3} - m_{x_ix_j1|3}. \qquad (2.101)$$

We again use that the first order contributions are equal to their equilibra and $m^*_{x_ix_jx_kx_l|1} = 0$. Also $m_{x_ix_j1|1}$ is equal to its equilibrium which has already been defined. Only the terms $\mathrm{v}_{j|1}\mathrm{v}_{i|0}$, $\mathrm{v}_{j|1}\mathrm{v}_{i|0}$ and ρ_1 enter and these are all zero. Accordingly, eq. 2.101 reduces to

$$-\partial_{x_k} m^*_{x_ix_jx_k|2} = m^*_{x_ix_j1|3} - m_{x_ix_j1|3}. \qquad (2.102)$$

At the same time we have for $m_{x_ix_jx_k|2}$

$$\partial_t m_{x_ix_jx_k|0} + \partial_{x_l} m^*_{x_ix_jx_kx_l|1} = m^*_{x_ix_jx_k|2} - m_{x_ix_jx_k|2}. \qquad (2.103)$$

The last term $m^*_{x_i x_j x_k x_l|1}$ vanishes, as shown in 2.95 and for terms of order $\varepsilon^0 = 1$ all derivatives are zero. We are thus left with

$$m^*_{x_i x_j x_k|2} = m_{x_i x_j x_k|2} = m^{eq}_{x_i x_j x_k|2} = \mathrm{v}_{i|2}\delta_{jl}c_s^2 + \mathrm{v}_{j|2}\delta_{ik}c_s^2 + \mathrm{v}_{k|2}\delta_{ij}c_s^2 \tag{2.104}$$

Eq. 2.100 thus simplifies to

$$\begin{aligned} &\partial_t \mathrm{v}_{x|2} \\ &\quad + \quad \partial_x\left(\rho_3 c_s^2 + 2\mathrm{v}_{x|1}\mathrm{v}_{x|2}\right) + \partial_y\left(\mathrm{v}_{x|2}\mathrm{v}_{y|1} + \mathrm{v}_{x|1}\mathrm{v}_{y|2}\right) + \partial_z\left(\mathrm{v}_{x|2}\mathrm{v}_{z|1} + \mathrm{v}_{x|1}\mathrm{v}_{z|2}\right) \\ &\quad - \quad \frac{1}{2}\sum_{ij}\partial_{x_i}\partial_{x_j} m^*_{xx_i x_j|2} = 0. \end{aligned} \tag{2.105}$$

We have already seen that $\mathrm{v}_{x|2} = \mathrm{v}_{y|2} = \mathrm{v}_{z|2} = 0$ are a possible solution of eq. 2.92 to obtain second order accuracy for the continuity equation. For ρ_3 we have the following evolution equation

$$\begin{aligned} \partial_t m_{0|3} \quad &+ \quad \partial_t^2 m_{0|1}/2 + \partial_{x_k} m^*_{x_k|4} \\ &- \quad \frac{1}{2}\sum_{kl}\partial_{x_k}\partial_{x_l} m^*_{x_k x_l|3} \\ &+ \quad \frac{1}{6}\sum_{jkl}\partial_{x_j}\partial_{x_k}\partial_{x_l} m^*_{x_j x_k x_l|2} \\ &- \quad \frac{1}{4!}\sum_{ijkl}\partial_{x_i}\partial_{x_j}\partial_{x_k}\partial_{x_l} m^*_{x_i x_j x_k x_l|1} \\ &= \quad m^*_{0|3} - m_{0|3}. \end{aligned} \tag{2.106}$$

Using that m_0 is conserved, the right hand side vanishes. $m^*_{x_i x_j x_k x_l|1}$ is zero as shown in 2.95. $\sum_{jkl}\partial_{x_j}\partial_{x_k}\partial_{x_l} m^*_{x_j x_k x_l|2}$ is also zero, confer eq. 2.104 and using that the second order contributions to the velocities have been set to zero. $\sum_{kl}\partial_{x_k}\partial_{x_l} m^*_{x_k x_l|3}$ is zero as a consequence of this and of eq. 2.101. ρ_1 has already been set zero when considering the continuity equation 2.92. We are left with

$$\partial_t m_{111|3} + \partial_{x_k} m^*_{x_k|4} = 0 \tag{2.107}$$

Now $\rho_3 = 0$ and $\partial_{x_k} m_{x_k|4} = 0$ is a possible solution of this equation which would make the scheme second order accurate if it was valid for the initial and boundary conditions. However, it remains to be shown $m_{x_k|4}$ stays divergence free during its evolution. The evolution equation of this term, however, contains more unknowns, namely $m_{xx_j|5}$ and $m_{xx_j x_k|4}$. For these terms further evolution equations need to be considered. Interestingly, though, all terms are either even-order derivatives of odd moments or odd order derivatives of even moments. These are terms that have a different symmetry than the terms of the leading-order solution. Using an induction argument [81] has shown, that $\partial_t m_{111|3}$ indeed holds due to the symmetry of the numerical stencil.

2.7 Lattice Boltzmann boundary conditions

From a practitioners point of view there exist three types of boundary conditions for single component fluid flows: solid walls, far-field conditions, and inflow conditions. Far-field conditions may be outflow conditions, for which the flow is perpendicular to boundary and slip boundaries, for which the flow is parallel to boundary. In mathematical terms there exist Neumann boundaries (derivatives are supplied), Dirichlet (values at boundary are supplied), and mixed Neumann-Dirichlet boundaries. Neumann boundaries occur e.g. at the outflow boundary with a zero gradient condition. No slip walls are Dirichlet boundaries. Mixed Neumann-Dirichlet include boundaries with wall laws. For slip-boundaries a zero gradient is imposed for wall-parallel components and a zero-velocity condition for the wall-normal component, which makes it a mixed boundary condition as well. Further, periodic boundary conditions occur. In Lattice Boltzmann boundary conditions have to be specified for the particle distributions. Most boundary conditions are inspired by the particle picture. They are based on an inversion of the characteristic velocities (or one of its components) at the boundary corresponding to the reflection or scattering of particles at the boundary. More advanced boundary conditions gain second order accuracy using next-nearest neighbor information and information from pre-and post-propagation distributions, such as [9] or [111]. For Poiseuille flow it has been possible to construct link-based boundary conditions which lead to the exact analytic solution [64]. Alternatively, boundary conditions can be specified for the moments [5]. This has the advantage of a direct parallelism to boundary conditions designed for discretizations of the Navier Stokes equations but the disadvantage that such boundary conditions are more difficult to design for curved boundaries.

2.7.1 Solid walls

Three types of boundary conditions for solid walls are presented: a link-based staircase boundary condition, a node-based staircase boundary condition, and a link-based boundary condition for interpolated boundaries.
The simplest and earliest no-slip scheme was the Bounce Back scheme. For all missing links the microscopic particle velocities are inverted or rather replaced by the probability to find a particle moving with the opposite velocity [43]. The scheme is only first order accurate, which is lower than the order of the Lattice Boltzmann algorithm for the bulk. Second order accuracy can be achieved if the boundaries happen to be aligned with the lattice [62]. Its advantages are its simplicity and strict conservation of mass.
For a GPGPU code a distinction between distribution components for different microscopic velocities should be avoided to keep the code and memory access as simple as possible. Instead, a node-based boundary condition is to be preferred. The probability distribution components of all discrete velocities are exchanged with the values for the opposing velocity. That way, first oder accuracy is preserved while reducing the number of conditional statements to one per node and avoiding additional access to global memory. Second order

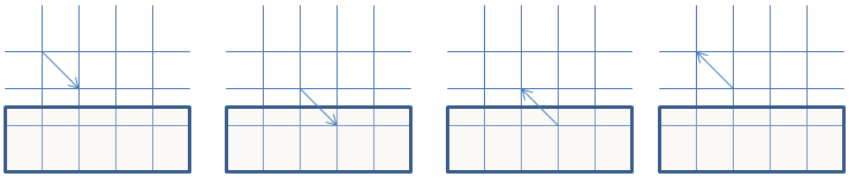

Figure 2.4: *Schematic of simple bounce back rule*

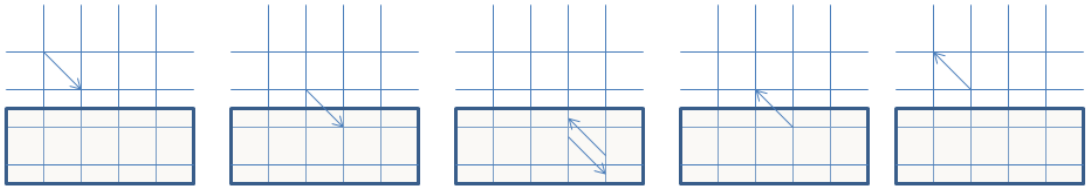

Figure 2.5: *Schematic of the simple bounce back rule for the GPU, timeshift*

boundary conditions that perform on GPGPUs have been developed in [48] and an efficient implementation of a interpolated boundary condition is presented in [125].

In order to deal with curved and non-axis parallel boundaries with second order accuracy [9] proposed a modified scheme. It slightly violates the conservation of mass. The method is used in VIRTUALFLUIDS and in some of our validation testcases, see e.g. sec. 4.4. Bouzidis approach distinguishes two areas for the location of the boundary: Distance $d > 1/2\Delta x$ and $d < 1/2\Delta x$.

$$f_q = \begin{cases} (1-2d)\, f_{\bar{q},\mathbf{x}-\mathbf{e}_q c\Delta t} + 2d f_{\bar{q}} - 2\rho w_q \frac{\mathbf{e}_{\bar{q}} v_w}{c_s^2} & 0 < d < 0.5 \\ \frac{(1-2d)}{2d} f_q + \frac{1}{2d} f_{\bar{q}} - \rho w_q \frac{\mathbf{e}_q v_w}{q c_s^2} & 0.5 \leq d \leq 1 \end{cases} \tag{2.108}$$

This formulation takes moving boundaries at speed v_w into account. Figure 2.6 illustrating the second-order accurate no-slip boundary condition of [9] shows the need for different interpolation points for different boundary positions. A different way to account for no-slip boundaries is to reconstruct the moments up to second order via the interpolation from neighboring nodes. Such boundary conditions can be found in this work in section 3.3. Similar schemes have been developed to deal with curved boundaries [48].

2.7.2 Slip boundaries conditions

Another important type of boundary conditions are the free slip boundary conditions, or symmetry conditions. They occur mostly as far field conditions. In some simulations they assume physical meaning as a simple model of the interface between two fluids. The two prevalent Lattice Boltzmann implementations are the bounce forward BC and a variant of the velocity boundary condition. In the case of the bounce forward condition the distribu-

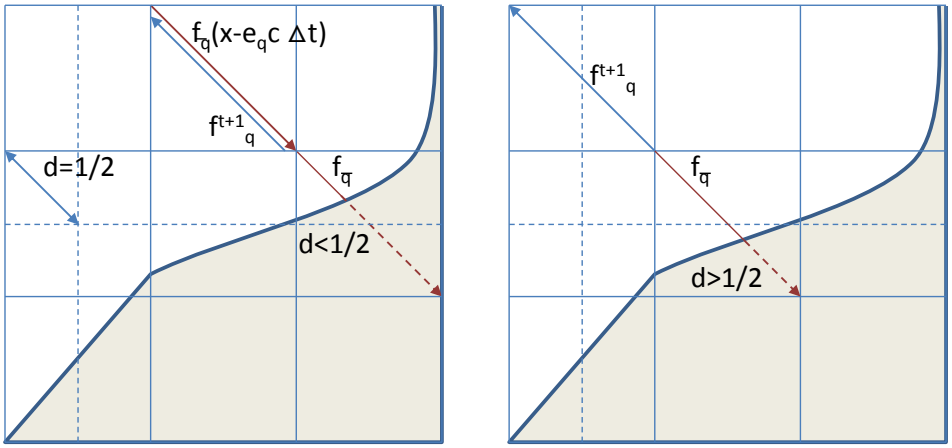

Figure 2.6: *Schematic of the interpolated Bounce Back rule by [9]*
left: Situation for the boundary being less than half a grid spacing away from the last node. f_q is interpolated for $f_{\bar{q}}$ at positions x and $x - c\Delta t$.
right: Situation if the boundary is located more than half a grid spacing from the last node. Now only $f_{\bar{q}}$ and f_q at position x itself are used to construct f_q.

tion components normal to the boundary are inverted and the parallel components remain unchanged, e.g. for the $D2Q9$ model for a boundary in N direction

$$\begin{aligned} f_S(\mathbf{x}+\mathbf{e}_s c\Delta t, t+\Delta t) &= f_N^*(\mathbf{x}, t) \\ f_{SE}(\mathbf{x}+\mathbf{e}_{se} c\Delta t, t+\Delta t) &= f_{NE}^*(\mathbf{x}, t) \\ f_{SW}(\mathbf{x}+\mathbf{e}_{sw} c\Delta t, t+\Delta t) &= f_{SE}^*(\mathbf{x}, t) \end{aligned} \tag{2.109}$$

For the second type of free slip boundary condition, the velocity at the last grid point is determined and a velocity condition with the tangential component of this velocity is imposed [1].

2.7.3 Inflow conditions

An inflow condition can be implemented as follows. First a no-slip boundary condition is applied. The components of the distribution function that point into the domain are replaced by the post-propagation counterparts that point out of the domain. After that, the equilibrium component in adjusted to match the new velocity [88]

$$f_q^* = f_{\bar{q}} + w_q \rho 2 \frac{\mathbf{e}_q \mathbf{u}}{c_s^2} \tag{2.110}$$

for straight inflow boundaries. Moving boundaries of complex shape can be dealt with in the same way using the interpolation rule 2.7.1 of [9]. The boundary condition prescribes

the correct flux and is second-order accurate for the in-plane components of the velocity. It is only first-order accurate for the wall-normal velocity component. For inflow conditions with a complex fluctuating velocity field the boundary condition may have to be improved to account for higher order contributions.

2.7.4 Outlet conditions

Usually, the values at the outer boundary of the domain are not known. As a far-field conditions it is usually save to assume that no derivatives normal to the boundary are present or that the pressure is constant at a reference value. Such a condition is used downstream of an obstacle in many of our simulations, such as e.g. the anti-bounce back condition of [159] in 4.4. A problem with such boundary conditions is that pressure waves that are reflected between inflow and outflow boundaries can negatively effect stability and accuracy of the simulation. This is an issue particularly in turbulent flow, where fluctuations are sometimes reflected at open boundaries. A common remedy are viscous damping layers. In such damping layers the viscosity increases towards the boundary which leads to a damping of the high-frequency components of the flow. Due to their robustness and simplicity they have been used for most of the turbulent flow problems described in this work. Sponge-layers have the problem that they increase the computational cost and often have unwanted effects at the interface with the free flow area. To deal with this problems, so-called characteristics-based boundary conditions have been proposed [146] and successfully applied to the LB method [77]. The idea of these methods is to solve the Euler-equations at the boundary and to dampen all incoming or outgoing characteristic waves for outflow and inflow conditions respectively.

2.8 Volume forces

Volume forces are present in many types of fluid flows. First and foremost, gravity is always present, even though it can often be neglected. Pressure differences are often modeled by volume forces as well. In Lattice Boltzmann volume forces can be applied in a simple way by adding the projection of the force vector F to the probability distribution components after the collision step.

$$\Delta f_q^* = \mathbf{e}_q w_q \mathbf{F} \Delta t / c_s^2 \tag{2.111}$$

with the weight-function w_q. This leads to the desired change in momentum

$$\Delta p_i = \sum_q \Delta f_q^* \mathbf{e}_{qi} = \mathbf{F}_i \Delta t \tag{2.112}$$

A second-order forcing term can be derived for LBM, as has been done in [67], [14], [64] for the BGK and TRT model and in [129], [130] for the MRT and CLB models. Starting from the continuous Boltzmann equation with BGK-approximation and Gaussian equilibrium with

variance $\frac{1}{2}c_s^2$ depending on the microscopic velocity $\mathbf{u}$ and centered around the macroscopic velocity $\mathbf{v}$ the following time-expansion is obtained

$$\begin{aligned}\frac{df(\mathbf{x},\mathbf{u},t)}{dt} &= \mathbf{u}\frac{\partial f(\mathbf{x},\mathbf{u},t)}{\partial \mathbf{x}} + \mathbf{F}/\rho\frac{\partial f(\mathbf{x},\mathbf{u},t)}{\partial \mathbf{u}} + \frac{\partial f(\mathbf{x},\mathbf{u},t)}{\partial t} \\ &\approx \mathbf{u}\frac{\partial f(\mathbf{x},\mathbf{u},t)}{\partial \mathbf{x}} + \mathbf{F}/\rho\frac{\partial f^{eq}(\mathbf{x},\mathbf{u},t)}{\partial \mathbf{u}} + \frac{\partial f(\mathbf{x},\mathbf{u},t)}{\partial t} \\ &= \mathbf{u}\frac{\partial f(\mathbf{x},\mathbf{u},t)}{\partial \mathbf{x}} + \frac{\mathbf{F}(\mathbf{u}-\mathbf{v})}{\rho c_s^2} f^{eq}(\mathbf{x},\mathbf{u},t) + \frac{\partial f(\mathbf{x},\mathbf{u},t)}{\partial t}.\end{aligned} \tag{2.113}$$

where $\partial\mathbf{p}/\partial t = \mathbf{F}$ was used with the momentum $\mathbf{p} = \rho\mathbf{u}$. We define a forcing vector $\mathbf{F}$ by

$$F_q = \frac{(e_{qi} - v_i)F_i}{\rho c_s^2} f_q^{eq}. \tag{2.114}$$

Now f^{eq} is inserted into the above equation which is also truncated at second order to obtain the following forcing term

$$F_q = \frac{w_i \rho F_i}{c_s^2}\left((e_{qi} - v_i) + 3\mathbf{e}_q\mathbf{v}\, e_{qi}/c_s^2 + O\left(v^2\right)\right) \tag{2.115}$$

Lattice Boltzmann equation for MRT with forcing can be made second-order accurate with a time-implicit ansatz for the force term.

$$\begin{aligned}f_q\left(\mathbf{x}+\mathbf{e}_q c\Delta t, t+\Delta t\right) &= f_q(\mathbf{x},t) + \left(M^{-1}SM\left(f(\mathbf{x},t) - f^{eq}(\mathbf{x},t)\right)\right)_q \\ &+ \frac{1}{2}\left(\mathbf{F}_q(\mathbf{x},t) + \mathbf{F}_q\left(\mathbf{x}+\mathbf{e}_q c\Delta t, t+\Delta t\right)\right)\Delta t.\end{aligned} \tag{2.116}$$

The probability distributions are now reinterpreted

$$\bar{f}_q(\mathbf{x},t) = f_q(\mathbf{x},t) - \frac{1}{2}F_q(\mathbf{x},t)\Delta t. \tag{2.117}$$

The equilibrium distribution depending on the macroscopic values $\bar{\rho}$ and $\bar{v}$ computed from the $\bar{f}_q$ instead of the f_q becomes

$$f_q^{eq}(\mathbf{x},\mathbf{v},t) = f_q^{eq}\left(\mathbf{x},\bar{\mathbf{v}} + \frac{1}{2}F_q, t\right). \tag{2.118}$$

and the collision term has to be re-written as

$$\left(M^{-1}SMf\right)_q = \left(M^{-1}SM\bar{f}\right)_q + \frac{1}{2}\left(M^{-1}SM\mathbf{F}\right)_q. \tag{2.119}$$

Summarizing, this yields the Lattice Boltzmann equation for MRT with a forcing term.

$$\begin{aligned}\bar{f}_q\left(\mathbf{x}+\mathbf{e}_q\Delta c t, t+\Delta t\right) &= \bar{f}_q(\mathbf{x},t) + \left(M^{-1}SM\left(\bar{f}(\mathbf{x},t) - f^{eq}(\mathbf{x},\bar{\mathbf{v}},t)\right)\right)_q \\ &+ \left(\left(1 - \frac{1}{2}M^{-1}SM\right)\mathbf{F}\right)_q \Delta t\end{aligned} \tag{2.120}$$

In our application we only deal with volume forces that are constant in time and space and several orders of magnitude smaller than the velocities. We thus decided to use the simple forcing given by eq. 2.111 in all studies, except for the convergence studies in sec. 3.7. There, the accuracy of the two forcing terms both the first-order accurate and the second-order accurate forcing are considered for a compressible $D3Q19$ MRT model.

2.9 Turbulence

Turbulence is the chaotic motion that a fluid experiences when its dissipative forces do not outweigh the convective forces. As any truly chaotic phenomenon it is very difficult to model although numerous modeling assumptions have been proposed over the last century. There does not even exist a widely accepted definition of turbulent flow. Following [45] we will regard flow as turbulent when the following criteria are satisfied

- disordered instantaneous flow field: the flow appears chaotic
- three-dimensional (almost always) and instationary motion of vortices
- various scales are involved in the motion, vortices interact at different scales
- the random flow field dissipates kinetic energy and leads to a rapid diffusion of passive scalars

All these criteria are empirical and subject to interpretation. Even the definition of a vortex is not obvious; one possibility is via the Q-criterion [74]. Some properties of turbulent flow can be derived for specific flow types. An influential concept is the Kolmogorov length $l_k = \left(\frac{\nu^3}{\varepsilon}\right)^{1/4}$ where ν is the kinematic viscosity and ε is the turbulent dissipation. The Kolmogorov length is the scale below which all vortices are dissipated. With growing Reynolds number (based on the large scale motions) the dissipation due to the turbulent fluid motion outweights the dissipation due to the fluid's viscosity and the Kolmogorov scale decreases. The Kolmogorov scale is not directly related to the mean free path of the molecules in a gas and is significantly larger for almost all applications.
The first idea coming to mind for modeling turbulence is to resolve all motions of the fluid as described by the Navier Stokes equation. This approach is called "'**d**irect **n**umerical **s**imulation"' or DNS. If only large scale vortices are simulated, but smaller vortices are modeled, one talks about a **L**arge **E**ddy **S**imulation or LES. This method is less computationally expensive, but in many engineering applications an even higher level of modeling is employed: only the (ensemble-) averaged Navier Stokes equations are simulated. The corresponding equations are called **R**eynolds **a**veraged **N**avier **S**tokes equations or RANS. We will now give an overview over all three roads to turbulence, starting from the lowest level of modeling. Almost all derivations of turbulence models start with a filtering of the Navier Stokes equations. We will explain this approach in the following section and then present the various turbulence models that were implemented in the work presented here. These are the Smagorinsky LES model with van Driest damping, the WALE model, the Vreman model and a one-equation RANS model.

2.9.1 DNS

For a direct numerical simulation all turbulent fluctuations have to be modeled, so the grid has to be fine enough to represent the Kolmogorov scale. This scale grows with the Reynolds number Re like

$$\frac{L}{l_k} = Re^{3/4} \tag{2.121}$$

where L is the integral length scale or the size of the largest eddies. The Reynolds number is based on L and the velocity that corresponds to the turbulent kinetic energy. Consequently the computational effort grows as Re^3 if one assumes the temporal scales to be proportional to the spatial scales. It is evident that DNS becomes impractical even for moderate Reynolds numbers. It is nevertheless a valuable tool for studying turbulence. Whenever one is interested in the nature of turbulence itself, e.g. the spectrum of the turbulent fluctuations and to gain reliable reference data for the validation of turbulence models, DNS simulations are indispensable. Secondly, one can study the properties of the discretization without having to consider its complex interplay with the turbulence model. This is what we will describe in section 3.1. The Lattice Boltzmann model is a suitable model for performing DNS because no information about previous timesteps has to be kept in the memory and no matrices have to be inverted. As a finite difference scheme on a Cartesian grid it can be efficiently parallelized. A drawback are large memory requirements due to large stencils (e.g. $D3Q27$). Single-distribution schemes such as [143] should be used when memory requirements are crucial.

2.9.2 Turbulence modeling and RANS

To resolve all features of the flow, the Reynolds number based on the cell dimension should be around one. This is clearly impossible for almost all relevant flows. From the beginning of turbulence research the aim was to find approximations which reduce the computational cost of turbulent flow simulations. The first class of models that was developed were RANS models. These models solve the time- or ensemble-averaged (so called Reynolds-averaged) Navier Stokes equations, splitting all quantities into a mean and an oscillating component

$$A \mapsto \bar{A} + A' \tag{2.122}$$

where $\bar{A}$ is the mean component of the quantity A, varying only on the coarse scales $t_2, \vec{x}_2$. A' is the fluctuating component of A. Applying this operation to the continuity equation and the Navier Stokes equation, one obtains

$$\begin{aligned} \frac{\partial \bar{\rho}}{\partial t} &= -\nabla \bar{\mathbf{v}} \rho \\ \rho \left(\frac{\partial \bar{\mathbf{v}}}{\partial t} + \overline{\mathbf{v} \nabla \mathbf{v}} \right) &= -\nabla \bar{p} + \nu \Delta \bar{\mathbf{v}} \end{aligned} \tag{2.123}$$

because the derivatives ∂t, ∇, and Δ are linear operations that commute with taking the average. (Additional assumptions have to be made for Favre-averaging of the compressible Navier Stokes equations.) One particular type of averaging operation is the ensemble-average. For such an averaging operation one imagines that there is a set of realizations of the system. One then takes the statistical mean of all states that the system assumes for the individual runs. The more probable a certain realization, the more often it will occur in the ensemble. If one considers the average $\bar{A}$ of variables A such an average, in this case also called the Reynolds average, the above equations are called the RANS equations. In literature one often finds the assertion that the RANS equations are time-averaged equations. This is true for time-invariant systems assuming ergodicity. If the averaging operation is a spatial filter, the LES equations will be obtained. The transport equations for the mean quantities $\langle u \rangle$ are solved. In these equations unknown terms of the form $\left\langle u_i^{'} u_j^{'} \right\rangle$, called Reynolds-stresses, occur. We may derive additional equations for these unknowns by (tensor-)multiplying the Navier Stokes equations with the velocity and performing the averaging operation $\bar{}$. Nine further equations are obtained, but the problem is only mitigated, not solved, because we now have even more unknowns of the form $\left\langle u_i^{'} u_j^{'} u_k^{'} \right\rangle$. We have a closure problem, for as many equations as we derive, we will always generate even more new unknowns. The Reynolds stresses $\left\langle u_i^{'} u_j^{'} \right\rangle$ thus need to be modeled. One assumes that the contribution of the Reynolds-stresses is isotropic and can be described by an artificial contribution to the viscosity

$$\langle \rho \rangle \langle u_i u_j \rangle = 2 \nu_\tau \left(S_{ij} - \partial_{ij} S_{ii} / 3 \right) \tag{2.124}$$

where S_{ij} is the strain rate. This assumption is called the Boussinesq hypothesis. The most common RANS models, such as e.g. the $k-\varepsilon$ or the SST model by Menter [115] rely on the Boussinesq hypothesis. More sophisticated models include Reynolds stress models. These are time-averaged models which do not rely on the Boussinesq hypothesis but model the terms $\left\langle u_i^{'} u_j^{'} \right\rangle$ separately; see [96] for the original approach. In other words, in the hierarchy of moments of the Navier Stokes equations one solves the equations for one more order. These models promise better results than RANS models for some complex flow types such as rotational flows.

2.9.3 LES models

LES models are a more recent class of turbulence models. Instead of averaging in time, the Navier Stokes equations are filtered in space. Usually a normalized symmetric filter-kernel G is used such that

$$\bar{A}(x,t) = \int_{\mathrm{R}^3} G(x,y) A(y,t) \, dy = \int_{\mathrm{R}^3} G(x-y) A(y,t) \, dy = (G * A)(x) \tag{2.125}$$

As the convolution $(G * A)$ is a multiplication in Fourier space, this operation can be interpreted as an amplification of some frequencies and an attenuation of others. The idea behind LES is that only the large scale fluctuations contribute significantly to the flow and the small

scale fluctuations can be neglected. This damping effect can be achieved by introducing an artificial viscosity, the eddy viscosity ν_τ that varies in space and time and depends on the flow properties. The Navier Stokes equations are then solved for the total viscosity $\nu_{tot} = \nu + \nu_\tau$. This assumption is again the Boussinesq hypothesis, but with a slightly different justification:
The fluctuations occur in a continuous frequency spectrum with a given maximum and minimum frequency. Small frequencies correspond to small eddies and large frequencies to large eddies. It has been shown experimentally that the transfer of energy from larger structures to smaller structures is the dominant direction of energy transfer. This process is called the energy cascade. Very small eddies interact with molecular fluctuations and dissipate. It is thus assumed that eddies below a certain size do not contribute significantly to the motion of the fluid. Such eddies can then be modeled as dissipation. Some advanced LES models filter the Navier Stokes equations directly or use anisotropic damping, such as similarity models, that model a turbulent strainrate tensor [59]. We will take one such model, Bardina's similarity model [4], into account into our discussion of LES models and Cascaded Lattice Boltzmann. A further class of LES models are spectral LES models, that solve the LES-equations in Fourier space. Again, an eddy viscosity can be introduced. But in this case it depends not on a grid spacing but on a cut-off wave number. These models are especially successful for simple geometries or isotropic turbulence [99]. In this work, only Boussinesq-type models are considered. This is partly because more experience exists with such models and partly because eddy viscosity models can be implemented for the Lattice Boltzmann method much more straightforwardly, as [158] pointed out as early as 1998. Other LES models have been developed specifically for Lattice Boltzmann, such as [138] that derived the "approximate deconvolution model" for Lattice Boltzmann.
In recent years, hybrid models have become increasingly popular. These models either explicitly couple RANS and LES models, solving the RANS equations in some regions of the flow, such as close to an object's surface where LES models are very expensive and conducting an LES in others, such as far away from obstacles where macroscopic eddy movements are prevalent. Alternatively, new models are used that have both RANS and LES capabilities, such as the DES [155] and SAS [116] models. Another trend is to use dissipative numerical schemes without any turbulence model. A common choice are shock-capturing schemes [46]. The LES-type spatial filtering is provided by the numerical scheme on a finite grid.

Smagorinsky

The simplest and most widely used Large Eddy approach is the Smagorinsky model [153]

$$\nu_{tot} = \nu_o + \nu_\tau \tag{2.126}$$

$$S_{ij} = \frac{1}{2}\left(\frac{\partial \bar{u}_i}{\partial x_j} + \frac{\partial \bar{u}_j}{\partial x_i}\right) \tag{2.127}$$

$$\nu_\tau = (C_s\Delta)^2\sqrt{2S_{ij}S_{ij}} \tag{2.128}$$

Here Δ is the discretization width and C_s the Smagorinsky constant. For homogeneous isotropic turbulence a value of $C_s = 0.17$ was determined [144]. For other types of flow, such as boundary layer flow, C_s is usually set to a value between 0.01 and 0.21, [135]. In the context of the Lattice Boltzmann method there is a particularly efficient way to compute the matrix S_{ij}. The non-equilibrium components of the distribution components $f^{neq} = f - f^{eq}$ are used to compute the momentum flux tensor Π

$$\Pi_{ij} = \sum_q f_q^{neq} \mathbf{e}_{qi} \mathbf{e}_{qj} \tag{2.129}$$

holds. It can be seen from the asymptotic analysis that for the BGK model Π is related to the strain rate S via

$$S = -\frac{3}{2\tau}\Pi. \tag{2.130}$$

For MRT models only

$$\left\|\Pi_{ij}\right\| = \frac{3}{2\tau}\left\|S_{ij}\right\| \tag{2.131}$$

is fulfilled, which is sufficient for the current application. Here the relaxation factor τ again depends on the total viscosity, so a quadratic equation has to be solved for ν_{tot}. One obtains ([72])

$$\tau_t = \frac{1}{2} * \left(\sqrt{\tau_0^2 + \sqrt{2} * 18.0 * C_s^2 * \Omega} - \tau_0\right) \tag{2.132}$$

$$\tau_{tot} = \tau_0 + \tau_t \tag{2.133}$$

This method is particularly efficient, because no additional information from neighboring nodes is needed, which is a desirable feature for parallel codes. The standard Smagorinsky model has two main flaws: one is the near-wall behavior, that will be discussed in the following sections. The other is the choice of Smagorinsky constant, which takes different values for different flow types. A possible remedy is the use of near-wall damping functions [120], another the dynamic Smagorinsky model ([58], [100]) or other advanced LES models, which are discussed below.

Van Driest damping and the near-wall damping problem

The standard Smagorinsky model is valid for flow far away from boundaries. When the shear forces become dominant locally, the model has to be adjusted [45]. A possible damping function was given by van Driest. He observed that a linear increase of the turbulent length scale corresponded to a logarithmic velocity profile while damping functions should be used to model the viscous and buffer region. For simple RANS models where the mixing length occurs explicitly, such as Prantl's mixing length model (see sec. 2.9.4), an appropriate damping function can be chosen. Van Driest's idea for the Smagorinsky model was to replace the grid spacing Δ with a modified grid spacing $\tilde{\Delta}$

$$\tilde{\Delta} = \Delta(1 - e^{-y^+/A^+}) \tag{2.134}$$

where A^+ is an empirical constant commonly chosen as $A^+ = 25$ and y^+ the non-dimensional wall-distance as defined in eq. 2.156. Variants of this model use a different exponent α in $(1 - e^{-y^+/A^+})^\alpha$ or a cutoff of the form $\tilde{\Delta} = min(\Delta, C)$ for some constant C. A drawback of this method is that the distance from the wall has to be known for every grid point, or at least for every grid point where the distance is assumed to be small ($y^+ < 100$). For complex geometries and especially for moving geometries this removes the locality of the basic Smagorinsky model. Also, the damping function is an empirical function that introduces additional free parameters. A better (less empirical) way to deal with the excessive production of turbulent viscosity near the wall is to use a dynamic model. The dynamic Smagorinsky model replaces the constant Δ with a dynamic function derived via a similarity assumption. To compute the dynamic Smagorinsky constant, the strain rate and second derivatives have to be filtered explicitly. Several filtering operations are needed and the computational expense of the model is significantly higher than for the standard model. In return, the near-wall behavior is improved and the arbitrariness is removed. Unfortunately, this model tends to become unstable, such that additional averages over equivalent points in space or time have to be used [100]. One can use the dynamic Smagorinsky model to counter-check the choice of the static Smagorinsky constant for characteristic flows. The dynamic model has not been implemented in the work presented here because for complex geometries and transitional flows the choice of equivalent points is dubious and the computational effort rises. Fortunately, there exist several eddy viscosity LES models that have shown an improved near-wall behavior without using explicit filtering or averaging. Two of these are considered in the following. The van-Driest damping function was used in sec. 3.2 to simulate turbulent channel flow. For the studies of flow around a bridge cross section (cf. sec. 4.4) and a flat plate (cf. sec. 4.2) a damping function was applied at the wall-adjacent points only.

WALE

A different way to deal with the near-wall deficiencies of the Smagorinsky model was taken by [32] ([122]). They include the vorticity of the flow $\bar{\Omega}_{ij} = \frac{1}{2}\left(\frac{\partial \bar{u}_i}{\partial x_j} - \frac{\partial \bar{u}_j}{\partial x_i}\right)$ into the description of the turbulent flow. The model is known as the **w**all-**a**dapting **l**ocal **e**ddy-viscosity (WALE)-model. It is an eddy-viscosity model and its turbulent viscosity is computed from

$$S^d_{ij}S^d_{ij} = \frac{1}{6}(\bar{S}^2_{ij}\bar{S}^2_{ij} + \bar{\Omega}^2_{ij}\bar{\Omega}^2_{ij}) + \frac{2}{3}(\bar{S}_{ij}\bar{S}_{ij} * \bar{\Omega}_{ij}\bar{\Omega}_{ij}) + 2(\bar{S}_{ik}\bar{S}_{kj}\bar{\Omega}_{jl}\bar{\Omega}_{lj}) \tag{2.135}$$

$$\nu_t = (C_m\Delta)^2 \frac{(\bar{S}^d_{ij}\bar{S}^d_{ij})^{3/2}}{(\bar{S}^d_{ij}\bar{S}^d_{ij})^{5/4} + (\bar{S}_{ij}\bar{S}_{ij})^{5/2}} \tag{2.136}$$

$$C_m = 10.6C_s^2 \tag{2.137}$$

Here we adopt the convention of summing over all indexes appearing twice. For pure shear flow, this model yields a zero eddy viscosity. To see this, take (without loss of generality)

$\delta_{x_i} u_{x_j} = 0$ for all i, j except $i, j = 1,2$. Then $\Omega_{ij} = -\Omega_{ji} = S_{ij} = S_{ji}$ and all other entries are zero. We then have

$$\begin{aligned} S^d_{ij} S^d_{ij} &= \frac{2}{6}(4\bar{S}^4_{12}) + \frac{2}{3}(4\bar{S}^4_{12}) + 2(2\bar{S}_{12}\bar{S}_{21}\bar{\Omega}_{12}\bar{\Omega}_{21}) \\ &= \frac{2}{6}(4\bar{S}^4_{12}) + \frac{2}{3}(4\bar{S}^4_{12}) - 2(2\bar{S}_{12}\bar{S}_{21}\bar{S}_{12}\bar{S}_{12}) = 0 \end{aligned} \tag{2.138}$$

This is a very desirable feature in boundary layer flow in the viscous region where the flow is increasingly dominated by shear forces, because near-wall damping is obtained without any explicit evaluation of the wall distance. [32] further showed that for turbulent flow in a circular duct the viscosity grows as y^3 with the wall distance y. This is the expected behavior for boundary layer flow as discussed e.g. in [45]. Note that the limit of ν_t is not defined for $\|\omega\| \mapsto 0$ and $\|S_{ij}\| \mapsto 0$. This poses a challenge with respect to numerical implementation, as the denominator may be close to zero. In the CPU code we calculate ν_t using long doubles. If the denominator is smaller than a threshold value, we calculate ν_t assuming $\bar{S}_{ij}\bar{S}_{ij} = 0$. All velocities were scaled as $u_0 \mapsto u/u_x$ to improve the conditioning of the problem.

Vreman model

The Vreman model is another LES model that promises to give an improved near-wall behavior and the capability to model laminar-turbulent transitions. The Vreman model has been developed in 2004 and tested on turbulent mixing layers and turbulent channel flow [167]. [73] compares the Smagorinsky, Wale and Vreman model for turbulent duct flow and find that the WALE model outperforms the Vreman model, which was too dissipative. Still, it showed a better performance than the simple Smagorinsky model. A dynamic version of the model has been proposed [127].
The eddy viscosity depends on a combination of first and second derivatives and the computational effort is similar to that of the WALE model. Like the WALE model, the Vreman model employs the stress tensor and the vorticity tensor. The eddy-viscosity of the model is given by

$$\nu_\tau = C_v \sqrt{\frac{B_\beta}{\alpha_{ij}\alpha_{ij}}} \tag{2.139}$$

$$\alpha_{ij} = \frac{\partial \bar{u}_i}{\partial x_j} \tag{2.140}$$

$$\beta_{ij} = \Delta^2 \alpha_{mi}\alpha_{mj} \tag{2.141}$$

$$B_\beta = \beta_{11}\beta_{22} - \beta^2_{12} + \beta_{11}\beta_{33} - \beta^2_{13} + \beta_{22}\beta_{33} - \beta^2_{23} \tag{2.142}$$

with the constant $C_\nu = 2.5C_s^2$. The eddy viscosity is set to zero in the case of a vanishing denominator. For pure shear flow the eddy viscosity vanishes, as can be seen from the definition by setting all terms except α_{12} to zero:

$$\nu_\tau = C_\nu \sqrt{\frac{B_\beta}{\alpha_{ij}\alpha_{ij}}} = C_\nu \sqrt{\frac{B_\beta}{\frac{\partial \bar{u}_1}{\partial x_2}^2}} \tag{2.143}$$

$$\beta_{12}^2 = \Delta^4 \left(\frac{\partial \bar{u}_1}{\partial x_2} \frac{\partial \bar{u}_2}{\partial x_2} \right)^2 = 0 \tag{2.144}$$

$$\beta_{11}^2 = \Delta^4 \left(\frac{\partial \bar{u}_1}{\partial x_2} \frac{\partial \bar{u}_2}{\partial x_1} \right)^2 = 0 \tag{2.145}$$

Vreman offers a Fortran-implementation of the model on his homepage, so the implementation for the GPU code was straightforward. In section 3.2 we show a validation and a comparison with other LES models for turbulent channel flow.

2.9.4 RANS models - Prandtls mixing length model

For a few standard flow types and in certain regions (e.g. not too close to the wall) exact algebraic RANS models can be derived. We follow the introductory book [174]. For channel flow the RANS-equations reduce to

$$0 = \frac{\partial}{\partial y} \left((\nu + \nu_\tau) \frac{\partial U}{\partial y} \right) \tag{2.146}$$

where U is the Reynolds-averaged velocity in flow direction and y is the wall-normal direction. Simple algebraic operations that yield a turbulent viscosity of

$$\nu_\tau = \kappa \, y \, u_\tau \tag{2.147}$$

give the correct logarithmic profile. This simple turbulence model was established by Prantl in analogy to the mean free path in thermodynamics and is called “Prantl’s mixing length model”. Consequently, the first grid point needs to be located outside the near-wall region and wall-functions need to be used. More recent algebraic turbulence models, such as the Cebeci-Smith model [154], extend the model by introducing near-wall damping functions and limiters for the wake region of the flow. We have only tested the basic mixing-length model for its principal application, the boundary layer flow, c.f. sec. 3.3.

Hybrid RANS-LES models - Scale adaptive simulation

It is often unclear whether or not the use of wall functions is appropriate for a particular flow situation. As we have discussed earlier the resolution requirements for pure LES are often prohibitively severe. It has thus become increasingly popular to use hybrid RANS-LES models. These models solve the RANS equations near the wall and use LES in the bulk flow. One

such model is the Scale Adaptive Simulation. The **S**cale **A**daptive **S**imulation (SAS) model was developed by Menter to illustrate how RANS- and LES- models can be combined [116]. It is based on a one-equation model called K1E1. The K1E1 equation for the turbulent viscosity ν_τ is given by

$$\frac{d\nu_t}{dt} = c_1 \nu_t S + \nabla\left(\frac{\nu_t}{\sigma}\nabla\nu_t\right) - c_2\left(\frac{\nu_t}{L_0}\right)^2 \tag{2.148}$$

where S is the strain rate and

$$L_0 = \frac{\partial_j u_i \partial_i u_j}{\partial_{kk} u_l \partial_{ll} u_k} \tag{2.149}$$

the van Karman mixing length-scale. The values of the constants c_1, c_2 and σ as well as some modifications can be found in [34]. The values chosen for our simulations are given in sec. 3.3. To achieve hybrid behavior, the RANS-length scale L_0 is replaced by $L = min(L_0, 0.6)$. This inhibits the destruction of turbulent energy to fall below a certain value. In the bulk, where the destruction outweighs creation of turbulent energy, an LES-like behavior is achieved. The model has later been extended by a wall-damping function and to more complicated models including the SST model. The commercial CFD code CFX has incorporated the basic and the SST version of the SAS model in its latest release. For the near-wall damping, a van-Driest type function, a damping of the production term and a limiter on the dissipation term are applied, as suggested in [34]. We set

$$\tilde{\nu}_t = \nu_t(1 - exp^{-(\nu_t/(A^+\kappa\nu))^2}) \tag{2.150}$$

with $A^+ = 13$ and introduce a limiter for the dissipation term $c_2\left(\frac{\nu_t}{L}\right)^2$ by replacing

$$\left(\frac{\nu_t}{L}\right)^2 \rightarrow min\left(\left(\frac{\nu_t}{L}\right)^2, (\nabla\nu)^2\right) \tag{2.151}$$

For the production term one sets

$$c_1 \rightarrow c_1 \frac{\nu + \nu_t}{\nu + \tilde{\nu}_t} \tag{2.152}$$

The one-equation-SAS model has been implemented to gain some experience with hybrid RANS-LES models in Lattice Boltzmann, see sec. 3.3 for some validation.

2.10 Parallel computation, GPU computing and VIRTUALFLUIDS

In the following section the two hardware architectures and software packages used are presented. The first is an advanced research code, called VIRTUALFLUIDS, that runs in parallel on CPU-clusters, e.g. on the HPC-cluster LUDWIG (TU Braunschweig) [76], which has 1400 CPU cores available, plus 96 nVidia Tesla c1060 GPGPU cards. The second is also an iRMB-based research code, that is much less extensive, but very fast as it utilizes GPGPUs.

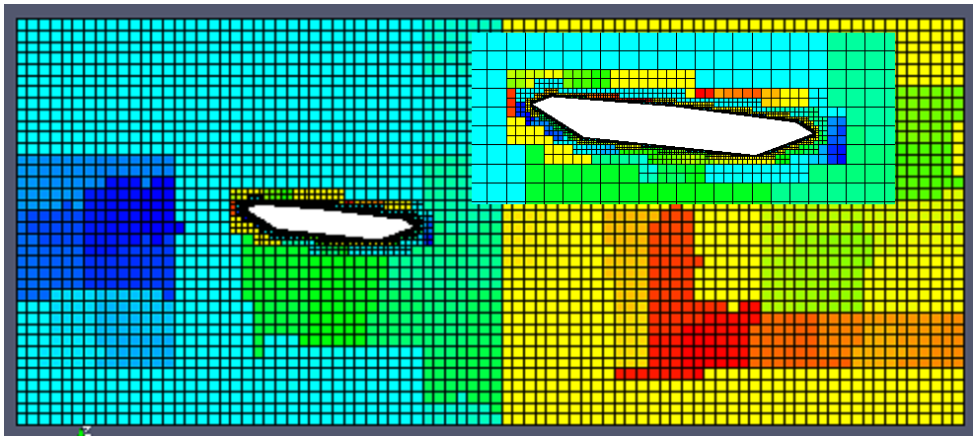

Figure 2.7: *METIS partitioning of a bridge deck section, upper right: detailed view of partitioning around the bridge (each square corresponds to* 6^3 *grid nodes.)*

2.10.1 The Lattice Boltzmann code VIRTUALFLUIDS

The VIRTUALFLUIDS code was developed and validated at iRMB mainly by [52] and [41]. It provides a common framework for different types of Lattice Boltzmann computations. Modules for data input and output, different collision schemes and boundary conditions can be used or amended for different applications. A basic validation study and comparison of the accuracy to other Navier Stokes solvers can be found in [54]. An interface for fluid-structure interaction has been developed [55] with different physics engines such as an FE model. It can also be easily coupled with other solvers. [42] parallelized the nodal code based on MPI and using the METIS [83] partitioning tool. Later in [41] a hybrid block data structure to overcome the bottlenecks of the previous approach was proposed. This block data structure enables partitioning of very large datasets, because only the block data structure has to be partitioned, not the entire set of grid nodes. Thereby, a framework to facilitate the parallelization of later extensions was provided. The framework was further used for multiphase flow [161]. Figure 2.7 shows a typical setup with a non-uniform grid and METIS partitioning (the corresponding testcase is presented in section 4.4). Each block contains several grid nodes (in this case 6^3). Adjacent blocks which are executed on different compute nodes have a different color coding.

Local grid refinement with hierachical block grids [41] and adaptive grids is possible, with a grid refinement scheme proposed in [36]. An extension of VIRTUALFLUIDS to free surface flows also exists [79]. Furthermore, several student projects have contributed to the development of VIRTUALFLUIDS, e.g. [78], [140], [23]. An emphasis was put on a state-of-the-art software structure. The code is entirely object-oriented (C++) and makes use of software patterns. The extension from the $D3Q19$ to the $D3Q27$ neighborhood scheme is template based, which allows to re-use most of the $D3Q19$ routines. In this work VIRTUALFLUIDS was used for the convergence study on the square duct and for the cube and bridge cross section bench-

marks, see sections 4.4 and 4.3, as well as during the implementation of the turbulence models presented in 2.9.2

2.10.2 GPU computing

For scientific computing parallel computation is often needed, especially for intrinsically complex problems like turbulent flow. Moreover, LBM is particularly suited for parallel computation due to its data locality. A recent trend in scientific computing is the use of GPGPUs (general purpose graphics processing units). Graphics processing units have emerged as specialized hardware for the processing of large graphics data sets. The challenge in GPU computing consists in adapting an algorithm to harness the power of this specific hardware.

First and foremost, GPGPUs are multiprocessor devices. The GPU architecture does not provide large data cache and hard-wired logic units. Instead it contains a smaller amount of shared cache memory. A much larger number of basic processors, called ALUs (algorithmic logic unit) is present than on CPUs. One set of ALUs can execute one task only. To avoid latency, ALUs have been grouped into cores that can execute different tasks. A GTX Fermi chip, for example, possesses fifteen cores, which are each subdived into two functional units. Each of these contains sixteen ALUs such that one Fermi GPU actually possesses 480 basic processors. Across one set of ALUs the instruction is executed on all data. This type of architecture is called SIMD (single instruction, multiple data). Specialized programming tools are needed to deal with the SIMD concept and access GPGPUs.

The NVidia CUDA (short for Compute Unified Device Architecture) technology [123] provides a software development kit (sdk) which allows to develop massively parallel applications for GPGPUs using standard high-level programming languages such as C [124]. This technology is now employed in various fields of science. An alternative is OpenCL [84].

The CUDA-sdk maps the GPGPUs architecture to programming concepts. Every single processor can execute multiple threads. The multiprocessors are grouped and each group, called block, shares fast L2 cache memory. The object that holds all blocks is called the grid. In other words, the block is a one-dimensional array of threads and the grid is a two-dimensional array of blocks. Portions of code expensive in data exchange or with massive branching can be executed in serial on the CPU, called the host. The host can call parallel routines on the GPGPUs, that is referred to as the device. Note that a grid is the array of blocks containing all the threads that are to be executed. For the main LB-kernel the grid contains the whole LB-Lattice. But this is not always the case, it can also contain only a certain selection of LB-nodes, for example all boundary nodes or a subset of nodes on which an averaging procedure is to be carried out.

Lattice Boltzmann as a nearest neighbor cellular automaton scheme is ideally suited for the application to GPGPUs, as communication between different lattice sites is in a favorable relation to the number of computations per site. For simple setups the performance gain of a GPGPUs-computation over a computation on a traditional CPU may reach one order of

magnitude, [160]. A first Lattice Boltzmann implementation for 3D was developed at iRMB as described in [162]. [68] compared the performance of different LB $D3Q19$ GPGPU implementations.

Our implementation of the $D3Q27$ Lattice Boltzmann model is based on implementations of [162] and [79]. [103] present a further development of this code for 3D and interactive steering. Multi-GPU solutions further extend the applicability of GPGPUs computations [143].

We use GPU-computing for most of our basic validation studies in chap. 3. It has been particularly useful for the turbulent channel flow simulations of sec. 3.1 where we benefit from comparatively short runtimes in spite of averaging intervals of over a million timesteps.

2.11 Flow around different types of objects

In this section we describe typical flow situations that occur in the build environment. First we give a rough estimate of the Reynolds numbers that occur in strong wind situations. Then we turn to specific flow types. Three main types of turbulent flow can be distinguished: boundary layer flow, flow around streamlined objects, and flow around bluff bodies. A fourth, complex type of flow is flow around an assortment of structures, where interference effects between the different components play a dominant role. Circulating flows, such as those that occur in turbines, are not considered, because they rarely occur in the built environment. Boundary layer flow occurs in the approach flow in the build environment, such as described in 2.11.2 and over surfaces of objects. 2.11.3 gives some details about the logarithmic turbulent boundary layer and 2.11.4 describes the development of such a boundary layer. Streamlined bodies are bodies of slim shape, such as airplane wings. Streamlined objects occur less frequently in the build environment, though bridge decks at zero angle of attack can be considered streamlined. The flow follows the contour of the object in a boundary-layer type flow. The total forces on the object are dominated by the viscous forces. RANS models are successful in modeling flow around such bodies. Bluff bodies flows are maybe the most important type of flows if one aims at modeling flow around building infrastructure. There is no precise definition of bluff bodies, but in this work we will refer to bluff bodies as objects for which the pressure induced drag dominates the shear-induced drag and the flow detaches. Bluff bodies are described in 2.11.6. Additionally, jet flow is described in 2.11.5 as an example of shear-dominated flow. For every type of flow one sample testcase will be studied in this thesis. Channel flow is studied for different collision models and LES models. For (semi)-streamlined bodies we chose a bridge deck at a non-zero angle of attack. For a bluff body we consider the flow around surface mounted cubes.

2.11.1 Numerical modeling of storm situations

A storm is a situation where the average wind speeds are above $20.8\frac{m}{s}$. A winter gale is a storm with average wind speeds of $32.7\frac{m}{s}$. Wind speeds in gusts can be considerably higher.

The Reynolds number is given by $Re = \frac{u_0 D}{\nu}$. ν is the kinematic viscosity of the fluid. For air we have $\nu \approx 1.5 \cdot 10^{-5}$. Assuming wind speeds of above $u_0 = 20.8 \frac{m}{s}$ and a characteristic length of $D = 10m$ we obtain

$$Re \approx 1.4 \cdot 10^7. \tag{2.153}$$

This clearly illustrates that such flows will be highly turbulent and that turbulence modeling is indispensable. Successful simulations of wind flow around buildings using various turbulence models can be found in e.g. [126].

2.11.2 Atmospheric boundary layer

While the air is unperturbed and dominated by planetary winds far away from the earth surface, a turbulent shear layer is present near the ground. Within this shear layer the velocity rises from zero at the earth's surface to an external value. In their guideline for the prediction of wind fields by CFD [39] state that any code should be able to reproduce the atmospheric boundary layer profile that we have if no buildings are present. This applies to both the turbulence model with periodic boundary conditions and the inflow conditions. Usually one assumes that thermal effects can be neglected and that the flow at the upper boundary is unperturbed. In this case the atmospheric boundary layer can be appropriately modeled by a logarithmic boundary layer. This boundary layer profile has been extensively studied in the case of the Poiseuille flow, for which an analytic solution for the mean velocity exists. According to [106], in atmospheric boundary layer flows the viscous sublayer has an extension of only a few millimeters while the logarithmic profile is valid for up to a distance of 100 meters from the ground. Above this height meteorological influences such as the Coriolis force become prevalent. For the logarithmic profile it was assumed that the temperature of the fluid does not play a role. In atmospheric flows this assumption is valid for the so-called neutral stratification. If the temperature distribution of the air differs from the adiabatic law, leading to a horizontal movement of air, the logarithmic velocity profile cannot be used. In the following we will describe the two main experiments that can be used to study turbulent boundary layers in a laboratory or with a computer simulation.

2.11.3 Logarithmic velocity profile

Poiseuille flow is the flow that is confined between two parallel no-Slip boundary plates. It is comprehensively described in [141]. The flow is accelerated by a constant force. In the steady state the forces in the flow are equilibrated:

$$\tau_w = \rho \nu \frac{d\bar{u}}{dy} - \rho \overline{u_x' u_y'} \tag{2.154}$$

where τ_w is the shear stress at the boundary. The last term describes the transport of momentum by turbulent fluctuations. τ_w is often written in terms of the shear velocity u_τ

$$u_\tau = \sqrt{\frac{\tau_w}{\rho}} \tag{2.155}$$

The velocity and the y-coordinate are further rescaled to turn u into a dimensionless scalar

$$y^+ = \frac{y u_\tau}{\nu} \tag{2.156}$$

$$u^+ = \frac{u}{u_\tau} \tag{2.157}$$

Away from the wall one has the following velocity profile

$$u^+(y^+) = \frac{1}{\kappa} \ln y^+ + C^+ \tag{2.158}$$

The von Karman-constant κ has to be determined from measurements. The value of $\kappa = 0.41$ appears to be valid for all types of turbulent boundary layer flow. For smooth surface surfaces C^+ has been determined experimentally to $C^+ = 5.0$ Function 2.158 has originally been derived in the limit of an infinite Reynolds number, or $\lim_{y^+ \mapsto \infty}$ where near-wall friction effects can be neglected. Later experimental findings indicate that it is valid for intermediate values of y^+ only. For very large y^+ the velocity grows faster than logarithmic. This "post-logarithmic"-region is called the wake region [21]. The point of transition from logarithmic to wake region depends on the Reynolds number. For larger Re the logarithmic region stretches over a larger area. The exact point of transition is still subject to investigations. In direct vicinity of the wall the motion of particles is influenced by the friction of the wall. Turbulent fluctuations play a minor role. This region is referred to as the viscous sublayer. Here the logarithmic profile is not valid, but the velocity increases linearly with the wall distance, as τ_w is assumed constant and $\rho \overline{u_x' u_y'}$ can be neglected. The viscous sublayer extends from $y^+ = 0$ to approximately $y^+ = 12$. Between the viscous sublayer and the fully turbulent logarithmic region lies a transitional zone, called the buffer layer. In these regions the velocity can be approximated by power laws such as the Werner-Wengle law [172]. Picture 2.8 shows a sketch of the near-wall velocity profile with viscous subregion, logarithmic region and wake region

For rough surfaces the velocity rises slower and the constant C^+ is smaller. The built environment outside the simulation area can be modeled as a surface roughness. Experimental studies have been conducted to determine the parameter C^+ for different built environments. Apparently the surface roughness is determined by the height of the surface elements. In [106] the values for some typical surroundings, from open sea to urban build environment, are given. An LES without wall model above a smooth surface should reproduce the corresponding logarithmic velocity profile. Rough surfaces could be modeled by a set of characteristic obstacles as is common practice in experimental wind tunnels. This will increase

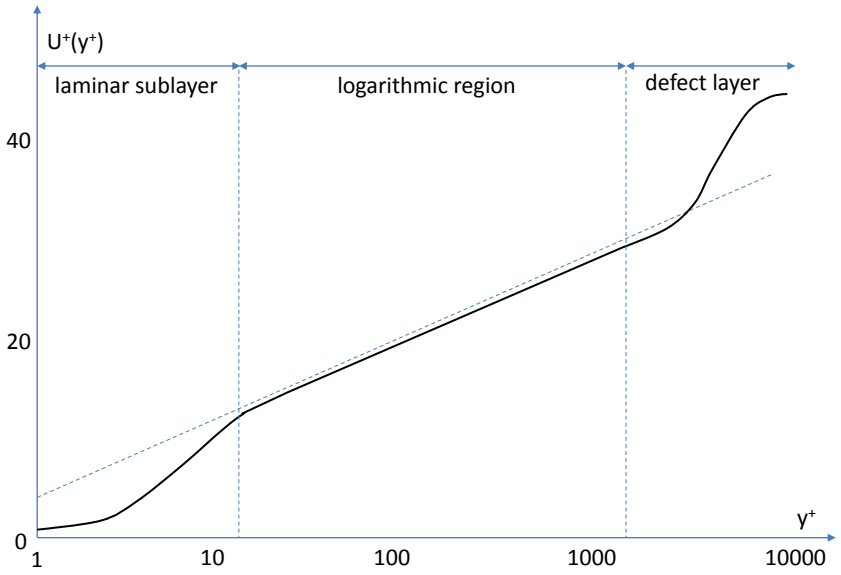

Figure 2.8: *Sketch of the logarithmic velocity profile, based on [174]*

the size of the simulation domain substantially, because the velocity-profile at the obstacle should not depend on the distance from the inflow. Alternatively, wall functions can be used to impose the desired profile near the wall.

We validate the turbulence model presented in sec 2.9.3 on periodic channel flow and compare with DNS data. DNS data is regarded preferential to experimental measurements, because those are subject to various uncertainties, e.g. the finite extension of the domain, the finite roughness of the wall and measurement uncertainties.

2.11.4 Developing boundary layer

The other standard experiment to study the properties of a turbulent boundary layer is flow over a flat plate. We again follow the discussion of [141]. A flat plate produces a turbulent boundary layer which evolves with growing distance from the front edge. Close to the front edge the boundary layer is laminar. We define δ_{99} as the distance from the plate in normal direction at which 99% of the far-field velocity U_{inf} are regained. Its thickness grows with a distance from the plate's front edge x and can be approximated as

$$\delta_{99} = 5\sqrt{\frac{\nu x}{U_{\text{inf}}}} \tag{2.159}$$

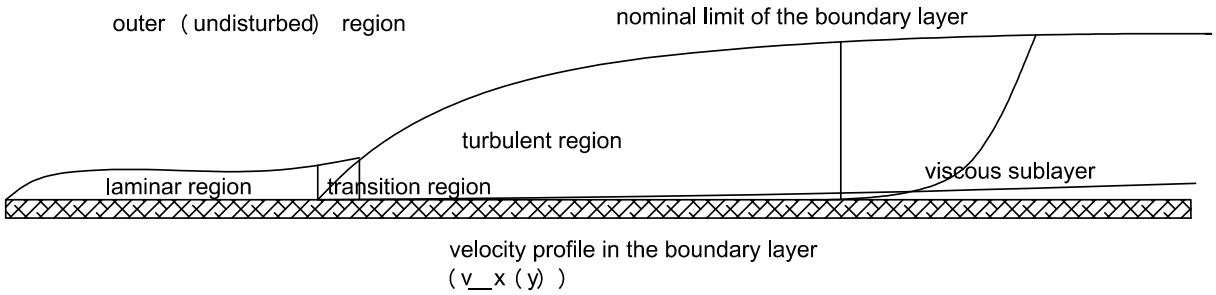

Figure 2.9: *Schematic of a developing boundary layer, based on [141]*

After some distance x a sharp transition to turbulence occurs. This distance depends on U_{inf} and the viscosity ν such that a critical Reynolds number can be defined

$$Re_{x,crit} = \frac{U_{\text{inf}} x}{\nu} \tag{2.160}$$

$Re_{x,crit}$ further depends on the disturbances that are present in the velocity field. It is higher for lower disturbances and lies between $Re_{x,crit} \in \left[3 \cdot 10^5, 3 \cdot 10^6\right]$. Measurements have led to the following relation

$$\frac{\delta_{99} U_{\text{inf}}}{\nu} = 0.14 \frac{Re_x}{ln\, Re_x} G(ln\, Re_x) \tag{2.161}$$

where G is a function that varies only weakly with Re_x. The boundary layer thickness thus grows (sublinearly) with x. For fixed x and growing Re, as occurs e.g. for decreasing ν, the boundary layer decreases. The laminar sublayer that is always present, grows with Re_x as well but slower than the total boundary layer thickness. Figure 2.9 shows a scetch of a typical developing boundary layer.

A similar experiment was used for validation purposes in sec. 4.2.

2.11.5 Jet flow

A jet is a flow type where a fast beam of fluid passes through a resting fluid region. It is similar to a mixing layer flow. We will be concerned with turbulent jet flows exiting a nozzle with parallel streamlines at low Mach number. The flow is statistically stationary and, for a round nozzle, axisymmetric. Following [141], such a flow can roughly be divided in three regions. Fig. 2.10 gives an overview over the three regions. In the initial region the flow is parallel and laminar. The velocity is a step function: it is zero in the surrounding region and constant inside the jet. In the subsequent transition region a (turbulent) boundary layer begins to form and spreads until the mixing occurs within the entire cross section of the jet. In the main region, the flow reaches its final self-similar velocity profile. The boundary layer equations are valid and give a solution, which is independent of the Reynolds number but leaves constants

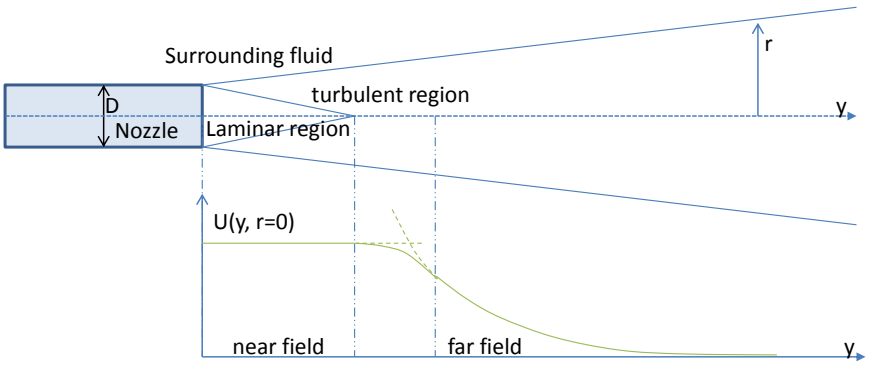

Figure 2.10: *Schematic of a turbulent jet, based on [141]*

that have to be determined experimentally. We give the solution in the form presented e.g. in [118], to facilitate later comparison with the experimental results of this publication.

$$\frac{u_x}{u_m} = \alpha_0 e^{-\alpha_1\left(\frac{r}{r_e}\right)^2} \tag{2.162}$$

$$r_e = ky \tag{2.163}$$

$$\frac{u_m}{u_0} = k\frac{D}{y} \tag{2.164}$$

where u_x is the velocity at some position (y,r), u_0 is the velocity at the inlet, and u_m is the velocity in the axis of the jet at some position $(y,r=0)$. D is the size of the opening and the parameters α_0, α_1 and k are free constants. r is the distance from the jets axis and y is the distance from a virtual origin of the flow. It is chosen such that $u_0 = u_m(y_0)$, where y_0 is the distance between the opening and the virtual origin.

Jet flow is a standard flow type that has been studied thoroughly both experimentally and numerically, such as in the early experimental work [176]. Jets occur almost everywhere in technical fluid dynamics, from microjets [114] to jets behind the nozzle of an aircraft turbine. The present study was conducted for a study of jet flow behind a ship propeller, where the large rotation jet can lead to river or channel bed erosion [53]. A Lattice Boltzmann study of a turbulent square jet flow has been carried out in [178]. The MRT and LBGK models with Smagorinsky LES have been compared on a uniform grid with a $D3Q19$ stencil. [114] conducted a further study of a square jet with Lattice Boltzmann. They used the $D3Q19$ LBGK model, dynamic Smagorinsky and a grid-stretching scheme on a non-uniform grid. Their setup, however, differs from ours as a) a square jet is considered instead of a round jet, b) the focus lies on periodically forced jets and the free jet is not studied in detail. Jet flow plays a minor role in flow around building structures. It is nevertheless an interesting validation case. It is a shear-flow like boundary layer flow but with a more complex geometry of the flow. Semi-analytical solutions and accurate measurements exist. It can thus be studied as a intermediate configuration between boundary layer flows and flows around objects with constant geometries.

2.11.6 Bluff bodies

Bluff bodies are a standard component of infrastructure. Turbulent flow around low rise buildings, but also high-rise buildings and and sometimes bridges is detached and its characteristics differ from flow around stream-lined objects. Often separation takes place along sharp edges and large recirculation zones are present. These recirculation zones coincide with regions of adverse pressure gradients. The most prominent case of flow around a bluff body is the Karman vortex street behind a two-dimensional cylinder. In fact, the alternating shedding of vortices is characteristic of flow around bluff bodies and Strouhal numbers can be determined even when the flow at higher Reynolds numbers seems completely chaotic at the first glance, as is stated in section 4.4 of [152]. Obviously three dimensional objects are not described well by 2D models. When a RANS model is used to compute the mean flow field around e.g. a wing profile, the computational cost is much lower than for a full three dimensional LES solution. If the object itself is already three-dimensional, some of the gain in efficiency of RANS models over LES models is lost. Flow around bluff bodies (cubes) is expected to be less sensitive towards a correct modeling of the boundary layer than flow without detachment or immediate reattachment. [139] state that URANS has traditionally been used for simulating separated flows, but has given unsatisfactory results when encountering massive separation. They attribute this to the modeling assumptions of RANS equations where more equilibrium-type flows are considered. Consequently, LES and Hybrid models should be used for such flows. In this work a surface mounted cube and an extruded bridge cross section at a finite angle of attack have been studied.

3 Validation studies

The outcome of various basic testcases is presented in the following. First, all models introduced in the introductory sections are tested on a turbulent channel flow benchmark. Both highly under-resolved and near-DNS simulations are carried out, depending on the model and the properties we are interested in. For the different collision models, the implementation is validated and convergence is assured. After studying the channel flow benchmark, we will proceed to several other tests. For these tests only a few variants of the collision models and LES models will be taken into account and the tests will be designed to show some specific properties of the models, such as the test of the frozen-in peak where differences between the MRT model and between the different CLB models can be observed. The confidence gained with some of the models then allows us to proceed with more complex flows in the next chapter.

3.1 Comparison of LB-collision models for turbulent channel flow

Turbulent flow between two flat plates is a basic benchmark for turbulence models and CFD solvers in general. Section 2.11.3 discusses the characteristics of this special flow type.
We compare the solutions for turbulent channel flow for different collision operators with the DNS solution of Kim, Moin and Moser [85] for $Re_\tau = u_\tau H/\nu = 180$ with the half-channel width H and the wall-friction velocity u_τ. No LES model is employed, but the resolution is coarser than it would be for a full DNS ($y^+ = 1.5$ at the first node and $y^+ = 3$ at all other nodes). This resolution was chosen for two reasons, because a significantly higher resolution would have exceeded the memory requirements on the available GPGPU card and because it was one goal to keep the results comparable to existing LB-channel flow studies. Similar work was previously carried out by Freitas et al [40]. For this work, an erratum and extension is currently in preparation [33]. Both the original work and the erratum use a grid resolution of (211x135x61) nodes in stream wise, normal, and spanwise direction, respectively. Another study on this subject has evaluated the Entropic Lattice Boltzmann method for turbulent channel flows by [156] on the same test case with a grid resolution of (513x257x129). We first reproduce Freitas simulation for the $D3Q19$ BGK model on the same grid. Then we consider the $D3Q27$ Factorized Cascaded and the $D3Q19$ BGK, TRT and MRT collision operators on the same grid but for the Reynolds number of the DNS data on the same grid as [33]. Also the Mach number was set to $Ma = 0.01$ for all cases as in [33]. For the MRT model the set of relaxation rates recommended in [29] was used. For the TRT model the relaxation factors for the odd moments were set to one. We presume that the set of magic relaxation factors by [63]

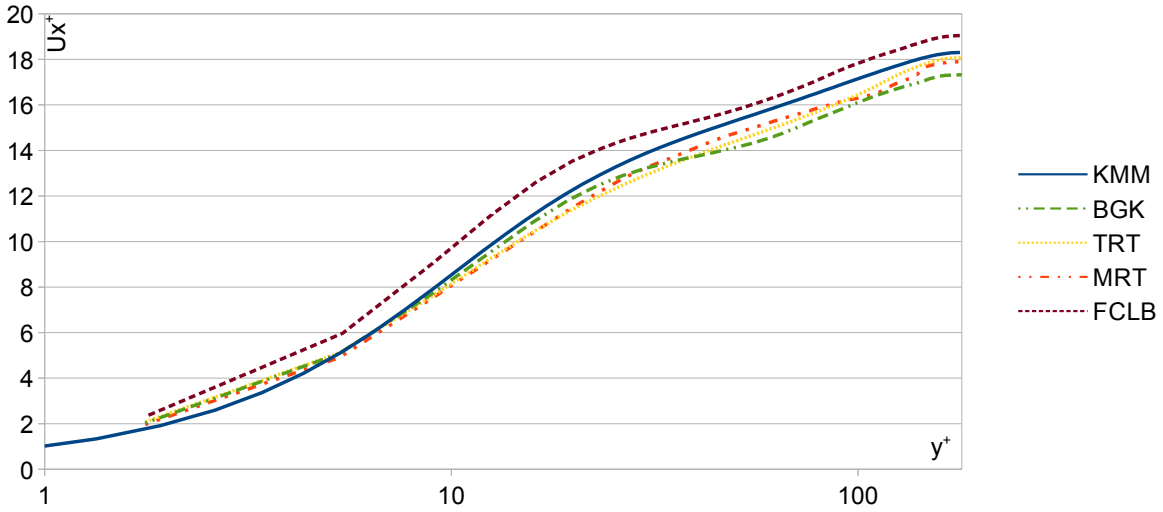

Figure 3.1: *Mean velocity for the four collision types*

is not sufficiently stable for these simulations, because for very low viscosities the relaxation factor of the odd moments is very close to zero. Because the stability depends on several parameters, such as initial conditions, viscosity and velocity, we cannot fully exclude that it is possible to conduct a stable simulation with the given setup for the TRT model with magic parameters. For the Factorized CLB model all the free relaxation parameters were set to one, except for the second-order ones.
The data were averaged in time for at least 500000 time steps or twenty-two eddy turnover times. Additionally, a spatial average over points of equal distance to the boundary was taken.
All simulations were carried out with single precision on GPGPUs. Because the forcing term in LB-units was smaller than the round-off error, a rescaled force was applied every ten timesteps.

Plots 3.1 to 3.4 show the mean velocity and the fluctuations for the three velocity components for all four models. The mean velocity is quite similar to the original DNS-result for all the methods considered, confer Figure 3.1. The mean velocity is over-predicted by the $D3Q27$ Factorized CLB model and under-predicted by the $D3Q19$ BGK model. For the RMS values of the three velocity components differences between the DNS result and our simulations can be observed, as can be seen from Figures 3.4, 3.2 and 3.3. The variance of the stream wise component is over-predicted near the boundary.
In [40] it is argued that stability considerations, predicting superiority for MRT and CLB models, would not necessarily hold for wall-bounded flows and show numerical evidence for lower stability. Further, they report on unphysical behavior at the boundaries for these models. We obtain different results. No oscillations as those shown by the authors of [40] were observed. In an erratum [33] of the original paper, the simulation results are similar to those presented here. The results shown therein were slightly more accurate than ours. We attribute this to round-off errors because double precision was used instead of single preci-

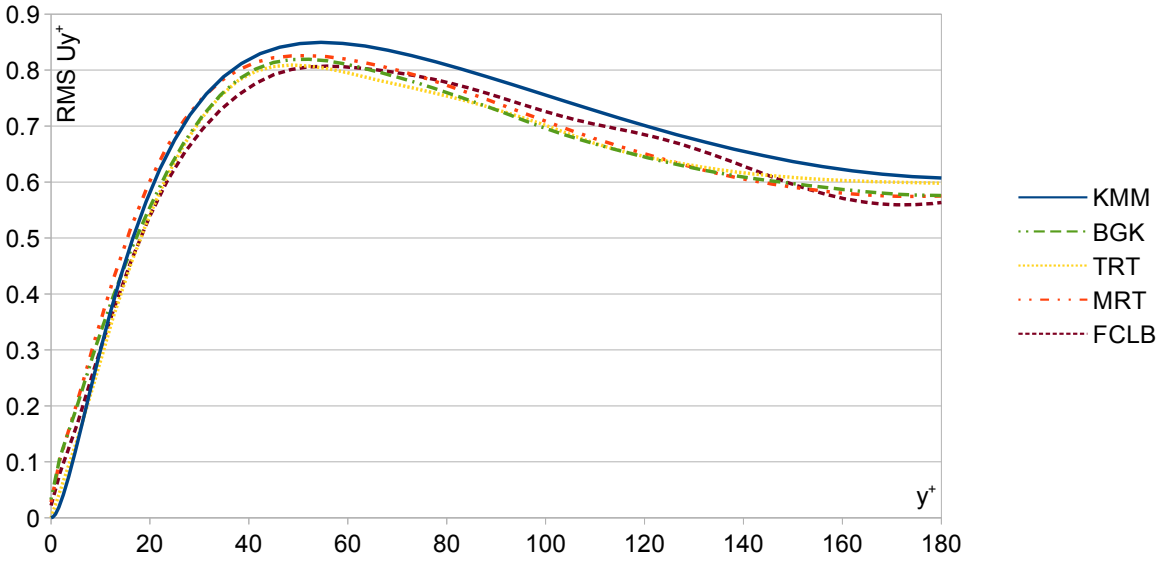

Figure 3.2: *RMS values for the spanwise velocity component*

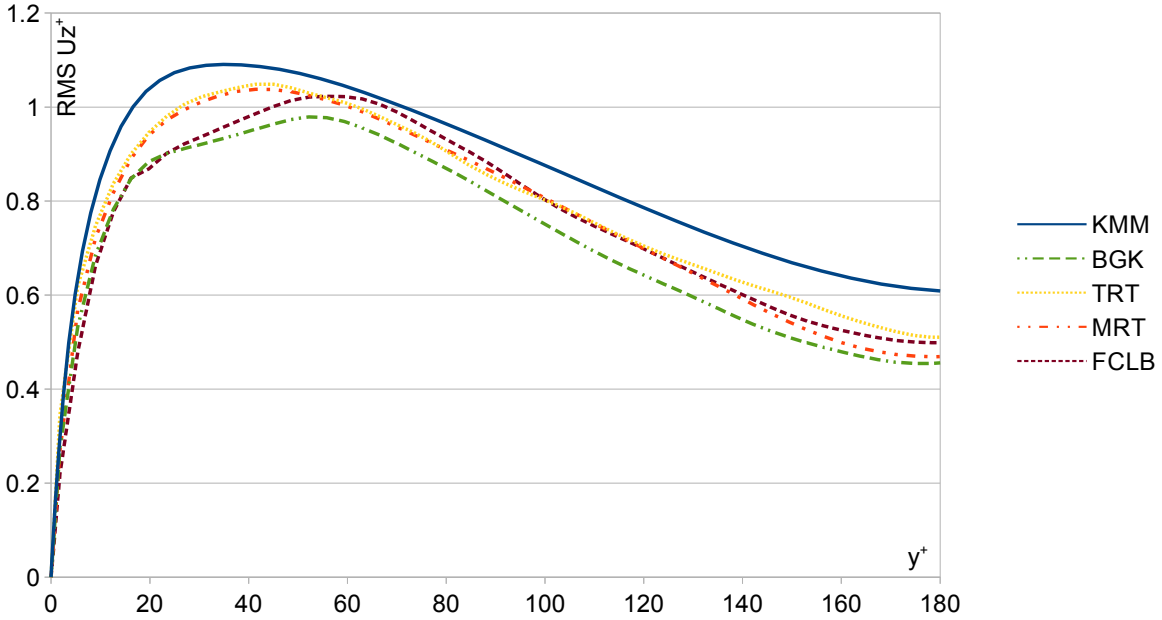

Figure 3.3: *RMS values for the wall-normal velocity component*

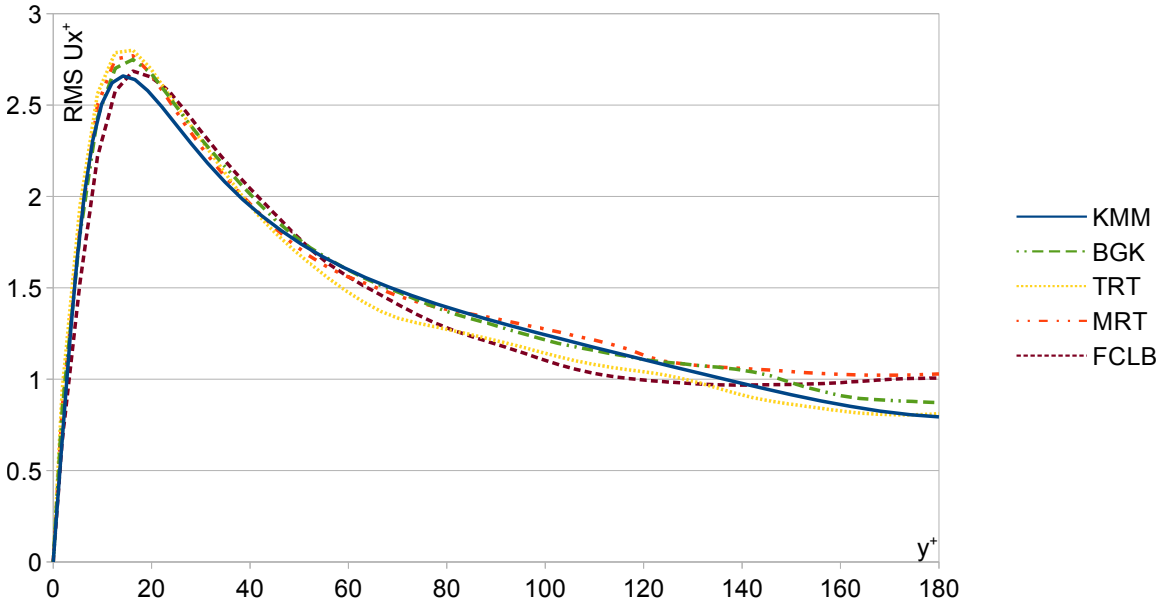

Figure 3.4: *RMS values for the streamwise velocity component*

sion in their work.
To confirm that the remaining deviation of our results from the results of [33] is due to round-off error, the BGK simulations were repeated with double precision. Figures 3.5 show the results. They are now in agreement with the results of [33].
Overall, all models are able to reproduce the mean velocities and fluctuations well. It is assumed that the remaining error is partly due to round-off errors. In particular, the "unphysical" behavior observed in [40] for the MRT model could not be confirmed and the model behaves satisfactorily.

3.2 Comparison of different LES models for turbulent channel flow

In the present section we want to find out to what degree a Lattice Boltzmann-based flow solver can reproduce mean flow and RMS fluctuations for this testcase if used with an LES model on an under-resolved grid. Such studies have been carried out before, e.g. in [131] for the static and dynamic Smagorinsky model or [170] for the WALE model. Our aim is to compare the various LES models presented in 2.9, also using several different grid resolutions. In the applications we consider later, the flow will often be under-resolved. This is quite common in engineering applications. Hence, this section intends to shed some light on the performance of the models for "inappropriate" resolutions.

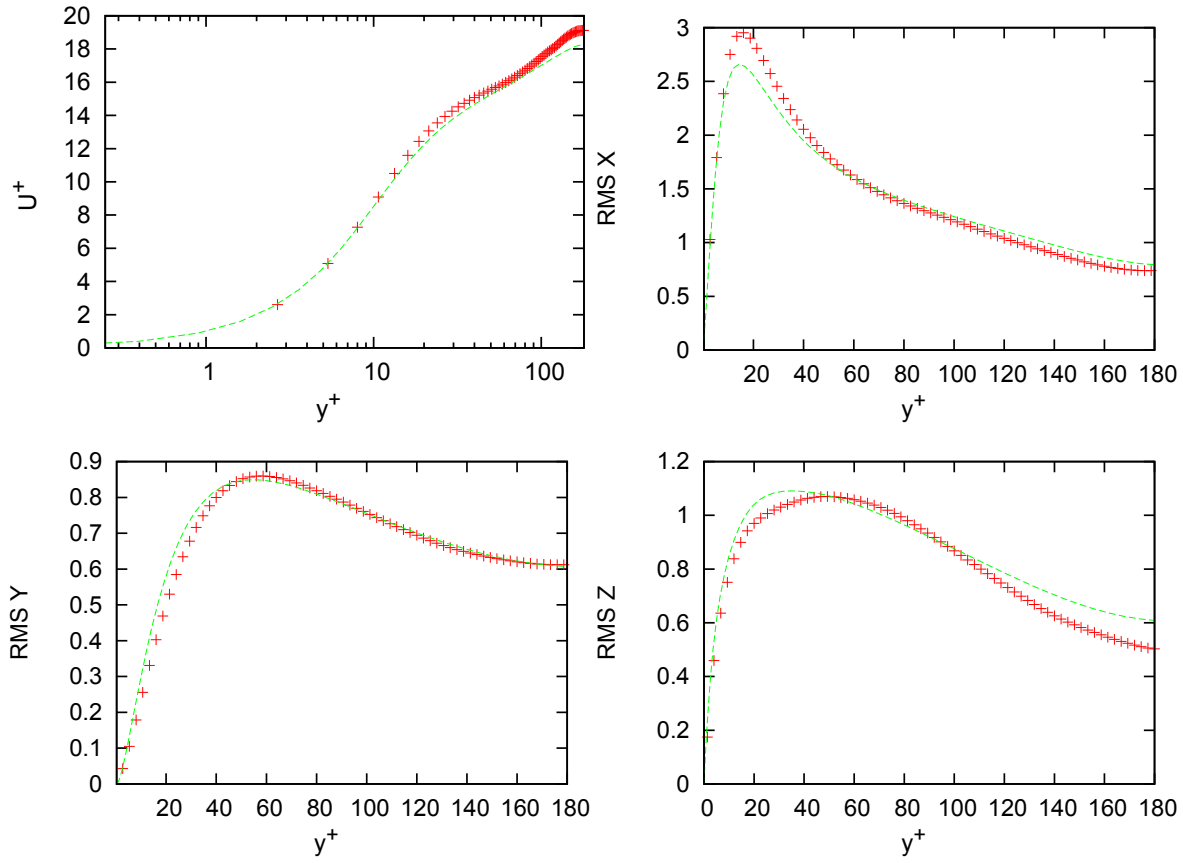

Figure 3.5: *Velocity and variances for the BGK model (red dots) with double precision accuracy in comparison to the reference data (green line)*

3.2.1 Setup

Turbulent channel flow simulations are carried out for different LES models, including the Cascaded Lattice Boltzmann (CLB) model as an implicit LES and for different grid resolutions. The Reynolds number based on the mean flow velocity and the full channel height is $Re = 4586$. This corresponds to $Re_\tau = 150$. The following models were studied:

- CLB
- Smagorinsky Model
- Smagorinsky Model with van Driest damping
- Wale model
- Vreman model

All models were tested with a resolution of 32, 48 and 64 grid points in wall normal direction on a uniform grid, except for the Vreman model, for which only the lowest resolution was considered. An additional study comparing the Vreman model to the WALE model will be presented in the following section. For the lowest resolution of 32 grid points in wall-normal direction we used 32 points in spanwise and 64 in mean flow direction. For the 48 points grid resolution we chose 48 points in spanwise direction and 90 points in flow direction. For the 64 grid points resolution in wall normal direction we used 64 points in spanwise and 128 points in mean flow direction. For all models the TRT relaxation coefficients (λ, 1) and the $D3Q27$ velocity set were used. For comparison simulations of the Smagorinsky model with the $D3Q19$ velocity set and the MRT relaxation coefficients suggested by [29] were carried out for the three grid resolutions. A Smagorinsky constant of $c_s = 0.18$ was used. DNS data for this flow case was available from the DNS database of the University of Tokyo [164]. It was obtained with a spectral model. Note that the near-wall resolution is far below the recommended value for wall-resolved LES simulations. Thus, the expected error is expected to be high for all models. To test the accuracy of the CLB model for a higher resolution, studies with near-DNS resolution were carried out, see the preceding chapter 3.1.

3.2.2 Qualitative discussion of the results

Figures (3.6,1) and (3.6,2) show snapshots of the streamwise velocity component for the x-, y- and z-plane of the channel. Note that the the fluctuations produced by the CLB model (with TRT relaxation coefficients) are smaller than those produced by the Smagorinsky-MRT model. The instantaneous eddy viscosity for the four LES models considered is shown in Figure 3.7. As expected, the van Driest damping reduces the eddy viscosity near the boundary and the Vreman and Wale models also yield a reduced eddy viscosity near the boundary. The Vreman and Wale model both give more a “spot-like” eddy viscosity, while the Smagorinsky eddy viscosity shows streaks.

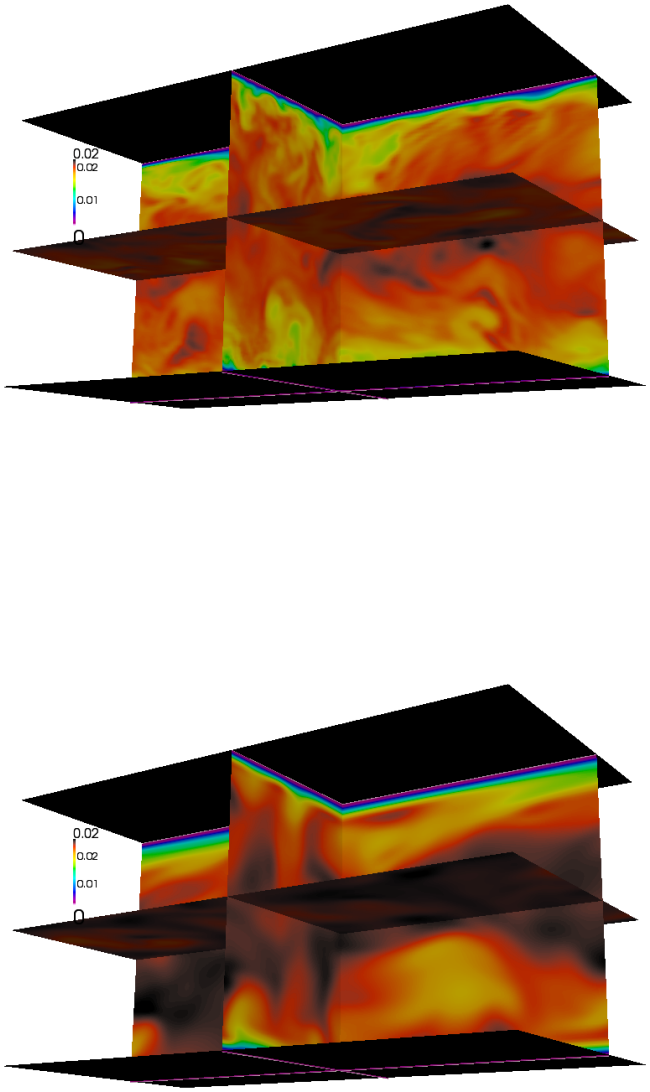

Figure 3.6: *Snapshot of the streamwise velocity components, top: CLB, bottom: Smagorinsky MRT*

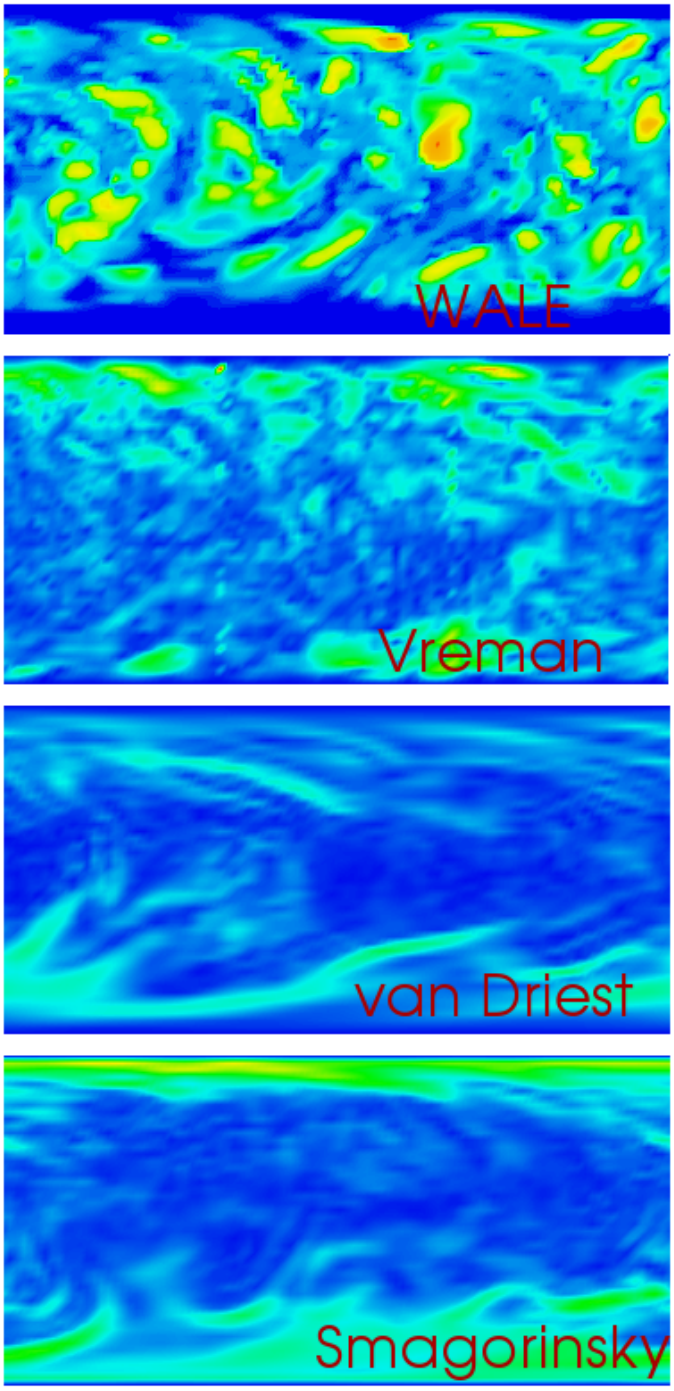

Figure 3.7: *Comparison of the instantaneous eddy viscosity ν_τ for four different models for snapshots of the xz-plane where orange marks the highest values and blue the lowest*

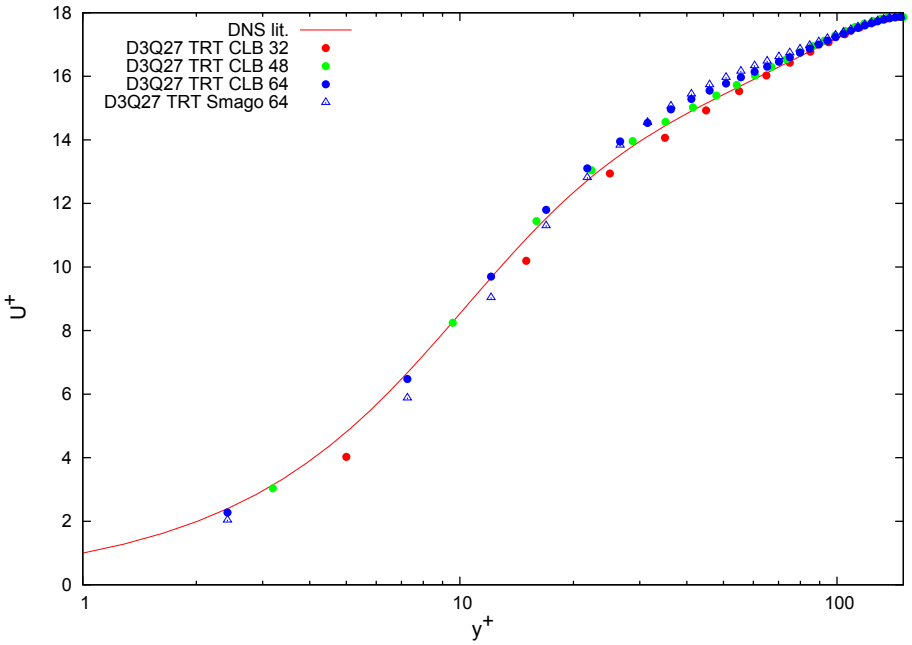

Figure 3.8: *CLB channel flow for different grid resolutions*

3.2.3 Quantitative discussion of the results

The resulting mean velocity profiles are given in Figures 3.8 to 3.10 where y^+ is the dimensionless wall distance and $u^+ = u/u_\tau$ the dimensionless velocity. The most apparent difference between the simulation results and the DNS reference data is that all models underestimate the velocity at the first few grid points. The greatest error is observed for the Smagorinsky model at the lowest grid resolution. For higher resolutions the results improve. We want to separate the effects of the collision operator from the effect of the LES model, so the Smagorinsky model was also tested with TRT relaxation coefficients. The error is smaller, but does not reach values as those seen for the D3Q27 TRT Wale, Vreman, van Driest and CLB model, which are almost identical. This is true for the two lowest resolutions. For the resolution of 64 grid points the $D3Q27$ model was additionally considered without any turbulence model. Its performance is in between that of the $D3Q19$ MRT Smagorinsky model and the advanced eddy viscosity models with a $D3Q27$ TRT collision model. The experiment was repeated at a higher Reynolds number of $Re_\tau = 400$, corresponding to $Re = 13900$. Only the Smagorinsky MRT and the CLB models with TRT relaxation coefficients were considered. As can be seen from Figure 3.10 the same behavior as before is observed. The mean velocities are matched quite well by the CLB model even with coarse resolution.

Figures 3.11 to 3.13 visualize the RMS fluctuations of the three velocity components. As the flow is not well-resolved, no good representation of the RMS-fluctuations are expected. Note

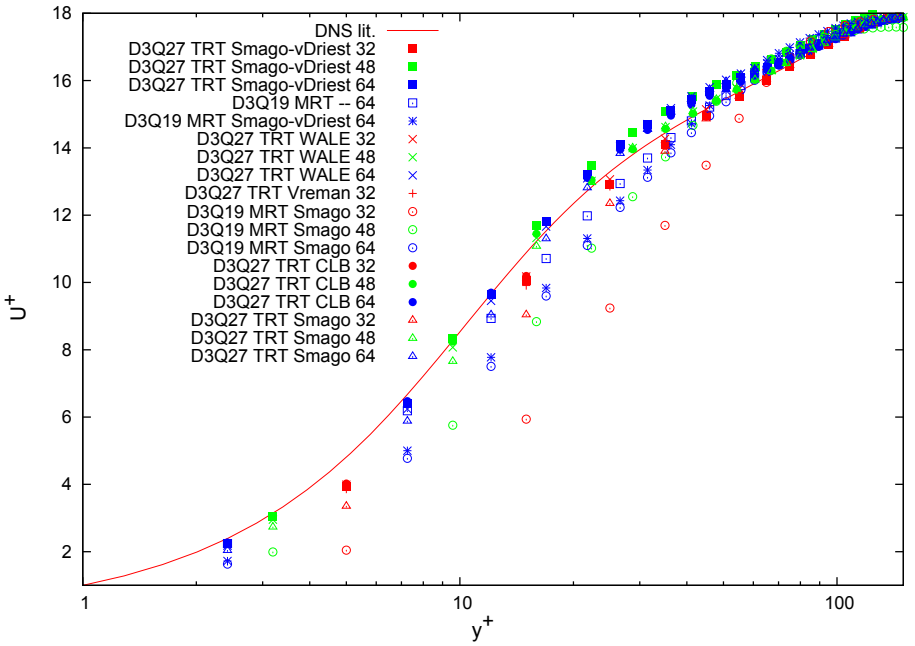

Figure 3.9: *Comparison of the mean velocity for different LES models*

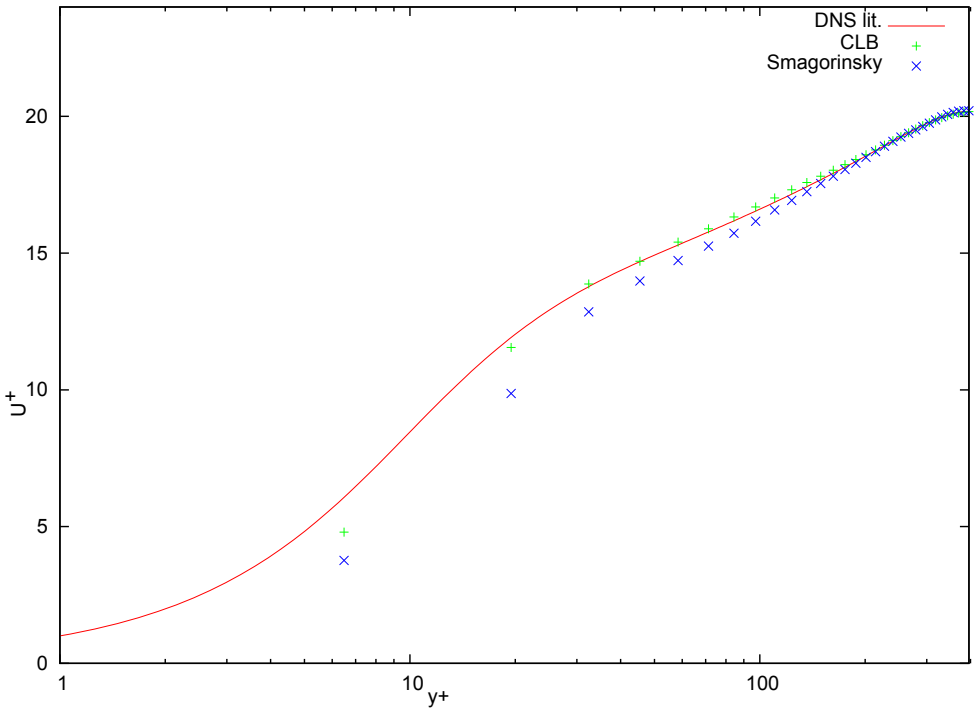

Figure 3.10: *Smagorinsky (blue) vs CLB (green) for grid resolution* $h/dz = 64$ *and* $Re_\tau = 400$

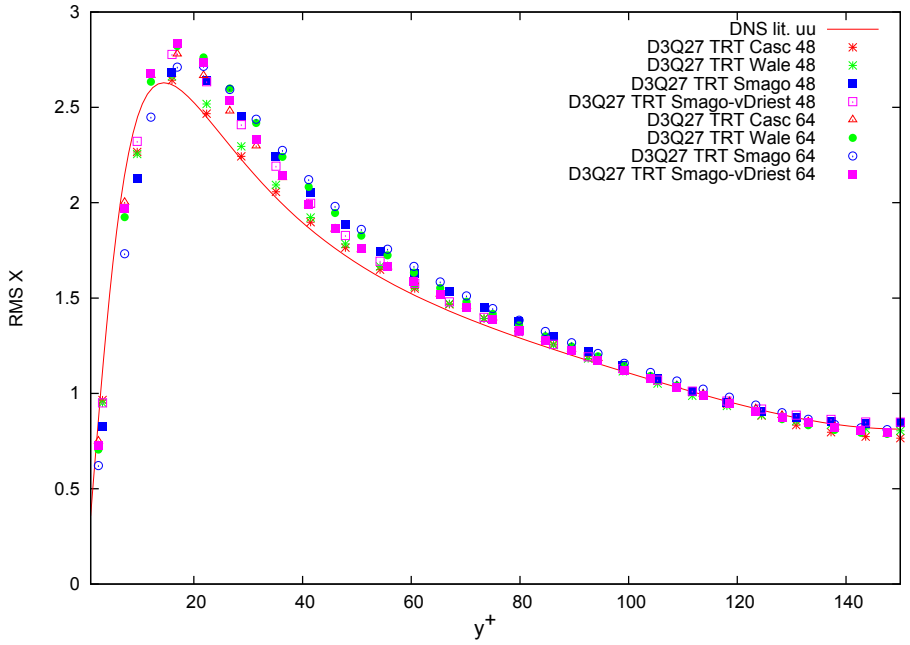

Figure 3.11: *RMS fluctuations of streamwise velocity component*

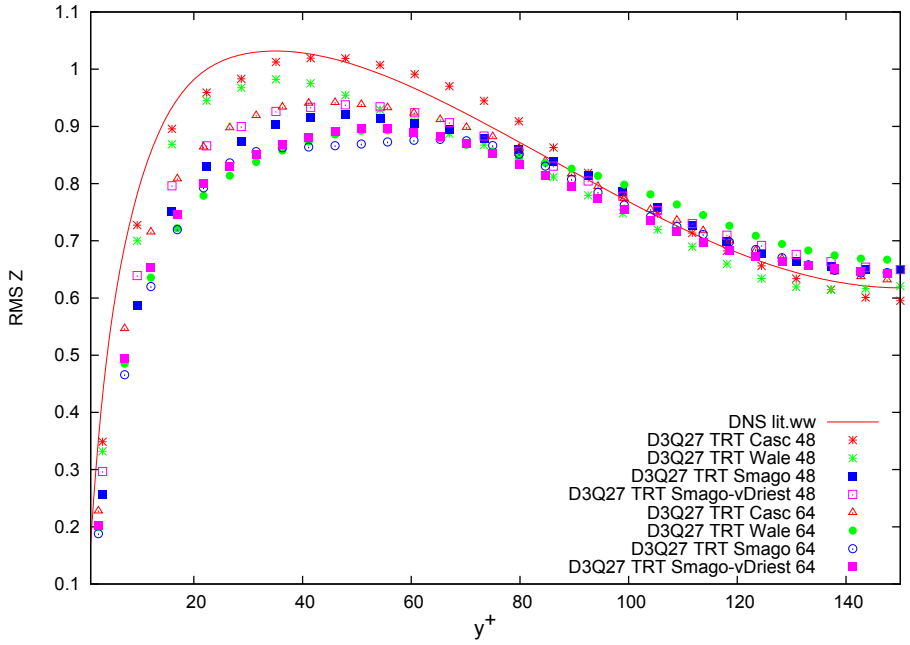

Figure 3.12: *RMS fluctuations of the velocity in wall normal direction*

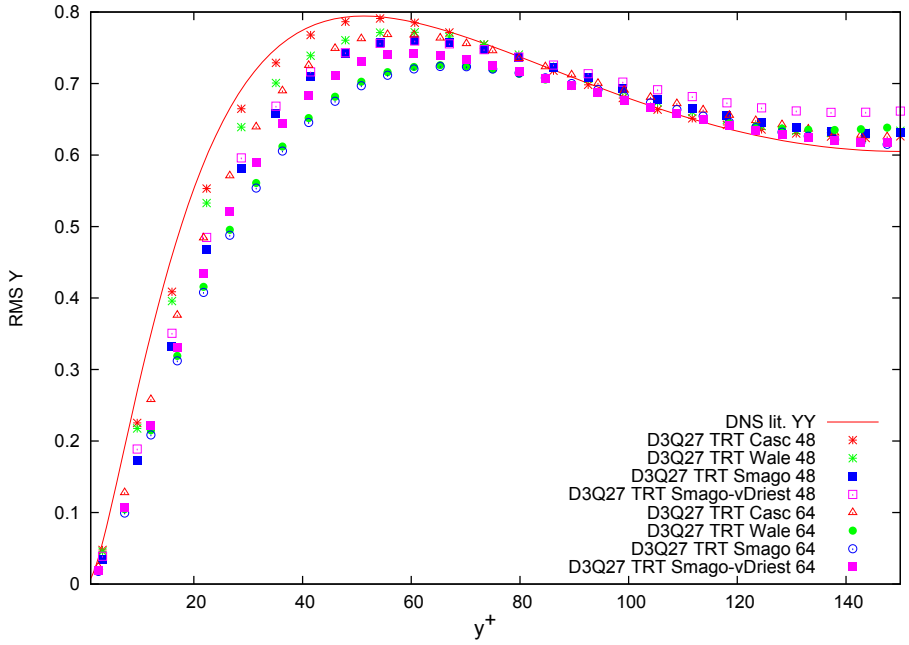

Figure 3.13: *RMS fluctuations spanwise*

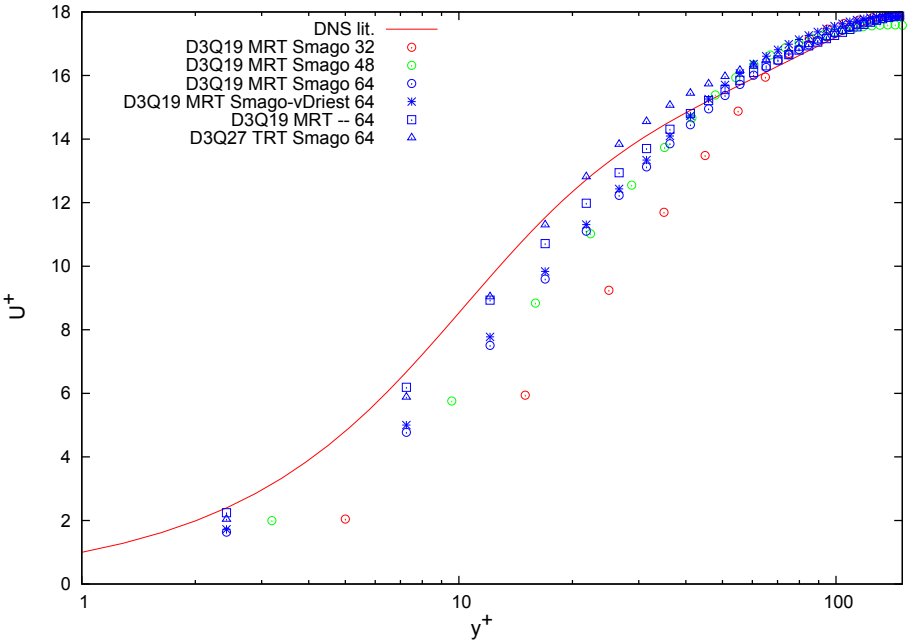

Figure 3.14: $\langle V\,x \rangle$ *for D3Q19 Smagorinsky for different levels of refinement*

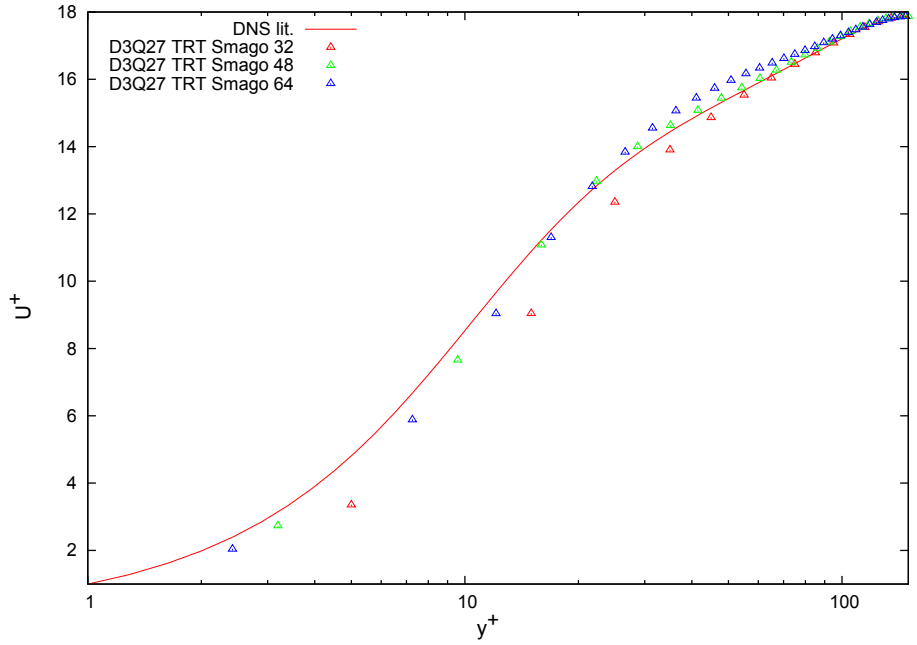

Figure 3.15: $\langle V\,x\rangle$ *for D3Q27 Smagorinsky for different levels of refinement*

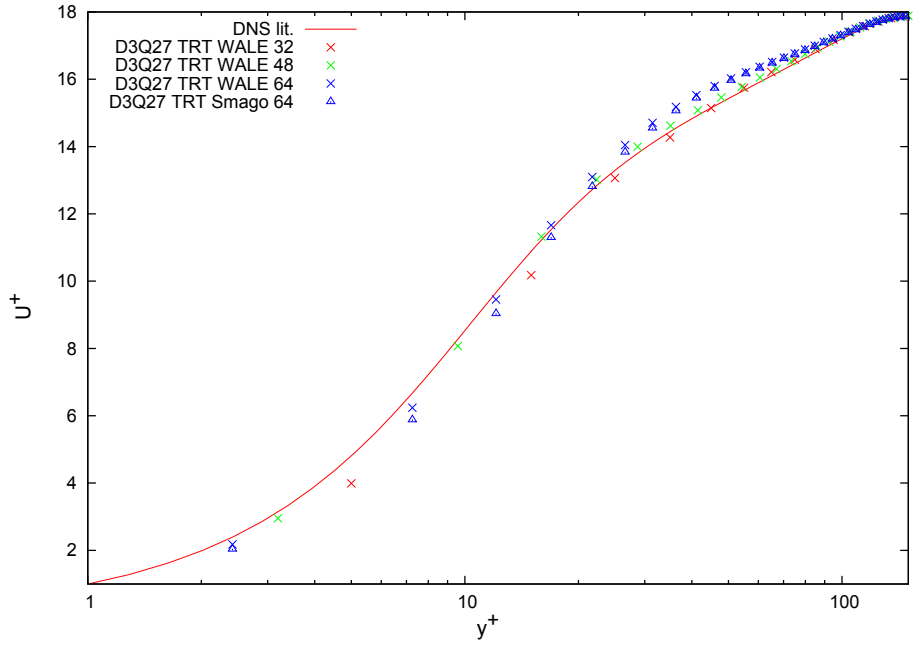

Figure 3.16: $\langle V\,x\rangle$ *for D3Q27 WALE for different levels of refinement*

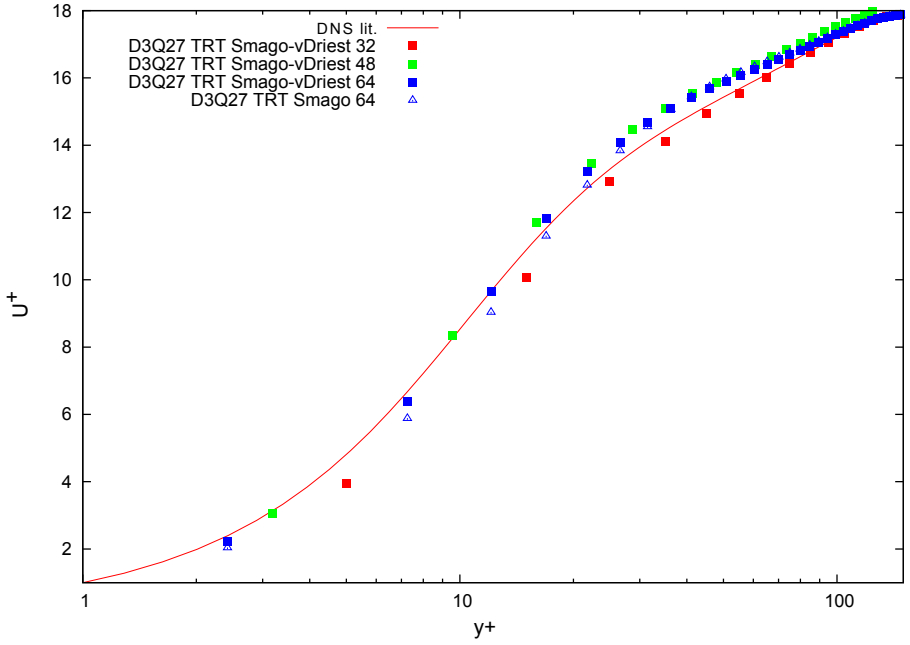

Figure 3.17: $\langle V x \rangle$ *for D3Q27 Smagorinsky model with van Driest damping for different levels of refinement*

nx	Case 1: $81\Delta x$, Case 2: $51\Delta x$
ny	$64\Delta x$
nz	$128\Delta x$
ν	$0.0001956(\Delta x)^2/\Delta t$
f_x	$1.8664310^{-8}\Delta x/(\Delta t)^2$
y^+	Case 1: 4.4, Case 2: 7.0
Re_τ	180

Table 3.1: *List of values for the Wale and Vreman channel flow simulation*

that the values both underestimate and overestimate the DNS-predictions for some resolutions.

3.2.4 Comparison of the Vreman- and the WALE model

Further, the Vreman model was implemented, which is expected to behave similarly to the WALE model. As opposed to the simulations with fixed mean velocity in mid channel plane, simulations carried out with fixed forcing. That way, the ability of the WALE model to reproduce the correct mean velocity could also be tested. Because the TRT had already performed well in the studies with fixed forcing, it was used exclusively for this testcase. In contrast to sec. 3.2 double precision was used, because this was possible on the more recent GPU (GTX 580) on which these simulations were carried out. Table 3.1 shows the details of the setup. In Figure 3.18 the mean velocities for the four cases considered can be found. Figures 3.21, 3.19, and 3.20 show the RMS-values. The very good match of the mean velocities for the low resolution is suspected to be by mere chance, because at $y^+ = 7$ no reliable near-wall results can be expected and the high accuracy for the mean component is not reflected by results for the fluctuation terms. The results for the higher resolution of $y^+ = 4.4$ give a more reasonable picture. In all, the accuracy is comparable for both models. The computational time of the current implementation was found to be 10% higher for the Vreman model than for the WALE model. [119] found the Vreman model to be 30% faster than the WALE model.

3.2.5 Conclusions

The results clearly demonstrate that all LES models considered, and especially the CLB model, produce better results than the simple Smagorinsky model. The $D3Q19$ MRT models with Smagorinsky LES yields the poorest results, the $D3Q27$ CLB model with TRT relaxation factors the best. The WALE and the Vreman model give very similar results. As will be seen later in sec. 3.1, the performance of the MRT model matches the performance of the other models for adequate resolutions ($y^+ = 1.3$ in our case).

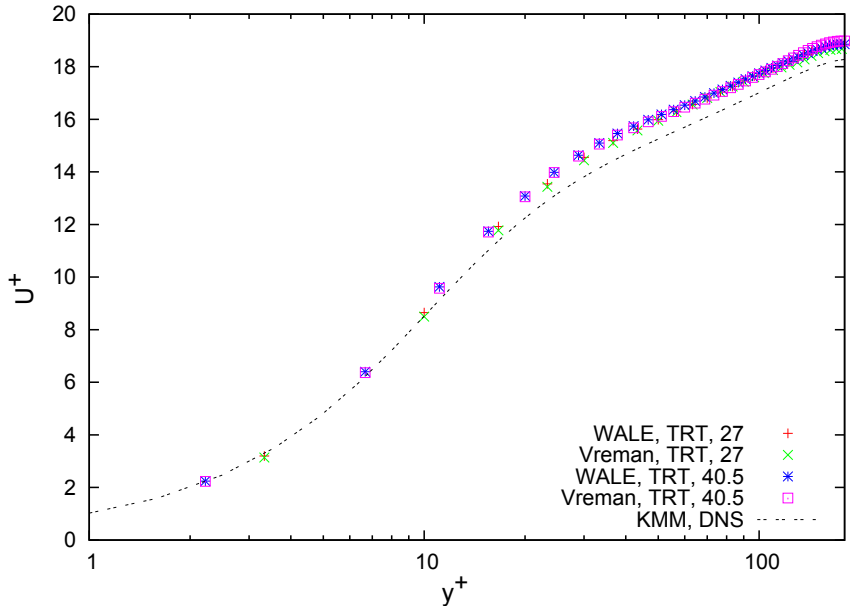

Figure 3.18: *Comparison of the mean velocities for WALE and Vreman at two different resolutions*

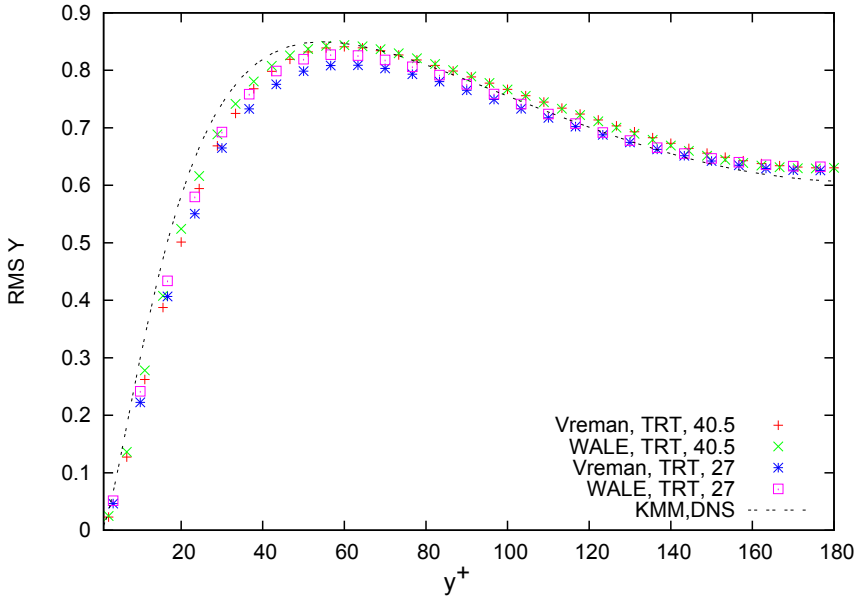

Figure 3.19: *Comparison of the spanwise fluctuations for WALE and Vreman at two different resolutions*

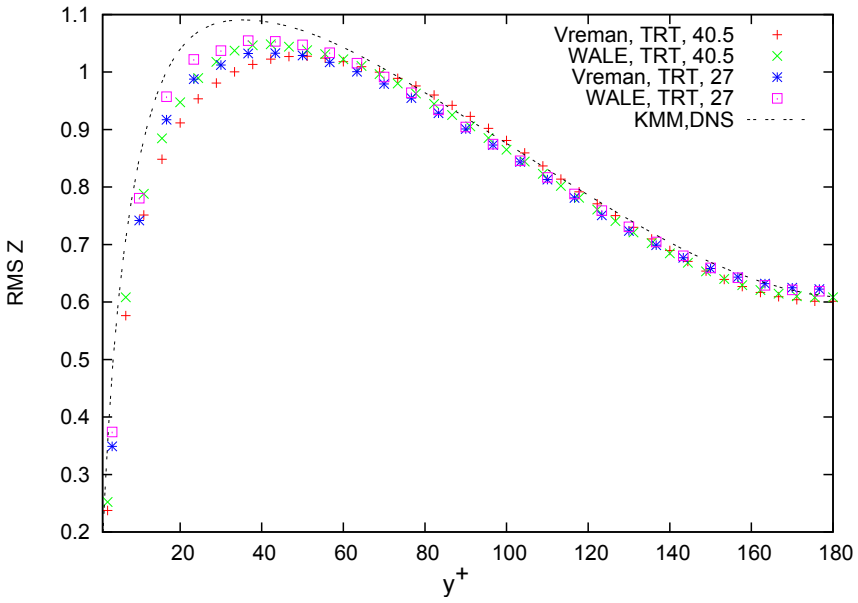

Figure 3.20: *Comparison of the wall-normal fluctuations for WALE and Vreman at two different resolutions*

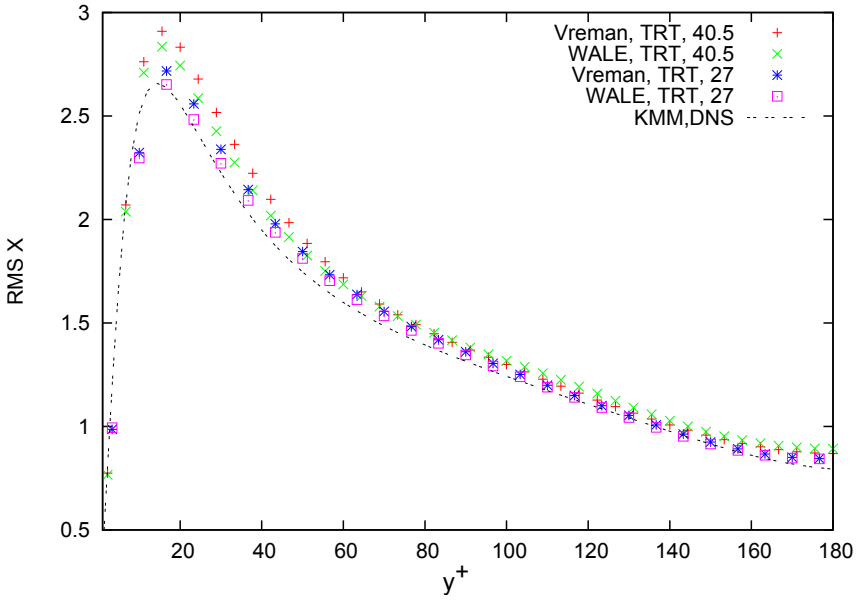

Figure 3.21: *Comparison of the streamwise fluctuations for WALE and Vreman at two different resolutions*

3.3 Validation of the SAS model

In the present section the SAS model is evaluated. As a preliminary test, the wall-boundary condition is first tested separately with a laminar Poiseuille flow test case without any turbulence model. The K1E1 model is then validated for channel flow. The results are compared with Prandtl's mixing length model and the logarithmic velocity profile. Both the near-wall and wall-model version are considered. Similar studies have been presented in [158] where an LB-based k-epsilon and a simple mixing length model were compared for a boundary layer in a circular tube.

Preliminary validation of the boundary condition: laminar Poiseuille flow

A simple wall model can be implemented using the relation for the second order moment and the derivatives. At the first fluid node we set the second moments according to

$$\tilde{\mu}_{xy}^{neq} = -2/6\rho\tau\left(\frac{\partial u_x}{\partial y}\right). \tag{3.1}$$

Laminar flow in a straight channel provides a straightforward first test case, as the analytical solution for the velocity profile is known. For a full channel height L and an external force

$$f = \frac{4v_{max}}{L^2}\,2\,\nu \tag{3.2}$$

the corresponding velocity profile is given by

$$v_x = 4\,v_{max}\frac{y\,(L-y)}{L^2}. \tag{3.3}$$

We ran a simulation with a total channel width L of 45 lattice units and a distance of $d = 10\Delta x$ between wall and boundary. Accordingly we have

$$\tilde{\mu}_{xy,BC}^{neq} = -2/6\rho\tau_{ges}\left(4\,v_{max}\frac{(L-2d)}{L^2}\right) \tag{3.4}$$

$$\mu_{x,BC} = \mu_{x=11\Delta x} - \Delta x\left(4\,v_{max}\frac{(L-2d)}{L^2}\right) \tag{3.5}$$

$$\mu_{y,BC} = \mu_{z,BC} = 0 \tag{3.6}$$

The forcing was set according to eq. 3.2 with $v_{max} = 0.03$ in lattice units per time steps. The simulation converged to a maximal velocity $v_{max}^{simu} = 0.0295\Delta x/\Delta t$ of and a velocity of $v_{BC}^{simu} = 0.0203\Delta x/\Delta t$. The analytical values are $v_{max} = 0.03\Delta x/\Delta t$ and $v_{BC} = 0.0207\Delta x/\Delta t$, so the error lies between 2.0% and 1.7%.
If $u_x(y)$ is a parabola as defined in eq. 3.3 we have

$$u_x^{(\Delta)} = 4v_{max}\frac{\Delta(L-\Delta)}{L^2} \tag{3.7}$$

$$u_x^{(\Delta+1)} = 4v_{max}\frac{(\Delta+1)\,(L-\Delta-1)}{L^2}. \tag{3.8}$$

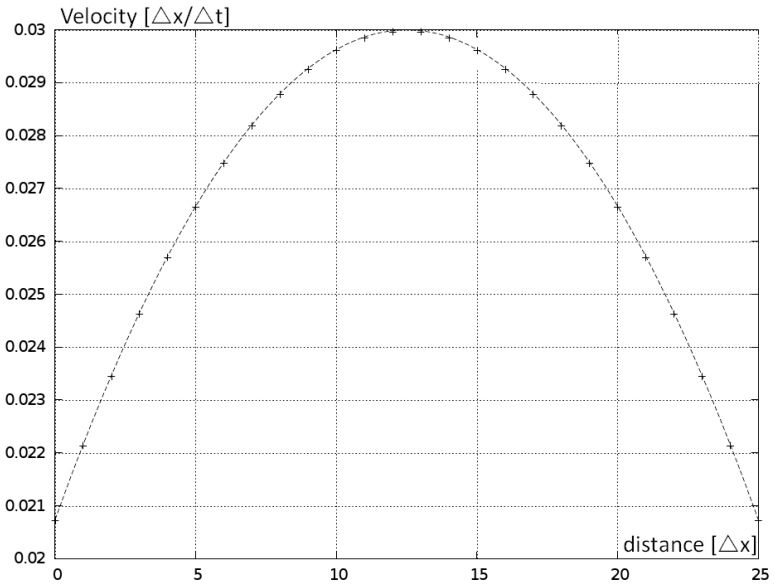

Figure 3.22: *v_x for a laminar Poiseuille flow with the moment-based method (dots), in comparison to the analytical solution (dotted line)*

Such that we can derive the following relation between the velocity at grid point Δ and at grid point $(\Delta+1)$

$$u_x^{(\Delta)} = \frac{\Delta(L-\Delta)\,u_x^{(\Delta+1)}}{(L-\Delta-1)(\Delta+1)}. \tag{3.9}$$

The velocity and its y-derivative can be linked via

$$\frac{\partial u_x^{(\Delta)}}{\partial y} = \frac{(L-2\Delta)\,u_x^{(\Delta+1)}}{(L-\Delta-1)(\Delta+1)}. \tag{3.10}$$

With this boundary condition and the same setup as above we obtain an l_1-error of less than 0.1%. The results for this simulation are shown in 3.22

3.3.1 Log-layer simulations with the K1E1 model

Now, after the initial validation of the wall-boundary condition, the K1E1 model and the off-wall boundary condition are applied to simulate the log-layer. The friction velocity u_τ and with it the shear stress μ_{xy}^{neq} are determined by numerically inverting the logarithmic law for a velocity at a near-wall grid point using a fixed-point iteration. Then, the derivative at the wall is enforced by setting the velocity and derivatives at the off-wall node correspondingly. In Lattice Boltzmann terms, the velocity and the second Lattice Boltzmann moments were set with the method that was tested in 3.3. The mixing-length turbulent viscosity was set as the wall boundary condition for the K1E1 model. The Reynolds number is 2650, based on

c_1	c_2	σ	κ	A^+
0.144	1.856	1	0.41	13

Table 3.2: *K1E1 model coefficients*

the maximum velocity and the half-channel width, with a grid resolution of 31 grid points for the off-wall model and 63 grid points for the low-Re formulation. The first grid node was located at a a distance $d = 5\Delta x$ from the solid wall for the off-wall case and $d = 1/2\Delta x$ for the low-Re case. A velocity of $0.012\Delta x/\Delta t$ was imposed on the other side of the domain. This corresponds to $Re_\tau = 176$ and y^+ values of $y^+_{wall-law}(1\Delta x) = 4.7$, $y^+_{nearwall}(1\Delta x) = 2.5$. For the resolved case with wall-damping function, the first node is located a $y^+ = 12.5$. This is just barely inside the buffer region and outside the logarithmic region, which begins roughly at $y^+ = 13$. For the wall-modeled case the first node lies at $y^+ = 23.6$. As a collision model, the $D2Q9$ MRT model was used, where all collision factors, except the one responsible for the shear velocity, were set to one. The testcase is effectively one-dimensional with periodic boundary conditions in flow direction. The aim is to use these models in the near-wall region of high-Reynolds number turbulent flows, for which the use of LES models is computationally expensive. The model constants were computed from the factors of the standard $k-\varepsilon$ model using the relations

$$c1 = (c_{\varepsilon 2} - c_{\varepsilon 1})\sqrt{c_\nu} \tag{3.11}$$

$$c2 = \frac{c_{\varepsilon 2} - c_{\varepsilon 1}}{\kappa}\sqrt{c_\nu} + \frac{1}{\sigma} \tag{3.12}$$

as shown in [116]. The low-Re formulation suggested in that paper was also implemented. The resulting model coefficients of the model and the low-Re-terms are given in Table 3.2. Figure 3.24 shows the velocity profile for the same testcase as before with the near-wall formulation in comparison with the logarithmic law.

Note that with and without wall-model the velocity is slightly overestimated. An error of 1 – 2% is found for both variants, depending on the boundary conditions used.

3.3.2 K1E1 validation on a surface mounted cube

The K1E1-SAS model was validated using the surface-mounted cube testcase as described in [108]. The Reynolds number was $Re = 40000$. As in sec 3.3.1 the D3Q27 MRT model with relaxation parameters $(1, \lambda_{shear})$ were used and the same model parameters were employed for the K1E1 model. A resolution of 30 grid points for the height of the cube was used. The grid was 60 points high, had 300 points in flow-wise direction and 128 points in spanwise direction. The rather high blockage ration had to be used because of limited resources (the code runs on a single Tesla GPU) and because the resolution was at its minimum. When less grid points (10,20) were spend on the cube the top vortex was not resolved. We use the formulation with near-wall damping and no-slip conditions, even though the boundary layer is

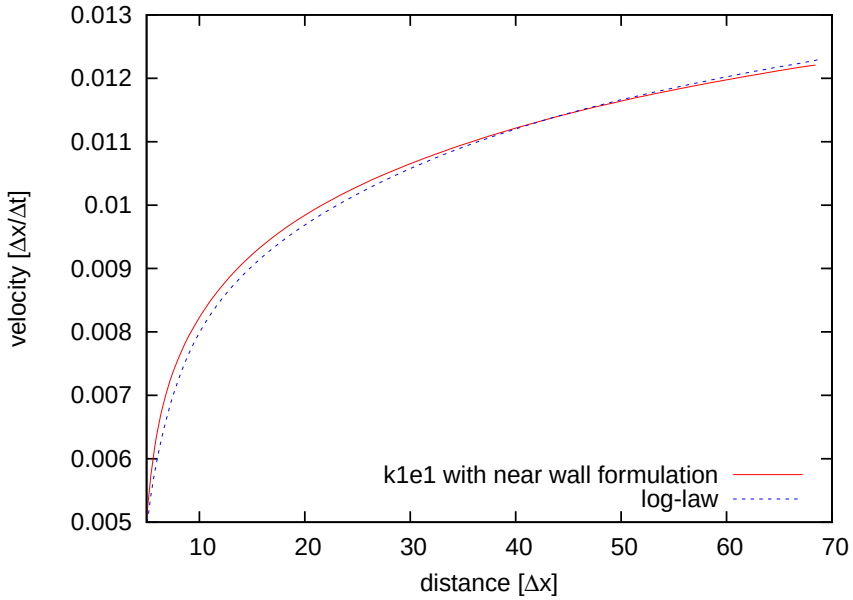

Figure 3.23: *Velocity profile for the K1E1-LB model with wall model in comparison to the log-law, shown here as a dashed line*

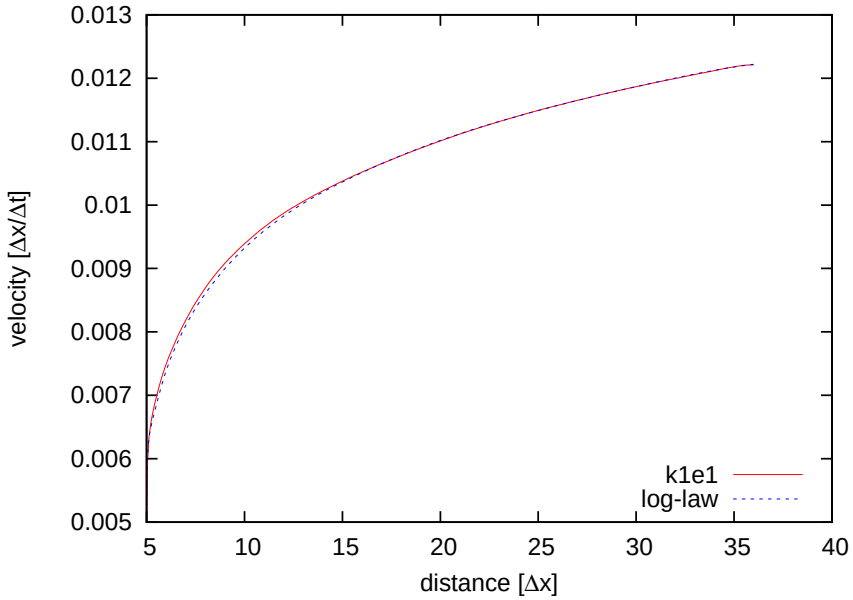

Figure 3.24: *Velocity profile for the K1E1 model with near-wall formulation, the dotted line shows the log-law solution*

Model	Yr	Xf	Xb
Exp	0.17	1.040	1.612
K1E1	0.183	0.53	2.217
LES	0.17-0.24	1.24-1.31	1.53-1.6
k-eps	0.0062-0.162	0.64-1.215	2.182-3.405

Table 3.3: *Comparison of the vortex extensions for some characteristic vortices, see fig 3.25*

not adequately resolved, as the implementation was valid for uniform grids only. We determined the position of the the major vortices. Experimental [108] data, data from LES simulations [87] and data from RANS simulations ([89] and references therein) were available for comparison. Table 3.3 shows a comparison, the positions of vortices are labeled as in Figure 3.25. Note that the extension of the rear vortex is overestimated by all RANS models. The values determined by our simulation lie within the range of values that are usually determined by RANS-models. In experiments X_f was measured as $X_f = 1.6$ and RANS-models usually overestimated the recirculation region in the rear of bulk bodies. Comparing to [89] we see that the basic $k-\varepsilon$-models with wall-functions that give a smaller value for the rear vortex extension also gave too small values for the front vortex extension. This is true also for our simulation results. Of the models considered in [89] only the two-layer models gave better values for the front vortex, but some dramatically overestimated the rear vortex. Some vortex shedding can be observed and is shown in Figure 3.26. This means that the time step and grid spacing are almost small enough for the model to operate either in the URANS or in a true hybrid mode. A study on a non-uniform grid would be necessary to obtain reliable results on the hybrid behavior.

3.3.3 Summary and Outlook

The one-equation RANS model K1E1 has been implemented an tested. First, it was validated for boundary layer flow and then applied to flow around a surface mounted cube. For the turbulent channel flow simulations at medium Reynolds number, the model reproduces the log-layer profile with both the near-wall model and an off-wall boundary condition with good accuracy. Preliminary tests on a surface mounted cube with a low resolution and a near wall model gave reasonable results, considering that the mesh was too coarse to resolve the boundary layer. So far, the implementation works with uniform meshes only which makes the application to flow situations with complex geometries difficult. Because of this, no flow around an object with hybrid RANS-LES behavior could be studied. The wall-model needs to be extended to include wall-normal velocity components and adverse pressure-gradients.

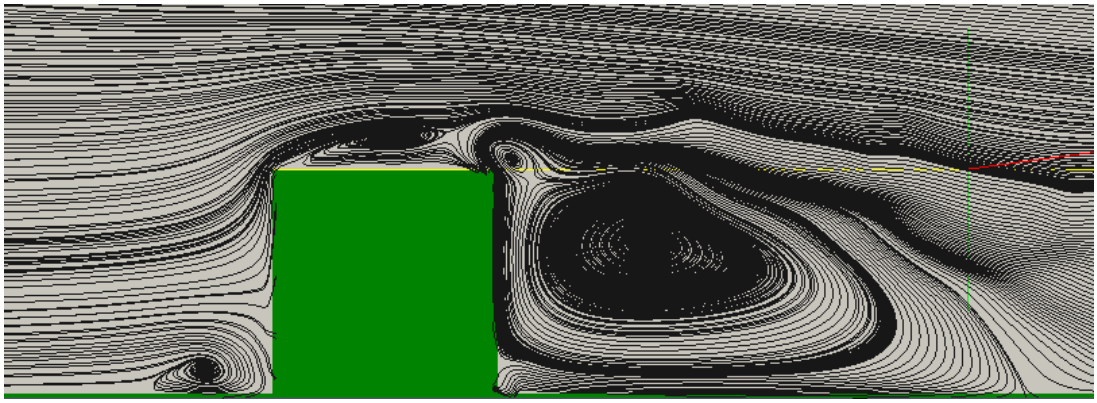

(a) Streamlines around the surface mounted cube for the SAS model

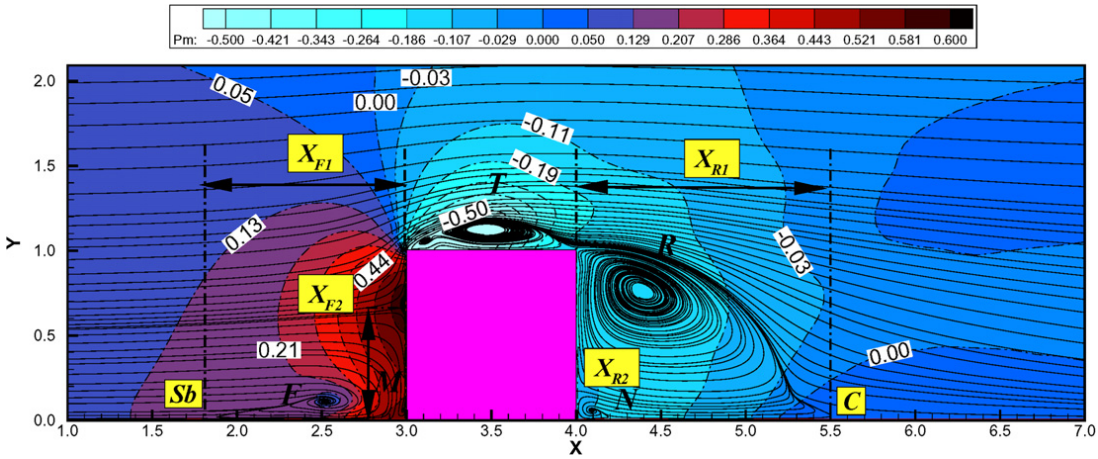

(b) Sketch of expected streamlines [177]

Figure 3.25: *Comparison between simulation results and expected streamlines from [177]*

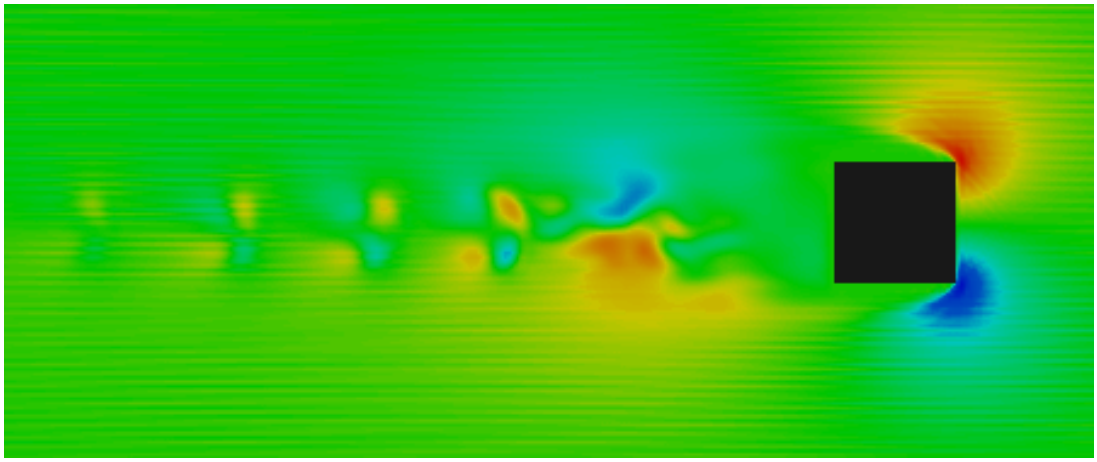

Figure 3.26: *Vortex shedding around the cube, the spanwise velocity component is shown*

3.4 Inflow boundary conditions for turbulent flow using auxiliary simulations

For simulations of turbulent flow, often inflow boundary conditions have to be provided which contain appropriate turbulent fluctuations to match a given turbulence intensity. Several approaches exist for reproducing the correct level of turbulent stresses, the correct spacial distribution and the correct temporal correlations. A viable method for producing the correct inflow profiles consists in using auxiliary simulations that run in parallel with the main simulation and supply the inflow data. For example, a turbulent channel flow with periodic boundary conditions can generate the inflow profile in cases like the one of the surface mounted cube. We chose to match only the turbulent intensity because the turbulent length scale is much more difficult to "'tune"' to a given desired value. For the turbulence intensity TI a number of slightly different definitions are in use and we use the following definition

$$\mathrm{TI}(x) = \frac{\sqrt{\langle U(x)^2 - \langle U\rangle^2\rangle}}{\langle U\rangle} \tag{3.13}$$

where $U(x)$ is the velocity vector and the average is intended as an average over time. The desired turbulent intensity can be obtained by rescaling the fluctuations

$$u_{in} = \langle U\rangle + u'_{aux}\frac{\mathrm{TI}_{target}}{\mathrm{TI}_{aux}}. \tag{3.14}$$

Now, the higher order moments have to be chosen. It seems acceptable to extrapolate the second order non-equilibrium moments from the neighboring node. Alternatively, the moments can also be obtained from the auxiliary simulation. Note that, if the auxiliary system and the main system work with different viscosities, the post-collision moments have to be rescaled

$$\mu^*_{ij} = \mu^{*,aux}_{ij}\frac{\lambda_{aux}}{\lambda}\frac{1-\lambda}{1-\lambda_{aux}}. \tag{3.15}$$

This formula is similar to the formula that is often used for rescaling the moments in simulations on non-uniform grids [87], but stated here for the post-collision terms instead of the pre-collision terms. To validate the method, turbulent flow for channel flow simulations was generated. In the auxiliary simulation the viscosity was set to $\nu = 0.00005\Delta x^2/\Delta t$, with $\langle v_{max}\rangle = 0.012438\Delta x/\Delta t$ and 64 grid point across the channel were used. The extension in the other two directions was 128 and 32 grid points. This corresponds to a Reynolds number of $Re = 15900$, a turbulence Reynolds number of $Re_\tau = 458$ and a grid spacing of $y^+ = 14.3$. For the main simulation a different inflow velocity was used. We chose a logarithmic profile with a mid-channel mean velocity of $\langle v_{max}\rangle = 0.0218912\Delta x/\Delta t$. For both models a $D3Q27$ CLB model with TRT collision factors (λ,1) was used. Figure 3.27 shows the development of the turbulent intensity at a fixed distance from the wall (20 grid points). For one of the four setups the turbulence intensity decays, for the other setups it stays constant. The rapid decrease behind $D = 120\Delta x$ is due to the outflow condition which enforces a constant density

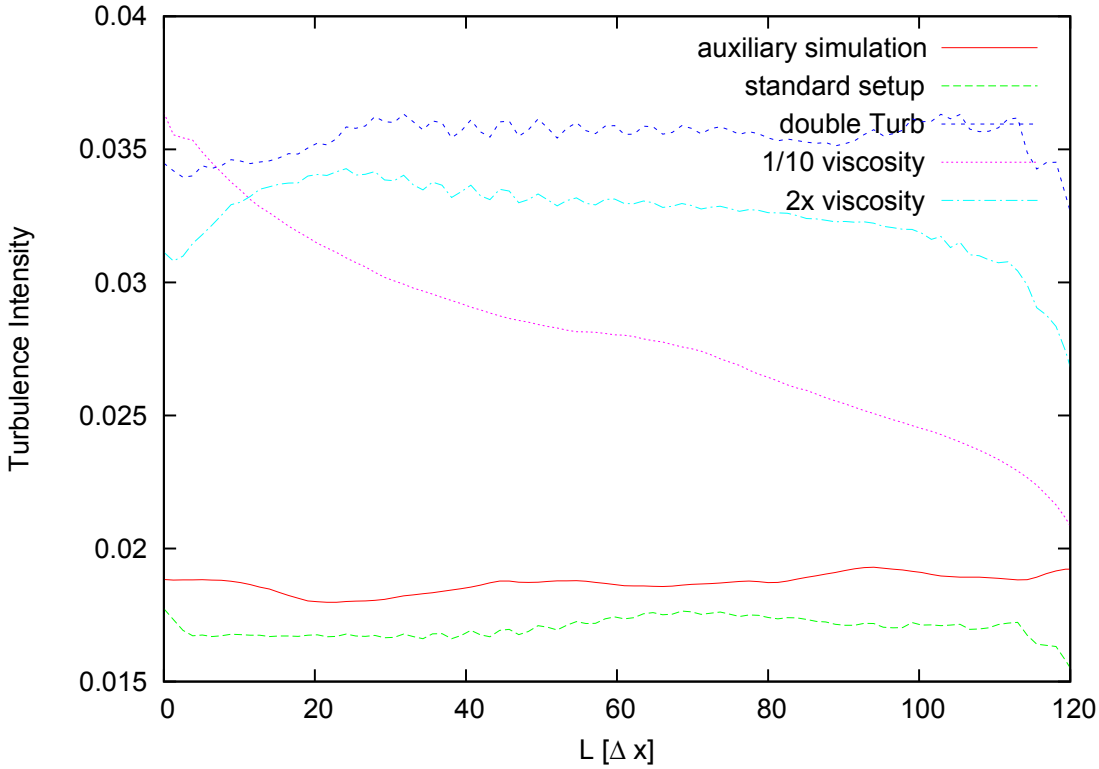

Figure 3.27: *Turbulence Intensity along channel at a fixed distance of 20 grid points from the wall*

across the outflow plane. Figure 3.28 shows the turbulence intensity over the distance from the wall for the first two setups and the auxillary simulation.
In the present section we have shown the principal validity of using auxiliary simulations with Lattice Boltzmann channel flow simulations, even if the main and the auxiliary setup differ in their viscosity and mean velocity. A classical, similar method is Lund's rescaling method, that is used to generate boundary layers of finite thickness [105]. Hence for us, such a method may be an option for studying details of the flat plate boundary layer (sec. 4.2). Turbulent fluctuations may further be generated synthetically based on a given turbulence velocity spectrum.

3.5 Interpretation of the CLB model as an implicit turbulence model

3.5.1 Introduction

In this section we motivate the interpretation of the CLB model as an implicit large eddy simulation (ILES) model. With some qualitative arguments and numerical examples we point out similarities and differences between eddy viscosity models, scale similarity models and the CLB models. As shown in [50] the CLB model is stable for relatively high Mach numbers

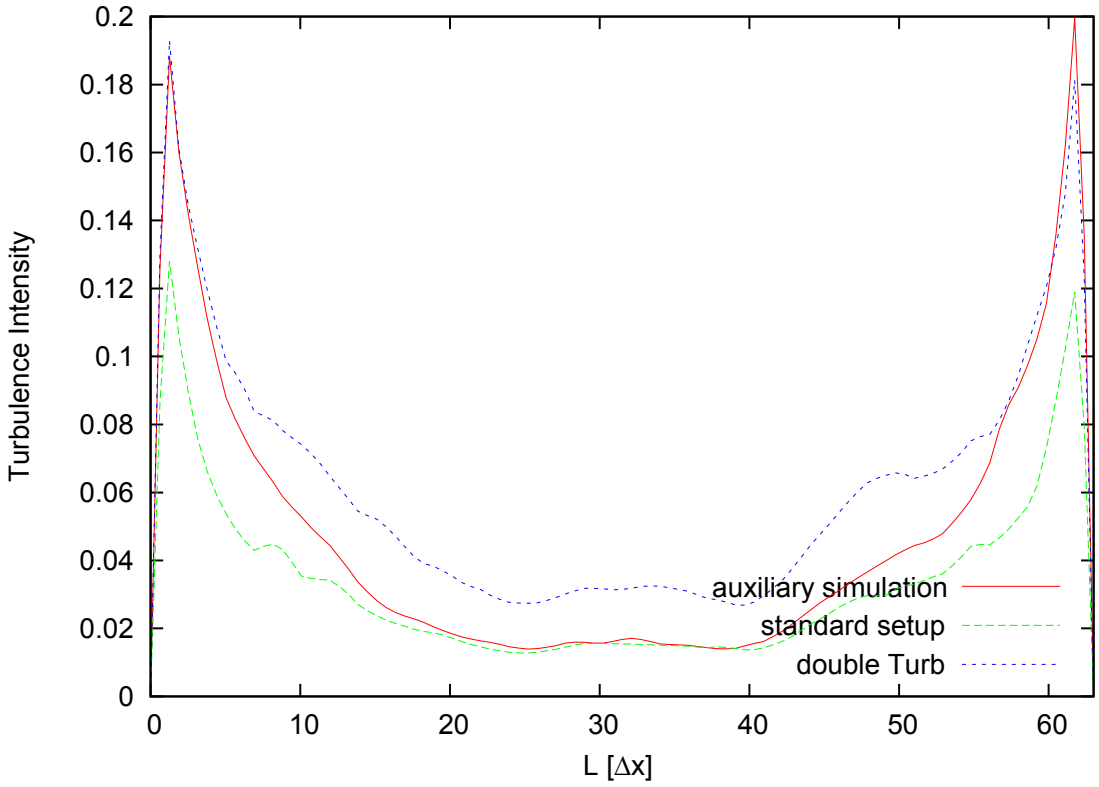

Figure 3.28: *Turbulence intensity across channel*

and yields the correct $E(k)^{-5/3}$ relation between the turbulent kinetic energy and the wave number. We first give some arguments that point to the qualities of CLB as an implicit turbulence model. After that, we show simulation results for flow around a rectangular object at a medium Reynolds number for the different models. A Taylor-Green vortex at low resolution is also considered.

3.5.2 Discussion of the CLB collision terms in terms of ILES models

We start with a discussion of the terms that we suspect responsible for the ILES behavior. Apparently, the contribution of terms specific to the CLB model to the fluid behavior is large, whenever gradients are large, because CLB differs from traditional LB models for third- and higher order moments. In the Navier Stokes-type equation derived from CLB-models additional error terms of the form $(\partial_{x_i}\mu_{x_j})(\partial_{x_j}\mu_{x_k})$ occur among other second-order error terms. These terms remind us of the LES models called similarity models. Bardina's similarity model [4] is derived from the assumption that the small scales behave in a similar way as the large scales. One thus assumes that the Reynolds stress tensor $R_{ij} = \overline{u_i u_j} - \bar{u}_i \bar{u}_j$ can be modeled by doing a Taylor expansion of u. This leads to $\tau_{ij} = C_{bardina} \sum_k (\partial_{x_i} u_k)(\partial_{x_k} u_j)$. The derivatives can be computed from finite differences [59]. $C_{bardina}$ is a constant of the order of unity. This model does not rely on the Boussinesq hypothesis, the eddy-viscosity term is not isotropic. The model is difficult to use for engineering-related flows because it is not sufficiently dis-

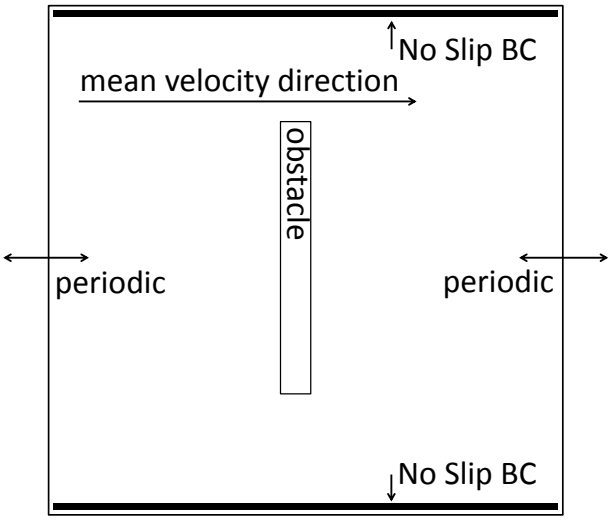

Figure 3.29: *Schematic of the flow around a rectangular obstacles*

sipative [113]. Instead, we want to apply it to some simple medium Reynolds number flows to compare its behavior to the CLB behavior. It should however be clear that the CLB model differs from Bardina's model because several terms occur in CLB that do not occur in Bardina's model, some of which apparently account for the stabilization. A set of "new terms" are those of the form $u_{x_i}(\partial_{x_i x_i} u_j)$.

3.5.3 Flow around a rectangular obstacle

We compare the models qualitatively for flow around a rectangular obstacle at a medium Reynolds number. The domain is periodic in flow direction and no-slip boundary conditions are applied at the top and bottom. The domain size is 128x128 and the plate covers 70 grid points in normal direction. It is seven grid points long. The initial velocity is $v_x = 0.01\Delta x/\Delta t$ and the Reynolds number is $Re = 7000$. The flow is then left to decay. Bardina's similarity term is applied directly to the second order moments. Schematic 3.29 illustrates the setup. Pictures 3.30 to 3.31 show screen-shots for the density of the fluid at different time steps ranging from $1300\Delta t$ to $1900\Delta t$. All simulations were conducted with $D3Q27$ models, the relaxation coefficients were set to one, except for the LBGK-coefficient. The plain MRT, MRT with the Smagorinsky model, MRT with Bardina's model, and the CLB model are compared. All four models are started from the same initial condition and diverge over time. The plain MRT and the MRT model with Smagorinsky LES behave similarly, while Bardina's model and CLB behave differently but similarly to each other.

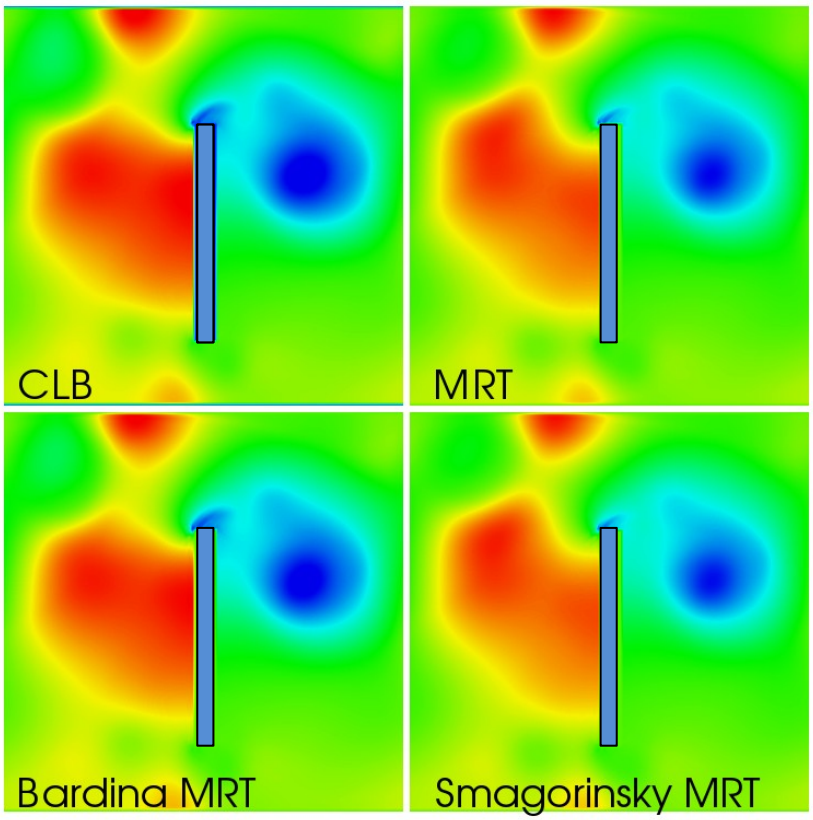

(a) Timestep 1300

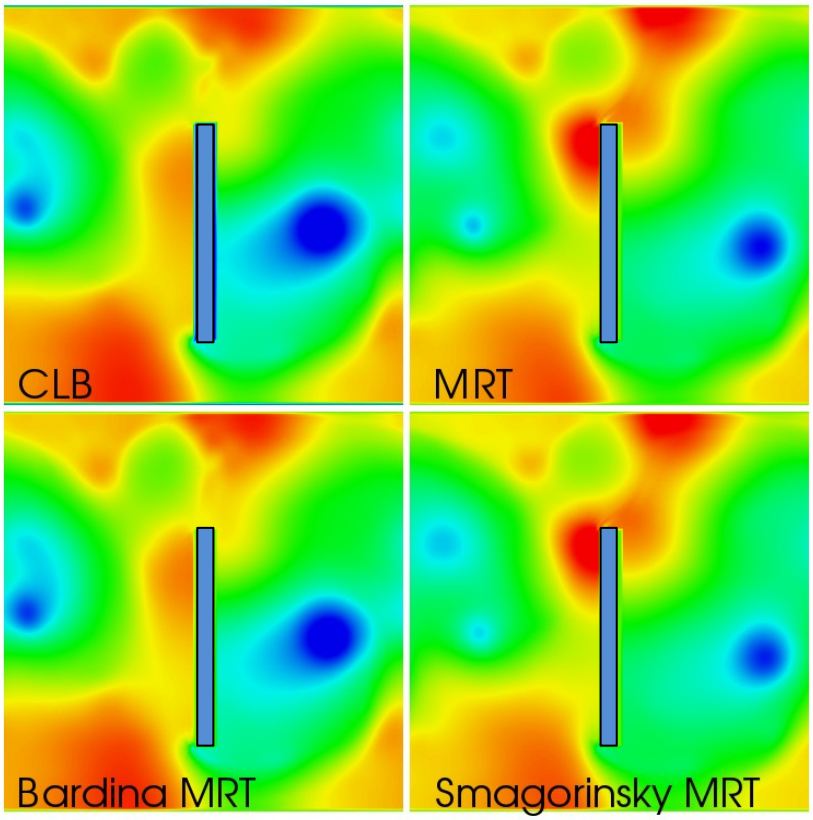

(b) Timestep 1500

Figure 3.30: *Snapshot of the density for the flow around a rectangular obstacle for different turbulence models, timesteps t=1300 and t=1500*

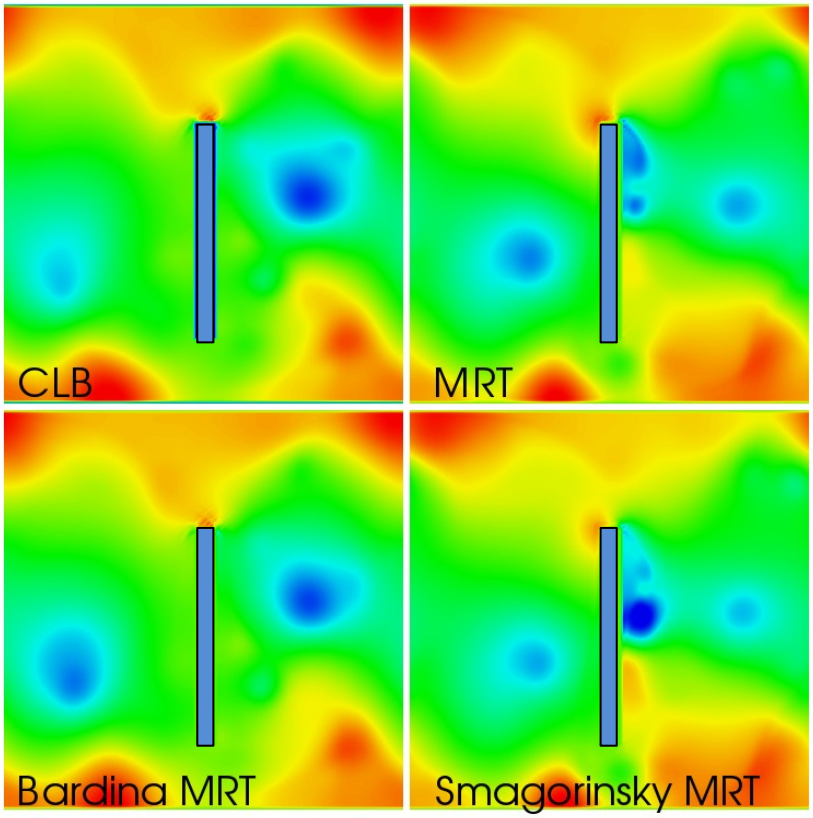

(a) Timestep 1700

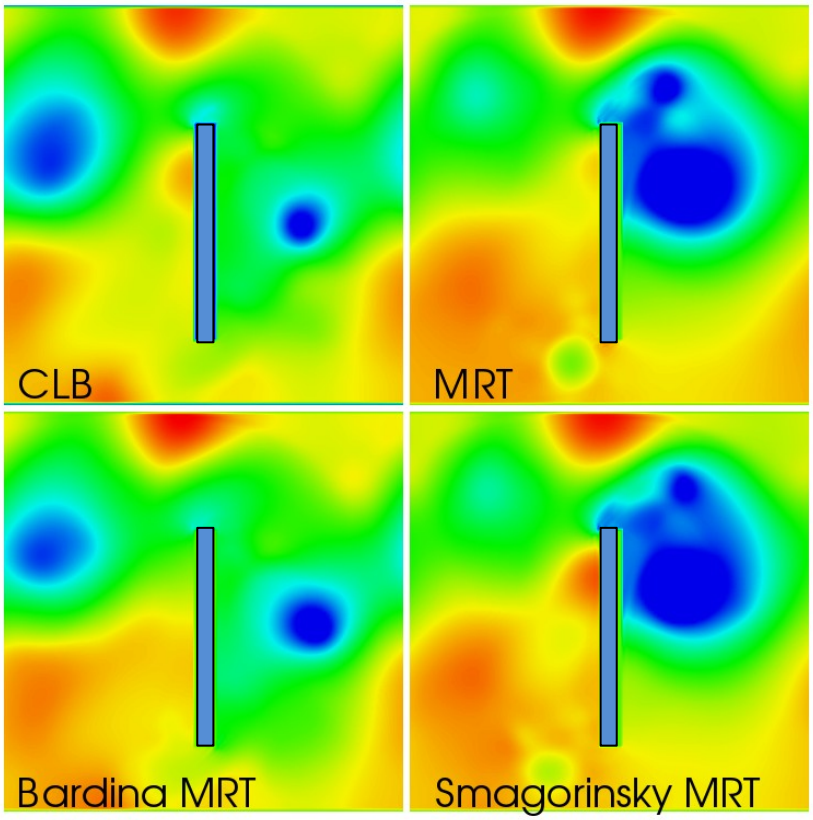

(b) Timestep 1900

Figure 3.31: *Snapshot of the density for the flow around a rectangular obstacle for different turbulence models, timesteps t=1700 and t=1900*

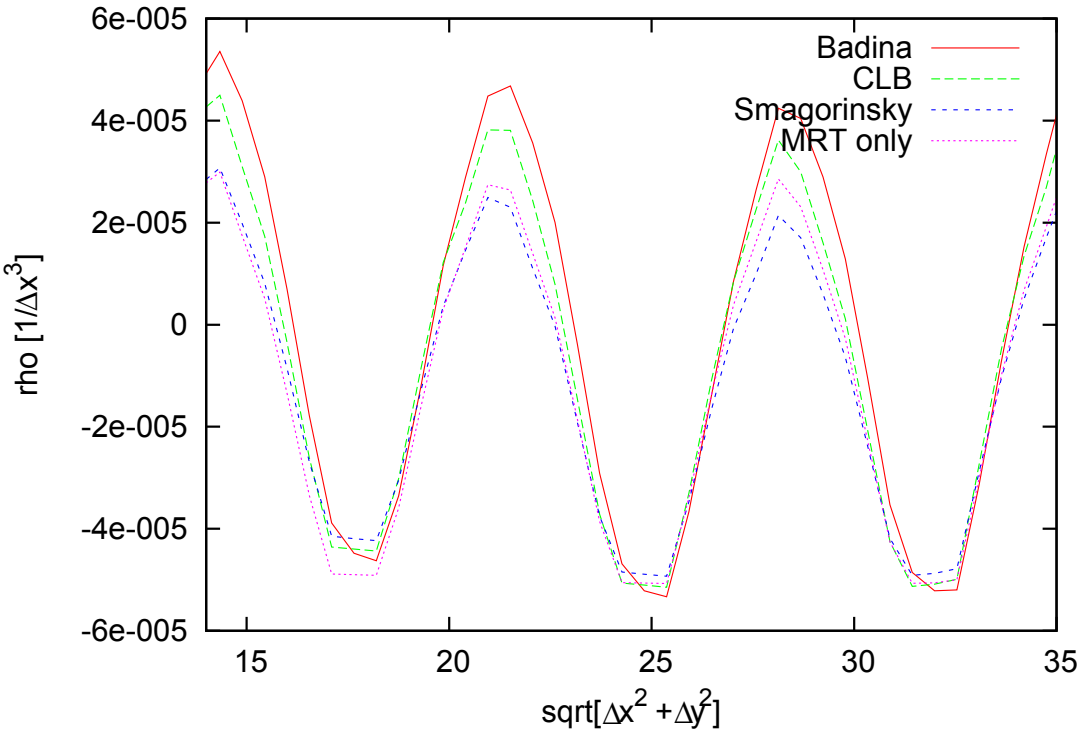

Figure 3.32: *Pressure fluctuation for Taylor-Green vortex, resolved with ten gridpoints plotted along a diagonal line $x = y$*

3.5.4 Taylor-Green vortex

We try to confirm the results using basic standard benchmarks, as the above testcase is rather arbitrary. A test on laminar Poisseuille flow is not in agreement with the results above, as the Smagorinsky viscosity is the prevailing effect. The three other models behave alike. As can be seen easily, Bardina's model does not give a contribution for pure shear.
It was thus decided to study a Taylor-Green vortex [157], which is a standard, but sufficiently complex testcase. For a Taylor Green vortex a similar behavior to that of the vortex shedding testcase described above is found. One vortex is resolved with ten grid points only. The viscosity was set to $0.001\Delta x^2/\Delta t$. The plot (3.32) shows the density variations of the four models after 1600 time steps along a coordinate axis. For different time steps and plots along different axis the situation is comparable and therefore not shown here. For prefactors $C_{bardina}$ in the range of $[0,6]$ the density variations for Bardina's model lie within the value found for the CLB model and the MRT model, where the case $C_{bad} = 0$ coincides with the MRT model and larger values of $C_{Bad} > 6$ were not tested because they were did not match the model assumptions. The simulation results shown here were obtained with an intermediate value of $C_{Bad} = 1$. The values for the velocity practically match. The Smagorinsky model is more dissipative than any of the other three models and the density variation and velocity amplitudes decay faster.

3.5.5 Conclusions

The above arguments and numerical test are of qualitative nature. Further quantitative investigation is necessary. On the other hand, meaningful empirical criteria are difficult to specify. An improved theoretical understanding of the effect of the CLB model as an implicit turbulence model is still needed. The complexity of the vortex shedding case, however, is a strong hint that the agreement between the CLB model and Bardina's self-similarity model is not completely coincidental. The idea was confirmed by tests on the Taylor Green vortex, such that we suspect that the $(\partial_{x_i} u_k)(\partial_{x_k} u_j)$-terms have a strong effect on the behavior of the CLB model as a turbulence model.

3.6 A simple test: advection of a frozen-in velocity peak

A simple test on the factorized CLB and the cumulant model is carried out. The aim here is to identify differences between CLB-variantsm such ath basic CLB, the FCLB, and the cumulant model for selected sets of relaxation factors. The tests are based on a numerical experiment described in [47], (sec 4.3.1), which will be explained first.
In this experiment the behavior of a velocity peak along a single line that is only one node thick when the velocity at all other nodes is zero, is investigated. The direction of the velocity is parallel to this line and the nominal viscosity is $\nu = 0$. The effective viscosity is only due to numerical diffusion. For this specific testcase, a stable solution can be obtained for particularly dissipative numerical schemes. No advection occurs, because the fluid is transported along one path only. In an ideal model no dissipation should occur and if the viscosity is zero, the velocity peak would be "frozen-in". A numerical model is expected to either become unstable or stabilize the flow by numerical dissipation. In the latter case, the velocity peak will decay over time. In [47]'s setup the domain was periodic and the simulation was carried out with a $D2Q9$ model, such that the domain was quasi-one dimensional. The BGK model was found not to be stable, the CLB model (with all free relaxation parameters set to one) was stable and showed dissipation only at the first few time-steps. After that it converged to an essentially time-invariant state.
We repeat the experiment with $D3Q27$ models in a three-dimensional setup (quasi two-dimensional). For the Mach-number of the velocity peak we choose $v_{LB} = 0.01\Delta x/\Delta t$ ($Ma \approx 0.005$).
If all free relaxation parameters are set to one, the CLB model, the factorized CLB model and the cumulant model are stable but the peak is not frozen-in. We further notice that the flow is not symmetrical. In Picture 3.33, the cross shape of the regions of equal velocity after 100 timesteps can be seen. The peak widens along the characteristic directions. The behavior of all three models is identical.
The relaxation parameters Set I from [49], which can be found in the appendix C, have been successfully used to improve isotropy in the case of the shear-wave [49] and for the square

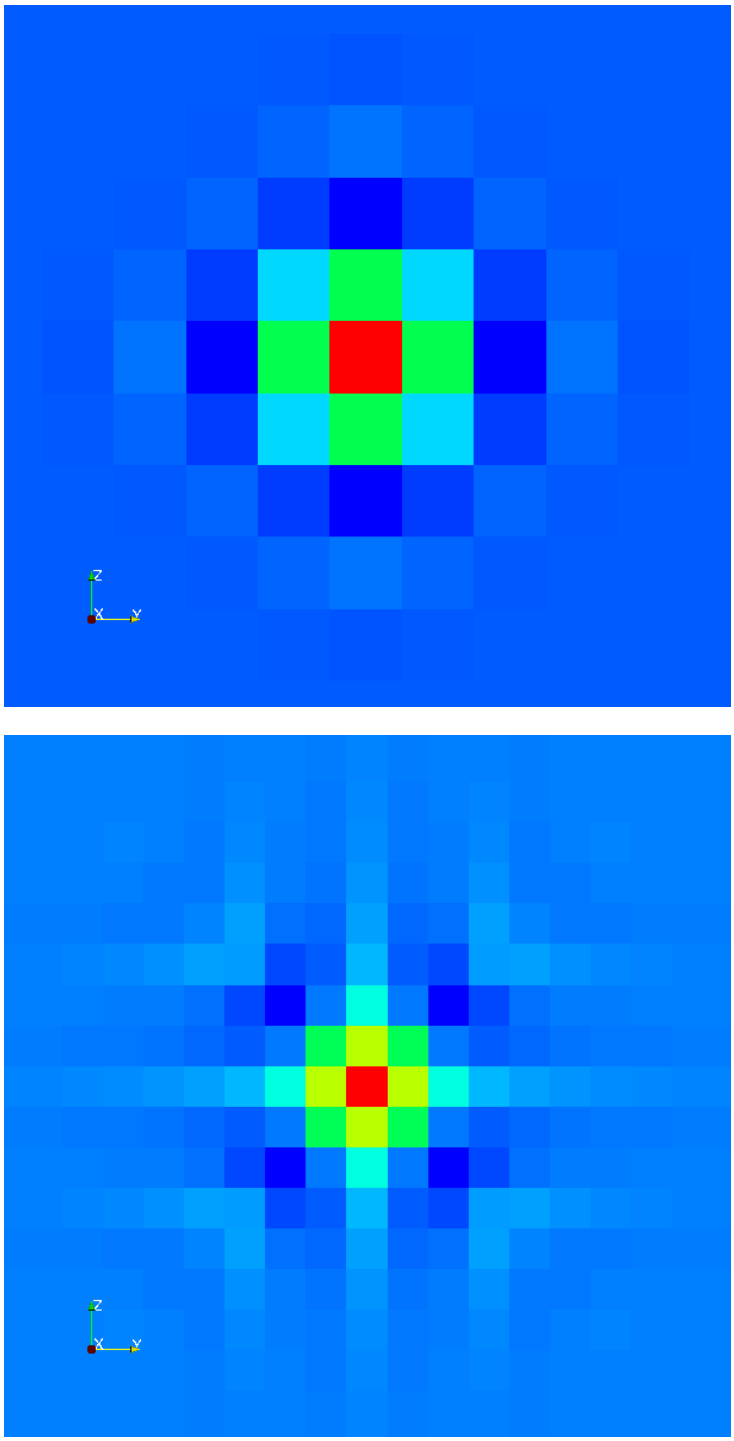

Figure 3.33: *Velocity for the cumulant model, top: all-to-one relaxation parameters, bottom: parameter set I*

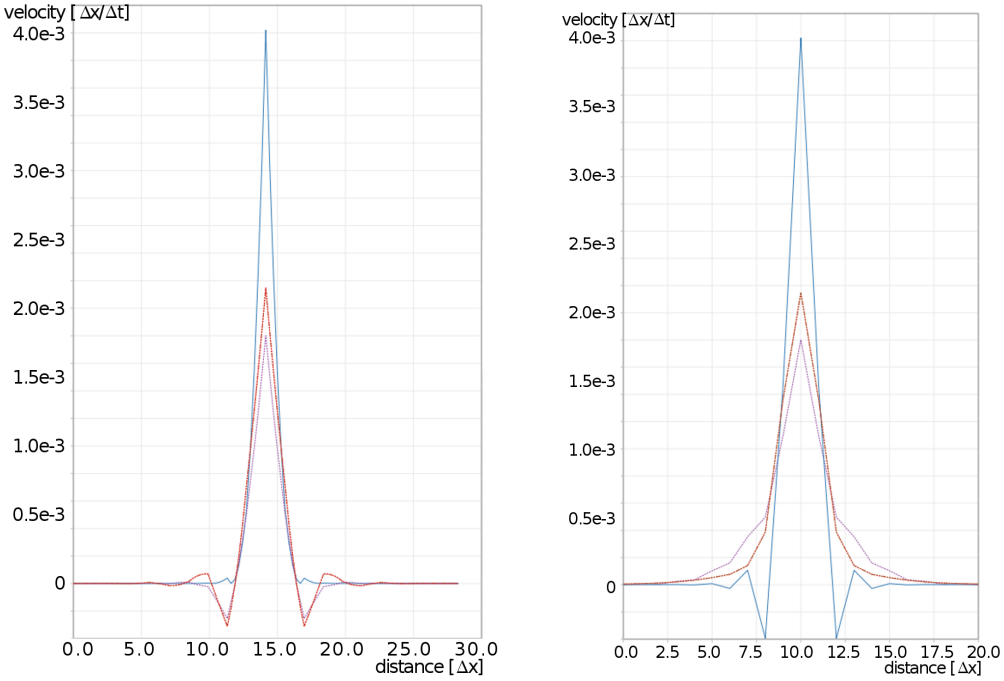

Figure 3.34: *Velocity after 100 timesteps for the FCLB and cumulant model will all-to-one relaxation factors (indistinguishable, red) , the cumulant set I (blue) and the CLB all-to-one (violet), left: along the $y = z$-diagonal, right: along an axis*

duct (section 3.7). Simulations are carried out for the factorized CLB and the cumulant model with this set of relaxation parameters. A frozen-in velocity peak with improved rotational symmetry is obtained for the cumulant model (cf. picture 3.33). The CLB and factorized CLB models become unstable. Plots (3.34,1) and (3.34,2) show the velocity along the $y = z$ and the z-axis respectively.

The dominant contribution seems to be the term $M^c_{yy}M^c_{xzz} + M^c_{zz}M^c_{xyy}$ to the fifth order moment M^c_{xyyzz}. In fact, the factorized CLB model will give almost identical results to those of the cumulant model for the first 100 time steps if this contribution is added, even though it still becomes unstable after that. It is sufficient if only the equilibrium contribution of the second order moments is considered ($(M^c_{xzz} + M^c_{xyy})/3$ instead of $\left(M^c_{yy}M^c_{xzz} + M^c_{zz}M^c_{xyy}\right)$.

We conclude that the cumulant model behaves differently from the factorized CLB and the CLB model for this testcase. Unlike the CLB and FCLB models, tt is stable for set I of relaxation parameters, which improves rotational symmetry. The effect of the different relaxation factors for CLB models is not yet well-understood. The non-linearity of the CLB models makes an analysis quite complex, especially since higher order contributions ($O(\varepsilon^4)$ and higher) are of interest.

Similar results have recently been obtained for turbulent jet flow. Flow entering a domain at rest through a circular orifice at a Reynolds number of 6700 is studied in [56] with the $D3Q19$

model with Smagorinsky LES and with the $D3Q27$ factorized CLB model. The former leads to a non-circular cross section of the jet.

3.7 Convergence studies

The Cascaded Lattice Boltzmann model and the Cumulant model are validated for flow in a square duct. Different collision factors and collision modules are compared. The $D3Q27$ model is compared to the $D3Q19$ model. A validation of LBM for the square duct problem was carried out previously in [112]. They compared the $D3Q15$, $D3Q19$ and $D3Q27$ LBGK models and found a good agreement with the analytical solution for all three models. Only the LBGK collision model was considered and no significant difference between the models was observed, which is in agreement with results for the LBGK model. For the testcase of the square duct the analytic solution is known

$$u_x(y,z) = \sum_{j=1}^{\infty} 16\frac{H^2}{\nu\pi^3} f(-1)^{j-1}\left(1 - \frac{\cosh((2j-2)\pi z/(2H))}{\cos((2j-1)\pi y/(2H))(2j-1)^3}\right) \tag{3.16}$$

f is the forcing, ν the viscosity and H the half channel width [150]. Picture 3.35 shows a contour plot of the analytical solution, in Figures 3.37 and 3.38 the velocity is plotted over the distance, once along the duct's diagonal and once in mid-channel, normal to the wall. We chose the flow in a square duct as a benchmark because it is a higher-order, three dimensional flow. As opposed to Poisseuille flow where all terms of the type $\frac{\partial^{m+n} u_x}{\partial y^m z^n}$ vanish for $m > 2$ and $n > 0$, higher order error terms may play a role in the numerical solution of the problem.

For this testcase, as well as for the testcase of a double shear wave [49] the velocity is underpredicted by the $D3Q27$ Cascaded Lattice Boltzmann model. The Lattice Boltzmann equation is known to be second order accurate when appropriate boundary conditions are used. In order to validate an implementation of the Lattice Boltzmann method, second order convergence for some testcase should be demonstrated as we do here. Furthermore, different variants of the Lattice Boltzmann equation can be compared with regard to their accuracy. To test convergence means to successively reduce the discretization errors and see how the output changes. In Lattice Boltzmann there are two types of errors: Those that stem from the finite grid spacing and those that are related to the time discretization. Apparently, there are different paths towards a fully resolved solution. We choose diffusive scaling for which $\varepsilon^2 = \Delta x^2 = \Delta t$ as introduced in sec 2.6. This means that, when we divide the grid spacing by two, we also divide the velocity by two and keep the viscosity constant. With the most common alternative, acoustic scaling, the viscosity is increased proportionally to the grid discretization. Diffusive scaling is chosen, because it reduces the errors of both spatial and the error in the velocity which is Mach-number dependent. Different collision factors were tried out, they are denoted by set 0 to set III and set all-to-one. The exact values can be found in the appendix.

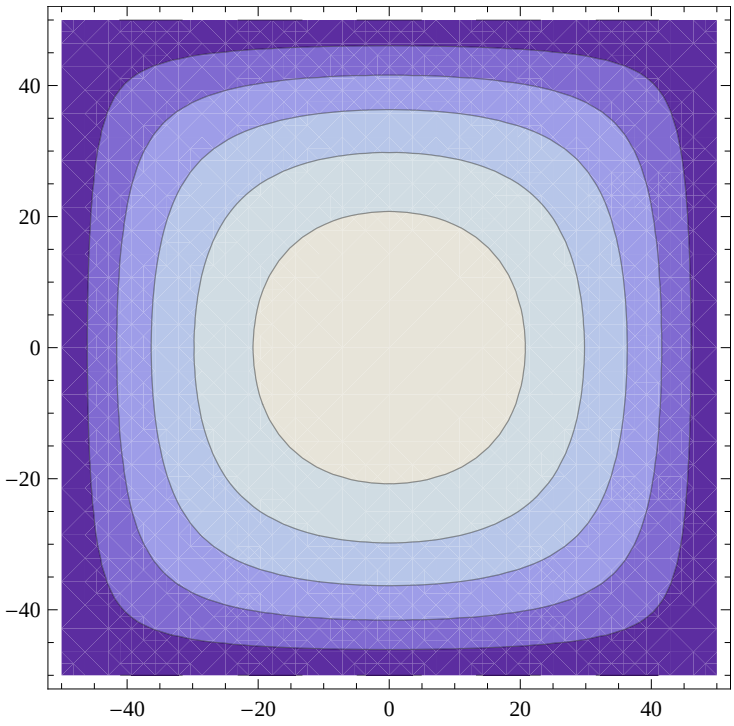

Figure 3.35: *Contour plot of the velocity in a duct*

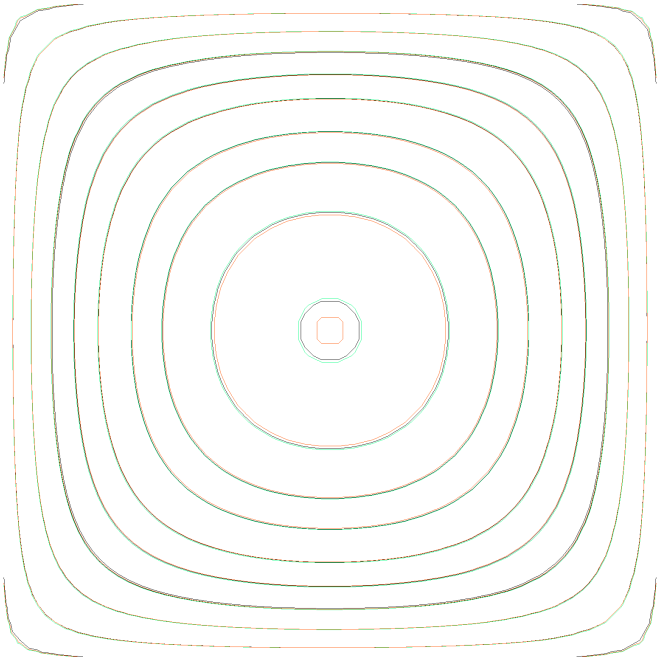

Figure 3.36: *Isolines for the BGK (black), CLB (green), and FCB (red) models*

To test the influence of the specific implementation of the forcing term, both the simple first-order forcing as defined in eq. 2.111 and the advanced forcing [129] were used for the simulations with the compressible $D3Q19$ MRT model. As the differences between the results for the two forcing terms were much smaller than the differences to the results for any of the other collision models, only the simple forcing was considered for those models.
From Figure 3.42 it can be seen that all models studied show quadratic convergence. The actual errors for this testcase, however, are very different for the different models. The cumulant method and factorized CLB method are quite successful, they show the smallest total error of all $D3Q27$ models considered. In fact, the magnitude of the errors of these two methods are almost equal. For the Cascaded Lattice Boltzmann method, different sets of relaxation rates were considered which had large variations among them. It appears that the Incompressible LBGK model shows a smaller error than the CLB models once the asymptotic limit is reached, but takes longer to reach this limit. The error for small resolution is larger for the LBGK model than for any other model. The $D3Q19$ MRT model with the set 0 of relaxation rates shows the smallest overall error.
To determine the convergence rate, we assume that the error behaves as $err = cy^{\alpha}$. Solving this equation for two neighboring points (y_1, err_1) and (y_2, err_2) one can determine the exponent of the decay of the error α. The results are shown in table 3.4. The differences between the analytic solution and the simulation along the duct's diagonal are shown in Figure 3.37. We consider only the error of the streamwise velocity component. The other two velocity components are two or more orders of magnitude smaller.
A Richardson extrapolation is carried out to test whether the solution converges towards the analytical value. Second-order convergence of the leading error term is assumed and $(10,20)$, $(20,40)$, $(30,60)$, $(40,80)$, $(50,100)$ are chosen as interpolation points. By construction, the Richardson-extrapolation should converge with third-order accuracy. For those models, which gave less accurate results, namely the LBGK, the CLB set 1 and 0 models and CLB with TRT factors third order convergence towards the analytical solution could be confirmed. For the cumulant and $D3Q19$ MRT model such a behavior was found for the first few extrapolation points only. After that, effects such as round-off errors might start to play a role. For the $D3Q19$ MRT model with second-order forcing term, for example, the extrapolation suggest a minimal relative error of $3e-6$. Simulations were carried out for a maximal resolution of 180 grid points, where a relative error of $5.3e-5$ was reached and the convergence was still second order.
The CLB model with relaxation factors from set 0 underestimates the velocity most significantly, while CLB with factors from set II overestimates the velocity. The LBGK model leads to a sharp peak near the boundary, which is present also for some other models, such as the CLB model with two relaxation rates, but less significant. The cumulant model and the factorized CLB give practically identical results and only the result for the cumulant model is shown. It is also very similar to the MRT model. In plots 3.40 and 3.38 the errors along the duct's diagonal and the wall-normal direction in mid-channel are shown for these two models only. Even though the MRT model (violet, dashed) is more successful at reproducing the maximum ve-

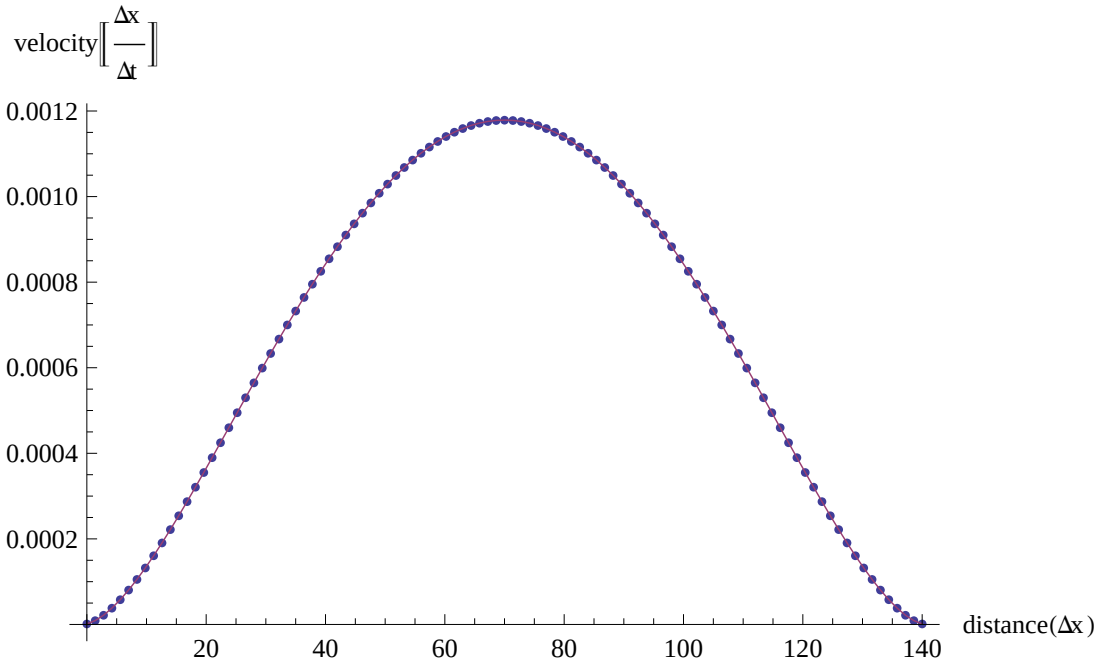

Figure 3.37: *Velocity along diagonal for the MRT model*

locity, the velocity at the boundary is less accurately predicted. The main difference between the simulation results are the maximum velocities they produce. The difference in the shape of the flow is less pronounced as can be seen from Figure 3.36.

Observing the outcome of the simulations one may group the models in two classes: The CLB set 1 and 0 models that perform less satisfactorily and the other models which show a better performance. The two CLB models have one thing in common: The moments μ_{xyz}, μ_{xyyz}, μ_{xyyzz}, μ_{xxyyzz} and permutations in x,y,z are non-zero and are relaxed with a different relaxation factor than the LBGK collision factor. For the D3Q19 model, these moments do not exist or are always zero. For the CLB model with TRT factors, the third and fifth order moments are relaxed with the LBGK collision factor. The sixth moment μ_{xxyyzz} and all other moments that contain a double "x" enter in the discretized Navier Stokes equation with a first derivative in x-direction due to the moment expansion, c.f. eq. 2.60. It follows that all these terms can be neglected in our discussion, because in our particular testcase all variables are constant in x-direction. The sixth moment is assumed to be of lesser influence because the second-order contribution in x-direction means at least one derivative in x-direction, which is zero. The moments μ_{xyz}, μ_{xyyz} and μ_{xyyzz} all have have as their lowest order contribution a term proportional to $\frac{\partial^4 u_x}{\partial yyzz}$. This term is a second-order error term to the Navier-Stokes equation and leads to a pre-factor in the second order convergence terms. For the factorized CLB the equilibrium is equal to the standard CLB equilibrium ${M^c_{xyyzz}}^{F,eq} = {M^c_{xyyzz}}^{eq} = 0$, so this term cannot be the source of the differences between the models and the lowest and the lowest order contribution will be zero, too.For the moments μ_{xyyz} and μ_{xyzz} the FCLB differs from the standard CLB. We have ${M^c_{xyyz}}^{F,eq} = {M^c_{xz}}^* {M^c_{yy}}^*$, but ${M^c_{xyyz}}^{c,eq} = 0$. The terms thus

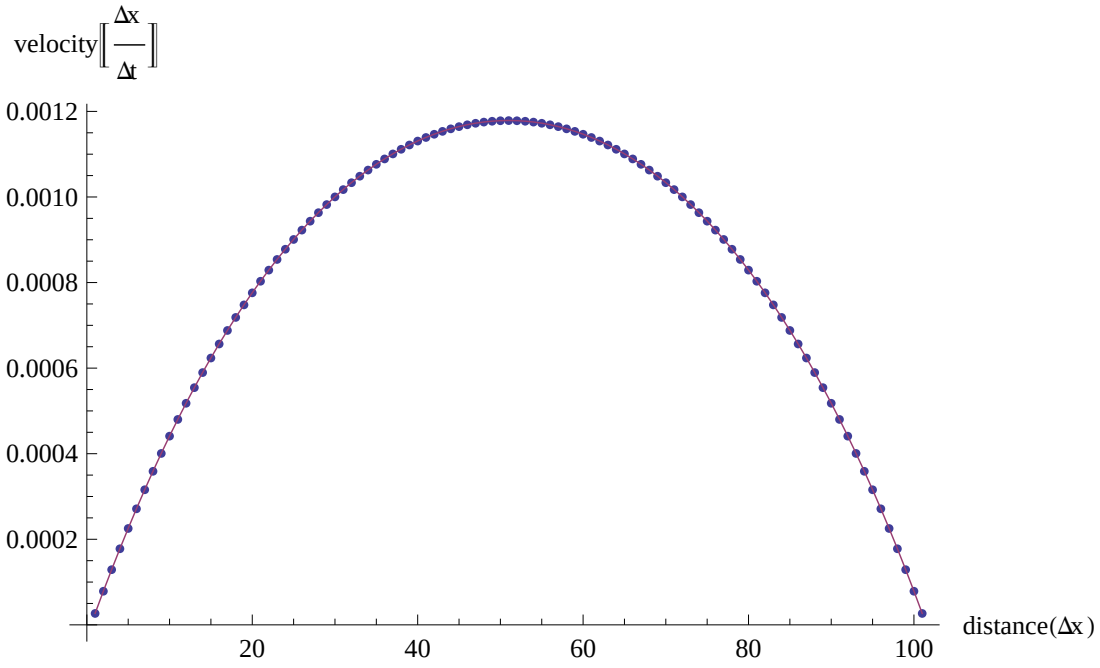

Figure 3.38: *Velocity in wall-normal direction for the MRT model*

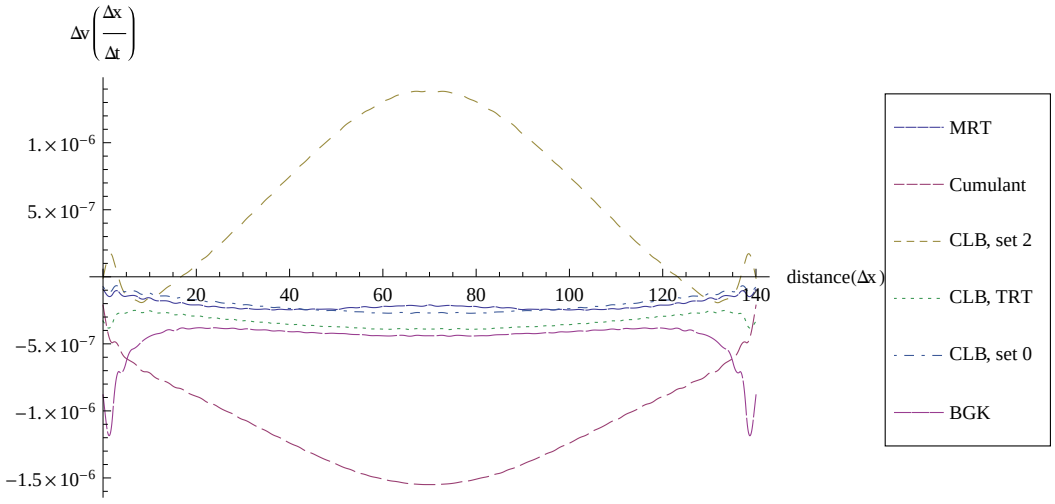

Figure 3.39: *Error along the diagonal for different collision models*

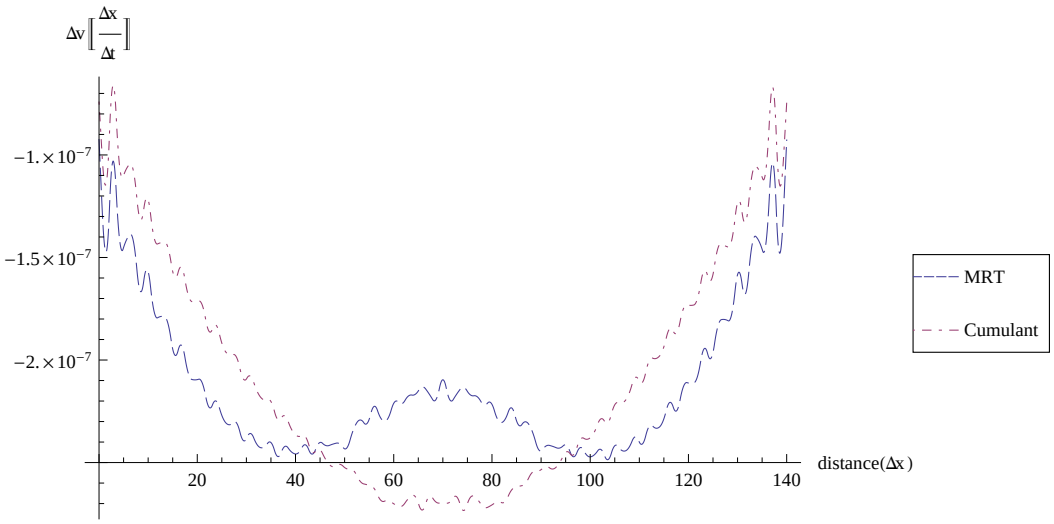

Figure 3.40: *Comparison of MRT and the Cumulant's errors along the diagonal*

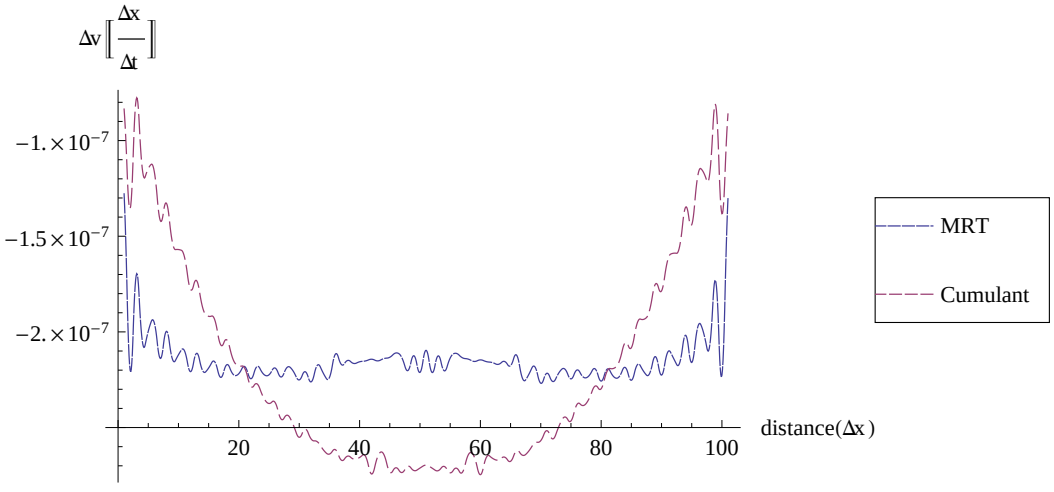

Figure 3.41: *Comparison of the MRT and the Cumulants errors in wall-normal direction*

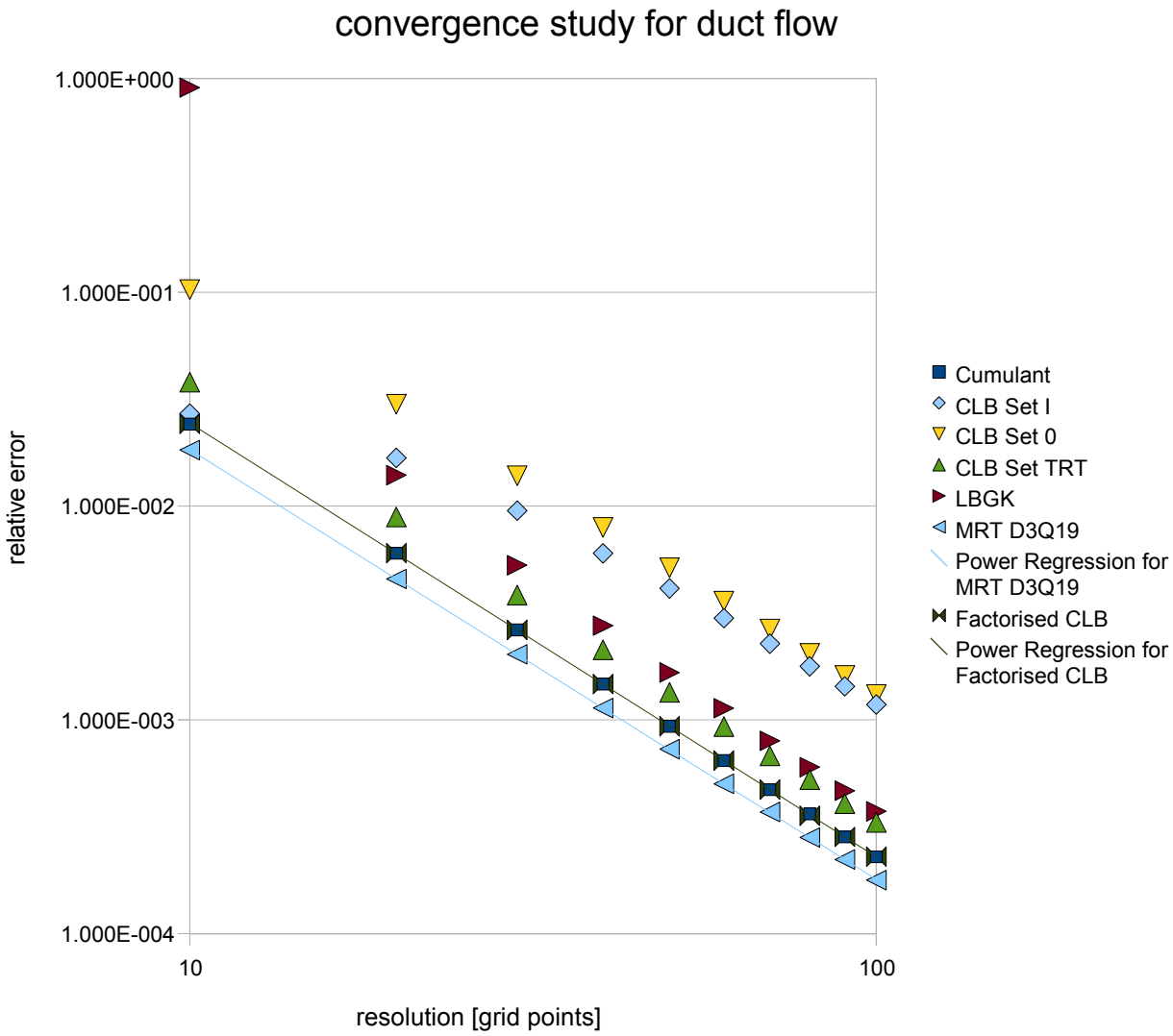

Figure 3.42: *Convergence rates for different collisions models*

differ by a term that is itself of second order contribution and is proportional to $\partial_z \mu_x$. This explains why we see different pre-factors for the FCLB and CLB model.
In conclusion, one can say that the $D3Q19$ MRT model yields the smallest error for the duct flow. The Cumulant and Factorized CLB model achieve comparable results. The $D3Q27$ MRT model and the CLB model with "all-to-one" relaxation factors are the least successful at reproducing the correct velocity. Second order convergence is obtained for all models studied.

NX	Cumulant	CLB II	CLB 0	CLB TRT	Inc. LBGK	MRT 19	MRT 19, f2
20	2.443	0.687	1.784	2.095	6.021	2.004	1.972
30	2.676	1.403	1.896	2.077	2.391	2.003	1.992
40	2.661	1.594	1.993	2.050	2.264	2.006	1.992
50	2.669	1.696	1.950	2.049	2.258	1.987	2.014
60	2.603	1.757	1.963	2.023	2.116	2.048	2.016
70	2.598	1.787	1.965	2.034	2.274	1.969	1.969
80	1.945	1.821	1.956	1.918	2.131	2.058	2.058
90	3.688	1.839	2.026	2.054	2.144	2.010	2.010
100	2.500	1.860	1.932	1.931	2.118	2.100	2.100

Table 3.4: *Convergence rates determined between two successive resolutions, $f2 \cong$ second order forcing*

3.8 Impedance tube

In this section we test the basic elements of an impedance tube with the LBGK model. The applicability of Lattice Boltzmann models to acoustics has been shown in various works, e.g. [15]. An impedance tube is a round or square tube with an inlet on one side and a probe section on the opposite side. Microphones inside the tube measure pressure fluctuations from which attenuation of sound by the probe can be computed. In the experimental realization a speaker is placed at the inlet that emits sound waves with a given frequency. In our simulation setup a pressure boundary is set which varies its signal in time accordingly.

3.8.1 Background: evaluation of data from impedance tubes

We present the basic functionality of an impedance tube with the two-microphone technique as specified in [25]. For this technique, two microphones are installed in the tube. They measure time-dependent pressure signals p_1 (at the first microphone) and p_2 (at the second microphone). First, the cross correlation of p_1 and p_2 divided by the auto-correlation of p_1, $\hat{p}$ denotes the Fourier transform and $\hat{p}^*$ it complex conjugate, has to be computed

$$H_{12} = \frac{\hat{p_2}\hat{p_1}^*}{\hat{p_1}\hat{p_1}^*} \tag{3.17}$$

For microphone positions x_1 and x_2 with a distance $s = x_1 - x_2$ we define transfer functions H_i and H_r

$$H_i = e^{iks} \tag{3.18}$$

$$H_r = e^{-iks}. \tag{3.19}$$

The complex relaxation factor r is then determined via

$$r = \frac{H_{12} - H_i}{H_r - H_{12}} e^{2ikx_1} \tag{3.20}$$

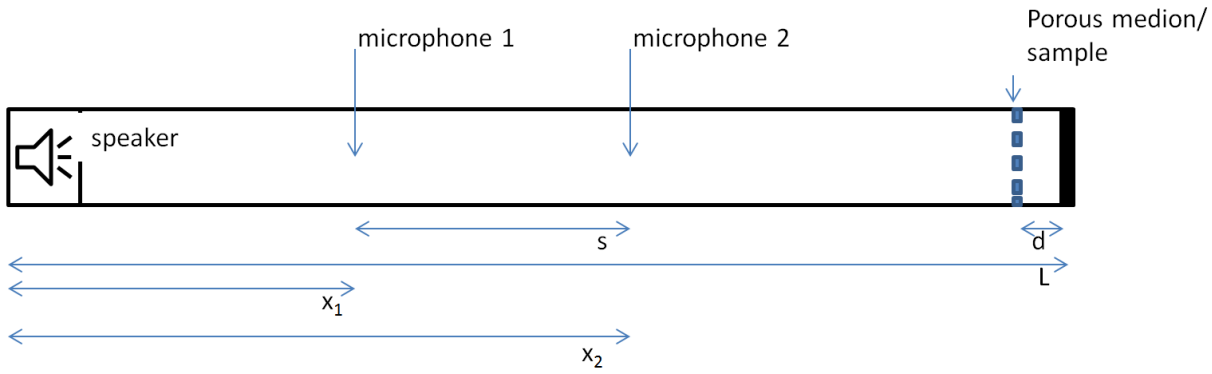

Figure 3.43: *Schematic of an impedance tube.*

Considering a perfect reflection and neglecting damping effects from the finite viscosity of the fluid and the tube's walls, H_{12} is a real function of the wave vector k, the microphone positions x_1 and x_2 and the tube length L

$$H_{12} = \frac{e^{-i2\pi k x_2} + e^{-i2\pi k(2L-x_2)}}{e^{-i2\pi k x_1} + e^{-i2\pi k(2L-x_1)}} \tag{3.21}$$

The absorption factor thus depends only on the phase shift and amplitude ratio between the signals. The amplitude imposed by the speaker does not enter in the formula. Figure 3.43 shows the setup for an impedance tube, including the notation used in the following. In a simulation, this setup corresponds to a periodic box of length L and a very low viscosity such that damping effects due to viscosity can be neglected.

3.8.2 Test of a perfectly reflecting wall

We use the viscosity of air and a tube of $80cm$ length, which is resolved with 1024 grid points. H_{12} is then determined for different wave numbers in the interval of $0.15/m$ to $0.03/m$. We use the LBGK model. The speaker is modeled via a time-dependent pressure boundary condition. A sinusoidal signal is imposed. At the microphone positions x_1 and x_2 the pressure and velocity fluctuations are recorded.
From Figure 3.44 it can be seen that the accuracy is good for the wave numbers studied when H_{12} is small. When the first microphone is located close to an antinode of the standing wave and the signal at this location is very weak, the error increases.

3.8.3 Test of the shift in wavelength due to wall friction

In real-life impedance tubes an outer tube is present. In such a tube two effects occur: The damping of the wave amplitude, and the shift in the wave number. Usually, impedance tubes

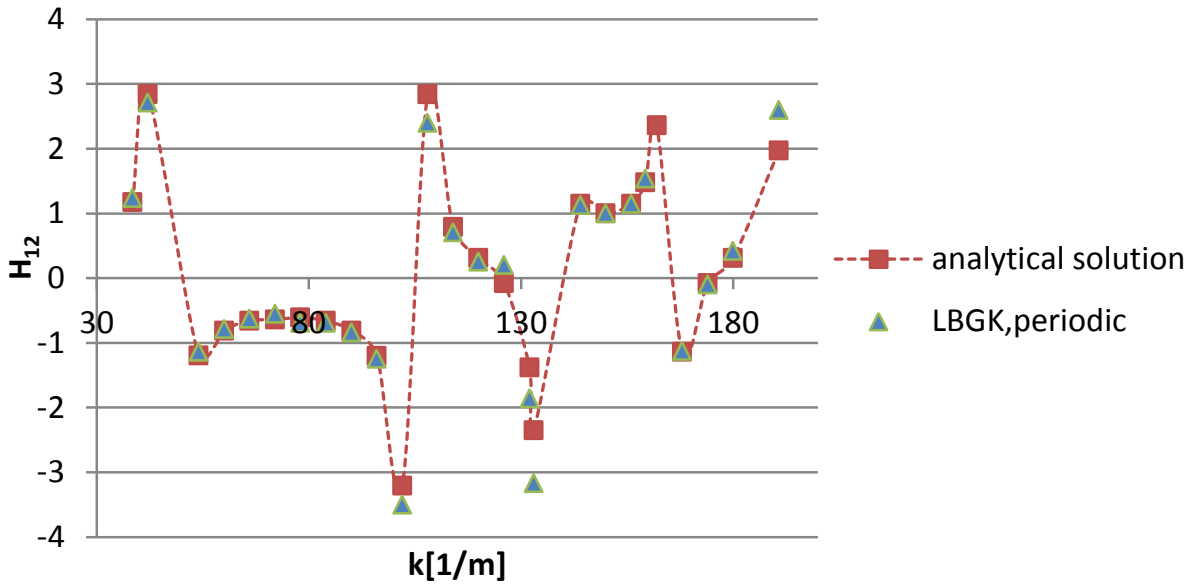

Figure 3.44: *Factor H_{12} for the reflection of sound waves in the impedance tube*

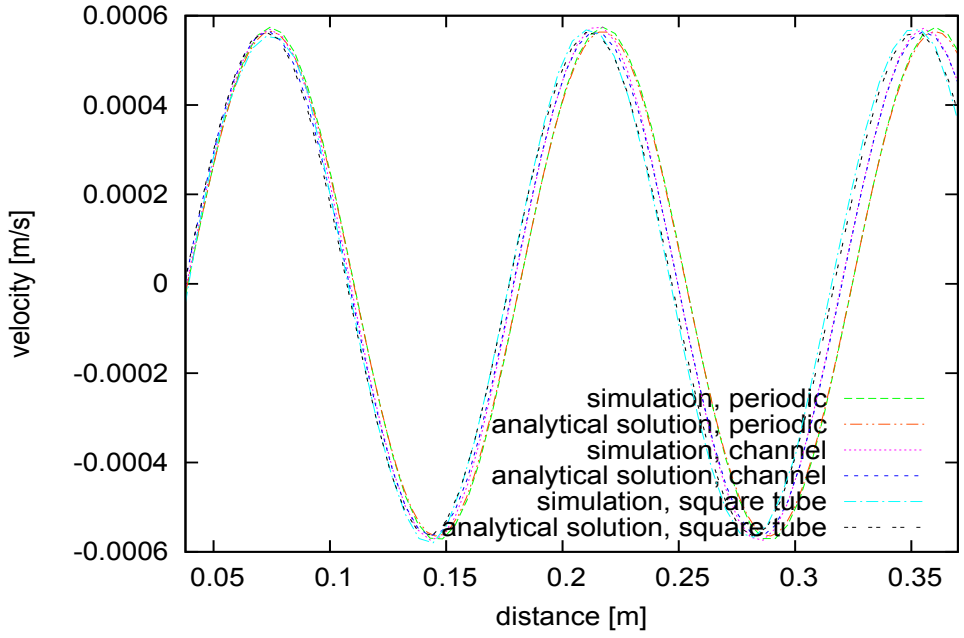

Figure 3.45: *Velocity fluctuations with and without a surrounding tube*

are very slim and the first effect can be neglected. The second effect can be quantified using an equation from [15]

$$c = c_0 \left(1 - \frac{1}{y_1}\sqrt{\frac{\nu}{2\omega}}\right) \tag{3.22}$$

with the speed of sound of an unconfined wave c_0, the viscosity ν, and the angular frequency ω. In two dimensions y_1 is the height of the channel. In three dimension it can be replaced by the ratio of the boundary to the cross section, which is $2h$ for a quadratic cross section with height h. The shift of the speed of sound leads to a modified wave length

$$\lambda = \lambda_0 \frac{c}{c_0} \tag{3.23}$$

In Figure 3.45 the density of a traveling wave with periodic boundaries and solid boundaries for a quadratic tube with $19mm$ diameter is shown. The figure also includes simulation results for a tube which is periodic in one direction and with no-slip boundaries in the other direction and shows the analytical solution for the two cases. We use the same setup as above for a wave number of $7/m$. The shift in the wave length is in accordance with the prediction of the formulas 3.22 and 3.23.
Overall, the LBGK model gives satisfactory accuracy for a reflection of sound waves on solid walls for a range of frequencies and is able to predict the friction effects of the tube walls.

3.8.4 Test with a simple porous medium

As a next step the modeling of an impedance tube with a well-resolved simple porous structure can be undertaken. We consider an impedance tube with a sound-reflecting grid located at a distance of $\lambda/4$ from a reflecting wall. In this case a resonance between the wave reflected at the wall and that reflected at the grid-shaped obstacle occurs. The tube's dimension is $20mm\,x\,20mm\,x\,1m$ and the wave length $\lambda = 10cm$. The simulation results are compared to a simulation with the Finite Element code for acoustics ElPaSo from the "Institut für angewandte Mechanik" (Infam) at TU Braunschweig. This code solves Kirchhoff's equation, which is the wave equation after Fourier transformation of the time domain. Only the converged state is considered. The code does not take a finite viscosity of the air into account, nor does it include wall-friction effects. We thus compare the results for a given wavelength, and not a given frequency. The code has been thoroughly validated, e.g. [93].
For our Lattice Boltzmann simulation we refine the grid near the obstacle. The grid resolution is $[2128\Delta x, 44\Delta x, 44\Delta x]$ on the coarse level. One wavelength is resolved with 212 grid nodes on the coarse level and 424 grid nodes on the fine level. We locate two microphones along the channel axis. The first microphone is located at $0.5m$ from the loudspeaker, the second microphone at $0.55m$ from the loudspeaker. For the present wavelength, both microphones are located in the middle of adjacent antinodes. The Finite Element results predict the same wave amplitude at both microphone positions. The phase difference is π, i.e. the sign of the momentary pressure fluctuations are opposed.

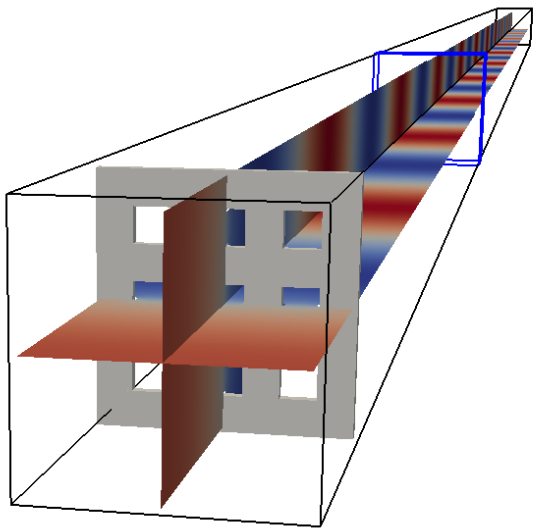

Figure 3.46: *Setup of the impedance tube with obstacle*

The setup is shown in picture 3.46. The obstacle, shown in grey, consists of four bars in the horizontal and vertical direction each. The blue square shows the interface between the two grid levels. Figure 3.47 shows the pressure fluctuations at the two microphones over time. The signal of the second microphone is multiplied by (-1) to better show the phase difference and the difference in the amplitudes. The error in the amplitude is 0.7% and the phase-error is 0.3%. This errors could be due to the finite streamwise extension of the obstacle. The extension is modelled by the FEM code, as well, but not the effect of the wall friction on the fluid passing through the grid's holes.

Next we consider the "off-resonance"-case, in which the wavelength is much larger than the distance between the obstacle and the reflecting wall. We choose $\lambda = 0.2m$. The microphones are further rearranged such that their distance from each other is only a fraction of a wavelength. We choose $x_{M1} = 0.125m$ and $x_{M2} = 0.1375m$ from the inlet. Because different grid resolutions are to be considered, the tube's length is shortened to $L = 0.25m$. Figure 3.49 shows the results obtained for the pressure amplitudes with the code elPaSo by Infam. The phase shift can be either $\pi/2$ or $-\pi/2$, a perfect standing wave is present. This is, however, not what we do observe for the simulation of the pressure wave inside the impedance tube. Figure 3.50 shows the timeline for the pressure oscillations. When the signal first reaches the microphones, it is a regular sine wave, but it gets distorted after it is hit by the reflected signal. The light blue line and the dotted gray line show the signals at the two microphones for a square tube. A finite phase shift is observed. We believe that this phase-shift is due to a damping effect that needs to be reduced if we want to reproduce the results of a non-viscous solver. We thus resimulate the flow field without any lining walls, but in a periodic domain. To reduce the damping effect due to the finite streamwise extension of the grid-obstacle, we reduce its width to $0.3mm$ and $0.1mm$ in our two simulation runs. To resolve the $0.1mm$

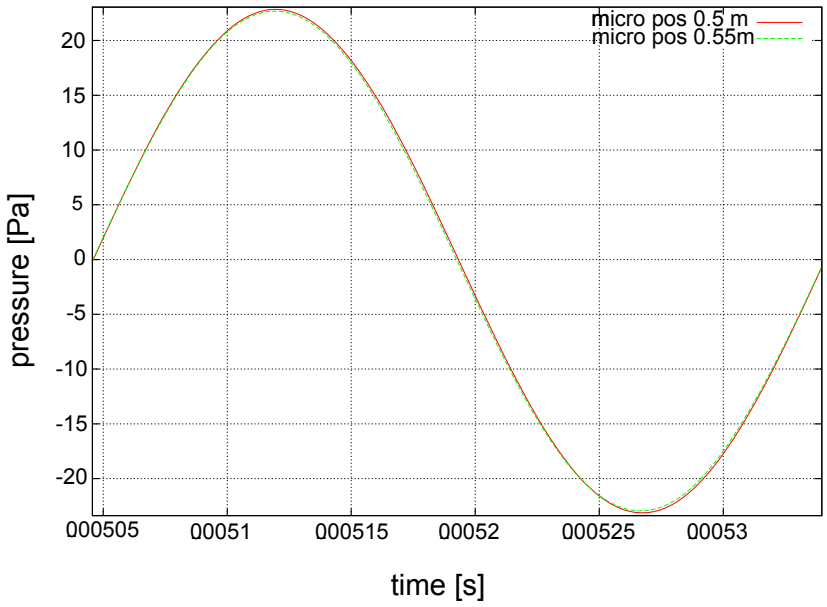

Figure 3.47: *Pressure variations at the two microphones over time, p_2 inverted*

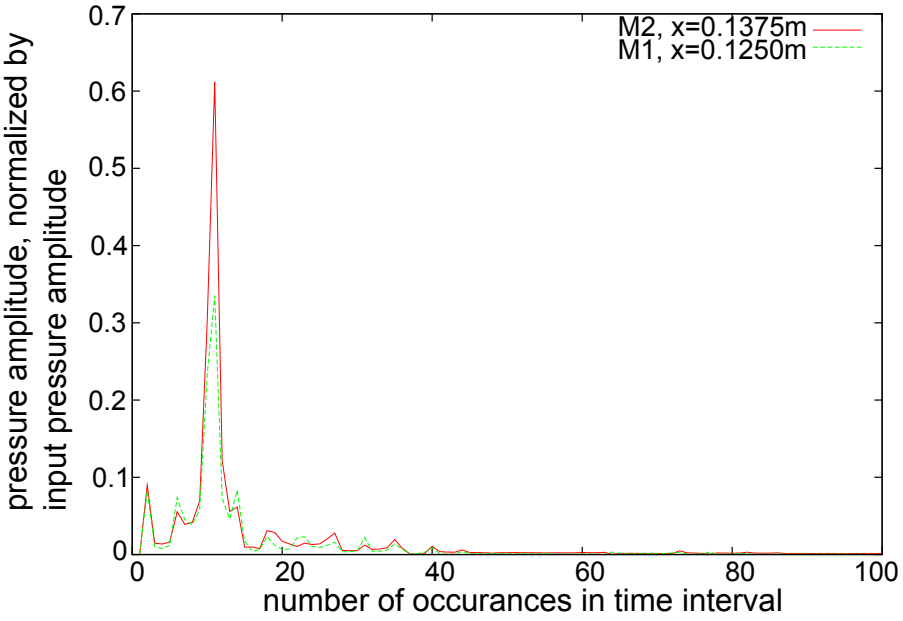

Figure 3.48: *FFT of pressure fluctuations for $\lambda = 0.2$*

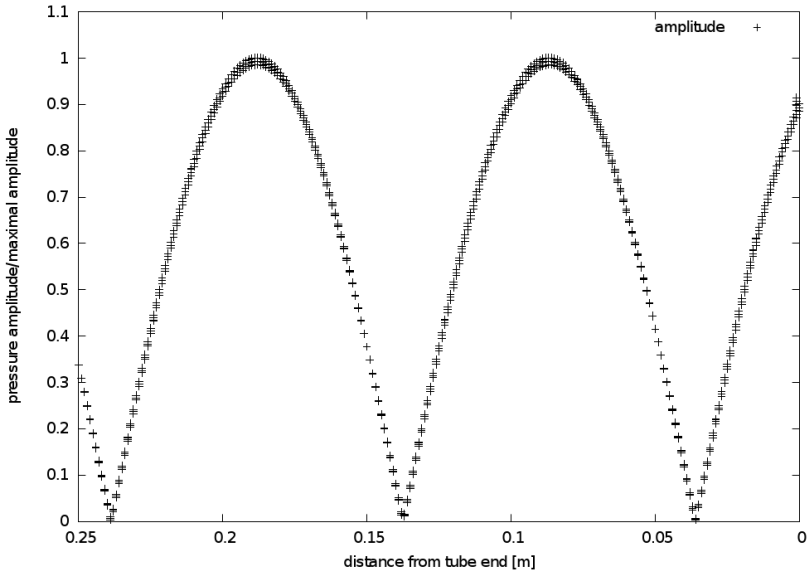

Figure 3.49: *Pressure amplitudes as computed by Infam with ELPASO,* $\lambda = 0.2$

grid-obstacle, the resolution had to be increased to 66 nodes in the cross-directions. The signal is now almost a standing wave. We determine the ratio of the pressure amplitudes for the 66-nodes case to $\left(p_1^*/p_2^*\right)_{LB} = 0.55$ by comparison of the main peak in the Fourier transform. The results of elPaSo are $\left(p_1^*/p_2^*\right)_{elpaso} = 0.54 \pm 0.01$.

We conclude that the resonance case for a simple grid-structured sample porous medium could be reproduced. Because we want to reproduce results from a code which neglects friction, the computational cost is quite high when non-resonance phenomena are to be reproduced. We now have all the building blocks present to study a real porous medium such as those from the laboratory experiments in [104]. The perforated plate studies in that work lend themselves to further study after the idealized setup studied in the present work. For more complex, less well resolved geometries the TRT model with magic parameters [63] is expected to improve the simulation results.

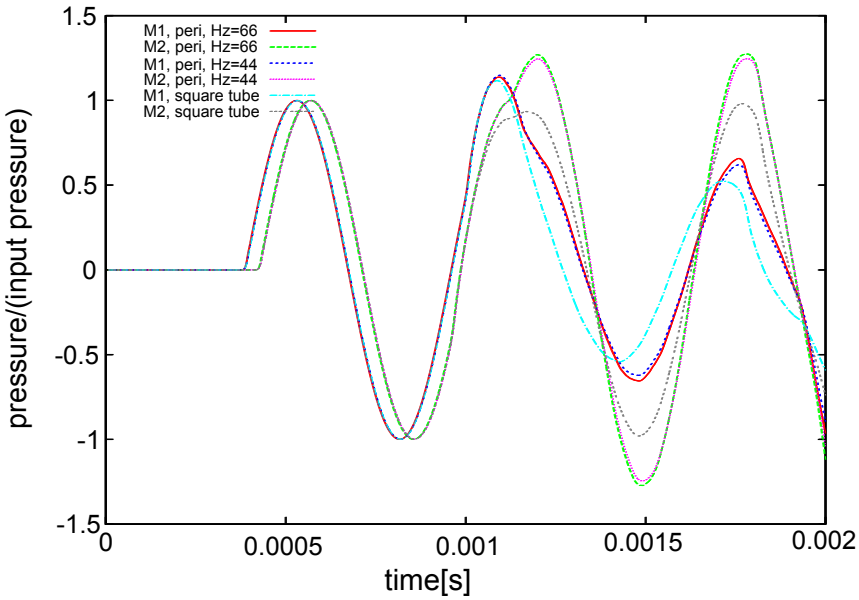

Figure 3.50: *Pressure oscillations over time with and without outer boundaries, two different resolutions,* $\lambda = 0.2$

4 Results

We apply the Lattice Boltzmann method to some complex testcases and compare our results to wind tunnel data. All testcases produce turbulent flows, but of different type. The specific testcases chosen are jet flow, flow around a flat plate and basic modules of the built environment such as a bridge cross section and a surface mounted cube. As an application case, the ventilation of an atrium building is considered.

4.1 Validation of the FCLB method with jet flow

In this section the FCLB method is validated for the turbulent jet. The study has been carried out in cooperation with Dr. Sebastian Geller and can also been found in [56]- A turbulent jet at $Re = 6700$ based on the size of the orifice and the inflow velocity was simulated using the FCLB method with the $D3Q27$ stencil and with the MRT model with Smagorinsky LES and the $D3Q19$ stencil. The simulation results are compared to experimental data from [118]. The section is structured as follows: Firstly, the experimental setup is described. For a description of the nature of the jet flow the reader is referred to the introductory section 2.11.5 where several flow types are presented. The numerical setup is described afterwards, followed by the results of the simulations. Finally, the results are discussed and differences between the results from the two approaches are pointed out.

4.1.1 Experimental setup

The simulations are based on an experiment described in [118]. The properties of a turbulent jet at a Reynolds number of 6760 based on the size of the opening of $4mm$ and on the inflow velocity of $1.69m/s$ were measured using Doppler laser anemometry. The experiment was carried out in a water tank of $6m$ length in flow direction, $0.2m$ width and $0.4m$ height. The tank is open and the jet enters the tank through a nozzle. At the back of the water tank a drain is present to keep the water level constant.

4.1.2 Numerical setup

With the numerical setup we try to mimic the experimental setup as closely as possible . We use the same domain size in horizontal, vertical, and spanwise direction. The same Mach and Reynolds numbers are used. Solid boundaries are modeled by no-slip boundaries. The

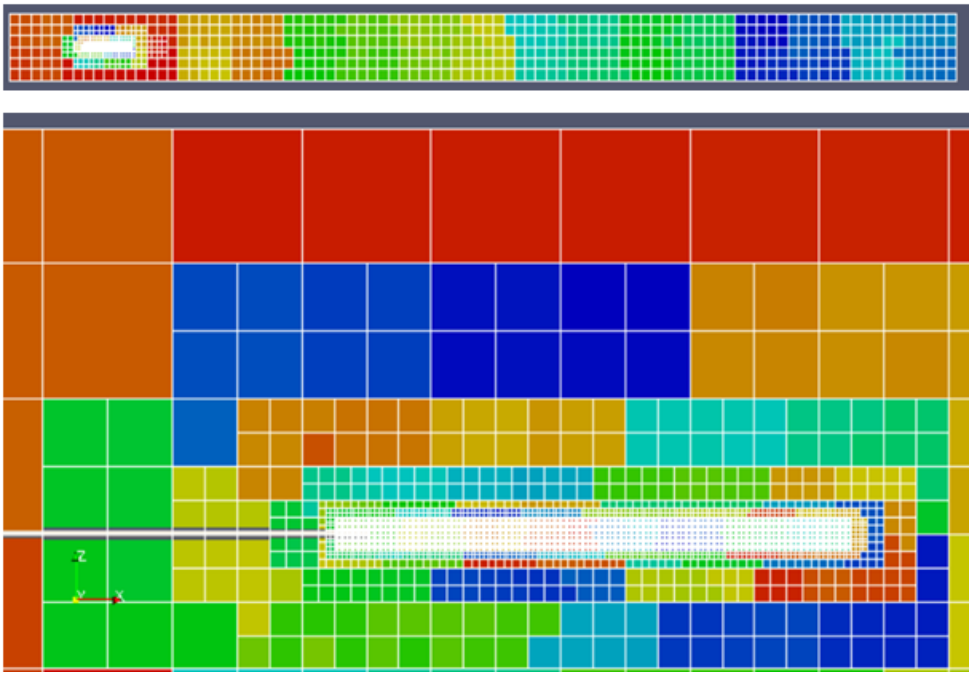

Figure 4.1: *Discretization of the domain for the jet flow simulation, each of the blocks shown contains* 11^3 *nodes. Top view and side view.*

air-water interface at the upper boundary is modeled by a free-slip condition because a free-surface condition would pose a major additional computational expense and the effect of the wave generation is regarded minor. A pressure boundary condition is employed at the artificial outlet instead of the weir outflow used in the experiment. The nozzle was positioned at $0.5m$ from the inlet and approximated as a cylinder with Bouzhidi boundary conditions. Only the flow outside the nozzle is simulated and a velocity boundary condition is used at the end of the nozzle. The velocity across the inflow plane is assumed to be constant. A nested grid refinement scheme was used with seven levels of grid refinement. The finest resolution of $0.0947mm$ is present at the orifice. The grid is then successively coarsened to a resolution of $6.061mm$. The overall number of grid points is 111 million. The time step varies between $0.000103522s$ (coarse) and $0.0000016s$ (fine). The total simulated time was $3.4s$.

4.1.3 Results

We compare the velocity along the axis to the semi-analytical results from [118], the FCLB and the MRT model. Figures 4.2 and 4.3 show a good match for both models. The FCLB model is slightly more successful at reproducing the decay of the velocity along the centerline and the correct spreadwidth for not too large distances from the inlet. For distances larger than approx. 7mm the MRT model give better results, but this may be due to insufficient averaging time. The reasons for the deviations observed for the MRT results may be due to the drawbacks of the Smagorinsky model. The excessive eddy viscosity might delay

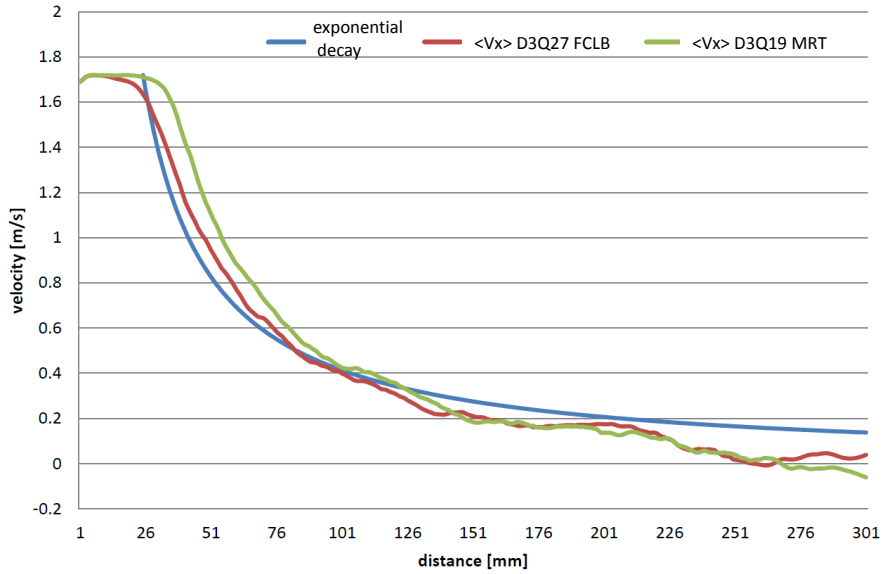

Figure 4.2: *Velocity profile of the jet along the main axis*

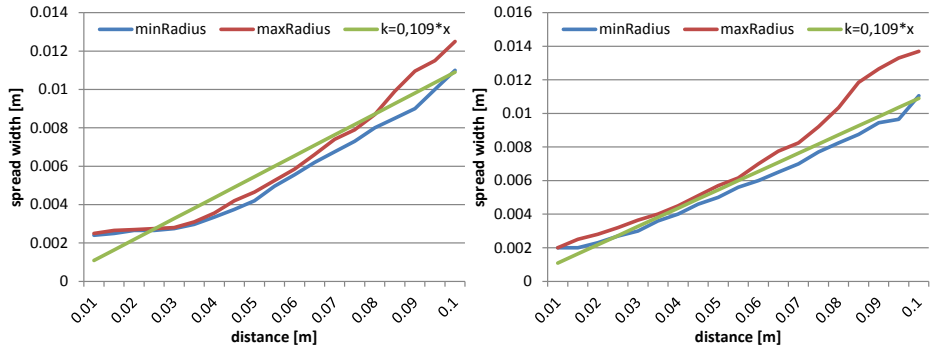

Figure 4.3: *Spreadwidth of the jet over the distance from the opening, left: D3Q19 MRT, right: D3Q27 FCLB*

the transition to turbulence in the mixing layer, leading to a lower slope of the spreadwidth close to the nozzle and to an offset in the velocity profile. Picture 4.5 gives a qualitative idea of the behavior of the flow. Immediately behind the opening the flow field is laminar. As eddies develop in the mixing layer between jet and surrounding flow, the jet widens. In Figure 4.4 the velocity contours normal to the jet axis are depicted. For the *MRT* model a deviation from it original, circular form can be observed. This effect shall be investigated in more detail for a laminar jet.

4.1.4 Circularity of a laminar jet for different collision models

The non-circularity of the flow is investigated further. It may be due to either the collision model or the velocity stencil of a combination of both factors. The *D3Q27* MRT model is in-

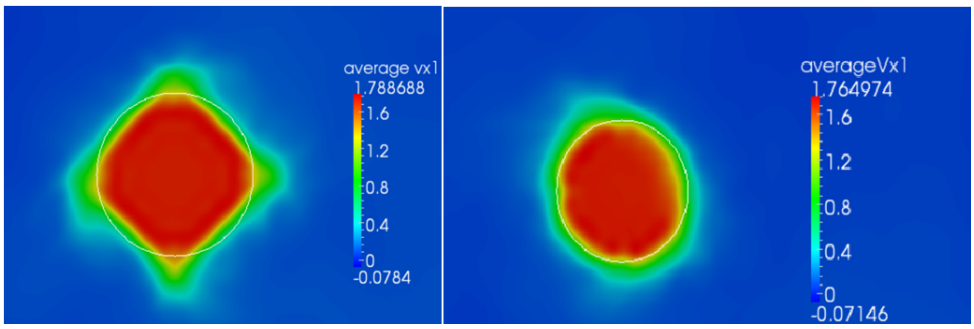

Figure 4.4: *Distortion of the circular jet for the D3Q19 MRT and D3Q27 FCLB models*

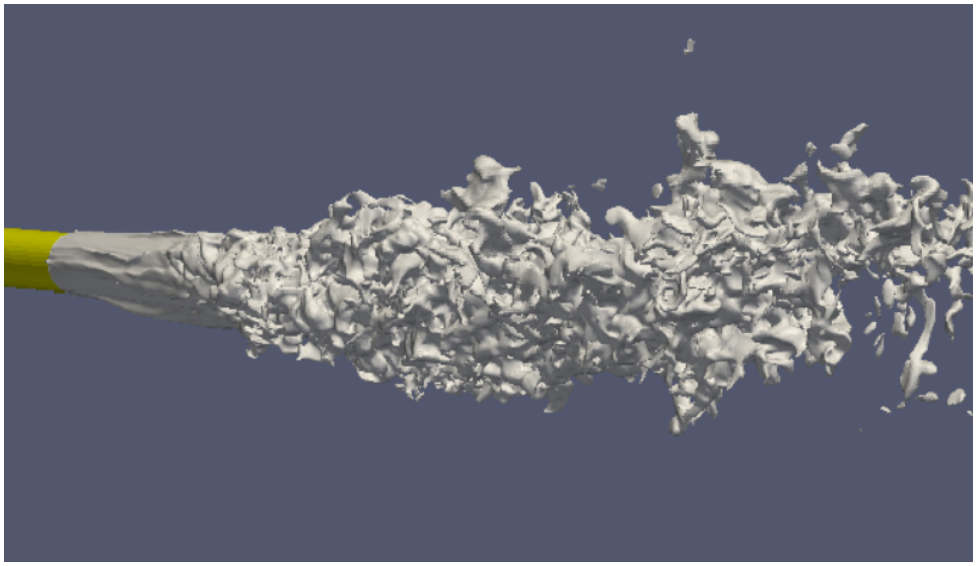

Figure 4.5: *Velocity contour of the D3Q19 MRT jet flow at* $0.5 m/s$

cluded in the investigation as a link between the $D3Q27$ cascaded model and the $D3Q19$ MRT model. For this we simulate the laminar entry section for few timesteps at a lower Reynolds number and using a uniform grid with different models and compare the deviation from circularity. In addition to the $D3Q27$ cascaded model we use the $D3Q27$ MRT model and the cumulant model. For the cumulant model three different sets of collision factors are used.

Contours of the velocity in flow direction for the five different models are shown in Figure 4.6. The results obtained with the FCLB model for the relaxation set 0 were identical to those obtained with the cumulant model. We observe that the stencil is not the sole reason for the non-circularity of the flow as the shape differs for the three models and even depends on the collision factors chosen. The flow velocity is $1m/s$, the viscosity is the viscosity of water, the domain is square, $0.4m$ wide with periodic boundary conditions. We measure the velocity field $0.09m$ behind the orifice after $100\Delta t$ which should minimize the influence of the domain shape. The domain is resolved with 60 grid points. The size of the orifice is $0.05m$. This corresponds to eight grid points only. As a consequence the orifice itself deviates from its circular shape. Bouzhidi boundary conditions are used for the nozzle.

We do not go more into detail, as the problem is similar to that of the frozen-in peak and the square duct flow, that have been presented in earlier sections. Nevertheless, it could be shown that a complex dependence of the flow shape on the stencil, but also the collision model and collision factors exist. Interestingly, for the case of the duct flow the most accurate behavior is observed for the $D3Q19$ models. Two reasons come to mind to explain the different behavior for the different testcases. Firstly, the duct flow was laminar and simulated with a comparatively high viscosity. This means that higher-order terms are comparatively small compared to the low-viscosity case and some additional terms may start to play a role for the testcase of jet flow that have not been relevant for the duct flow. Secondly, the alignment of the coordinate system for the duct flow computations of the present work is favorable for the $D3Q19$ stencil. This advantage is lost partly for the jet flow where no confinement corresponding to the shape of the stencil is present.

4.1.5 Conclusions

The results from experiment [118] can be reproduced with good accuracy. The decaying of the axial velocity is in good agreement with the semi-analytical solution. the solution from $D3Q27$ factorized cascaded model matches the semi-analytical results better than the $D3Q19$ LES model. In the domain 10 cm behind the nozzle the spreading functions are comparable with the empirical function. Near the nozzle the velocity profile of a cross section matches well with the Gaussian function given by theory. One important aspect is that the $D3Q19$ LES model shows anisotropy whereas the $D3Q27$ factorized cascaded model has no such defect. The smaller stencil is not the sole reason for this. An investigation of a laminar jet points to the collision model and specific choice of relaxation parameters as a source of

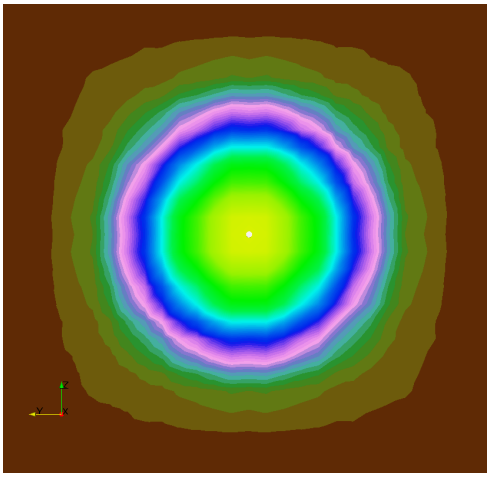

(a) D3Q27 cumulant, set 0

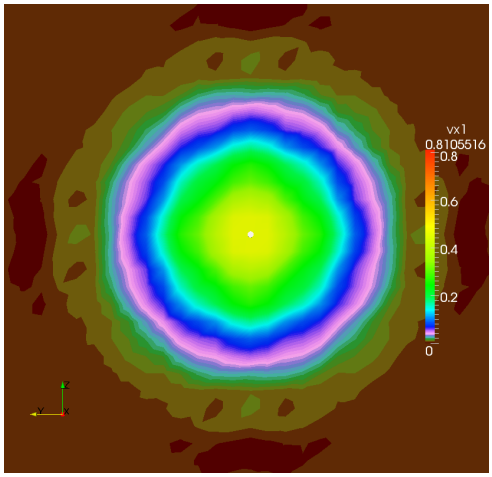

(b) D3Q27 cumulant, set 2

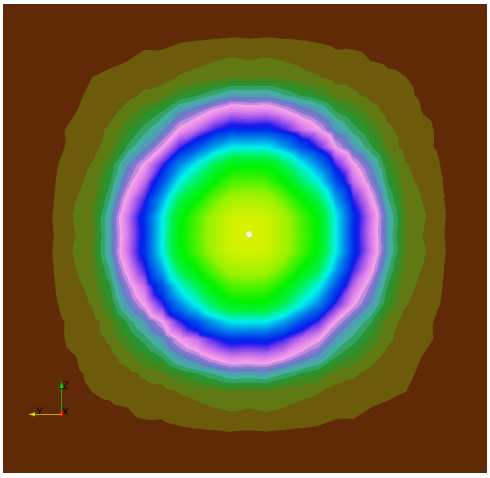

(c) D3Q27 FCLB, set 0

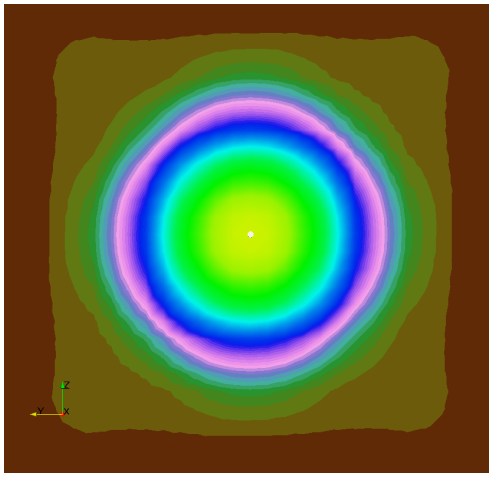

(d) D3Q27 MRT, set 0

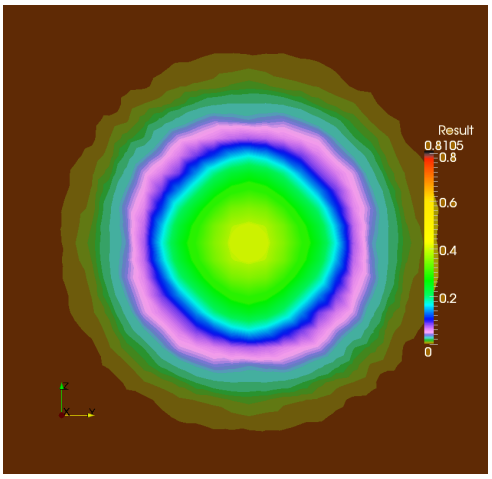

(e) D3Q19 MRT, set 0

Figure 4.6: *Test of jet circularity, velocity for the MRT D3Q19 model, set 0, the D3Q27 MRT set 0, FCLB set 0, cumulant, set 0 and cumulant, set 2*

the anisotropy. We conclude that the Lattice Boltzmann method is suitable for jet induced subcritical flows even with a simple turbulence model (LES). Better results are obtained for the FCLB model.
Further investigations could include the noise generated by a jet.

4.2 Flow around a flat plate

4.2.1 Introduction and setup

The flat plate turbulent boundary layer is a standard testcase in CFD, e.g. [31], but it has rarely been studied with LBM. With DNS and LES techniques the transition from laminar to turbulent flow can be examined. In contrast to fully developed turbulent channel flow, the boundary layer has a finite thickness, outside of which the flow remains undisturbed. We simulate flow around a flat plate with a setup matching the experimental one a closely as possible. The experiment was carried out at the low-noise wind tunnel of the Institute for Fluid Dynamics at the TU Braunschweig (ISM). It is a small low speed wind tunnel with dimensions 600 x 400 x 1500 mm^3 and an open recirculation region (Eiffel type) with a closed test section. Velocities can be measured using Particle Image Velocimetry (PIV). For this case a flat plate of size (1.05 cm x 40 cm x 1m) was positioned in the wind tunnel at an angle of attack of 0°. The Mach number of the flow was about $Ma = 0.05$, which leads to a Reynolds number of about $Re = 10^6$ based on the plate's length. A rigged ribbon was attached to the upper front edge of the plate to trigger turbulence. We were provided with the exact dimensions of the ribbon, such that it could be included in the numerical setup. From the PIV measurements mean velocity profiles are available as well as turbulent fluctuations of the streamwise and vertical component of the velocity at a distance of $1m$ from the front edge along a line normal to the planes surface. Pictures 4.7 and 4.8 show photos of the experimental setup. The turbulence intensity of the incoming velocity is very low ($Ti < 0.1\%$). In the numerical setup it was assumed to be zero. The simulation was carried out on the department's cluster Ludwig on 640 CPU cores. The simulation parameters are shown in Table 4.1. Figure 4.9 shows the computational grid. Each of the cells shown contains 10^3 grid nodes.

The simulation time was $0.48s$ starting from a uniform distribution of the velocity of $u_{in} = 17m/s$. Averaging started after $0.32s$. The simulation was carried out using the $D3Q19$ MRT model with Smagorinsky LES. A near-wall damping was introduced at the points closest to the upper surface of the plate. For grid points closer than $2.3mm$ to the plate's surface, the Smagorinsky number was reduced by 10%. For wall-adjacent points the Smagorinsky number was reduced to 10% of its original value. Based on the experimental data a value of $u_\tau = 0.6679m/s$ was assumed. This leads to a distance of $y+ = 4.2$ between the boundary and the first node and $y^+ = 8.4$ in the near-wall region. The Smagorinsky model is purely dissipative. It is a well-known observation (e.g [98]) that the standard Smagorinsky model is unable to predict transition in a boundary layer over a flat plate. The flow remains lami-

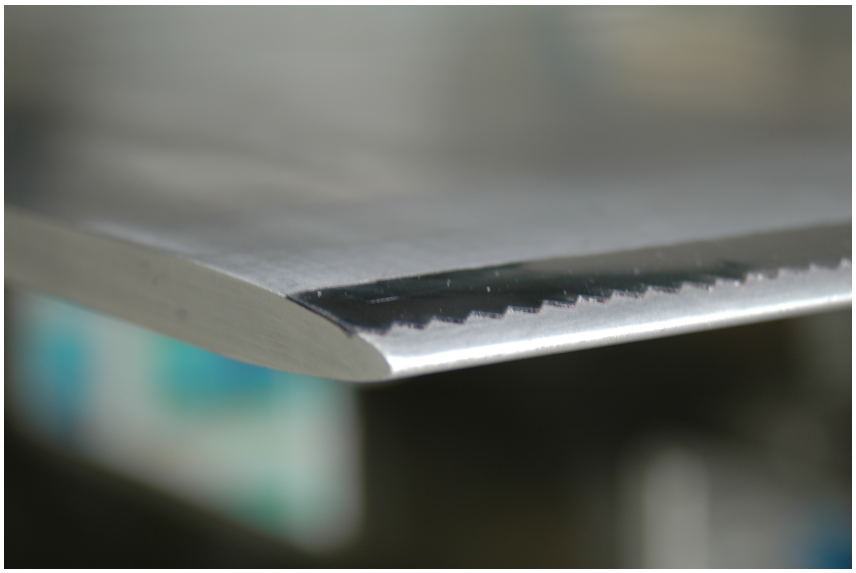

Figure 4.7: *Photo of the ribbon on the plate*

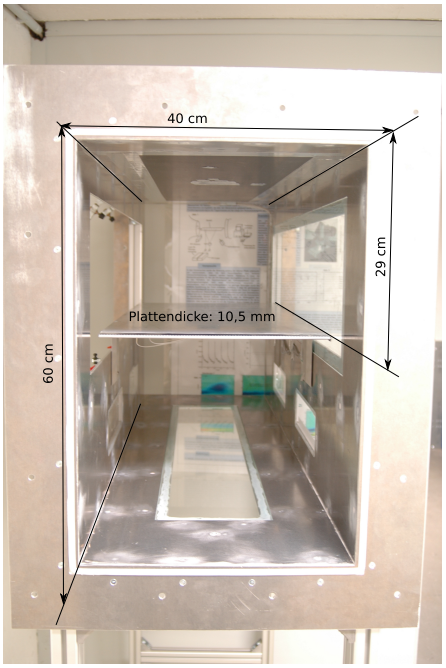

Figure 4.8: *Experimental setup for the flat plate at ISM*

parameter	value
Re	$1.13 \cdot 10^6$
u_{in}	$17 m/s$
Δx_{fine}	$0.000234283 m$
Δt_{fine}	$3.98e-7 s$
Level	4
domain length (x)	$2.25 m$
domain width (y)	$0.0825 m$
domain height (z)	$0.6 m$
length of the plate	$1 m$
number of nodes	235 Mio
Smagorinsky constant	$0.17-0.18$

Table 4.1: *Simulation parameters*

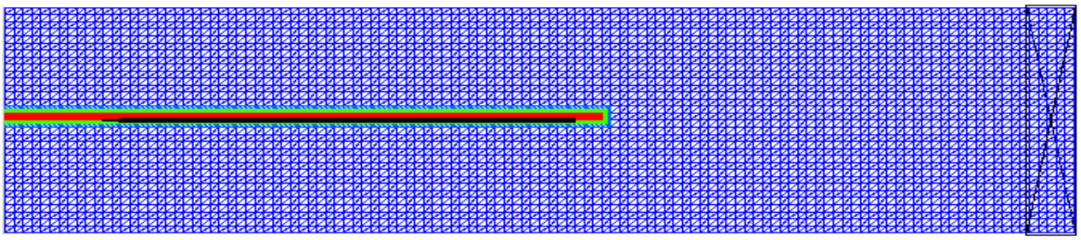

Figure 4.9: *Grid for the simulation of flow around a flat plate, each square corresponds to* 10^3 *nodes*

nar unless strong perturbations are present. In our case such a perturbation is given by the rigged ribbon.

4.2.2 Results

The agreement of the simulated mean velocity with the experimental data is satisfactory as shown in Figure 4.10. The first grid node is located $0.13 mm$ from the plates surface. At this first node the velocity is underestimated by 7%. An underestimation of the near-wall velocity is to be expected for low grid resolution in a turbulent boundary layer, as has been observed in sec. 3.2. The error then quickly dimuinishes and the velocities match the experiment within in measurement uncertainty for a distance of $4 mm$ or more off the planes surface. A further source of errors are the PIV measurement devices that are fixed on a horizontal beam a few centimeters above and behind the plate and were not modelled. Picture 4.10 visualizes the streamwise component of the instantaneous velocity field around the plate. Note how the turbulent boundary layer develops on the upper surface of the plate due to the existence of the ribbon. Figure 4.12 shows the RMS-fluctuations of the streamwise component $\sqrt{\left\langle u_x'^2 \right\rangle}$, the horizontal component $\sqrt{\left\langle u_y'^2 \right\rangle}$ and of the Reynoldsstress $\sqrt{\langle u_x' u_y' \rangle}$. The

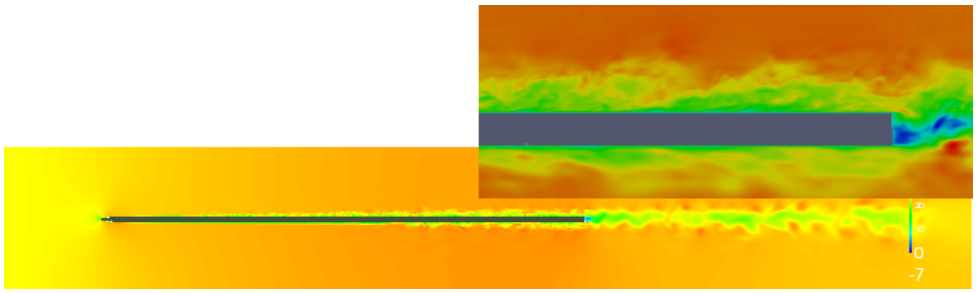

Figure 4.10: *Visualization of the flow field around the flat plate with a close-up of the rear edge*

offset for $\sqrt{\langle u_x'^2 \rangle}$ appears to be due to pressure fluctuations. We observed that it is larger for smaller averaging times and expect it to vanish for very large averaging times or improved boundary conditions. Picture 4.13 shows a snapshot of the vorticity of the flow around the plate. The approaching flow is laminar. Two-dimensional tube-like vortical structures then develop. They form wavelike-patterns in stream-wise directions, which then break up into irregular patterns.

4.2.3 Conclusions

An LES simulation with near-wall damping has been carried out for flow around a flat plate. The mean quantities were matched well, and also the RMS values are in accordance with the experimental data. For the flow-wise component pressure-waves led to an offset in the RMS-values. To lower the overall simulation time non-reflecting boundary conditions could be used at the outflow. The simulation is currently being repeated at the ISM with different porous inlays near the rear end of the plate. One hopes to gain insight into how the porous surface influences the boundary layer and, eventually, the noise generated by the turbulence. To this end we plan to simulate some of the more coarse-grained inlays.

4.3 Flow around a surface mounted cube at Re=126000

4.3.1 Introduction

For a validation of turbulent flow around a bluff body a surface mounted cube simulation will be conducted. Similar benchmarks have been studied thoroughly for various CFD applications. These range from a Re=5000 DNS study [177] to RANS simulations [89] at Re=40000, including Lattice Boltzmann LES results from [87] and [170]. For this testcase experimental data exists for comparison ([108]). The complex nature of the flow field makes this testcase particularly interesting and challenging. Separation occurs at the front edge of the cube, reattachment at the rear edge and in the wake. Vortex shedding can be observed behind the cube

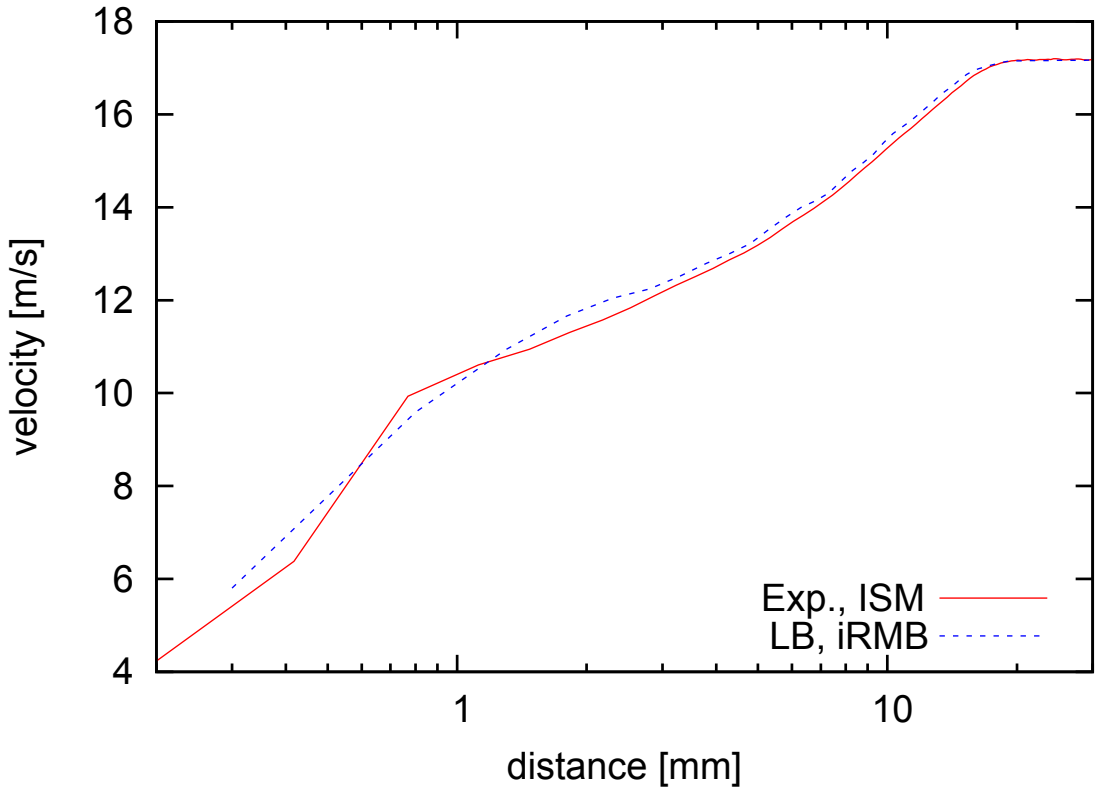

Figure 4.11: *Mean velocity for a line perpendicular to the plates surface*

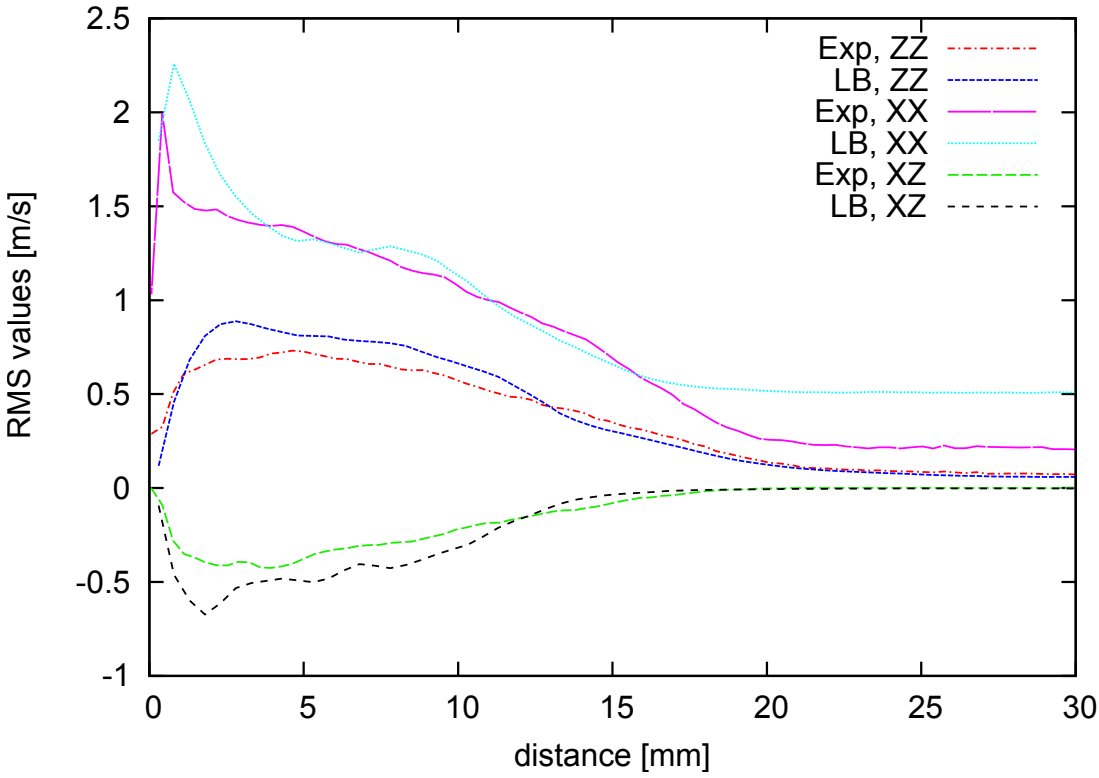

Figure 4.12: *RMS values for a line perpendicular to the plates surface*

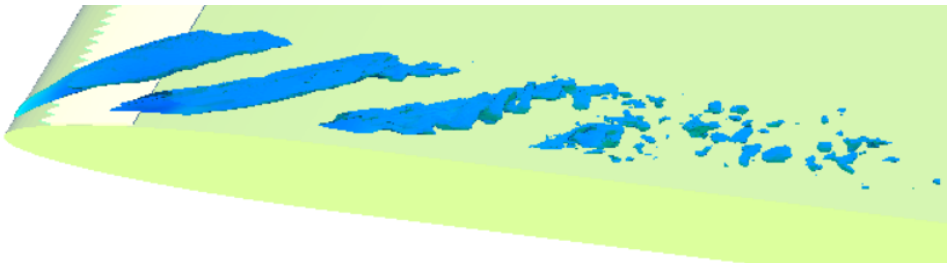

Figure 4.13: *Isosurface of the vorticity around the flat plate*

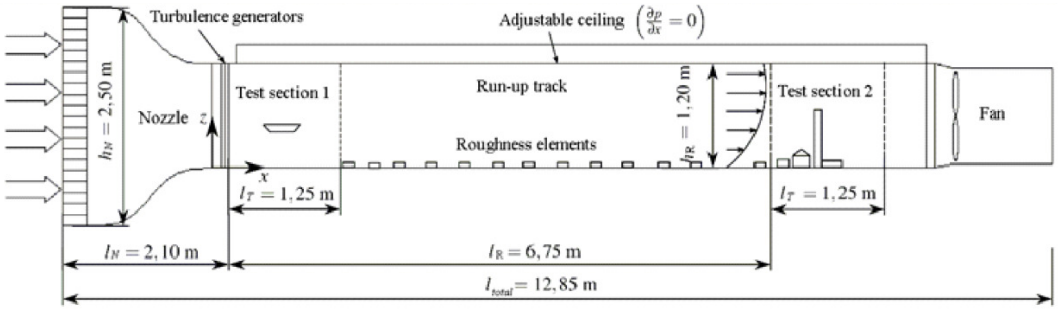

Figure 4.14: *Schematic of the BLWT at the Institute for Steel Structures (from [19])*

and stationary vortex systems exist. We compare the c_p values on the surface of the cube to experimental values. c_p is the dimensionless pressure coefficient and is defined as

$$c_d = \frac{p_o - p(x)}{\rho U^2} \tag{4.1}$$

4.3.2 Experimental setup

We compare simulation results to wind tunnel data from the Institute for Steel Structures at the TU Braunschweig (IS). They operate a boundary layer wind tunnel (BLWT) of open suction Eifel type. It is driven by an axial fan. The turbulent boundary layer is produced by an arrangement of spires in the entrance-section and roughness elements in the run-up track. Figure 4.14 shows a schematic of the BLWT. It is $1.2m$ high, $1.4m$ wide and $12.85m$ long including the fan. The experimental data used in this study was obtained as part of a measurement campaign on interference effects of power houses on slender chimney structures, where the cube represents the building without chimney. Details about the related measurements, the properties of the turbulent boundary layer and the BLWT in general can be found in [19].

4.3.3 Numerical setup

The $D3Q19$ Smagorinsky MRT model was tested on the basis of wind channel data for the surface mounted cube. The approached flow in the wind tunnel can be well approximated

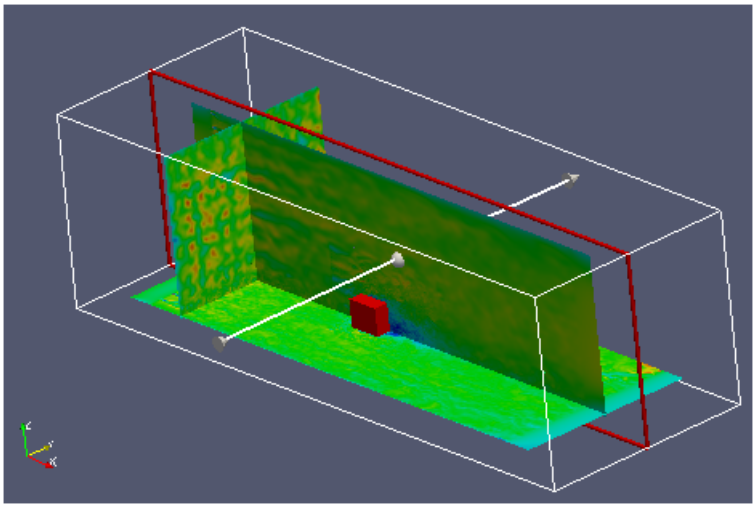

Figure 4.15: *Computational domain around the cube, the instantaneous velocity is shown in the background*

using a logarithmic curve. The turbulence intensity of the approached flow in the experiment varies between 10% and 26% depending on the distance from the bottom surface [19]. Figure 4.19 shows the velocities of the approacing flow that were measured in the wind tunnel. The green line shows the velocities that were prescribed as the inflow velocity for the simulation. The flow has a Reynolds number of 126000 considering the height of the cube and the mean wind speed of the approaching flow at the height of the upper edge of the cube. The setup can be seen in figure 4.15. The blockage ratio is the same as in the wind tunnel.

The mean pressure has been measured at different points on the surface of the cube. The turbulent inflow was generated using a grid consisting of equidistant vertical and horizontal bars. The inflow length was considerably shorter than in the experiment and the turbulence intensity was lower (around 7%). The grid and the bottom was refined with two levels of grid refinement, while four levels were used around the cube. Each level doubles the resolution. Figure 4.16 shows a close-up of the grid around the cube. Each of the squares depicted contains $6x6x6$ grid points. A yet more detailed view 4.17 shows the nodes at the two finest grid levels at the back edge of the cube. The behavior of the velocity at the grid interface is illustrated by coloring the grid with the intantaneous velocity. Using the inflow velocity profile as a reference, the y^+ value at the boundaries for the finest grid level are around $y^+ = 5.5$. Peak values computed from the time-averaged values near the boundaries may be up to three times as high, but values in the stagnation zones in front of the cube and on most of the cubes surface are lower, as fig. 4.18 shows. This was the highest resolution that could be reached on the present hardware when the simulations were conducted in 2011. It is also not clear, to which extend the $y^+ = 1$-criterion is relevant for flows that do not resemble a non-boundary layer flow, such as the flow around the edges of the cube.

The overall number of nodes was 103 million with five different grid levels. The simulation takes four days on 200 CPUs. The simulated time is roughly $0.5s$ or 100 000 coarse time steps.

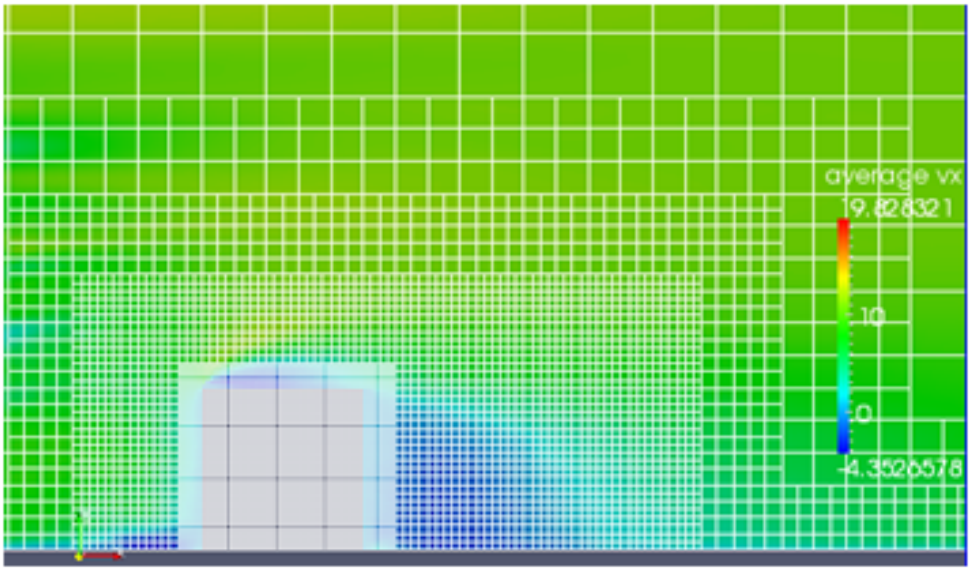

Figure 4.16: *Grid (blocks:*[6*x*6*x*6]*) around the cube, background: mean flow field from left to right*

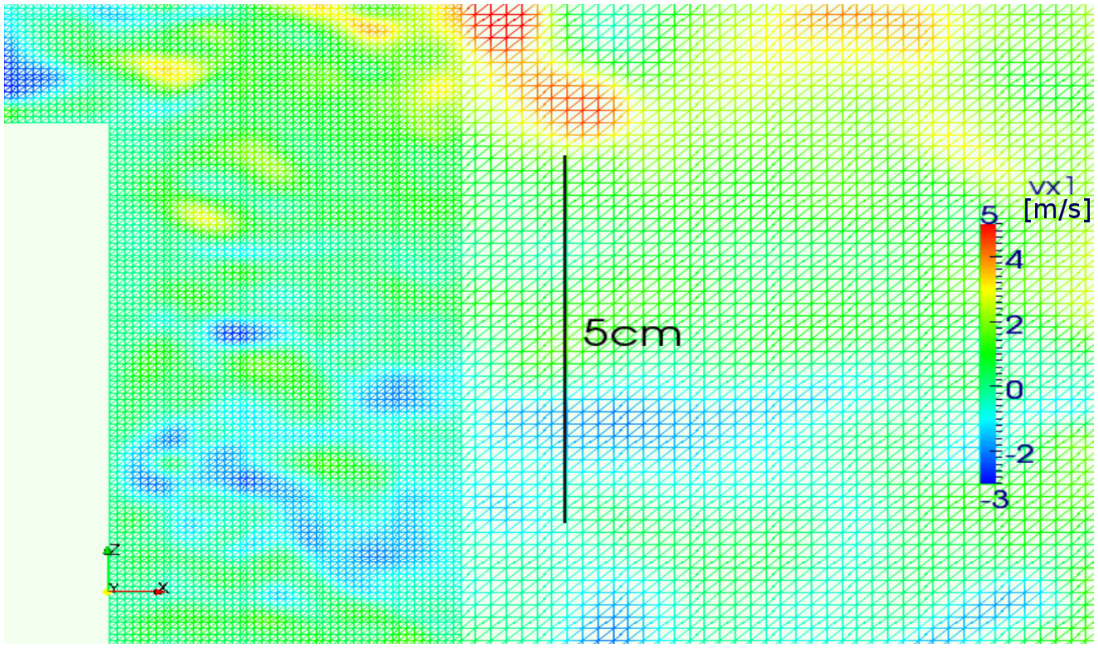

Figure 4.17: *Grid(nodes) around the cube, colored by instantaneous velocity from left to right*

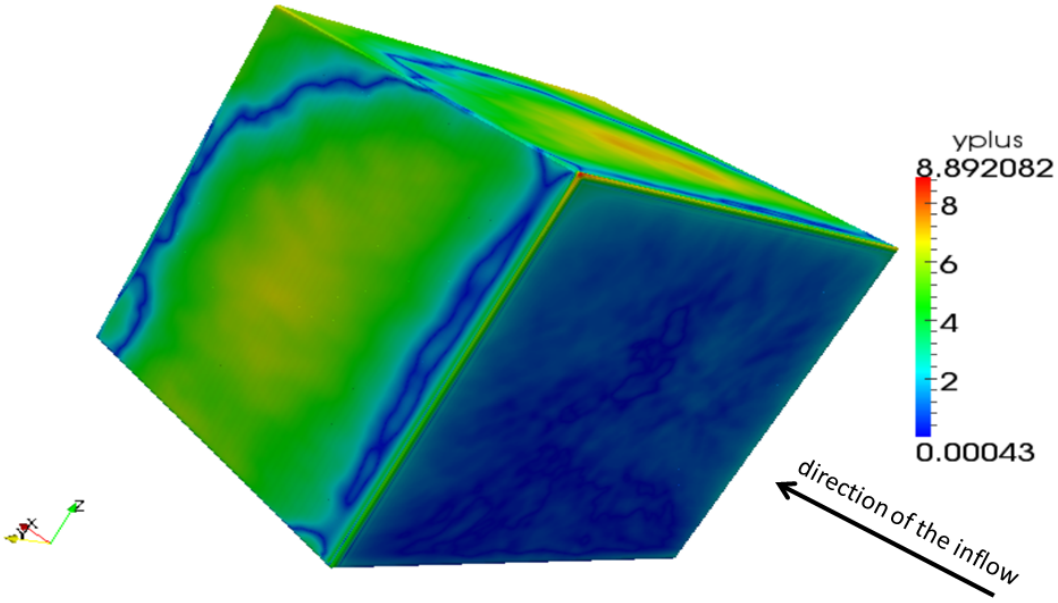

Figure 4.18: y^+-*values for the boundary nodes of the cube computed from the velocity at these nodes*

The average is computed from instantaneous values between $t = 50000\Delta t$ and $t = 100000\Delta t$. This corresponds to an averaging interval of roughly 2.5 turnover times based on the height of the domain, or the largest possible size for the eddies and the far-field velocity of $12m/s$.

4.3.4 Results

We start with a qualitative comparison of the velocity profile to literature results. After that the c_p values from the simulation are compared to those obtained in the experiment described above. A graphical representation of the streamlines corresponding to the experimental data was not possible, so we compare with established literature results. Care has to be taken, because those results were obtained with a slightly different setup. In particular, a lower Reynolds number ($Re = 40000$) and higher blockage ratio was used. Figure 4.20 shows the time-averaged streamlines around the cube as computed with the D3Q19 MRT model using the standard Smagorinsky model. The top, front and the two rear-vortices can be seen. The position and extension of the vortices is similar to their position for the experimental data, in spite of the differences in the setup. The inflow profile was similar. There is no secondary vortex in the immediate wake of the cube, but such a structure was observed in several numerical studies, see e.g. [87]. Note that the extend of the main rear vortex is similar to that of the $Re = 40000$-setup, while it is usually overestimated by underresolved LES-simulations. Figure 4.21 shows streamlines for experimental data for comparison. Apparently there are some discrepancies between the setups, such as blockage ratio, inflow profile, and Reynolds number. Nevertheless the qualitative match between the numerical streamlines and those from literature is satisfactory. The satisfactorily estimated length of

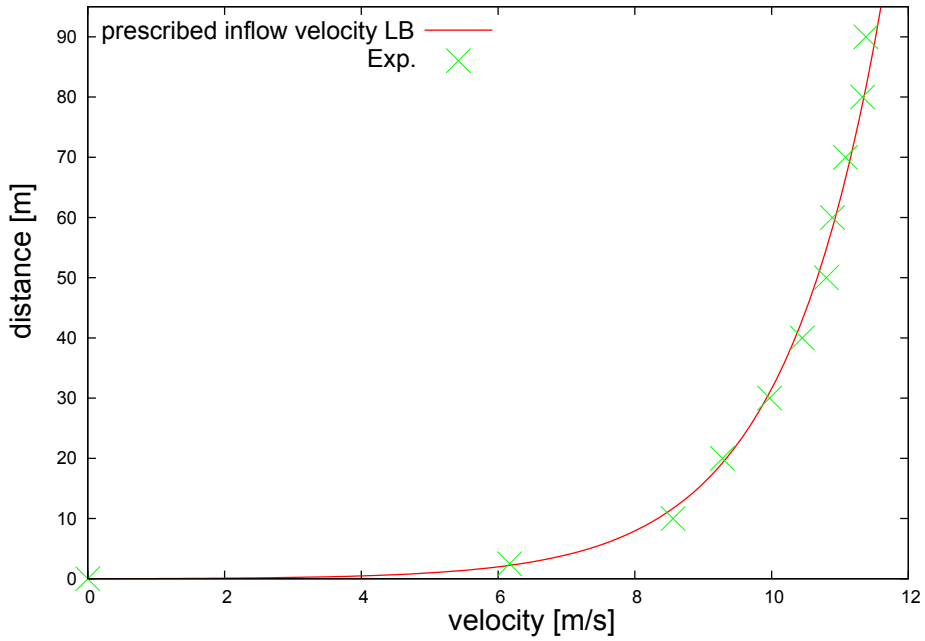

Figure 4.19: *Inflow velocities in the wind tunnel*

the recirculation zone points to an appropriate resolution. For the experiment of the IS no such data was available. It was not possible to determine the recirculation points for the current Reynolds number due to limitations in the experimental setup. Later measurements of the velocity at certain points were carried out, which did not match our simulation data well. We attribute this to differences between the experimental setup and the numerical setup. Roughness elements were present in the experiment even in the vicinity of the cube, but not in the numerical setup. While we used a constant-pressure boundary condition as outlet, a rotating fan was present in the experiment. There are also considerable measurement uncertainties if small velocities are to be measured with a pressure probe (TFI Cobra). These differences are less relevant for the pressure values on the object's surface. In the following we compare the c_p-values along different lines on the surface for IS-measurements and our simulation data.

Figures 4.22 to 4.24 show the Cp-values on the surface of the cube. The pressure values at the edge of the cube, especially the top front edge, are highly dependent on the resolution. For too coarse a grid the pressure differences will be overestimated. With the resolution used, the c_p values are quite accurately reproduced. Some discrepancies are present on the top surface of the cube, where the experimentally determined pressure minimum occurs at a larger distance from the front of the cube.

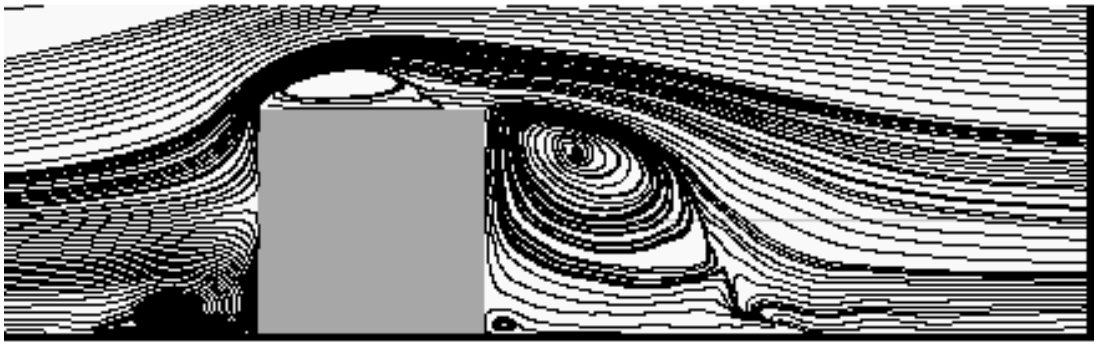

Figure 4.20: *Time-averaged streamlines obtained from the simulation*

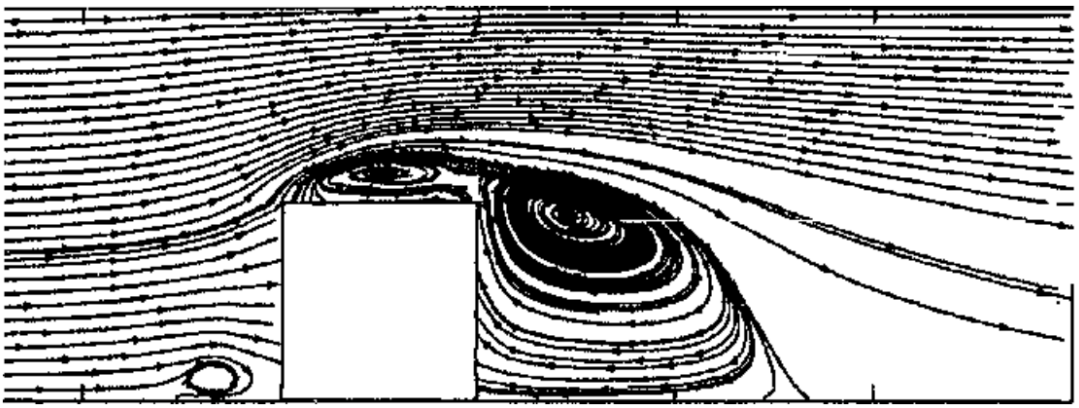

Figure 4.21: *Streamlines from experimental data obtained by Martinuzzi, [108]*

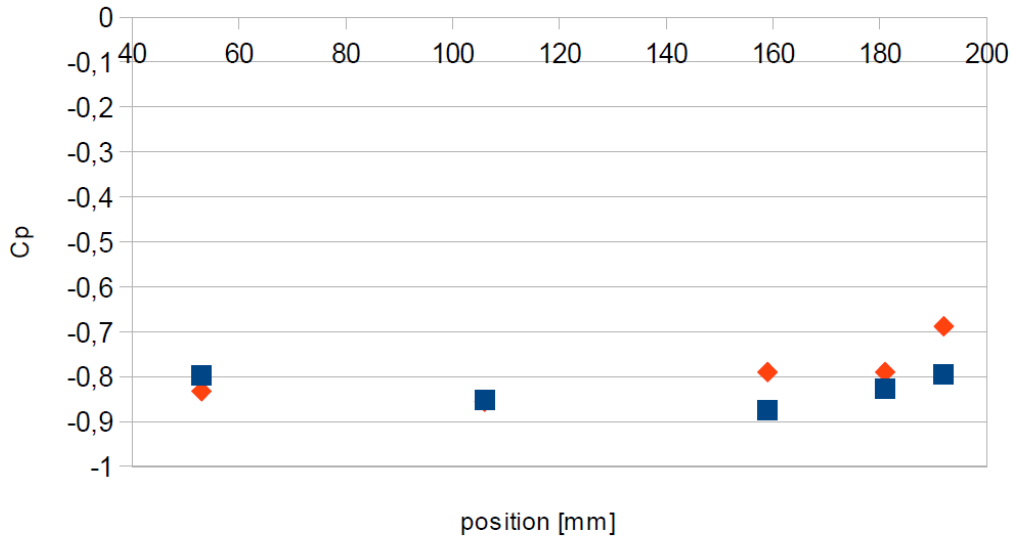

Figure 4.22: *Cp values along the side of the cube*

4.3.5 Conclusions

Overall, the Lattice Boltzmann model with Smagorinsky LES is successful at modeling flow around a surface mounted cube at $Re = 126000$. It reproduces the pressure distributions on the cubes surface well. The qualitative behavior of the flow could only be compared to slightly different experimental data which are matched reasonably. The quality of the simulation could be improved by a better model of the incoming turbulent boundary layer. The cubes that generate a grid-type turbulent field model the actual conditions only very roughly. Instead, an auxiliary simulation as discussed in section 3.4 or a recycling technique could be used.

4.4 Study of a bridge profile

4.4.1 Introduction

The Great Belt bridge was chosen as the object of study for turbulent flow around a bridge profile. The bridge, which is located in Denmark, has a width of 31m and a height of 4.34m. Wind channel data and numerical data are available for comparison [11]. Particularly, many 2D (usually RANS), simulations have been conducted for fluid-structure interaction, such as e.g. [11]. They conducted a flutter analysis and could reproduce the values determined in rescaled wind tunnel experiments. Nevertheless in 1998 large wind-induced oscillations were observed on the Great Belt bridge deck [94]. This shows the need for continuous development and evaluation of more elaborate CFD approaches. As has been shown in [147], 2D simulations have difficulties in reproducing the correct drag value for the Great Belt Bridge

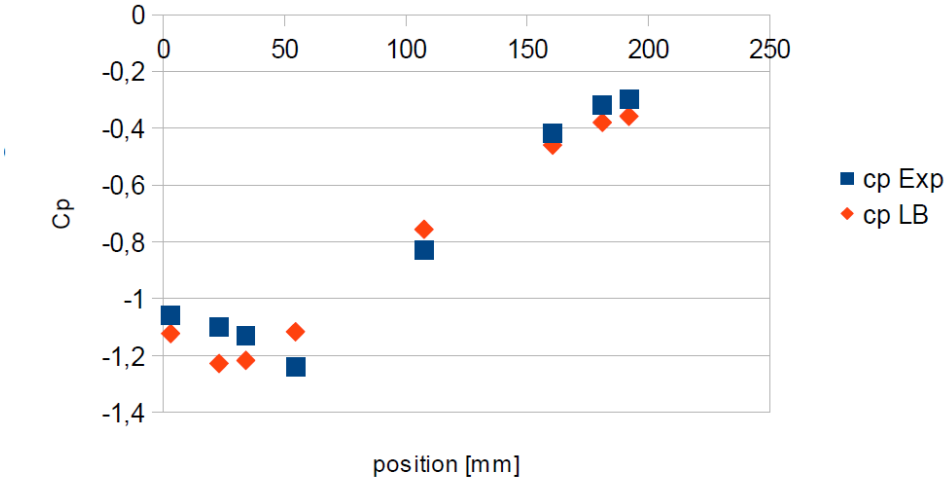

Figure 4.23: *Cp values on the top of the cube*

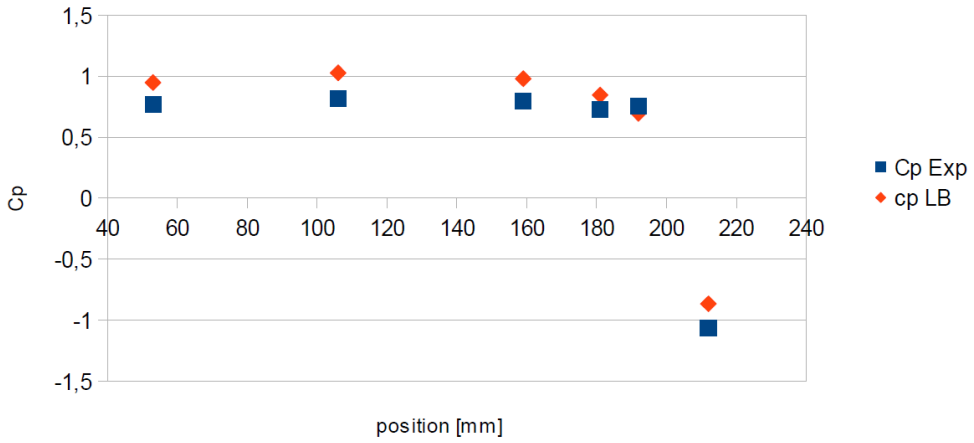

Figure 4.24: *Cp values in front of the cube*

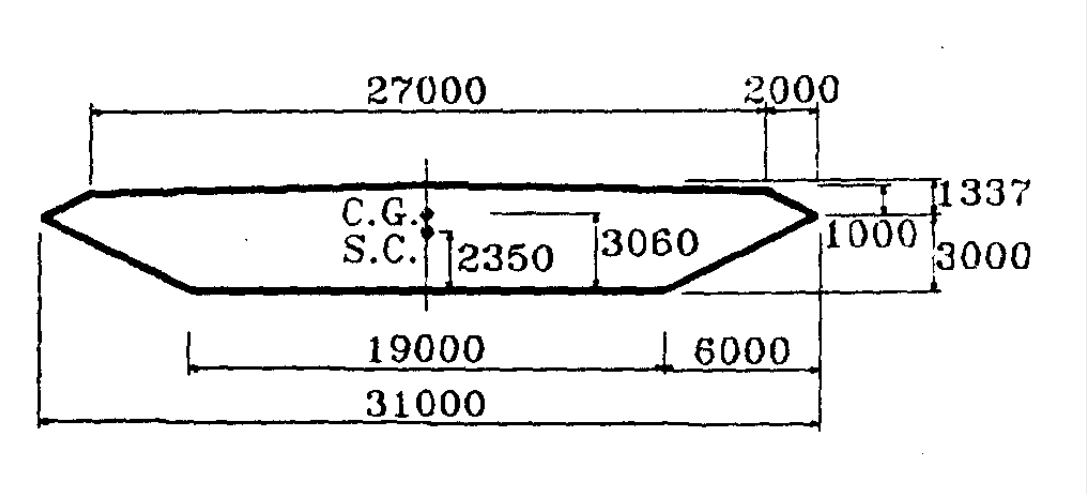

Figure 4.25: *Geometry of the full scale Great Belt East Bridge cross section. Dimensions are given in mm. (from [169])*

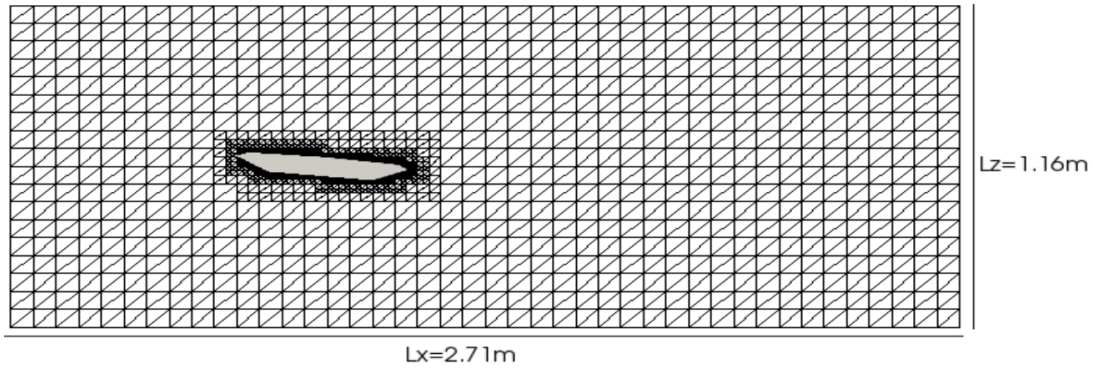

Figure 4.26: *Computational domain (shown here for the blocks)*

approach span while 3D simulations are more accurate. They can be tuned, e.g. by adjusting the Smagorinsky constant [13], but 3D simulations still seem more reliable. We therefore study the 3D flow across a rescaled extruded bridge cross section which has been studied extensively both numerically and experimentally during the design phase. A fixed cross section wind tunnel experiment was carried out by [133] for a Reynolds number of 100.000 based on a 1:80 model. Different angles of attack were examined. We concentrate on the 6° case and compare our simulation results to their experimental data.

4.4.2 Setup

We study the 1:80 model of the extruded bridge cross section as shown in 4.25. Figures 4.26 and 4.27 show the grid used for an inflow angle of 6°. One box contains [6x6x6] grid nodes.

We use the MRT collision model with a $D3Q19$ stencil and the ''all-to-one''-set of relaxation parameters (see Appendix 5.3). Furthermore, a nested time stepping technique is used, so

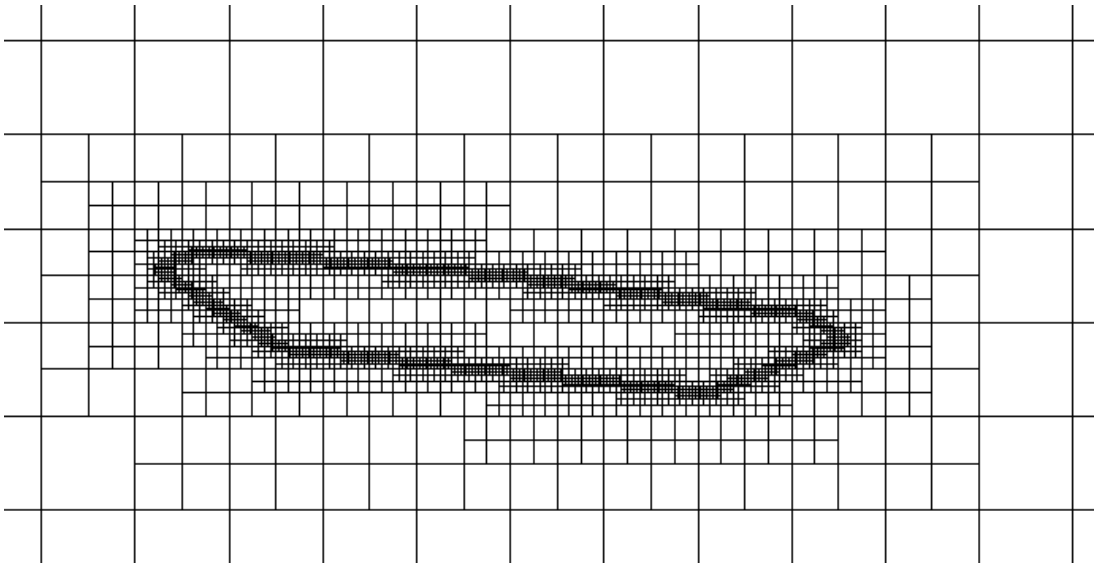

Figure 4.27: *Close-up of the grid around the bridge. Note that we display only blocks, where each block corresponds to 63 nodes*

the grid spacing and the time step decrease by a factor two with each level of grid refinement. The grid spacing at the bridge surface was 0.33mm based on the bridge model or 2.64cm based on the full bridge. At the middle of the lower side of the bridge, where the flow is of boundary-layer type, this corresponds to a y^+-value of about 5.0 at the first grid node and $y^+ \approx 15$ at the second node. Similar values were found for the upper bridge deck. As we apply the van Driest damping only at the wall adjacent nodes, that means that on average, we apply the van Driest damping only in the viscous sublayer and part of the buffer layer ($y^+ < 30$). In most of the logarithmic region in which $y^+ < 100$ and where the van Driest Damping takes relevant values, only the standard Smagorinsky model is used. The total number of grid nodes is 32 Million. The simulation on 192 CPU cores took approximately four days to compute a real time interval of approximately three seconds. Periodic boundary conditions were used at the top and the bottom as well as in span-wise direction. At the inlet a constant velocity of 10.1m/s was prescribed. The domain was [40,2,17] times the bridge's height. Second order accurate (Bouzidi) boundary conditions were used to account for the curved and inclined surfaces. For the Smagorinsky constant we used a value of $c_s = 0.18$.The c_p value on the bridge surface is recorded.

4.4.3 Results

The pressure on the surface of the bridge is compared to wind tunnel data of [133] as well as simulation results by other researchers. For Re=45.000, literature data for a 3D LES simulation exists [148]. Recently, another 3D Smagorinsky LES Simulation for the Great Belt bridge was carried out [148], but no Cp curve was published. We thus carried out simulations for the Reynolds number Re=45.000. For higher Reynolds numbers considered, e.g. Re=100.000,

the grid chosen turned out to be too coarse, and pressure jumps at the recirculation points disturbed the pressure distribution. For the far-field velocity v_∞ and pressure p_∞ we use the values at the inflow and outflow respectively. As can be seen from a comparison of Figures 4.29 and 4.28, the pressure distribution on the upper surface is reproduced quite accurately and matches the experiment more closely at the front of the bridge than other simulations. Due to the large blockage ratio, the velocity around the bridge was slightly higher than the inflow velocity. We assume that the pressure drop at the bottom of the bridge was underestimated because the velocity at this height was larger than it would be in free stream. When the blockage ratio was increased further with the domain height 11 times the bridge's height, the pressure drop increased to $C_p = -0.8$. When the spanwise direction was reduced by a factor of four, the pressure drop at the front edge decreased only by around 5%. A decay of the pressure on the upper trailing edge by around 10% was observed for the reduced span. The C_p curve on the lower surface was almost identical for the two setups. This is in agreement with [148], who studied spanwise extension of vertical structure around the bridge for Reynolds numbers in the range of Re=2.000 to Re=15.000 for an angle of attack of 0°. They propose that for higher Reynolds numbers the extension of the spanwise structure continues to decrease and simulations with a very small spanwise extension should be accurate for Re>55.000.

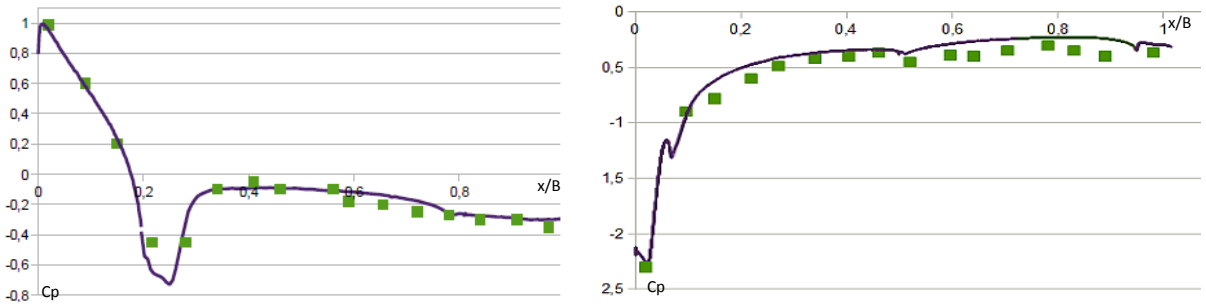

Figure 4.28: *Simulation results for the Cp curve, dots: literature results for the section model, line: LB simulation results*

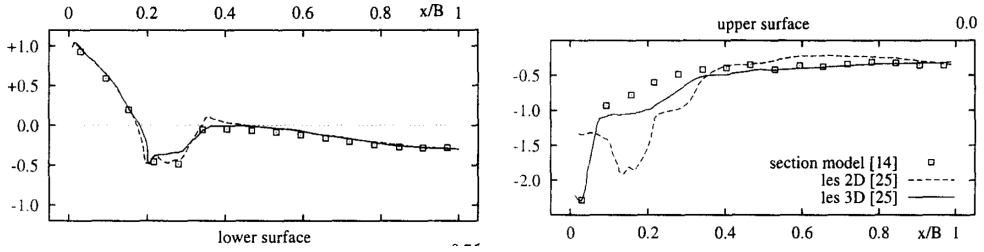

Figure 4.29: *Literature results for the Cp curve (image by Bruno et al. 2003),dots: section model [133], dotted line 2D, solid line 3D (both Selvam, [147])*

The vortex shedding mechanism can be observed clearly from the instantaneous and mean vorticity field: small vortices form at the upper front of the bridge and the lower corners and

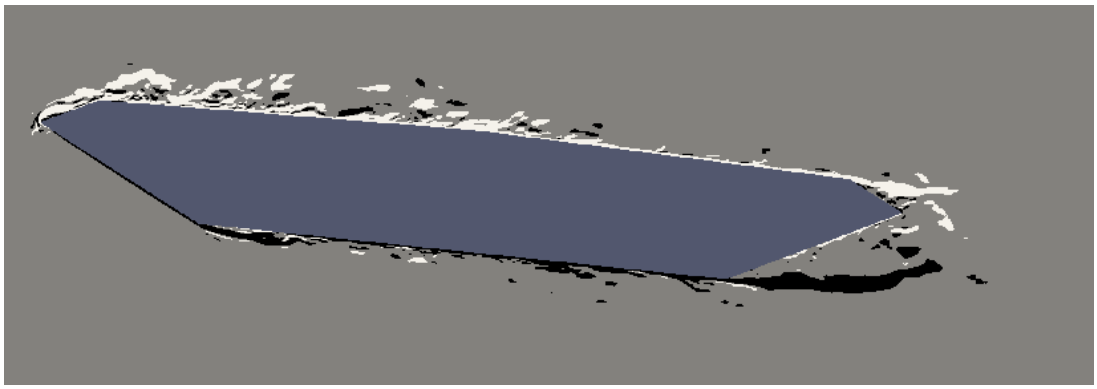

Figure 4.30: *Instantaneous vorticity (white represents clockwise and black counterclockwise rotation)*

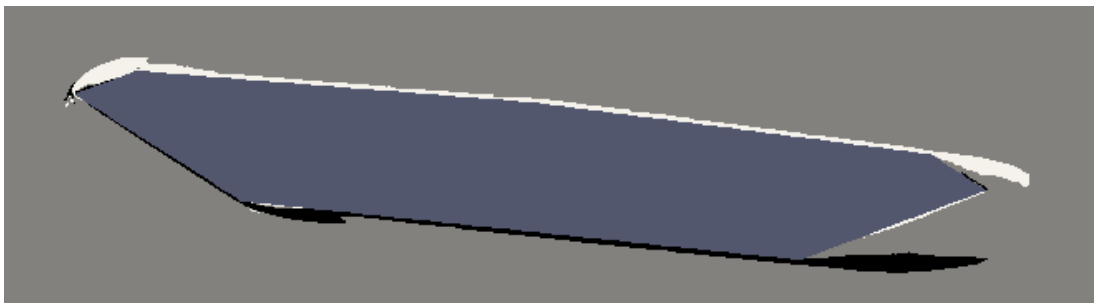

Figure 4.31: *Time-averaged vorticity (white represents clockwise and black counterclockwise rotation)*

are advected downstream. As expected the vorticity shows peaks near the bridge surface, at the recirculation areas at the front edges, and in the vortex shedding region behind the bridge. Figure 4.30 shows a snapshot of the instantaneous velocity field around the bridge and the induced vortex shedding behind the bridge can be observed. The time-averaged vorticity is shown in Figure 4.31.

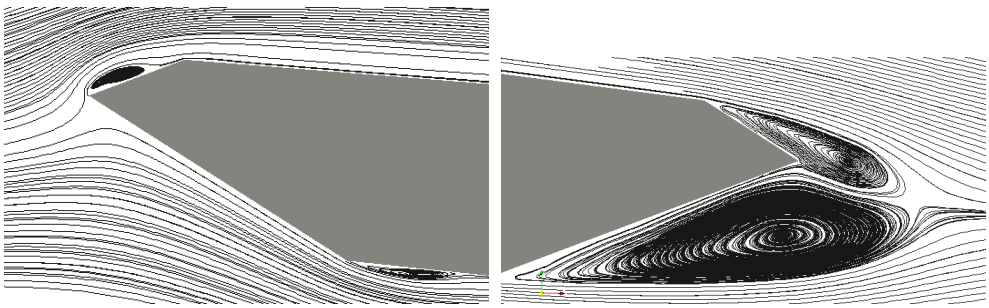

Figure 4.32: *Stream lines of the time-averaged velocity field in front (left) and behind (right) of the bridge*

We conducted a simulation with a much coarser, uniform grid and a streamwise extension of 4.6 times the bridge's height. In that case we saw large vertical structures develop. These are not as tube-like as those shown in [148], but bend in vertical and streamwise direction, see Figure 4.33. Another difference is that the fluctuation are large in the region above the tilted

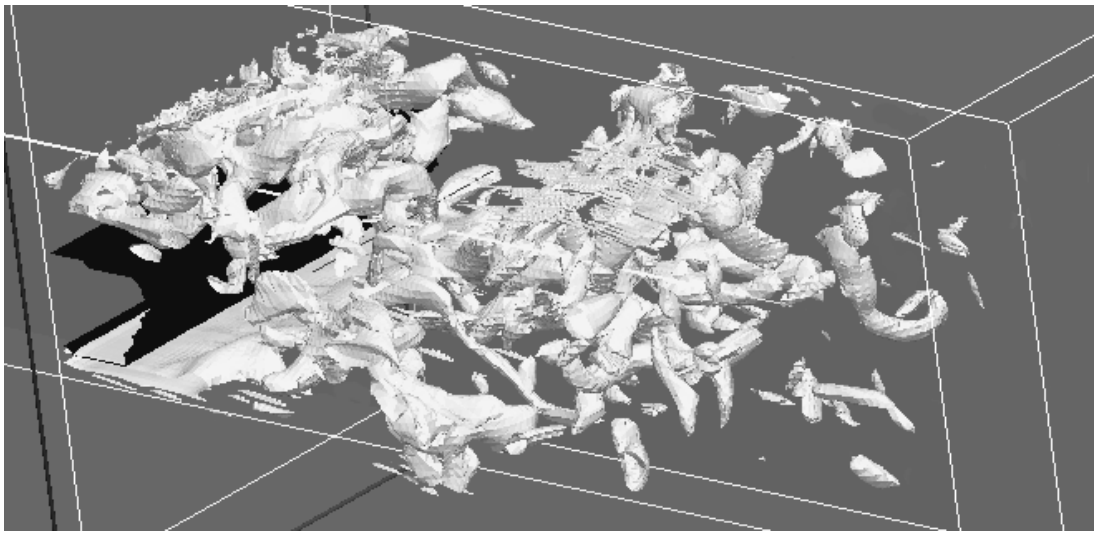

Figure 4.33: *Contours of the instantaneous vorticity for a width* $H_{span} = 4.6 D_{Bridge}$

bridge deck, as can also be seen in Figures 4.30 and 4.31. This is probably because we use an angle of attack of 6°, whereas they use an angle of attack of 0°. Accordingly, in our setup the bridge shows properties of a bluff body rather than a streamlined body.

4.4.4 Conclusions

We evaluated the behavior of the MRT Lattice Boltzmann method with a Smagorinsky LES model in 3D for the Great Belt East bridge cross section. The Cp curves for an incidence angle of 6° match the wind tunnel data satisfactorily. The pressure on the top surface is reproduced well, while it is underpredicted at the leading edge of the bottom surface. We attribute this to the increased blockage ratio used in the simulation. Additional simulations have shown that the results deteriorate when the blockage ratio is increased further, but are rather insensitive to a change of the spanwise extension. Overall, we conclude that the use of the Lattice Boltzmann model is feasible for simulations of turbulent flow around rescaled bridge deck models. To date, these computations still require substantial computational resources. Yet, LBM codes for GPU clusters already exist [103] and 3D codes including grid refinement for the GPU are under development. With these new technologies one will soon be able to predict such flows in a few hours on a Desktop-PC equipped with three GPUs. The results of this section were published in [165].
Flow around bridge cross sections is usually aimed at getting insight into the behavior of the wind in storm situation. One may ask whether and at what velocities instabilities, such as lock-in, divergence, or flutter occur. The simulation of a moving bridge cross section can answer these question. A simulation similar to the one presented above could be coupled with a simple solver for a two-degree of freedom (vertical movement and rotation) oscillator of the bridge. That way the flutter derivatives and the flutter velocity could be determined.

4.5 Application to building ventilation

4.5.1 Motivation

We study ventilation effects for a model of the EnergieForum Berlin, which is an atrium building realized in 2002 and designed as a minimum energy consumption building. One pillar of this concept is seasonal heating and cooling. Seasonal storage of excess heat combined with natural ventilation can be used to reduce energy consumption for heating by around 70% and make air conditioning unnessesary. Figures 4.34 and 4.35 show the atrium building and the aerial view of the location at the waterfront of the river Spree (all images by [35]). At the Institut für Gebäude und Solartechnik of the TU Braunschweig, atrium buildings are being studied experimentally and with CFD methods. The energy demands of the atrium and the air quality inside the atrium are being evaluated in the projects Atrien I [37] and Atrien II [38]. One of the objects of study is the atrium of the EnergieForum. For those projects an atrium was simulated with the CFD code Fluent and a $k-\varepsilon$ model [57]. Being an ensemble-averaged model, it does not give information about the fluctuations at the openings of the atrium. It is however suspected that pumping effects have a significant effect on the ventilation performance of the building. If, for example, old air gets periodically pushed in and out of the building, the ventilation will function very differently from what is predicted by time/ensemble-averaged models. Because of this the atrium will be studied with an LES-turbulence model. Due to the high computational cost of 3D time-resolved methods, few LES studies of natural building ventilation with buoyancy exist to-date. A prominent example is [80] who compare RANS and LES simulations with full-scale laboratory experiments of a room with a single opening. They find that in their case LES gives more reliable results than RANS for air temperature and ventilation efficiency. In their case the ventilation induced by the mean velocity was dominant over ventilation induced by velocity fluctuations. They propose that, even though laboratory experiments are still the most reliable method for studying building ventilation, LES may have advantages for flows with high temperature differences and very low external velocities. According to their study, it is very difficult to reach the high Grasshoff numbers present in such cases and to produce very low wind velocities reliably. Such a case, namely atrium ventilation due to buoyancy in an almost-quiet situation, will be the focus of our study. The work presented here can also be found in [166].

4.5.2 Basic concepts

First, the basic concepts of building ventilation will be described. In [107] the ventilation of a single room is investigated both experimentally and numerically. In the review article [101] the physical processes in building ventilation are described.
Ventilation aims at replacing old (warm, low-oxygen) air by fresh air. Three kinds of ventilation can be distinguished: Displacement ventilation is caused by a macroscopic movement of the air due to wind. Mixing ventilation is caused by turbulent diffusion processes. Dis-

Figure 4.34: *The object of study: EnergieForum Berlin*

Figure 4.35: *View of the atrium*

placement ventilation is often preferred to mixing ventilation because it is faster and the effect of heat conduction in winter is not desired. On the other hand, noticeable winds may cause discomfort. Buoyancy-driven ventilation is effective for cooling, as hot air rises and is replaced by air from low-lying openings. In the absence of winds, the ventilation airflow rate may be predicted by simple formulae using only the temperature difference, the vertical distance between the openings, and some empirical parameters. It is difficult to predict in what ways external winds effect the discharge. Thermal flows are characterized by several dimensionless numbers, such as the Froude number to describe buoyancy effects in Boussinesq-type flow, or the Nusselt number for near-wall thermal effects. The Prandtl and Rayleigh number were used in this study to relate numerical to physical quantities. The Prandtl number describes the ratio between the heat transfer properties (heat diffusivity α) and momentum transport properties (viscosity) of the medium. For gases the Prandtl number depends only weakly on the temperature and can be assumed to be a constant with $Pr \in [0.7, 1]$. For turbulent flows the diffusion of heat and mass occurs not only due to molecular transport, but also via turbulent fluctuations. For such cases a turbulent Prandtl number can be defined that balances the total transport mechanisms. For air it has been determined experimentally to $Pr_\tau \in [0.8, 0.9]$. Following [163] we can compute a turbulent heat conductivity α_τ from the turbulent viscosity of an LES model based on the definition of the turbulent Prandtl number.

$$Pr = \frac{\nu + \nu_\tau}{\alpha + \alpha_\tau} \tag{4.2}$$

A second dimensionless number is needed to establish a similarity relationship between the real and modeled temperature. Turbulent flows that are driven by a temperature gradient can be characterized by the Rayleigh number

$$Ra = \frac{g\beta\Delta T L^3}{\nu\alpha} \tag{4.3}$$

where $\beta = 1/T_0$ for a reference temperature T_0. For low Rayleigh numbers the dominant mechanism for the transport of thermal energy is heat conduction. For Rayleigh numbers of around $Ra = O(10^3)$ and beyond convective heat transport is the dominant mechanism.
The temperature is modeled using the HTLBE model of [91]. In this method the equation for temperature diffusion- and convection is described by one additional finite difference equation. The model uses the Boussinesq approximation.This means that the temperature differences are assumed to be sufficiently small to influence the flow field through buoyancy effects only. All other contributions of the density variations caused by the temperature difference to the Navier Stokes equations are being neglected.

4.5.3 Computational setup

A Smagorinsky LES with the D3Q19 MRT model on a GPU with EsoTwist propagation scheme is used. The code is implemented in CUDA as described in sec. 2.10.2 and is being executed

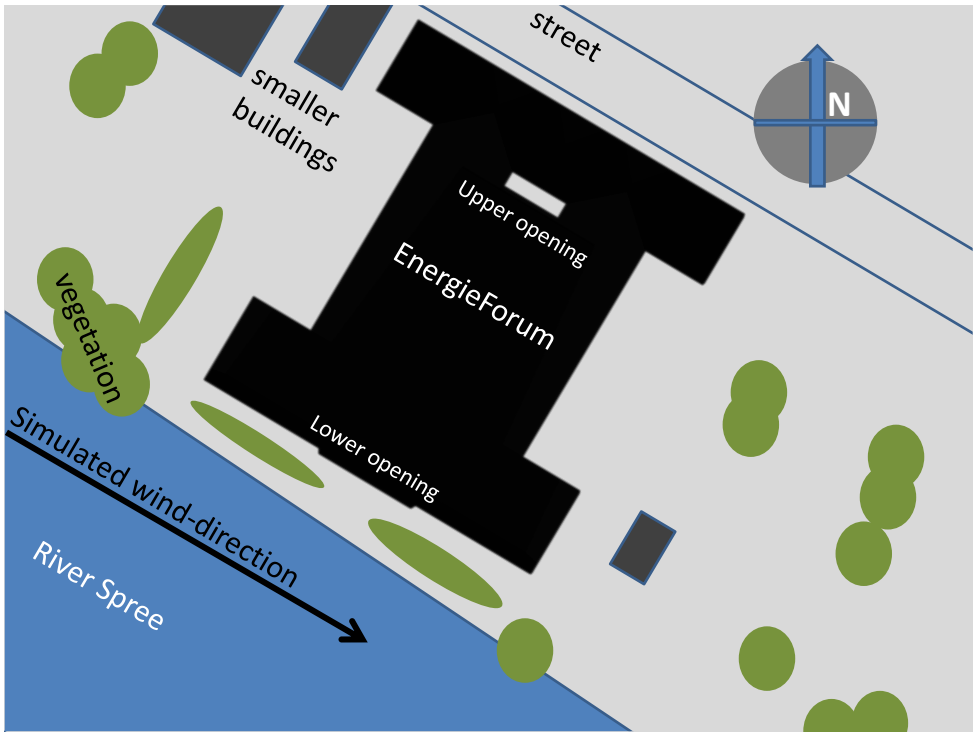

Figure 4.36: *Aerial view of the EnergieForum*

on an NVidia Geforce GTX580. The Temperature is modeled using the HTLB model [91]. The implementation is not validated in this work, as this has been done before in [7]. A passive scalar transport equation was implemented to determine the ventilation efficiency. The values of the quantities used in the simulation are listed in Table 4.2. Two different temperature differences between the outer building were considered.

The outer boundaries were modeled as no-slip boundaries for the flow as would be the case in a wind tunnel experiment and set to the far-field value for the temperature and the passive scalar. A constant velocity was imposed at the inflow and a constant pressure at the outflow. The inflow velocity was set parallel to the lower opening of the atrium to have the external flow induce only a weak internal flow. This wind direction is also a wind direction that can be expected to occur frequently, as it corresponds to wind in a north-westerly direction following the river Spree. Picture 4.36 shows the atrium in an aerial view. The details relevant for the simulations, namely the wind direction and the opening, are scetched in the drawing. First the flow and temperature field was allowed to develop over $24s$. After that the tracer gas was released. Its decay was recorded for another $12s$. Five different cases are considered, varying temperature and external velocity. An LES simulation is only one of all the possible realizations of the flow field, so two simulations with slightly different initial conditions were carried out for every setup. The fluxes determined in these simulations were used to test whether the decrease of the tracer gas can be reproduced with a reduced setup as will be elaborated in the following section. As a third step an even more drastic simplification was attempted. The decrease of the tracer gas with time was compared to an exponential

quantity	value
temperature difference	$3°C/30°C$
external temperature	$20°C$
Re	15000
Ra	$1.7\,10^{10}$ / $1.7\,10^{11}$
Pr	0.75
building height (model)	$3m$
length of domain	$10.2m$
height of domain	$4.8m$
width of domain	$9.6m$
overall simulation time	$36s$
overall number of timesteps	300000
numerical viscosity	$0.00005m^2/s$
grid resolution	$0.0375m/\Delta x$

Table 4.2: *List of the quantities used in the numerical setup*

case name	Velocity $[m/s]$	Temperature $[°C]$
c1	6	30
c2	0	30
c3	6	3
c4	0	3
c5	6	0

Table 4.3: *Denotation and parameters of the different simulations*

decay function. It was investigated whether an exponential decay function $e^{-\gamma t}$ with a constant coefficient γ depending linearly on the flux through the building could be assumed. As a reference value the half-live for the case C_2 was fitted to the data from the simulation. The values for the other four cases were then determined via

$$\gamma_i = \gamma_2 \frac{I_i}{I_2} \tag{4.4}$$

where I_i is the flux for the case C_i. This approach was adopted from [128] where

$$V \frac{dk}{dt} = Ik. \tag{4.5}$$

Here V is the volume of the room, k the concentration and I the flux. Different rooms and the surrounding space can be coupled via the fluxes at the room openings. Such zonal approaches are common in application and codes, as described in [2].

4.5.4 Results

Plot 4.37 shows the decrease of the tracer gas concentration over time. The fastest decrease was observed for the highest temperature difference and no external wind (case C_1). For the smaller temperature difference and a weak, but non-vanishing external wind (case C_3) the exchange of air reaches its lowest value. The mean fluxes at the lower opening were also determined. The fluxes shown in Table 4.4 were determined as a mean of the output from two different simulations with an uncertainty of around $0.01 m^3/s$. It can be seen that the fluxes that were generated by the temperature difference are opposed to those generated by the external wind. Accordingly, the slow decay of the tracer gas concentration observed for the case C_3 corresponds to a lower mean flux. In case C_1 the flow seems to be dominated by the high pressure difference, such that the relative difference between C_1 and C_2 is smaller than between C_3 and C_4. Note further that the fluxes are much smaller than would be expected from a laminar displacement-type flow with the given behavior of the tracer gas concentration. Time-dependent turbulent effects seem to play an important role. For the two realizations with slightly different initial conditions an almost identical decrease of the tracer gas is observed. The mean fluxes, however, differ significantly. The instantaneous velocities vary considerably in time: for the case C_3 the turbulence intensity in the atriums interior is at about 100% and similar values are observed for the other cases. We thus assume that the values for the fluxes, that were only averaged in time and in the plane of the buildings lower opening are error-prone. An averaging interval that would eliminate this uncertainty could not be chosen due to limited computational resources. The fluxes determined from the simulations discussed above were used to run two additional simulations with a reduced setup using the parameters shown in Table 4.3. For the case C_2 in which the flow is driven exclusively by the temperature difference a good match is observed, as can be seen from Figure 4.37. For the second case considered the decrease was expected to be slightly faster than for case C_4 due to the slightly higher prescribed flux. Instead, the decrease is slower. This leads

case name	flux $[m^3/s]$
c1	0.18
c2	0.21
c3	-0.01
c4	0.04
c5	-0.07

Table 4.4: *Time-averaged fluxes through the atrium for the five different cases studied*

to the hypothesis that the turbulent fluctuations at the openings, that were not accounted for in the reduced setup, have an important effect on the exchange of air.
It was further subject to investigation to what extend an exponential decay as described in the introductory part of the section, eq. 4.4 can reproduce the temporal behavior of the tracer gas concentration. This is shown in plot 4.38. Taking the considerable measurement uncertainties for the fluxes and the extreme simplicity of the model into account, the approach is quite successful for most of the datasets. Case C_3 constitudes an exception. An approach based on mean fluxes alone can obviously not produce good results when these fluxes almost vanish and the fluctuating component is dominant.
In the following some qualitative features of the flow are discussed based on pictures of the flow field. All pictures were generated for data at time 4.8s after the release of the tracer gas. Picture 4.41 gives an impression of the temperature distribution in the atrium for case C_2 where the warm air rises almost vertically above the building. In Figure 4.40 the instantaneous velocities are shown in a top view of the atrium at the height of the lower opening for the cases C_1 (on top) and C_2 (below). The magnitude of the velocity inside the building is similar for both cases, even though no outer wind is present in the upper case. In picture 4.39 the concentration of the tracer gas after 4.8s is shown as well as the time-averaged streamlines. It can be seen that the concentration of the tracer gas is lower for cases C_1 and C_2. For the case C_5, where no temperature difference was present, the flow direction is opposite to that of the other cases. Here, the lowest concentration is found at the upper opening and not at the lower opening. A similar behavior would be expected also for C_3. The reason why it is not observed is that the flow in fluctuating strongly and only one snapshot is shown. For the simulation of 36s of flow in and around the building 4h of computational time were needed. This corresponds to 170 million node updates per second for the fluid solver, the solver for the temperature equation and the solver for the tracer gas using 8.1 million fluid nodes.

4.5.5 Conclusions

A temperature driven flow of air in the atrium building with low external wind was simulated. The description included the air flow field around the building. To estimate the effect of the external wind and the temperature difference five different cases have been considered. To this end the decrease of the concentration of the tracer gas over time has been determined.

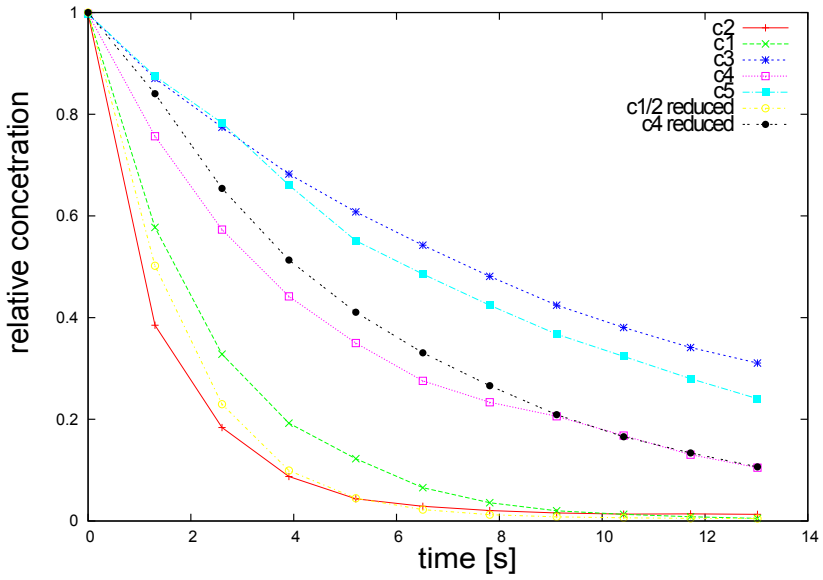

Figure 4.37: *Decay of the concentration of the tracer gas inside the atrium over time for the five primary cases and the two reduced setups*

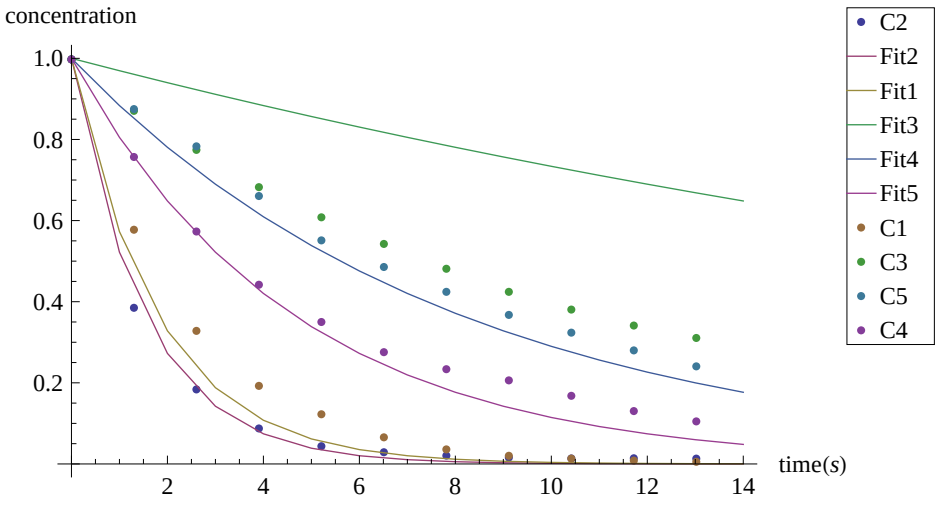

Figure 4.38: *Comparison of the simulation results and an exponential decay fit function depending on the flux, C_1: beige, C_2: pink, C_3: violet, C_4: green, C_5 turquoise*

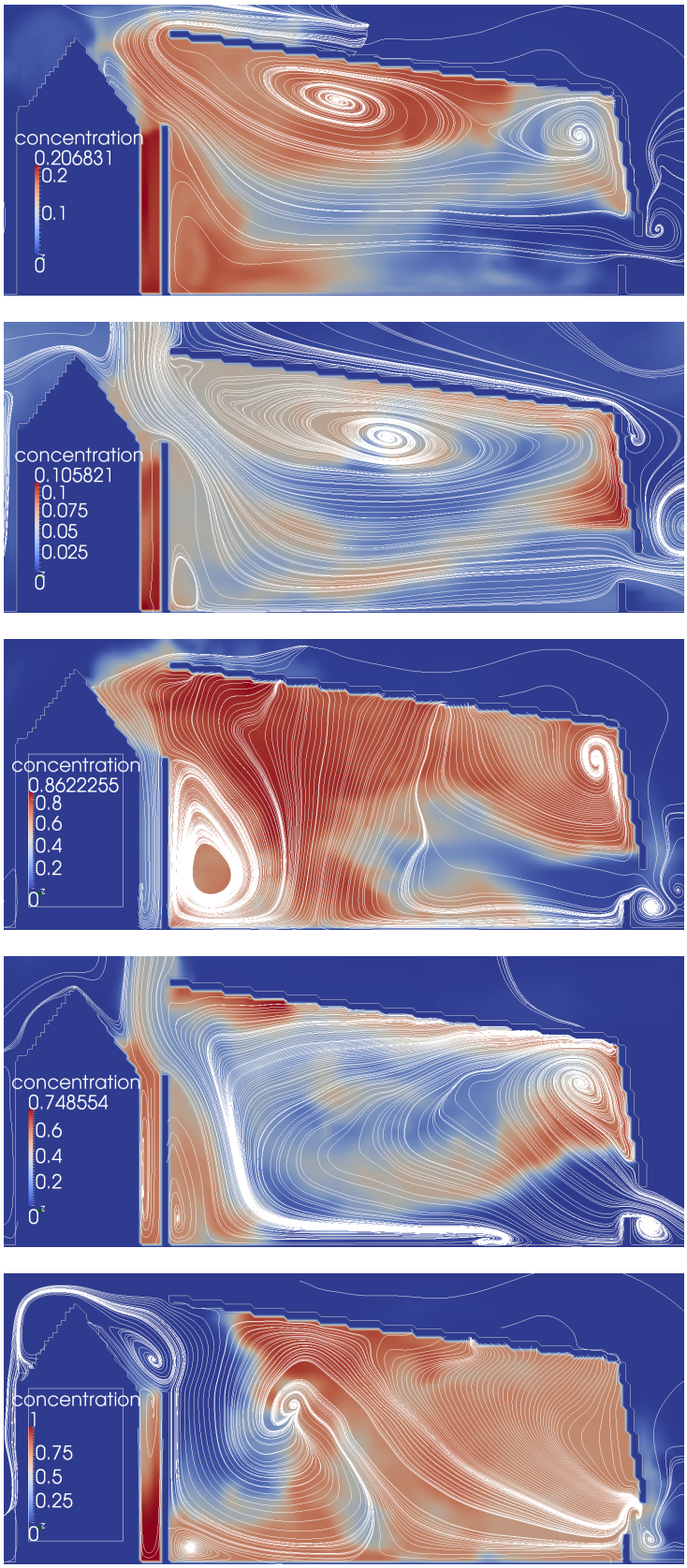

Figure 4.39: *Time-averaged streamlines and tracer-gas concentration from top to bottom for cases* C_1 *to* C_5

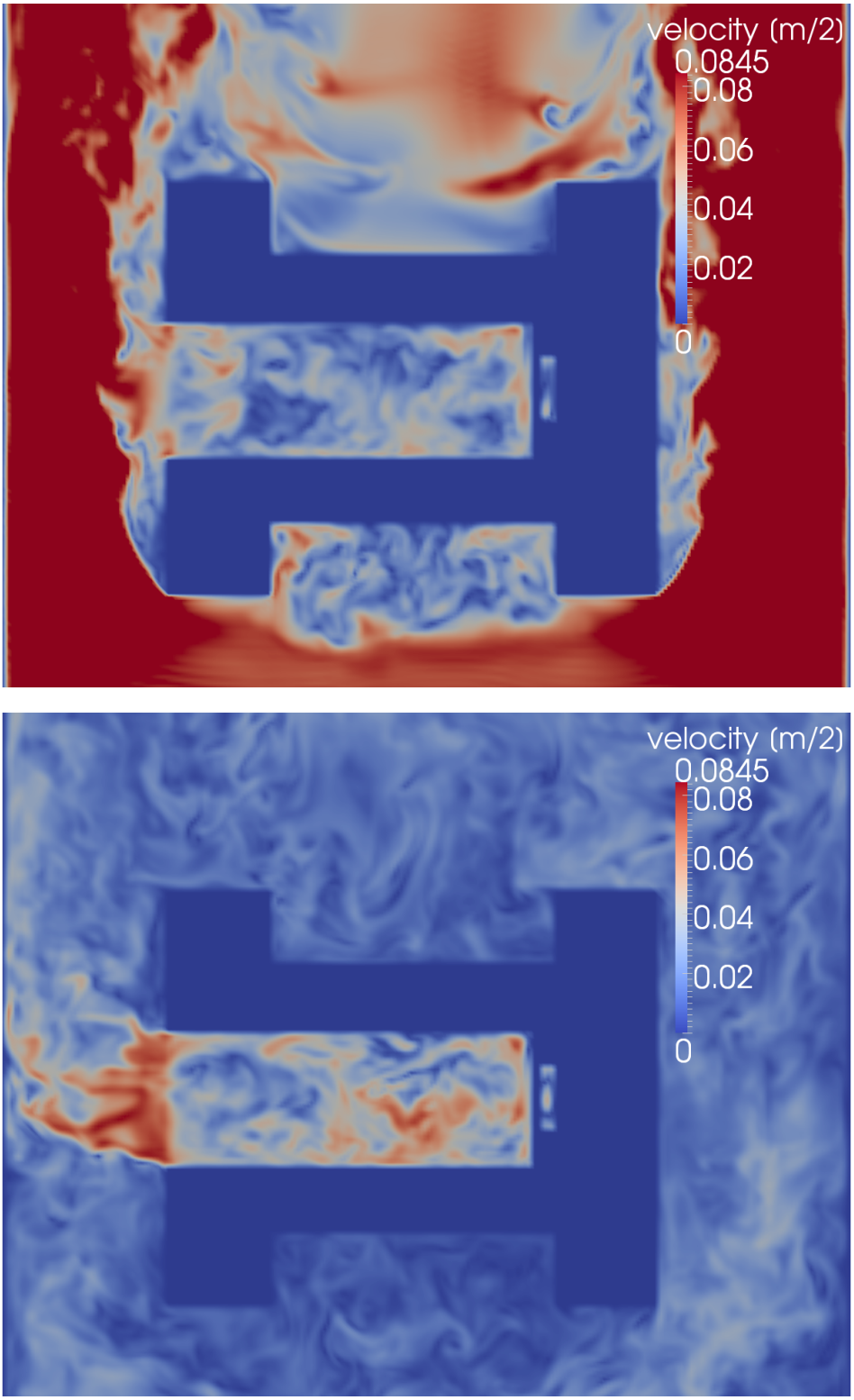

Figure 4.40: *Instantaneous velocities for cases c1 and c2*

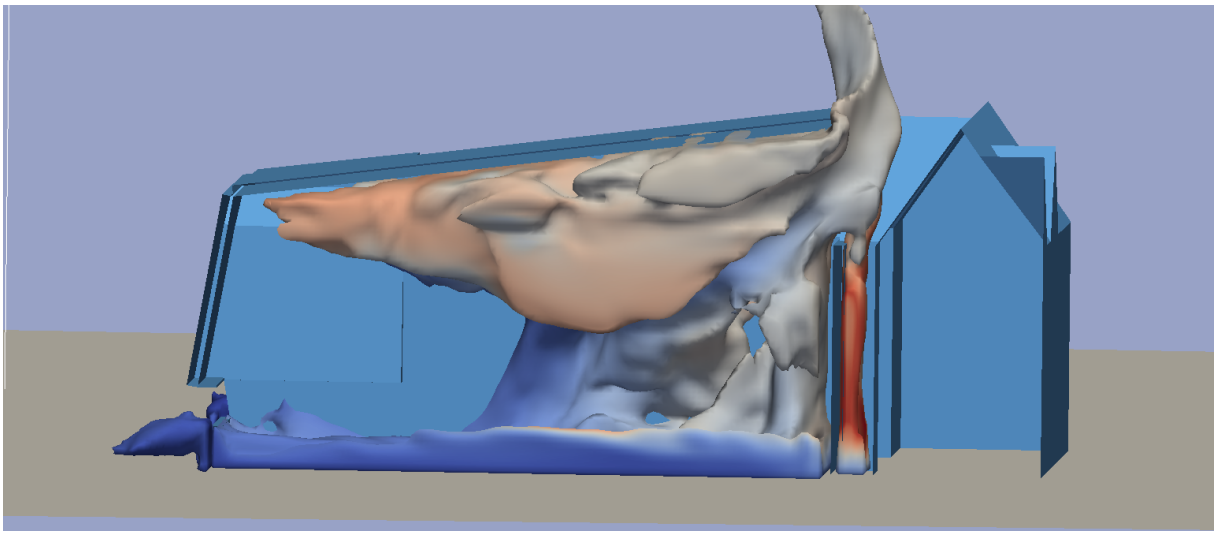

Figure 4.41: *Isocontour of the temperature at* $\Delta T = 6.4°C$ *for c*1*, colored by the tracer gas concentration*

As the flow induced by the external wind was opposed to the one induced by the temperature difference, the most effective ventilation process occurred for vanishing external wind and the highest temperature differences considered. This case could be reproduced for a reduced setup, in which only the flow inside the atrium was modeled using the previously determined fluxes to specify boundary conditions. In other cases, however, the mixing of air due to turbulence plays an important role in the ventilation process. For the comparatively low temperature difference of $3°C$ the flux dramatically drops when the outer flow field is present. The decay of the tracer gas is also the slowest for the case C_3, but not as slow as one would expect considering the mean fluxes only and neglecting turbulent mixing effects. Simple models, which consider only either the external wind or the temperature difference as the dominant factor cannot yield reliable predictions in such cases.
It could be shown that GPU-based LES-simulations can provide reasonable trends about the behavior in such complex situations and thus help identify critical situations and complements the more common models for these cases.
For a more detailed investigation validation studies based on the existing wind tunnel results should be conducted. A finer grid should be used in the vicinity of the atriums surfaces, as has been done for the CPU based LB studies presented e.g. in sections 4.4 and 4.3 of the work presented here. For GPU-based simulations approaches using non-uniform grids are still under development, see [143].

5 Conclusions

5.1 Summary

This dissertation evaluated LB models in the case of turbulent flow. A range of test cases with different properties were studied. First, we validated our implementations and compared properties of different LB models using laminar flow conditions. As a next step, geometrically simple setups such as channel flow were studied. As examples of more complex geometries, a bridge cross section at non-zero angle of attack and the flow around a surface mounted cube were considered. Several Lattice Boltzmann variants have been implemented and evaluated, such as the $D3Q27$ MRT model and the $D3Q27$ Cascaded and Factorized Cascaded Lattice Boltzmann models. The different LES models that have been implemented and tested were the simple Smagorinsky model, the Smagorinsky model with van-Driest damping, the WALE model and the Vreman model. Different hardware has been used to run the Lattice Boltzmann code. With the IRMB research code VIRTUALFLUIDS, both single CPU and distributed-memory parallel computation was possible. Trial computations and computations over a large number of time steps have usually been carried out on single GPUs.

It could be shown that the Lattice Boltzmann model can be used for turbulent flow computations of various test cases with good accuracy. For some cases, differences between Lattice Boltzmann variants and differences between turbulence models could be observed. In particular, the validity of variants of the CLB model could be validated for turbulent flow testcases. To our knowledge, reasonably resolved validations for turbulent flow cases have not been carried out before for the FCLB model. For the two cases of a turbulent channel flow and a turbulent jet flow, advantages over traditional LB approaches with the Smagorinsky LES model could be observed. We propose that the CLB model acts as a type of implicit LES model and underpin this idea by a numerical comparison with Badina's model.
It can thus be concluded that unsteady flow computation with LBM can indeed contribute to the prediction of building scale flows in civil engineering. The present work contributes to the reliability of such computations by evaluating different LBM variants for turbulent flow. So far no full wall-resolved LES could be carried out, which would be necessary for a reliable prediction of all instationary components. Even so, the C_p values can already be reproduced well for different basic building blocks such as a surface mounted cube. The influence of instationary processes on a buildings performance, such as the influence of vortex shedding on the ventilation of an atrium can be studied.

5.2 Outlook

Future work in the area of model development and validation could include the implementation of other turbulence models, such as dynamic models. Furthermore, improved inflow conditions for turbulent flows are needed. Up to now, a large run-up area has to be simulated to establish a valid turbulent boundary layer. A lot of computational effort can be spend otherwise, when existing CFD methods to synthetically generate such boundary layers at the inflow are made available for Lattice Boltzmann. In the spirit of ILES modeling, a better understanding of the effects of different non-linear higher-order LB-error terms could lead to the ability to adjust these terms to match well established LES models for some limit state. An uncontrolled interdependence between the explicit LES model and the numerical scheme could thus be avoided. Efforts to extend LBM to anisotropic grids with cuboid cells have so far been of limited success. In [8] an anisotropic MRT scheme is constructed and stability issues of such schemes are addressed. Nevertheless, grid-stretching algorithms would be of immense value to turbulent boundary layer flow computations.
Various application areas can benefit from improved, more reliable Lattice Boltzmann models. The turbulent flow kernel that has been developed in the present work could be applied to further turbulent flow problems in the wind-engineering domain. Such applications include fluid structure interaction with complex geometries. For such applications, the griding process for traditional solvers can be very expensive especially when object and grid are moving. LBM has provided accurate results in this field, e.g. [52]. The current validation studies on the pressure on a bridge surface could be extended to determine the aerodynamic derivatives of bridges.
Furthermore, applications in aeroacoustics are going to be studied and first steps can be found in the corresponding section of this work. LB is well suited to the study of aeroacoustics because of its ability to directly model acoustic pressure fields. The ability of LB to model sound waves was explored already in [92] and some early applications such as [70]. In recent years first steps have been made towards the modeling of sound fields in turbulent flows with LBM, such as the development of sound-absorbing boundary conditions for LBM [77] or application studies on the sound emitted by flow over a cavity [175]. The CLB model with low bulk viscosity, such as the CLB model with TRT relaxation coefficients, was evaluated in the present work in several testcases and showed good stability properties without an artificial damping of sound waves. This makes it a promising candidate for aeroacoustics simulation. A project that involves LBM computations of aeroacoustics, namely the SFB880, on the sound emitted by airplane wings is already in progress.

Bibliography

[1] Ahrenholz, B.: *Massively parallel simulations of multiphase - and multicomponent flows using Lattice Boltzmann methods*. PhD thesis, Technische Universität Braunschweig, 2009.

[2] American Society of Heating, Refrigerating, and Air Conditioning Engineers, Inc.: *Standard 62-1989, Ventilation for Acceptable Indoor Air Quality, Atlanta, GA*, 1989.

[3] Bailey, P., Myre, J., Walsh, S.D., Lilja, D.J., and Saar, M.O.: *Accelerating lattice boltzmann fluid flow simulations using graphics processors*. In *Parallel Processing, 2009. ICPP'09. International Conference on*, pp. 550–557. IEEE, 2009.

[4] Bardina, J., Ferziger, J., and Reynolds, W.: *Improved subgrid-scale models for large-eddy simulation*. In *13th AIAA Fluid and Plasma Dynamics Conference, Snowmass, Colo.,1980*, vol. 1, p. 10, 1980.

[5] Bennett, S., Asinari, P., and Dellar, P.: *A Lattice Boltzmann model for diffusion of binary gas mixtures that includes diffusion slip*. International Journal of Numerical Methods in Fluids, 69:171–189, 2012.

[6] Bhatnagar, P., Gross, E., and Krook, M.: *A model for collision processes in gases. I. Small amplitude processes in charged and neutral one-component systems*. Physical Review, 94(3):511–525, 1954.

[7] Bindick, S.: *Ein integrierter Ansatz zur interaktiven dreidimensionalen Simulation gekoppelter thermischer Prozesse*. PhD thesis, Technische Universität Braunschweig, 2010.

[8] Bouzidi, M., D'Humières, D., Lallemand, L., and Luo, L.: *Lattice Boltzmann Equation on a Two-Dimensional Rectangular Grid*. Journal of Computational Physics, 172:704–717, 2001.

[9] Bouzidi, M., Firdaouss, M., and Lallemand, P.: *Momentum transfer of a Lattice Boltzmann fluid with boundaries*. Phys. Fluids, 13:3452–3459, 2001.

[10] Boyd, J., Buick, J., and Green, S.: *A second-order accurate Lattice Boltzmann non-Newtonian flow model*. Journal of Physics A: Mathematical and General, 39:14241–14247, 2006.

[11] Braun, A. and Awruch, A.: *Numerical simulation of the wind action on a long-span bridge deck*. Journal of the Brazilian Society of Mechanical Sciences and Engineering, 25:352–363, 2003.

[12] Bröcker, T.: *Analysis 1*. BI Wissenschaftsverlag, 1992.

[13] Bruno, L. and Khris, S.: *The validity of 2D numerical simulations of vortical structures around a bridge deck*. Mathematical and Computer Modelling, 37:795–828, 2003.

[14] Buick, J. and Greated, C.: *Gravity in a Lattice Boltzmann model*. Physical Review E, 61(5):5307–5320, 2000.

[15] Buick, J., Greated, C., and Campbell, D.: *Lattice BGK simulation of sound waves*. Europhysics Letters, 43:235–240, 1998.

[16] Cercignani, C.: *Mathematical Methods in kinetic theory*. Plenum Press, New York, 1969.

[17] Chen, S. and Doolen, G.: *Lattice Boltzmann method for fluid flows*. Annual review of fluid mechanics, 30(1):329–364, 1998.

[18] Chikatamarla, S.S., K.I.: *Lattices for the Lattice Boltzmann method*. Physical Review E, 79:046701, 2009.

[19] Clobes, M. and Aizpurua Aldasoro, H.: *Interference effects of power house on the gust buffeting response of slender chimneys*. In *CICIND-Technical Meeting, St. Petersburg, Russia, CICIND-Report*, 2011.

[20] Cochrana, L. and Derickson, R.: *A physical modeler's view of computational wind engineering*. In *The Fifth International Symposium on Computational Wind Engineering, (ICWE2010), Chapel Hill, North Carolina, USA.*, 2010.

[21] Coles, D.: *The law of the wake in the turbulent boundary layer*. Journal of Fluid Mechanics, 1(02):191–226, 1956.

[22] Cornubert, R., d'Humières, D., and Levermore, D.: *A Knudsen layer theory for lattice gases*. Physica D: Nonlinear Phenomena, 47(1-2):241–259, 1991.

[23] Dankowski, H.: *Lattice boltzmann slip boundary conditions for the modeling of transient flow around a ship hull*. student research project, 2007.

[24] Dellar, P.: *Lattice kinetic schemes for magnetohydrodynamics*. Journal of Computational Physics, 179(1):95–126, 2002.

[25] Deutsches Institut für Normung e.V.: *Akustik - Bestimmung des Schallabsorptionsgrades und der Impedanz in Impedanzrohren - DIN EN ISO 10534-2, Berlin*, 2001.

[26] Deutsches Institut für Normung e.V.: *Antennentragwerke aus Stahl - DIN EN 4131, Berlin*, 2010.

[27] d'Humières, D.: *Generalized Lattice-Boltzmann equations*. In Shizgal, B.D. and Weave, D.P. (eds.): *Rarefied Gas Dynamics: Theory and Simulations*, vol. 159 of *Prog. Astronaut. Aeronaut.*, pp. 450–458, Washington, D.C., 1994. AIAA.

[28] d'Humières, D., Bouzidi, M., and Lallemand, P.: *Thirteen-velocity three-dimensional Lattice Boltzmann model*. Physical Review E, 63(6):066702, 2001.

[29] d'Humières, D., Ginzburg, I., Krafczyk, M., Lallemand, P., and Luo, L.: *Multiple-relaxation-time Lattice Boltzmann models in three dimensions*. Royal Society of London Philosophical Transactions Series A, 360:437–451, 2002.

[30] Dubois, F.: *Equivalent partial differential equations of a Lattice Boltzmann scheme.* Computers and mathematics with applications, 55(7):1441–1449, 2008.

[31] Ducros, F., Comte, P., and Lesieur, M.: *Large-eddy simulation of transition to turbulence in a boundary layer developing spatially over a flat plate.* Journal of Fluid Mechanics, 326:1–36, 1996.

[32] Ducros, F., Nicoud, F., and Poinsot, T.: *Wall-adapting local eddy-viscosity models for simulations in complex geometries.* Numerical Methods for Fluid Dynamics, 4:293–299, 1998.

[33] Eitel-Amor, G., Meinke, M., and Uphoff, S.: *Comment on "Analysis of Lattice-Boltzmann methods for internal flows".* submitted to Computers & Fluids, 2012.

[34] Elkhoury, M.: *Assessment and modification of one-equation models of turbulence for wall-bounded flows.* Journal of Fluids Engineering, 129:921–928, 2007.

[35] Fachinformationszentrum (FIZ) Karlsruhe (ed.): *Forschung für Energieoptimiertes Bauen*, visited: May 2012. `url:http://www.enob.info`.

[36] Filippova, O. and Hänel, D.: *Grid refinement for Lattice-BGK models.* Journal of Computational Physics, 147(1):219–228, 1998.

[37] Fisch, M.N. and Zargari, M.: *Analyse und Bewertung von Atrien in Bürogebäuden. Abschlussbericht.* Fraunhofer Irb Verlag, 2011.

[38] Fisch, M.N. and Zargari, M.: *Optimierung von Atrien und Verbesserung der Anwendung von Planungswerkzeugen (ATRIEN II).* Techn. rep., Insitut für Gebäude- und Solartechnik, 2012.

[39] Franke, J., Hellsten, A., Schlünzen, H., and Carissimo, B.: *Best practice guideline for the CFD simulation of flows in the urban environment.* In *COST action*, vol. 732, Hamburg, 2007.

[40] Freitas, R., Henze, A., Meinke, M., and Schröder, W.: *Analysis of Lattice-Boltzmann methods for internal flows.* Computers & Fluids, 47(1):115–121, 2011.

[41] Freudiger, S.: *Entwicklung eines parallelen, adaptiven, komponentenbasierten Strömungskerns für hierarchische Gitter auf Basis des Lattice-Boltzmann-Verfahrens.* PhD thesis, Technische Universität Braunschweig, 2009.

[42] Freudiger, S., Hegewald, J., and Krafczyk, M.: *A parallelisation concept for a mult-physics Lattice Boltzmann prototype based on hierarchical grids.* Progress in Computational Fluid Dynamics, 8(1):168–178, 2008.

[43] Frisch, U., d'Humières, D., Hasslacher, B., Lallemand, P., Pomeau, Y., and Rivet, J.: *Lattice gas hydrodynamics in two and three dimensions.* Complex systems, 1(4):649–707, 1987.

[44] Frisch, U., Hasslacher, B., and Pomeau, Y.: *Lattice-gas automata for the Navier-Stokes equation.* Physical Review Letters, 56(14):1505–1508, 1986.

[45] Fröhlich, J.: *Large Eddy Simulation turbulenter Strömungen.* Teubner, Wiesbaden, 2006.

[46] Garnier, E., Mossi, M., Sagaut, P., Comte, P., and Deville, M.: *On the use of shock-capturing schemes for large-eddy simulation.* Journal of Computational Physics, 153(2):273–311, 1999.

[47] Geier, M.: *Ab Initio Derivation of the Cascaded Lattice Boltzmann Automaton.* PhD thesis, Universität Freiburg, 2006.

[48] Geier, M.: *Konsistente Multiskalenströmungsmechanik mit der kaskadierten Lattice Boltzmann Methode, DFG-Projekt GE 1990/2-1.* Abschlussbericht, TU Braunschweig, 2010.

[49] Geier, M., Greiner, A., and Korvink, J.: *Reference frame independent partitioning of the momentum distribution function in Lattice Boltzmann methods with multiple relaxation rates.* unpublished.

[50] Geier, M., Greiner, A., and Korvink, J.: *Cascaded digital Lattice Boltzmann automata for high reynolds number flow.* Physical Review E, 73(6):66705, 2006.

[51] Geier, M., Greiner, A., and Korvink, J.: *A factorized central moment Lattice Boltzmann method.* The European Physical Journal-Special Topics, 171(1):55–61, 2009.

[52] Geller, S.: *Ein explizites Modell fur die Fluid-Struktur-Interaktion basierend auf LBM und p-FEM.* PhD thesis, Technische Universität Braunschweig, 2010.

[53] Geller, S., Janßen, C., and Krafczyk, M.: *A Lattice Boltzmann approach for distributed three-dimensional fluid-structure interaction.* In *Progress in Computational Physics*, pp. 193–209, 2012.

[54] Geller, S., Krafczyk, M., Tölke, J., Turek, S., and Hron, J.: *Benchmark computations based on Lattice-Boltzmann, finite element and finite volume methods for laminar flows.* Computers & Fluids, 35(8-9):888–897, 2006.

[55] Geller, S., Tölke, J., Krafczyk, M., Kollmannsberger, S., Düster, A., and Rank, E.: *A coupling algorithm for high order solids and Lattice Boltzmann fluid solvers.* In *European Conference on Computational Fluid Dynamics, Egmond aan Zee, the Netherlands*, 2006.

[56] Geller, S., Uphoff, S., and Krafczyk, M.: *Turbulent jet computations based on MRT and Cascaded Lattice Boltzmann models.* submitted to Computers & Mathematics with Applications, arXiv: 1206.0389, 2012.

[57] Gerder, F.: *Bestimmung des durchschnittlichen, windinduzierten Luftwechsels in einem Atrium am Beispiel des EnergieForums Berlin.* PhD thesis, Technische Universität Braunschweig, 2006.

[58] Germano, M., Piomelli, U., Moin, P., and Cabot, W.H.: *A dynamic subgrid scale eddy viscosity model.* Physics of Fluids A, 3:1760–1767, 1991.

[59] Geurts, B.: *Elements of direct and large-eddy simulation.* RT Edwards, Philadelphia, Pa, 2004.

[60] Ginzburg, I.: *Equilibrium-type and link-type Lattice Boltzmann models for generic advection and anisotropic-dispersion equation.* Advances in Water Resources, 28(11):1171–1195, 2005.

[61] Ginzburg, I.: *Une variation sur les propriètès magiques de modèles de Boltzmann pour l' ècoulement microscopique et macroscopique.* Habilitation, Universit'e Pierre and Marie Curie, Paris, September 2008.

[62] Ginzburg, I. and Humières, D. d': *Multireflection boundary conditions for Lattice Boltzmann models.* Physical Review E, 68(6):066614, 2003.

[63] Ginzburg, I., Verhaege, F., and d'Humières, D.: *Study of simple hydrodynamic solutions with the two-relaxation-time Lattice Boltzmann scheme.* Communications in Computational Physics, 3(3):519–581, 2008.

[64] Ginzburg, I., Verhaege, F., and d'Humières, D.: *Two-relaxation-time Lattice Boltzmann scheme: About parametrization, velocity, pressure and mixed boundary conditions.* Communications in Computational Physics, 3(2):427–478, 2008.

[65] Glück, M., Breuer, M., Durst, F., Halfmann, A., and Rank, E.: *Computation of fluid–structure interaction on lightweight structures.* Journal of wind engineering and industrial aerodynamics, 89(14):1351–1368, 2001.

[66] Gorban, A. and Karlin, I.: *General approach to constructing models of the Boltzmann equation.* Physica A, 206:401–420, 1994.

[67] Guo, Z., Zheng, C., and Shi, B.: *Discrete lattice effects on the forcing term in the Lattice Boltzmann method.* Physical Review E, 65(4):46308, 2002.

[68] Habich, J., Zeiser, T., Hager, G., and Wellein, G.: *Speeding up a Lattice Boltzmann kernel on nVIDIA GPUs.* Proceedings of the First International Conference on Parallel, Distributed and Grid Computing for Engineering, Civil-Comp Press, p. 17, 2009.

[69] Hardy, J., De Pazzis, O., and Pomeau, Y.: *Molecular dynamics of a classical lattice gas: Transport properties and time correlation functions.* Physical Review A, 13(5):1949–1961, 1976.

[70] Haydock, D. and Yeomans, J.: *Lattice Boltzmann simulations of acoustic streaming.* Journal of Physics A: Mathematical and General, 34(25):5201–5213, 2001.

[71] He, X. and Luo, L.: *Lattice Boltzmann model for the incompressible Navier-Stokes equation.* Journal of Statistical Physics, 88(3):927–944, 1997.

[72] Hou, S., Sterling, J., Chen, S., and Doolen, G.: *A Lattice Boltzmann subgrid model for high Reynolds number flows.* Pattern formation and lattice gas automata, 6:151–166, 1994.

[73] Huijnen, V., Somers, L., Baert, R., and Goey, L. de: *Validation of the LES approach in Kiva-3V on a square duct geometry.* International Journal for Nnumerical Methods in Engineering, 64(7):907–919, 2005.

[74] Hunt, J., Wray, A., and Moin, P.: *Eddies, streams, and convergence zones in turbulent flows.* In *Studying Turbulence Using Numerical Simulation Databases, 2, Proceedings of the 1988 Summer Program*, pp. 193–208, Moffett Field, Calif., 1988.

[75] Huo, S., Zuo, Q., Chen, S., Doolen, G., and Cogley, A.C.: *Simulation of cavity flow by the Lattice Boltzmann method.* Journal of Computational Physics, 118:329–347, 1995.

[76] Institute for Computational Modelling in Civil Engineering, Technische Universität Braunschweig (ed.): *Ludwig*, visited: September 2012. `url:http://wiki.irmb.bau.tu-bs.de/ludwig/`.

[77] Izquierdo, S. and Fueyo, N.: *Characteristic nonreflecting boundary conditions for open boundaries in Lattice Boltzmann methods.* Physical Review E, 78:046707(7), 2008.

[78] Janßen, C.: *Free surface tracking with the Lattice Boltzmann Method.* student research project, 2007.

[79] Janßen, C.: *Kinetic approaches for the simulation of non-linear free surface flow problems in civil and environmental engineering.* PhD thesis, Technische Universität Braunschweig, 2010.

[80] Jiang, Y. and Chen, Q.: *Buoyancy-driven single-sided natural ventilation in buildings with large openings.* International Journal of Heat and Mass Transfer, 46(6):973–988, 2003.

[81] Junk, M., Klar, A., and Luo, L.: *Asymptotic analysis of the Lattice Boltzmann equation.* Journal of Computational Physics, 210(2):676–704, 2005.

[82] Karlin, I., Ansumali, S., Angelis, E. de, Öttinger, H., and Succi, S.: *Entropic Lattice Boltzmann method for large scale turbulence simulation.* Arxiv: cond-mat/0306003, 2003.

[83] Karypis, G. and Kumar, V.: *METIS – a software package for partitioning unstructured graphs, partitioning meshes, and computing fill-reducing orderings of sparse matrices, version 4.0.* 1998.

[84] Khronos Group (ed.): *OpenCL - The open standard for parallel programming of heterogeneous systems*, visited: Oct. 2010. `url:www.khronos.org/opencl`.

[85] Kim, J., Moin, P., and Moser, R.: *Turbulence statistics in fully developed channel flow at low Reynolds number.* Journal of Fluid Mechanics, 177(-1):133–166, 1987.

[86] Kornreich, P. and Scalo, J.: *Supersonic lattice gases: restoration of Galilean invariance by nonlinear resonance effects.* Physica D: Nonlinear Phenomena, 69(3-4):333–344, 1993.

[87] Krafczyk, M.: *Gitter-Boltzmann-Methoden: Von der Theorie zur Anwendung.* Habilitation, Technische Universität München, 2001.

[88] Ladd, A.: *Numerical simulations of particulate suspensions via a discretized Boltzmann equation, part 1.* Journal of Fluid Mechanics, 271(1):285–339, 1994.

[89] Lakehal, D. and Rodi, W.: *Calculation of the flow past a surface-mounted cube with two-layer turbulence models.* Journal of Wind Engineering and Industrial Aerodynamics, 67:65–78, 1997.

[90] Lallemand, P. and Luo, L.: *Theory of the Lattice Boltzmann method: Dispersion, dissipation, isotropy, Galilean invariance, and stability.* Physical Review E, 61:6547–6562, 2000.

[91] Lallemand, P. and Luo, L.: *Hybrid finite-difference thermal Lattice Boltzmann equation.* International Journal of Modern Physics B, 17(1/2):41–47, 2003.

[92] Lallemand, P. and Luo, L.S.: *Theory of the Lattice Boltzmann method: Acoustic and thermal properties in two and three dimensions.* Phys. Rev. E, 68(3):036706, Sep 2003.

[93] Langer, S.: *Schalltransmission durch Isolierverglasung.* PhD thesis, Technische Universität Braunschweig, 2001.

[94] Larsen, A., Esdhal, S., Andersen, J., and Verjum, T.: *Vortex shedding excitation of the Great Belt suspension bridge.* In *Proc. 10th International Conference on Wind Engineering. Balkema, Copenhagen*, pp. 947–954, publ. Rotterdam, 1999.

[95] Larsen, A. and Walther, J.: *Discrete vortex simulation of flow around five generic bridge deck sections.* Journal of Wind Engineering and Industrial Aerodynamics, 77/78:591–602, 1998.

[96] Launder, B., Reece, G., and Rodi, W.: *Progress in the development of a Reynolds-stress turbulence closure.* Journal of Fluid Mechanics, 68(03):537–566, 1975.

[97] Lee, T. and Lin, C.: *A stable discretization of the Lattice Boltzmann equation for simulation of incompressible two-phase flows at high density ratio.* Journal of Computational Physics, 206(1):16–47, 2005.

[98] Lesieur, M. and Metais, O.: *New trends in large-eddy simulations of turbulence.* Annual Review of Fluid Mechanics, 28(1):45–82, 1996.

[99] Lesieur, M., Métais, O., and Comte, P.: *Large-eddy simulations of turbulence.* Cambridge University Press, Cambridge, 2005.

[100] Lilly, D.: *A proposed modification of the Germano subgrid scale closure method.* Physics of Fluids, 4:633–635, 1992.

[101] Linden, P.: *The fluid mechanics of natural ventilation.* Annual Review of Fluid Mechanics, 31(1):201–238, 1999.

[102] Linxweiler, J.: *Ein integrierter Softwareansatz zur interaktiven Exploration und Steuerung von Strömungssimulationen auf Many-Core-Architekturen.* PhD thesis, Technische Universität Braunschweig, 2011.

[103] Linxweiler, J., Krafczyk, M., and Tölke, J.: *Highly interactive computational steering for coupled 3d flow problems utilizing multiple GPUs.* Computing and visualization in science, 13(7):299–314, 2010.

[104] Lippitz, N.: *Analyse der Schallabsorptionseigenschaften in Abhängigkeit der Struktur verschiedener metallischer Vliese.* Studienarbeit, TU Braunschweig, 2011.

[105] Lund, T.S., Wu, X., and Squires, K.D.: *Generation of turbulent inflow data for spatially-developing boundary layer simulations.* Journal of Computational Physics, 140(2):233 – 258, 1998.

[106] Lux, R.: *Modellsimulationen zur Strömungsverstärkung von orographischen Grundstrukturen bei Sturmsituationen.* PhD thesis, Universität Karlsruhe, 2007.

[107] Maas, A.: *Experimentelle Quantifizierung des Luftwechsels bei Fensterlüftung.* PhD thesis, Universität Gesamthochschule Kassel, 1995.

[108] Martinuzzi, R. and Tropea, C.: *The flow around surface-mounted, prismatic obstacles placed in a fully developed channel flow.* J. Fluids Eng, 115(1):85–92, 1993.

[109] Mayer, G. and Házi, G.: *Direct numerical and large eddy simulation of longitudinal flow along triangular array of rods using the Lattice Boltzmann method.* Mathematics and Computers in Simulation, 72(2-6):173–178, 2006.

[110] McNamara, G. and Zanetti, G.: *Use of the Boltzmann equation to simulate lattice gas automata.* Phys. Rev. Lett., 61(20):2232–2335, 1988.

[111] Mei, R., Luo, L.S., and Shyy, W.: *An accurate curved boundary treatment in the Lattice Boltzmann method.* Journal of Computational Physics, 155(2):307–330, 1999.

[112] Mei, R., Shyy, W., Yu, D., and Luo, L.: *Lattice Boltzmann method for 3-D flows with curved boundary.* Journal of Computational Physics, 161(2):680–699, 2000.

[113] Meneveau, C. and Katz, J.: *Scale-invariance and turbulence models for large-eddy simulation.* Annual Review of Fluid Mechanics, 32(1):1–32, 2000.

[114] Menon, S. and Soo, J.: *Simulation of vortex dynamics in three-dimensional synthetic and free jets using the large-eddy Lattice Boltzmann method.* Journal of Turbulence, 5(1):32, 2004.

[115] Menter, F.: *Improved Two-Equation k-omega Turbulence Models for Aerodynamic Flows*, vol. 103975. NASA Technical Memorandum, Moffet Field, Calif., 1992.

[116] Menter, F.R.: *Eddy viscosity transport equations and their relation to the k-epsilon model.* Journal of Fluids Engineering, 119(4):876–884, 1997.

[117] Meroney, R.N., Leitl, B.M., Rafailidis, S., and Schatzmann, M.: *Wind-tunnel and numerical modeling of flow and dispersion about several building shapes.* Journal of Wind Engineering and Industrial Aerodynamics, 81:333–345, 1999.

[118] Ming, H., Hongwu, T., and Huimin, W.: *Applying ADV to a round jet flow.* In *Proceedings of the Congress - International Association for Hydraulic Research*, pp. 455–460, 2001.

[119] Ming, L., Xiao-Peng, C., and Premnath, K.N.: *Comparative Study of the Large Eddy Simulations with Lattice Boltzmann Method using the Wall-Adapting Locak Eddy Viscosity and Vreman Subgrid Scale Models.* Chinese Physics Letters, 29(10):104706–1–5, 2012.

[120] Moin, P. and Kim, J.: *Numerical investigation of turbulent channel flow.* Journal of Fluid Mechanics, 118:341–377, 1982.

[121] Murakami, S.: *Current status and future trends in CWE.* In *Second International Symposium on Computational Wind Engineering, Colorado State University*, 1996.

[122] Nicoud, F. and Ducros, F.: *Subgrid-scale stress modelling based on the square of the velocity gradient tensor.* In *Flow, Turbulence and Combustion*, vol. 62, pp. 183–200, 1999.

[123] NVIDIA Corporation (ed.): *CUDA Parallel Computing Platform*, visited: Dezember 2011. `http://www.nvidia.com/object/cuda_home_new.html`.

[124] NVIDIA Corporation (ed.): *CUDA Toolkit Documentation*, visited: Dezember 2011. `http://developer.nvidia.com/nvidia-gpu-computing-documentation`.

[125] Obrecht, C., Kuznik, F., Tourancheau, B., and Roux, J.: *Efficient gpu implementation of the linearly interpolated bounce-back boundary condition.* Computers and Mathematics with Applications, 2012.

[126] Oliveira, P. and B.A.Younis: *On the prediction of turbulent flows around full-scale buildings.* Journal of Wind Engineering and Industrial Aerodynamics, 86(2):203–220, 2000.

[127] Park, N., Lee, S., Lee, J., and Choi, H.: *A dynamic subgrid-scale eddy viscosity model with a global model coefficient.* Physics of Fluids, 18:125109, 2006.

[128] Perera, M. and Walker, R.: *Strategy for measuring infiltration rates in large, multicelled and naturally ventilated buildings using a single tracer gas.* Building Services Engineering Research and Technology, 6(2):82–88, 1985.

[129] Premnath, K. and Abraham, J.: *Three-dimensional multi-relaxation time (mrt) lattice-boltzmann models for multiphase flow.* Journal of Computational Physics, 224:539–559, 2007.

[130] Premnath, K. and Banerjee, S.: *Incorporating forcing terms in cascaded Lattice Boltzmann approach by method of central moments.* Physical Review E, 80(3):36702, 2009.

[131] Premnath, K., Pattison, M., and Banerjee, S.: *Dynamic subgrid scale modeling of turbulent flows using Lattice-Boltzmann method.* Physica A: Statistical Mechanics and its Applications, 388(13):2640–2658, 2009.

[132] Qian, Y., d'Humieres, D., and Lallemand, P.: *Lattice BGK models for Navier-Stokes equation.* Europhysics Letters, 17:479–484, 1992.

[133] Reinhold, T., Brinch, M., and Damsgaard, A.: *Wind tunnel tests for the Great Belt link.* In *Aerodynamics of Large Bridges, Proceedings of the first international symposium of aerodynamics of large bridges*, pp. 255–267, Copenhagen, 1992.

[134] Rinne, H.: *Taschenbuch der Statistik*. 3. Deutsch, Frankfurt am Main, 2003.

[135] Rogallo, R. and Moin, P.: *Numerical simulation of turbulent flows*. Annual Review of Fluid Mechanics, 16(1):99–137, 1984.

[136] Rothmann, D. and Zaleski, S.: *Lattice-Gas Cellular Automata*. Cambridge University Press, 2004.

[137] Rubinstein, R. and Luo, L.: *Theory of the Lattice Boltzmann equation: Symmetry properties of discrete velocity sets*. Physical Review E, 77(3):036709, 2008.

[138] Sagaut, P.: *Toward advanced subgrid models for Lattice-Boltzmann-based large-eddy simulation: theoretical formulations*. Computers & Mathematics with Applications, 59(7):2194–2199, 2010.

[139] Sagaut, P., Deck, S., and Terracol, M.: *Multiscale and multiresolution approaches in turbulence*. Imperial College Press, London, 2006.

[140] Schauer, M.: *Fluid Struktur Interaktion auf Basis der Lattice Boltzmann und Finite Elemente Methode in 3D*. student research project, 2007.

[141] Schlichting, H.: *Grenzschicht-Theorie*. 9. Springer, 1997.

[142] Schönherr, M., Geier, M., and Krafczyk, M.: *3D GPGPU LBM implementation on non-uniform grids*. International Conference on Parallel Computational Fluid Dynamics, 2011.

[143] Schönherr, M., Kucher, K., Geier, M., Stiebler, M., Freudiger, S., and Krafczyk, M.: *Multi-thread implementations of the Lattice Boltzmann method on non-uniform grids for CPUs and GPUs*. Computers & Mathematics with Applications, 61(12):3730–3743, 2011.

[144] Schumann, U.: *Subgrid scale model for finite difference simulations of turbulent flows in plane channels and annuli*. Journal of Computational Physics, 18:376, 1975.

[145] Seeger, S. and Hoffmann, K.: *The cumulant method applied to a mixture of maxwell gases*. Continuum Mechanics and Thermodynamics, 14:321–335, 2002.

[146] Selle, L., Nicoud, F., and Pointsot, T.: *The actual impedance of non-reflecting boundary conditions: implications for the computation of resonators*. AIAA Journal, 42(5):958–964, 2004.

[147] Selvam, P.: *Computational procedures in grid based computational bridge arerodynamics*. Bridge Aerodynamics, pp. 327–336, 1998.

[148] Selvam, P., Bosch, H., and Joshi, R.: *Comparison of 2D and 3D CFD modeling of bridge aerodynamics*. In *Proc. 5th International Symposium on Computational Wind Engineering*, Chapel Hill, NC, 2010.

[149] Severini, T.: *Elements of distribution theory*. Cambridge series on statistical and probabilistic mathematics. Cambridge University Press, Cambridge, 2005.

[150] Shah, R. and London, A.: *Laminar flow forced convection heat transfer and flow friction in straight and curved ducts-a summary of analytical solutions.* Techn. rep., DTIC Document, 1971.

[151] Shan, X., Yuan, X., and Chen, H.: *Kinetic theory representation of hydrodynamics: a way beyond the Navier-Stokes equation.* Journal of Fluid Mechanics, 550:413–441, 2006.

[152] Simiu, E. and Scanlan, R.: *Wind effects on structures: An Introduction to Wind Engineering*, vol. 1. John Wiley & Sons, New York, 1978.

[153] Smagorinsky, J.: *General circulation experiments with the primitive equations – I The basic experiment.* 91(3):99–164, 1963.

[154] Smith, A.M.O. Cebeci, T.: *Numerical solution of the turbulent boundary layer equations.* Douglas Aircraft division report DAC, 33735, 1967.

[155] Spalart, P., Jou, W., Strelets, M., and Allmaras, S.: *Comments of feasibility of les for wings, and on a hybrid RANS/LES approach.* In *First AFOSR International Conference on DNS/LES, Rouston, La*, 1997.

[156] Spasov, M., Rempfer, D., and Mokhasi, P.: *Simulation of a turbulent channel flow with an entropic Lattice Boltzmann method.* International Journal for Numerical Methods in Fluids, 60:1241–1258, 2009.

[157] Taylor, G. and Green, A.: *Mechanism of the production of small eddies from large ones.* Proceedings of the Royal Society London, 158(895):499–521, 1937.

[158] Teixeira, C.: *Incorporating Turbulence Models into the Lattice-Boltzmann method.* International Journal of Modern Physics C, 9(8):1159–1175, 1998.

[159] Thürey, N.: *A single-phase free-surface Lattice-Boltzmann method.* Universität Erlangen-Nürnberg, Diplomarbeit, 2003.

[160] Tölke, J.: *Implementation of a Lattice Boltzmann kernel using the compute unified device architecture developed by nVIDIA.* Computing and Visualization in Science, 13(1):29–39, 2010.

[161] Tölke, J., Freudiger, S., and Krafczyk, M.: *An adaptive scheme using hierarchical grids for Lattice Boltzmann multi-phase flow simulations.* Computers & Fluids, 35(8-9):820–830, 2006.

[162] Tölke, J. and Krafczyk, M.: *TeraFLOP computing on a desktop PC with GPUs for 3D CFD.* International Journal of Computational Fluid Dynamics, 22:443–456, 2008.

[163] Treeck, C. van, Rank, E., Krafczyk, M., Tölke, J., and Nachtwey, B.: *Extension of a hybrid thermal LBE scheme for large-eddy simulations of turbulent convective flows.* Computers and Fluids, 35(8-9):863–871, 2006.

[164] Turbulence and Heat Transfer Laboratory, Department of Mechanical Engineering, The University of Tokyo (Ed.): *DNS database to turbulence and heat transfer*, visited: Oktober 2010. `url:http://www.thtlab.t.u-tokyo.ac.jp/`.

[165] Uphoff, S., Geller, S., and Krafczyk, M.: *study of flow around a bridge cross section with a Lattice Boltzmann LES model.* In *International Conference on Wind Engineering 13*, Amsterdam, 2011.

[166] Uphoff, S., Krafczyk, M., Schönherr, M., and Stiebler, Maik und Zagari, M.: *Numerische Simulation von Gebäudebelüftung bei aüsserem Wind mit einem Lattice Boltzmann LES Model.* In *BauSim*, Berlin, 2012.

[167] Vreman, A.W.: *An eddy-viscosity subgrid-scale model for turbulent shear flow: Algebraic theory and applications.* Physics of Fluids, 16(10):3670–3681, 2004. `http://link.aip.org/link/?PHF/16/3670/1`.

[168] Wagner, T. and Peil, U.: *Ice formation on transmission line cables in tandem arrangement.* In *International Conference on Wind Engineering 13*, 2011.

[169] Walther, J.: *Discrete Vortex Method for Two-dimensional Flow past Bodies of Arbitrary Shape Undergoing Prescribed Rotary and Translational Motion.* PhD thesis, Technical University of Denmark, Kgs. Lyngby, 1994.

[170] Weickert, M., Teike, G., Schmidt, O., and Sommerfeld, M.: *Investigation of the LES WALE turbulence model within the Lattice Boltzmann framework.* Computers & Mathematics with Applications, 59(7):2200–2214, 2010.

[171] Weintraub, S.: *Representation Theory of Finite Groups, Graduate Studies in Mathematics*, vol. 59. American Mathematical Society, Procidence, RI, USA, 2003.

[172] Werner, H. and Wengle, H.: *Large-eddy simulation of turbulent flow over and around a cube in a plate channel.* In *Proc. 8th symposium on turbulent shear flows*, pp. 155–168, Berlin, 1993. Springer.

[173] WHO Collaborating Centre for Research on the Epidemiology of Disasters (eds.): *International disaster database*, visited: July 2011. `url:http://www.emdat.be/`.

[174] Wilcox, D.: *Turbulence modeling for CFD.* D C W Industries, La Canada, Calif., 1993.

[175] Wilde, A.: *Application of the lattice-boltzmann method in flow acoustics.* In *Fourth SWING Aeroacoustic Workshop, Aachen*, 2004.

[176] Wygnanski, I. and Fiedler, H.: *Some measurements in the self-preserving jet.* Journal of Fluid Mechanics, 38(03):577–612, 1969.

[177] Yakhot, A., Liu, H., and Nikitin, N.: *Turbulent flow around a wall-mounted cube: A direct numerical simulation.* International journal of heat and fluid flow, 27(6):994–1009, 2006.

[178] Yu, H., Luo, L., and Girimaji, S.: *LES of turbulent square jet flow using an MRT Lattice Boltzmann model.* Computers and Fluids, 35(8-9):957–965, 2006.

Appendix

A Lattice Boltzmann stencils

Below, the stencils of the models used in this work are listed.
$D2Q9$

$$\{\mathbf{e}_i, i=0,\dots,8\} = \begin{Bmatrix} 0 & 1 & -1 & 0 & 0 & 1 & -1 & 1 & -1 \\ 0 & 0 & 0 & 1 & -1 & 1 & -1 & -1 & 1 \end{Bmatrix},$$

$D3Q19$

$$\{\mathbf{e}_i, i=0,\dots,18\} = \begin{Bmatrix} 0 & 1 & -1 & 0 & 0 & 0 & 0 & 1 & -1 & 1 & -1 & 1 & -1 & 1 & -1 & 0 & 0 & 0 & 0 \\ 0 & 0 & 0 & 1 & -1 & 0 & 0 & 1 & -1 & -1 & 1 & 0 & 0 & 0 & 0 & 1 & -1 & 1 & -1 \\ 0 & 0 & 0 & 0 & 0 & 1 & -1 & 0 & 0 & 0 & 0 & 1 & -1 & -1 & 1 & 1 & -1 & -1 & 1 \end{Bmatrix},$$

$D3Q27$

$$\{\mathbf{e}_i, i=0,\dots,15\} = \begin{Bmatrix} 0 & 1 & -1 & 0 & 0 & 0 & 0 & 1 & -1 & 1 & -1 & 1 & -1 & 1 & -1 & 0 \\ 0 & 0 & 0 & 1 & -1 & 0 & 0 & 1 & -1 & -1 & 1 & 0 & 0 & 0 & 0 & 1 \\ 0 & 0 & 0 & 0 & 0 & 1 & -1 & 0 & 0 & 0 & 0 & 1 & -1 & -1 & 1 & 1 \end{Bmatrix}$$

$$\{\mathbf{e}_i, i=16,\dots,26\} = \begin{Bmatrix} 0 & 0 & 0 & 1 & -1 & 1 & 1 & -1 & -1 & 1 & -1 \\ -1 & 1 & -1 & 1 & 1 & -1 & 1 & -1 & 1 & -1 & -1 \\ -1 & -1 & 1 & 1 & 1 & 1 & -1 & 1 & -1 & -1 & -1 \end{Bmatrix}$$

B The Central Moment Method in tables

In the following a 2D guide to implementing cascaded models is given. In 2D for the $D2Q9$ model only nine distinct moments exist which are listed in Table 5.1

order	moments		
0	μ_0		
1	μ_1	μ_2	
2	μ_{11}	μ_{22}	μ_{12}
3	μ_{112}	μ_{211}	
4	μ_{1122}		

Table 5.1: $D2Q9$ *moments*

these moments are computed as for the MRT model. (For the $D2Q5$ model only the moments μ_0, μ_1, μ_2, μ_{11}, and μ_{12} can be distinguished, so no cascaded model can be defined). Central moments for the non-conserved moments (second order and higher) can be found in Table 5.2

central moment	transformation	equilibrium
M_{11}	$\mu_{11} - \mu_1^2$	1/3
M_{22}	$\mu_{22} - \mu_2^2$	1/3
M_{12}	$\mu_{12} - \mu_1\mu_2$	0
M_{112}	$\mu_{112} - \mu_{11}\mu_2 - 2\mu_1\mu_{12} + 2\mu_1\mu_1\mu_2$	0
M_{122}	$\mu_{122} - \mu_{22}\mu_1 - 2\mu_2\mu_{12} + 2\mu_1\mu_2\mu_2$	0
M_{1122}	$\mu_{1122} - 2\mu_{112}\mu_2 - 2\mu_{122}\mu_1 + 4\mu_{11}\mu_{22}$ $+\mu_1^2\mu_{22} + \mu_{11}\mu_2^2 + 4\mu_1\mu_2\mu_{12} - 3\mu_1^2\mu_2^2$	1/9

Table 5.2: *D2Q9 central moments*

The spaces spanned by the following subsets (Table 5.3) are left invariant under 90° rotations of the coordinate system and under inversions ($q \to \bar{q}$)

name	moments
0e	μ_0
1o	μ_1 μ_2
2e	$\mu_{11} + \mu_{22}$
2o	$\mu_{11} - \mu_{22}$ μ_{12}
3e	$\mu_{112} + \mu_{211}$
3o	$\mu_{112} - \mu_{211}$
4e	μ_{1122}

Table 5.3: *Subsets of D2Q9 moments invariant under rotation and inversion*

For each of these subsets only one relaxation factor should be used. In two dimensions only the fourth-order cumulant differs from the central moment. In order to clarify the concept, the higher-than-third-order cumulants in three directions are listed below in Table 5.4

cumulant	transformation	equilibrium
C_{XXYY}	$M^c_{XXYY} - M^c_{XX}M^c_{YY} - 4{M^c_{XY}}^2$	0
C_{XXZZ}	$M^c_{XXZZ} - M^c_{XX}M^c_{ZZ} - 2{M^c_{XZ}}^2$	0
C_{YYZZ}	$M^c_{YYZZ} - M^c_{YY}M^c_{ZZ} - 2{M^c_{YZ}}^2$	0
C_{XXYZ}	$M^c_{XXYZ} - M^c_{XX}M^c_{YZ} - 2M^c_{XY}M^c_{XZ}$	0
C_{XYYZ}	$M^c_{XYYZ} - M^c_{XZ}M^c_{YY} - 2M^c_{XY}M^c_{YZ}$	0
C_{XYZZ}	$M^c_{XYZZ} - M^c_{XY}M^c_{ZZ} - 2M^c_{XZ}M^c_{YZ}$	0
C_{XXYYZ}	$M^c_{XXYYZ} - (M^c_{XX}M^c_{YYZ} + 4M^c_{XY}M^c_{XYZ} + 2M^c_{XZ}$ $M^c_{XYY} + 2M^c_{XXY}M^c_{YZ} + M^c_{XXZ}M^c_{YY})$	0
C_{XYYZZ}	$M^c_{XYYZZ} - (2M^c_{XY}M^c_{YZZ} + M^c_{XYY}M^c_{ZZ} + 4M^c_{XYZ}M^c_{YZ}$ $+M^c_{XZZ}M^c_{YY} + 2M^c_{XZ}M^c_{YYZ})$	0
C_{XXYZZ}	$M^c_{XXYZZ} - (M^c_{XX}M^c_{YZZ} + 2M^c_{XY}M^c_{XZZ} + M^c_{XXY}M^c_{ZZ}$ $+4M^c_{XYZ}M^c_{XZ} + 2M^c_{YZ}M^c_{XXZ})$	0
C_{XXYYZZ}	$M^c_{XXYYZZ} - C_{XXYY}M^c_{ZZ} - C_{XXZZ}M^c_{YY}$ $-C_{YYZZ}M^c_{XX} - 2M^c_{XXY}M^c_{YZZ} - 2M^c_{XYY}M^c_{XZZ}$ $-2M^c_{XXZ}M^c_{YYZ} - M^c_{XYZ}M^c_{XYZ} - M^c_{XX}M^c_{YY}M^c_{ZZ}$ $-4M^c_{XX}M^c_{YZ}M^c_{YZ} - 4M^c_{XY}M^c_{XY}M^c_{ZZ}$ $-8M^c_{XY}M^c_{XZ}M^c_{YZ} - 4M^c_{XZ}M^c_{XZ}M^c_{YY}$	0

Table 5.4: $D3Q27$ *cumulants*

The factorized equilibria are the same as the centralized equilibria for third order and lower order central moments. In Table 5.5 we again give the equilibria for the $D3Q27$ model for those equilibria which differ from the basic CLB method.

central moment	equilibrium	factorized CLB equilibrium
M^c_{1122}	$\frac{1}{9}$	$M^c_{11}M^c_{22}$
M^c_{1133}	$\frac{1}{9}$	$M^c_{11}M^c_{33}$
M^c_{2233}	$\frac{1}{9}$	$M^c_{22}M^c_{33}$
M^c_{1233}	0	$M^c_{33}M^c_{12}$
M^c_{1223}	0	$M^c_{22}M^c_{13}$
M^c_{1123}	0	$M^c_{11}M^c_{23}$
M^c_{112233}	$\frac{1}{27}$	$M^c_{11}M^c_{22}M^c_{33}$

Table 5.5: *Factorized CLB equilibria*

After relaxation in the chosen space, the inverse transformation is carried out and the distribution functions are propagated.

C Sets of relaxation parameters

Table 5.6 lists the relaxation coefficients and corresponding moments. In the following several sets $D3Q27$ of relaxation parameters will be defined that are used throughout the present work.

μ_{12}, μ_{13}, μ_{23}, $\mu_{11}-\mu_{22}$, $\mu_{11}-\mu_{33}$	s_1
$\mu_{11}+\mu_{22}+\mu_{33}$	s_2
$\mu_{122}+\mu_{133}$, $\mu_{112}+\mu_{233}$, $\mu_{133}+\mu_{233}$	s_3
$\mu_{122}-\mu_{133}$, $\mu_{112}-\mu_{233}$, $\mu_{133}-\mu_{233}$	s_4
μ_{123}	s_5
$\mu_{1122}-2\mu_{1133}+\mu_{2233}$, $\mu_{1122}+\mu_{1133}-2\mu_{2233}$	s_6
$\mu_{1122}+\mu_{1133}+\mu_{2233}$	s_7
μ_{1223}, μ_{1223}, μ_{1233}	s_8
μ_{12233}, μ_{11233}, μ_{11223}	s_9
μ_{112233}	s_{10}

Table 5.6: *Relaxation parameters and corresponding moments*

Set I

$$\begin{aligned} s_3 &= s_1 \\ s_2 &= s_6 = s_7 = s_8 = s_9 = s_{10} = 1 \\ s_4 &= s_5 = 2 - s_1 \end{aligned} \tag{5.1}$$

Set II

$$\begin{aligned} s_3 &= s_6 = s_8 = s_1 \\ s_2 &= s_7 = s_9 = s_{10} = 1 \\ s_4 &= s_5 = 2 - s_1 \end{aligned} \tag{5.2}$$

Set all-to-one

$$\begin{aligned} s_3 &= s_6 = s_8 = 1 \\ s_2 &= s_7 = s_9 = s_{10} = 1 \\ s_4 &= s_5 = 1 \end{aligned} \tag{5.3}$$

Set III

$$\begin{aligned} s_3 &= s_4 = s_5 = s_6 = s_8 = s_1 \\ s_2 &= s_7 = s_9 = s_{10} = 1 \end{aligned} \tag{5.4}$$

D Table of central moments in three dimensions

Finally, all central moments for the $D3Q27$ model are listed with their transformation from moments to central moments and the equilibrium of the central moment for the standard CLB model.

central moment	transformation	equilibrium
M^c_{11}	$\mu_{11} - \mu_1^2$	1/3
M^c_{22}	$\mu_{22} - \mu_2^2$	1/3
M^c_{33}	$\mu_{33} - \mu_3^2$	1/3
M^c_{12}	$\mu_{12} - \mu_1\mu_2$	0
M^c_{13}	$\mu_{13} - \mu_1\mu_3$	0
M^c_{23}	$\mu_{23} - \mu_2\mu_3$	0
M^c_{112}	$\mu_{112} - \mu_{11}\mu_2 - 2\mu_1\mu_{12} + 2\mu_1\mu_1\mu_2$	0
M^c_{122}	$\mu_{122} - \mu_{22}\mu_1 - 2\mu_2\mu_{12} + 2\mu_1\mu_2\mu_2$	0
M^c_{113}	$\mu_{113} - \mu_{11}\mu_3 - 2\mu_1\mu_{13} + 2\mu_1\mu_1\mu_3$	0
M^c_{133}	$\mu_{133} - \mu_{33}\mu_1 - 2\mu_3\mu_{13} + 2\mu_1\mu_3\mu_3$	0
M^c_{223}	$\mu_{223} - \mu_{22}\mu_3 - 2\mu_2\mu_{23} + 2\mu_2\mu_2\mu_3$	0
M^c_{233}	$\mu_{233} - \mu_{33}\mu_2 - 2\mu_3\mu_{23} + 2\mu_2\mu_3\mu_3$	0
M^c_{123}	$\mu_{123} - \mu_{12}\mu 3 - \mu_{23}\mu 1 - \mu_3\mu 12 + 2\mu_1\mu_2\mu_3$	0
M^c_{1122}	$\mu_{1122} - 2\mu_{112}\mu_2 - 2\mu_{122}\mu_1 + 4\mu_{11}\mu_{22}$ $+\mu_1^2\mu_{22} + \mu_{11}\mu_2^2 + 4\mu_1\mu_2\mu_{12} - 3\mu_1^2\mu_2^2$	1/9
M^c_{1133}	$\mu_{1133} - 2\mu_{113}\mu_3 - 2\mu_{133}\mu_1 + 4\mu_{11}\mu_{33}$ $+\mu_1^2\mu_{33} + \mu_{11}\mu_3^2 + 4\mu_1\mu_3\mu_{13} - 3\mu_1^2\mu_3^2$	1/9
M^c_{2233}	$\mu_{2233} - 2\mu_{223}\mu_3 - 2\mu_{233}\mu_2 + 4\mu_{22}\mu_{33}$ $+\mu_2^2\mu_{33} + \mu_{22}\mu_3^2 + 4\mu_2\mu_3\mu_{23} - 3\mu_2^2\mu_3^2$	1/9
M^c_{1233}	$-3\mu_3^2\mu_2\mu_1 + \mu_{33}\mu_2\mu_1 + 2\mu_3\mu_{23}\mu_1 - \mu_{233}\mu_1 +$ $2\mu_3\mu_2\mu_{13} - \mu_2\mu_{133} + \mu_3^2\mu_{12} - 2\mu_3\mu_{123} + \mu_{1233}$	0
M^c_{1223}	$-3\mu_2^2\mu_3\mu_1 + \mu_{22}\mu_3\mu_1 + 2\mu_2\mu_{23}\mu_1 - \mu_{223}\mu_1 +$ $2\mu_3\mu_2\mu_{12} - \mu_3\mu_{122} + \mu_2^2\mu_{13} - 2\mu_2\mu_{123} + \mu_{1223}$	0
M^c_{1123}	$-3\mu_1^2\mu_2\mu_3 + \mu_{11}\mu_2\mu_3 + 2\mu_3\mu_{12}\mu_1 - \mu_{112}\mu_3 +$ $2\mu_1\mu_2\mu_{13} - \mu_2\mu_{113} + \mu_1^2\mu_{32} - 2\mu_1\mu_{123} + \mu_{1123}$	0
M^c_{11223}	$4\mu_3\mu_2^2\mu_1^2 - 2\mu_2\mu_{23}\mu_1^2 - \mu_3\mu_{22}\mu_1^2$ $+\mu_{223}\mu_1^2 - 2*\mu_2^2\mu_1\mu_{13} - 4*\mu_3\mu_2\mu_1\mu_{12} + 4*\mu_2\mu_1\mu_{123} +$ $2*\mu_3\mu_1\mu_{122} - 2\mu_1\mu_{1223} - \mu_3\mu_2^2\mu_{11} + \mu_2^2\mu_{113} +$ $2*\mu_3\mu_2\mu_{112} - 2\mu_2\mu_{1123} - \mu_3\mu_{1122} + \mu_{11223}$	0
M^c_{11233}	$4\mu_3^2\mu_2\mu_1^2 - \mu_{33}\mu_2\mu_1^2 - 2\mu_3\mu_{23}\mu_1^2$ $+\mu_{233}\mu_1^2 - 4\mu_3\mu_2\mu_1\mu_{13} +$ $2\mu_2\mu_1\mu_{133} - 2\mu_3^2\mu_1\mu_{12} +$ $4\mu_3\mu_1\mu_{123} - 2\mu_1\mu_{1233} - \mu_3^2\mu_2\mu_{11} +$ $2\mu_3\mu_2\mu_{113} - \mu_2\mu_{1133} + \mu_3^2\mu_{112} - 2\mu_3 * mu_{1123} + \mu_{11233}$	0
M^c_{12233}	$4\mu_3^2\mu_2^2\mu_1 - \mu_{33}\mu_2^2\mu_1 - 2\mu_3\mu_{13}\mu_2^2$ $+\mu_{133}\mu_2^2 - 4\mu_3\mu_2\mu_1\mu_{23} + 2\mu_2\mu_1\mu_{233} -$ $2\mu_3^2\mu_2\mu_{12} + 4\mu_3\mu_2\mu_{123} - 2\mu_2\mu_{1233} -$ $\mu_3^2\mu_1\mu_{22} + 2\mu_3\mu_1\mu_{223} - \mu_1\mu_{2233} + \mu_3^2\mu_{122} - 2\mu_3 * mu_{1223} + \mu_{12233}$	0
M^c_{112233}	$-5\mu_3^2\mu_2^2\mu_1^2 + \mu_{33}\mu_2^2\mu_1^2 + 4\mu_3\mu_2\mu_{23}\mu_1^2 - 2\mu_2\mu_{233}\mu_1^2 +$ $\mu_3^2\mu_{22}\mu_1^2 - 2\mu_3\mu_{223}\mu_1^2 + \mu_{2233}\mu_1^2 + 4\mu_3\mu_2^2\mu_1\mu_{13} -$ $2\mu_2^2\mu_1\mu_{133} + 4\mu_3^2\mu_2\mu_1\mu_{12} - 8\mu_3\mu_2\mu_1\mu_{123} + 4\mu_2\mu_1\mu_{1233} -$ $2\mu_3^2\mu_1\mu_{122} + 4\mu_3\mu_1\mu_{1223} - 2\mu_1\mu_{12233} + \mu_3^2\mu_2^2\mu_{11}$ $-2\mu_3\mu_2^2\mu_{113} + \mu_2^2\mu_{1133} - 2\mu_3\mu_3\mu_2\mu_{112} + 4\mu_3\mu_2\mu_{1123}$ $-2\mu_2\mu_{11233} + \mu_3^2\mu_{1122} - 2\mu_3\mu_{11223} + \mu_{112233}$	1/27

Table 5.7: *Central moments, transformation, and equilibria in three dimensions*